LEABHARLANN CHOLÁISTE NA TRÍONÓIDE, BAILE ÁTHA CLIATH
Ollscoil Átha Cliath

TRINITY COLLEGE LIBRARY DUBLIN
The University of Dublin

Terms and Conditions of Use of Digitised Theses from Trinity College Library Dublin

Copyright statement

All material supplied by Trinity College Library is protected by copyright (under the Copyright and Related Rights Act, 2000 as amended) and other relevant Intellectual Property Rights. By accessing and using a Digitised Thesis from Trinity College Library you acknowledge that all Intellectual Property Rights in any Works supplied are the sole and exclusive property of the copyright and/or other IPR holder. Specific copyright holders may not be explicitly identified. Use of materials from other sources within a thesis should not be construed as a claim over them.

A non-exclusive, non-transferable licence is hereby granted to those using or reproducing, in whole or in part, the material for valid purposes, providing the copyright owners are acknowledged using the normal conventions. Where specific permission to use material is required, this is identified and such permission must be sought from the copyright holder or agency cited.

Liability statement

By using a Digitised Thesis, I accept that Trinity College Dublin bears no legal responsibility for the accuracy, legality or comprehensiveness of materials contained within the thesis, and that Trinity College Dublin accepts no liability for indirect, consequential, or incidental, damages or losses arising from use of the thesis for whatever reason. Information located in a thesis may be subject to specific use constraints, details of which may not be explicitly described. It is the responsibility of potential and actual users to be aware of such constraints and to abide by them. By making use of material from a digitised thesis, you accept these copyright and disclaimer provisions. Where it is brought to the attention of Trinity College Library that there may be a breach of copyright or other restraint, it is the policy to withdraw or take down access to a thesis while the issue is being resolved.

Access Agreement

By using a Digitised Thesis from Trinity College Library you are bound by the following Terms & Conditions. Please read them carefully.

I have read and I understand the following statement: All material supplied via a Digitised Thesis from Trinity College Library is protected by copyright and other intellectual property rights, and duplication or sale of all or part of any of a thesis is not permitted, except that material may be duplicated by you for your research use or for educational purposes in electronic or print form providing the copyright owners are acknowledged using the normal conventions. You must obtain permission for any other use. Electronic or print copies may not be offered, whether for sale or otherwise to anyone. This copy has been supplied on the understanding that it is copyright material and that no quotation from the thesis may be published without proper acknowledgement.

Electronic structure studies of *p*-type semiconducting oxides

David O. Scanlon

Trinity College Dublin.

Supervisor : Prof. Graeme W. Watson

A thesis submitted in partial fulfillment of the requirements
for the degree of Doctor of Philosophy at the University of Dublin.
2011

Declaration

I hereby declare that:

This thesis has not been submitted as an exercise for a degree at this or any other University.

The work contained herein is entirely my own except where otherwise cited, referenced, or acknowledged in the text.

I agree that the library of the University of Dublin may at their discretion lend or copy the thesis upon request

Trinity College Dublin

Summary

Transparent conducting oxides (TCOs) are a unique class of materials which combine the normally mutually exclusive properties of transparency and conduction. Despite the many applications and widespread interest in TCO materials, there are a number of unanswered questions regarding the electronic structure and defect chemistry of TCO materials, in particular with regard to *p*-type TCOs. The main motivation for the work presented in this thesis has been to fully understand the complex chemistry of the Cu^{I}-based delafossite oxides, and to ascertain if high performance *p*-type TCOs can be produced from these materials.

We begin by examining the electronic structure of $CuM^{III}O_2$ (M^{III} = Al, Cr, Sc, Y) in an attempt to rationalize the conductivity trends reported in the literature. We demonstrate the influence the electronic structure of the M^{III} ion has on the valence band features of these materials, and hence on the mobility of holes in these systems, and use this knowledge to explain the conductivity anomalies reported in experiment, and gain insight into why $CuCrO_2$ is currently the leading *p*-type TCO. We also examined the electronic structure and geometry of the latest *p*-type TCO to be discovered, $CuBO_2$, finding that geometries presented in the sole experimental study on this material are not in keeping with our calculations, or indeed with the structural trends of all other group 13 delafossites.

Next we investigated the defect chemistry of Cu_2O, the parent compound to all the delafossite oxides. We tested three levels of computational complexity on this system, in a bid to rationalize the previous experimental and theoretical results, which quite clearly contradicted each other. Our results demonstrate the failure of PBE and PBE+U to accurately model the polaronic nature of Cu_2O. A hybrid DFT approach is found to be necessary to get a true representation of the defect chemistry of Cu_2O, with our results explaining for the first time the experimentally seen deep trap levels. We also show that the repeated reports of *n*-type conductivity in Cu_2O *cannot* stem from intrinsic defects or adventitious hydrogen impurities.

Using our new understanding of the defect chemistry of Cu^{I}-based oxides gleamed from our Cu_2O results, we investigated the defect chemistry of the prototype Cu^{I}-based delafossite oxide, $CuAlO_2$, and of the most promising p-type TCO, $CuCrO_2$. Our results for both systems showed that the defect chemistry of these systems is activated, and is not conducive to good TCO ability. Interestingly, our results demonstrated that the most energetically favourable defect in $CuAlO_2$ is the Cu_{Al} antisite, and not V_{Cu} as had been proposed previously. We also identified the defect absorptions seen experimentally and the source of the defect signal often mistaken as indirect band gaps for these systems. We found that the ionization levels of p-type defects in $CuCrO_2$ are shallower than those in $CuAlO_2$, which explains the higher conductivities noted for $CuCrO_2$. This result also validates our earlier work on the influence of the electronic structure of M^{III} on mediating conductivity in these systems.

Lastly, with the knowledge that Cu^{I}-based delafossite oxides are not going to produce the elusive degenerate p-type TCO, we examined the electronic structure of $ZnM^{III}_2O_4$ (M^{III} = Co, Rh, Ir) spinels and the layered oxychalcogenide $[Cu_2S_2][Sr_3Sc_2O_5]$ as platform for improved p-type ability. The spinel structure was found to be unsuitable for good p-type ability, but $[Cu_2S_2][Sr_3Sc_2O_5]$ was shown to possess many of the characteristics necessary for good p-TCO ability.

Acknowledgments

First and foremost, I would like to thank my advisor, Prof. Graeme W. Watson, for his guidance and support throughout my postgraduate experience in Trinity. I count myself as very fortunate for having him as a research mentor and collaborator during these years. I would also like to thank Prof. Grayson as Head of the School of Chemistry for allowing me to pursue this PhD and for the use of the facilities of the School of Chemistry.

I wish to acknowledge funding for my PhD from SFI and from the HSE for the IITAC PTRLI (Cycle III) grant. I also would like to thank ICHEC and in particular TCHPC for access to their computing facilities. In particular I want to thank Geoff, Dermot, Jimmy, Neil, Paddy, Jose and Nicola for putting up with my constant demands for more computer time, and all the laughs over the past four years.

A huge thanks goes to my two sensei: Dr. Aron Walsh and Dr. Ben Morgan, who put up with my constant questioning daily, and have not been able to escape it, even after leaving the group. Thanks also to thank Dr. Jeremy Allen for all his advice on making pictures, and using graphical programs. I would like to thank the rest of the Watson research group: Aoife, Kalle, Natasha, Paddy, Mario, Kate, John, Souad, Ni Chaoimh for making our office a fun place to work.

I want to express my gratitude to my brother and especially to my father, Eamon, for his unconditional support throughout the years, even when it did not look like I was going to make it! I think mum would be proud!

Finally, all my deepest thoughts go to Gemma: for all the love and support you have given me during these past years. Your determination and optimism have been a constant source of inspiration to me. You made this possible.

Publications

Related to Thesis Work

1. D. O. Scanlon and G. W. Watson, "Uncovering the complex behaviour of Hydrogen in Cu_2O", Physical Review Letters, 106, 186403 (2011)

2. D. O. Scanlon and G. W. Watson, "Band gap anomalies of the $ZnM_2^{III}O_4$ (M^{III} = Co, Rh, Ir) spinels", Physical Chemistry Chemical Physics, 13, 9667 (2011)

3. D. O. Scanlon and G. W. Watson, "Understanding the *p*-type defect chemistry of $CuCrO_2$", Journal of Materials Chemistry, 21, 3655 (2011)

4. D. O. Scanlon and G. W. Watson, "Conductivity Limits in $CuAlO_2$ from Screened-Hybrid Density Functional Theory", Journal of Physical Chemistry Letters, 1, 3195 (2010)

5. D. O. Scanlon and G. W. Watson, "Undoped *n*-type Cu_2O: Fact or Fiction?", Journal of Physical Chemistry Letters, 1, 2582 (2010)

6. D. O. Scanlon, K. G. Godinho, B. J. Morgan, and G. W. Watson, "Understanding conductivity anomalies in Cu^I-based delafossite transparent conducting oxides: Theoretical insights", Journal of Chemical Physics, 132, 024707 (2010)

7. K. G. Godinho, J. J. Carey, B. J. Morgan, D. O. Scanlon and G. W. Watson, "Understanding conductivity in $SrCu_2O_2$: stability, geometry and electronic structure of intrinsic defects from first principles," Journal of Materials Chemistry, 20, 1086 (2010)

8. D. Shin, J. S. Ford, D. J. Payne, T. Arnold, D. J. Aston, R. G. Egdell, K, G. Godinho, D. O. Scanlon, B. J. Morgan, G. W. Watson, E. Mugnier, C. Yaicle, A. Rougier, L. Colakerol, P. A. Glans, L. F. J. Piper and K. E. Smith, "Comparative study of bandwidths in copper delafossites from x-ray emission spectroscopy", Physical Review B, 80, 233105 (2009)

9. D. O. Scanlon and G. W. Watson, "$[Cu_2S_2][Sr_3Sc_2O_5]$ A layered, Direct Band Gap, *p*-Type Transparent Conducting Oxychalcogenide: A theoretical Analysis", Chemistry of Materials, 21, 5435 (2009)

10. D. O. Scanlon, B. J. Morgan, G. W. Watson and A. Walsh, "Acceptor Levels in p-Type Cu_2O: Rationalizing Theory and Experiment", Physical Review Letters, 103, 096405 (2009)

11. D. O. Scanlon, B. J. Morgan and G. W. Watson, "Modeling the polaronic nature of p-type defects in Cu_2O: The failure of GGA and GGA + U", Journal of Chemical Physics, 131, 124703 (2009)

12. D. O. Scanlon, A. Walsh and G. W. Watson, "Understanding the p-Type Conduction Properties of the Transparent Conducting Oxide $CuBO_2$: A Density Functional Theory Analysis", Chemistry of Materials, 21, 4568 (2009)

13. T. Arnold, D. J. Payne, A. Bourlange, J. P. Hu, R. G. Egdell, L. F. J. Piper, L. Colakerol, A. De Masi, P. A. Glans, T. Learmonth, K. E. Smith, J. Guo, D. O. Scanlon, A. Walsh, B. J. Morgan and G. W. Watson, "X-ray spectroscopic study of the electronic structure of $CuCrO_2$", Physical Review B, 79, 075102 (2009)

14. D. O. Scanlon, A. Walsh, B. J. Morgan, G. W. Watson, D. J. Payne and R. G. Egdell, "Effect of Cr substitution on the electric structure of $CuAl_{1-x}Cr_xO_2$", Physical Review B, 79, 035101 (2009)

Not Related to Thesis Work

1. A. B. Kehoe, D. O. Scanlon and G. W. Watson, "On the nature of the band gap of Tl_2O_3", Physical Review B, In Press (2011)

2. K. G. Godinho, B. J. Morgan, J. P. Allen. D. O. Scanlon and G. W. Watson, "Chemical bonding in copper-based transparent conducting oxides: $CuMO_2$ (M = In, Ga, Sc)", Journal of Physics: Condensed Matter, In Press (2011)

3. J. P. Allen, M. K. Nilsson, D. O. Scanlon, and G. W. Watson, "A comparison of the defective pyrochlore and ilmenite polymorphs of $AgSbO_3$ using GGA and hybrid-DFT", Physical Review B, 83, 035207 (2011)

4. D. O. Scanlon, B. J. Morgan, and G. W. Watson, "The origin of the enhanced oxygen storage capacity of $Ce_{1-x}(Pb/Pt)_xO_2$", Physical Chemistry Chemical Physics, 13, 4297 (2011)

5. D. O. Scanlon and G. W. Watson, "Stability, geometry, and electronic structure of an alternative I-III-VI_2 material, $CuScS_2$: A hybrid density functional theory analysis", Applied Physics Letters, 97, 131904 (2010)

6. J. P. Allen, D. O. Scanlon, and G. W. Watson, "Electronic structure of mixed-valence silver oxide AgO from hybrid density-functional theory", Physical Review B, 81, 161103(R) (2010)

7. D. O. Scanlon, G. W. Watson, D. J. Payne, G. R. Atkinson, R. G. Egdell and D. S. Law, "Theoretical and Experimental Study of the Electronic Structures of MoO_3 and MoO_2", Journal of Physical Chemistry C, 114, 4636 (2010)

8. P. R. L. Keating, D. O. Scanlon, and G. W. Watson, "Intrinsic ferromagnetism in CeO_2: dispelling the myth of vacancy site localization mediated superexchange", Journal of Physics: Condensed Matter, 21, 405502 (2009)

9. D. O. Scanlon, N. M Galea, B. J. Morgan and G. W. Watson, "Reactivity on the (110) Surface of Ceria: A GGA plus U Study of Surface Reduction and the Adsorption of CO and NO_2", Journal of Physical Chemistry C, 113, 11095-11103, (2009)

10. B. J. Morgan, D. O. Scanlon and G. W. Watson, "Small polarons in Nb- and Ta-doped rutile and anatase TiO_2", Journal of Materials Chemistry, 19, 5175-5178 (2009)

11. B. J. Morgan, D. O. Scanlon and G. W. Watson, "The Use of the '+U' Correction in Describing Defect States at Metal Oxide Surfaces: Oxygen Vacancies on CeO_2 and TiO_2, and Li-doping of MgO", E-journal of Surface Science and Nanotechnology, 7, 389-394 (2009)

12. N. M. Galea, D. O. Scanlon, B. J. Morgan, and G. W. Watson, "A GGA+U study of the reduction of ceria surfaces and their partial reoxidation through NO_2 adsorption", Molecular Simulation 35, 577-583 (2009)

13. D. O. Scanlon, A. Walsh, B. J. Morgan and G. W. Watson, "Competing defect mechanisms and hydrogen adsorption on Li-doped MgO low index surfaces: A DFT+U study", E-journal of Surface Science and Nanotechnology, 7, 395-404 (2009)

14. N. M. Galea, D. O. Scanlon, P. Martin and G. W. Watson, "Defect Ceria Surfaces : Comparing Interatomic Potentials with Density Functional Theory", E-journal of Surface Science and Nanotechnology, 7, 413-420 (2009)

15. D. O. Scanlon, A. Walsh, B. J. Morgan and G. W. Watson, "An *ab initio* study of reduction of V_2O_5 through the formation of oxygen vacancies and Li intercalation", Journal of Physical Chemistry C, 112, 9903-9911 (2008)

16. D. O. Scanlon, A. Walsh, B. J. Morgan, M. Nolan, J. Fearon and G. W. Watson, "Surface sensitivity in Li-doping of MgO: A density functional theory study with correction for on-site coulomb interactions", Journal of Physical Chemistry C, 111, 7971-7979, (2007)

Abbreviations

AIM: Atoms in Molecules
CI: Configuration Interaction
CB: Conduction band
CBM: Conduction band minimum
DFT: Density Functional Theory
EDOS: Electronic density of states
EXAFS: Extended x-ray absorption fine structure
FTO: Fluorine tin oxide
GGA: Generalised gradient approximation
IR: Infra-red
ITO: Indium tin oxide
HF: Hartree-Fock
HDFT: Hybrid density functional theory
HSE: Heyd Scuseria Ernzerhof hybrid-DFT functional
LDA: Local density approximation
LYP: Lee Yang Parr functional
MP: Monkhorst-Pack
NEB: Nudged elastic band
PAW: Projector augmented wave
OTL: Optical transition level
PBE: Perdew Burke Ernzerhof DFT functional
PEDOS: Partial electronic density of states
PW91: Perdew Wang 91 functional
SCF: Self Consisten Field
SCSOS: $[Cu_2S_2][Sr_3Sc_2O_5]$
SIE: Self-interaction error
SPL: Single particle level
TCO: Transparent conducting oxide
TL: Transition level (thermodynamic)
UPS: Ultraviolet photoelectron spectroscopy
UV: Ultraviolet
VASP: Vienna Ab-Initio Simulation Package
VB: Valence band
VBM: Valence band maximum
XANES: X-ray absorption near edge spectroscopy
XAS: X-ray absorption spectroscopy
XES: X-ray emission spectroscopy
XPS: X-ray photoelectron spectroscopy

Contents

List of Figures

List of Tables

Chapter 1

Introduction

1.1 Transparent Conducting Oxides

Transparent conducting oxides (TCOs) are unique materials that combine concomitant electrical conductivity and optical transparency in a single material. The majority of materials that are transparent to visible light (e.g. glass), behave as electronic insulators, i.e. they do not conduct electricity, and often possess electrical conductivities as low as $10^{-10}\,\mathrm{S\,cm^{-1}}$. Conversely, materials that possess high conductivities, such as metals (conductivities in the range $10^4 - 10^7\,\mathrm{S\,cm^{-1}}$), generally do not transmit visible light. Combining both of these normally mutually exclusive properties in a single compound is therefore quite unusual, and gives TCO materials a very important role in modern optoelectronic applications.[1–3]

Historically, TCO ability was first discovered over a century ago when transparent films of cadmium oxide (CdO) were found to possess conductivities of $\sim 10^3\,\mathrm{S\,cm^{-1}}$. [4] Following on from this, TCO ability was noted in tin dioxide (SnO_2) in 1931,[5], and interestingly, SnO_2 TCO thin films were utilized to defrost windshields on military airplanes during World War II.[6] The next TCO to be discovered was indium oxide (In_2O_3, also known as india) in 1947[7] and this was followed by zinc oxide (ZnO) in 1971.[8] Many other materials which are transparent to visible light and are able to conduct electricity have subsequently been discovered,[?] but to date their performances have not reached the levels of SnO_2, ZnO and In_2O_3, which have been incrementally improved as the years progress, Figure 1.1.[9]

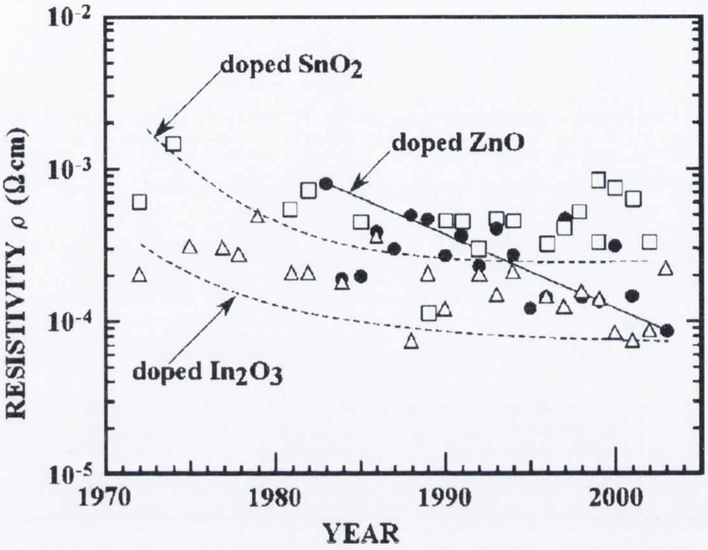

Figure 1.1: Resistivity of doped TCO films from 1972 to 2005. Squares, triangles and circles denote SnO_2, In_2O_3 and ZnO respectively.[9]

The industry standard TCO is Sn doped In_2O_3 (known as indium tin oxide or ITO), which is due to the fact that lower resistivities have been reported in ITO than in any other TCO. Transparency in ITO can be maintained as high as 90 %, while achieving as low a resistivity as 7.2×10^{-5} Ω cm.[10] This high performance has led to a huge increase in demand for ITO, and to a huge increase in the cost of indium metal. Indium is also used in the production of Cu(In/Ga)S_2 (CIGS) solar cell absorbers, which has also served to increase the cost of indium metal.[9] Indium is a rare metal, having an abundance in the Earth's crust of just 160 ppb by weight. To put this into context, the abundances of Zn and Sn are 7900 ppb and 2200 ppb respectively.[9] Therefore, the low abundance of indium has sparked a renewed research drive to unearth indium-free n-type TCOs, and to this end the optimization of conductivity and transparency in ZnO and SnO_2 has become a major research goal.

Although TCOs have been used extensively in many optoeletronic devices, including as transparent electrodes in solar cells, front electrodes in flat panel displays, lowemissivity windows etc.,[6] their applications are somewhat limited by the fact that *all* the high performance TCOs display soley *n*-type conductivity.[11] The development of fully transparent electronics, in which all components (e.g. wires, transistors, capacitors etc.) are essentially invisible, is predicated upon the development of high performance *p*-type TCOs. To date, however, the development of a high figure-of-merit *p*-type TCO has proved very challenging with the development of a TCO showing *native* *p*-type ability first reported in 1997.[12] However the resistivities of the *p*-type TCOs developed thus far have proved to be extremely high compared to their *n*-type counterparts, limiting the development of transparent devices.

1.2 TCO Applications

Following on from the initial use of SnO_2 in defrosting aeroplane windows in World War II,[6] the range of applications of transparent conducting films has steadily increased, to the point where they are now in wide commercial use in applications such as solar cells, electrochromic windows, touch panel displays, oven windows and flat panel displays.[13] The development of *p*-type TCOs and thus "transparent electronics" can only expand the applications of TCOs, ensuring their position as an integral feature in everyday devices and a vital ingredient of the consumer electronics industry.

1.2.1 Flat Panel Displays

Flat screens first appeared in laptop computers in the mid-1980s, and since then flat screen technology has steadily increased to the point where cathode ray tubes have been replaced as the industry standard for display monitors. At first, plasma technology dominated the flat screen television market, but now liquid crystal displays (LCDs) has overtaken plasma in the market, primarily due to the lower cost of the LCDs.[14]

A typical LCD screen is made up of a sandwich like structure in which the liquid crystal lies between two glass plates, as displayed in Figure 1.2 The outside of each plate is coated with a polarising material while the inside is coated with a transparent conducting ITO film which acts as an electrode. The polarisers at the front and back of the LCD are aligned perpendicularly. Nematic liquid crystals are made up of thread-like molecules which align in a twisted helical structure. In the LCD, the molecules in the liquid crystal are twisted such that the molecules at the front and back are aligned with each of the polarisers. When light passes through the liquid crystal its polarisation axis is aligned along the molecular axes so that the light twists and exits the liquid crystal with the same polarisation as the front film. A colour filter in the front glass plate then results in a red, green or blue pixel on the flat screen display. The role of the ITO electrodes is to create an electric field which untwists the liquid crystal molecules, preventing light from passing through and creating a black pixel on the display. Currently ITO is the main TCO used in flat screen displays because of its low resistance and high etchability.[6] SnO_2, unfortunately, has too high a resistivity and is also too difficult to etch, so it has yet to be used commercially in LCDs despite its lower cost. However, the low resistivity of Al-doped zinc oxide films, coupled with their high etchability, makes it a prospective candidate for lower cost indium-free flat panel displays.

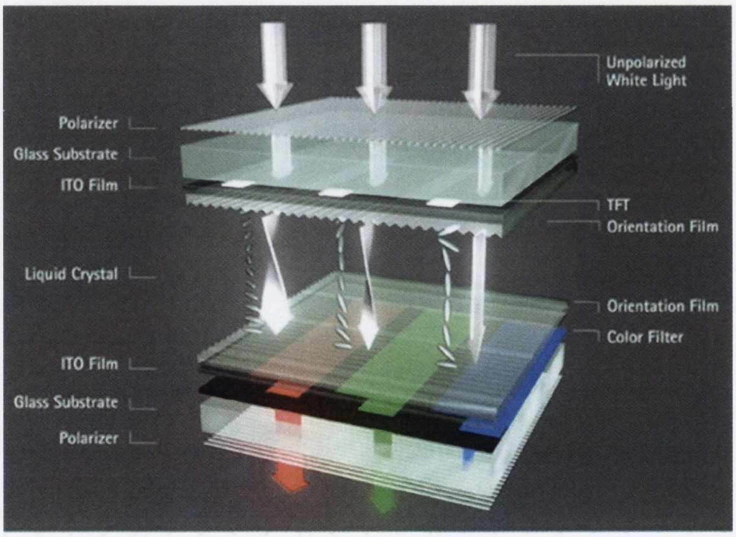

Figure 1.2: Structure of a liquid crystal display (LCD) illustrating the polarisation of light as it passed through the device.[15]

1.2.2 Smart Windows

The biggest application by far of TCOs is as functional coatings on windows. SnO_2 has become the most widely used material for this purpose. In supermarkets, TCOs allow a current to be passed through fridge and freezer door, preventing condensation from obscuring the consumers' view of products. Oven windows are commonly coated with SnO_2 so that the glass reflects infra-red light back into the oven, keeping the oven hot while the outside glass remains cool. TCOs can also be used as invisible security circuits on glass to protect valuable paintings from thieves while also providing some protection from UV light.[6]

One major commercial application of TCO coatings is in electrochromic "smart" windows. Electrochromic (EC) materials can change their optical properties upon the application of a voltage. The EC materials used in smart windows darken when a current is passed through and become transparent under zero voltage. This allows the transmittance to be varied allowing heat or light in or out of a window depending on the climate conditions. Smart windows consist of five layers as shown in Figure 1.3 The central layer is an ionic conductor which acts as an electrolyte to carry ions from one side of the device to the other. On one side of the ionic conductor is an EC film which can conduct both electrons and ions (for example WO_3).[16] On the other side of the ionic conductor is an ion storage film. (e.g. NiO) The central three-layer film is coated on both sides by a transparent conducting layer (typically ITO or SnO_2). When a voltage is applied between the TCO films, ions are shuttled from the ion storage layer through the electrolyte to the EC film making the glass opaque. Reversing the voltage results in ion transfer from the EC film to the ion storage layer and returning the transparency of the glass. Through applied voltage adjustment, different levels of transparency can be achieved, depending on the solar glare or the degree of privacy required.[17]

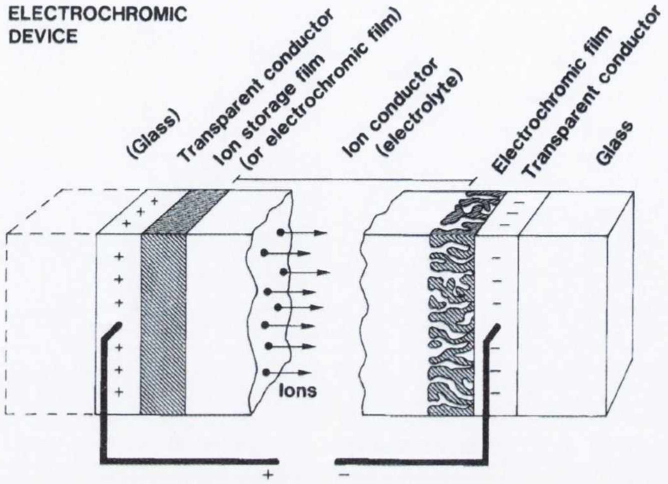

Figure 1.3: Schematic outlining the structure of an electrochromic device used in smart windows.[16]

1.2.3 Solar cells

Another major use of TCOs is in solar cells. Various types of solar cells are available including thin film solar cells, dye sensitised solar cells and most commonly crystalline silicon based solar cells. The basic solar cell structure is shown in Figure 1.4 The main component of the supercell to generate electricity is the p-n junction. This is made up of a layer of *n*-type material on top of a p-type layer. Most commonly a homojunction made up out of *n*-type P-doped silicon and *p*-type B-doped silicon is used. However, thin film solar cells of *n*-type CdS combined with *p*-type CdTe or Cu(In/Ga)Se_2 (CIGS) are also used. Incident photons from sunlight result in the excitation of electrons at the p-n junction creating unpaired holes and electrons. This results in the flow of holes towards the *p*-type layer and the flow of electrons towards the n-type layer so that an electric current flows across the junction. By placing a metal cathode under the *p*-type layer and a TCO anode above the *n*-type material, a current can be made to flow in an external circuit. Although the cathode does not need to be transparent, as the anode is located above the p-n junction, transparency is a necessity for the solar cell to function. The most common TCOs used for this purpose are ITO and SnO_2:F.

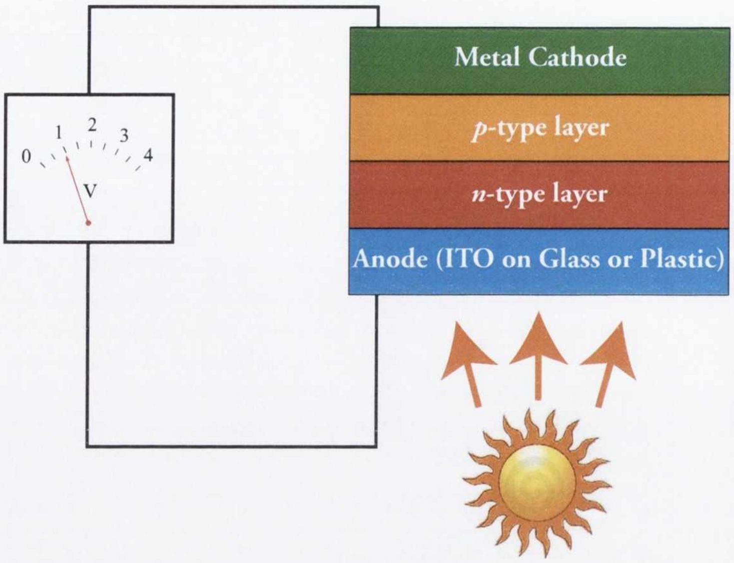

Figure 1.4: Schematic showing the basic internal structure of a layered solar cell.

1.2.4 Electronic Structure Requirements for TCOs

Optical Band Gaps

To ensure transparency to visible light, the *optical* band gap of a material must be greater than the highest frequency of visible light, i.e. $\geq 3.1\,\mathrm{eV}$. In materials possessing optical band gaps lower than 3.1 eV, visible light can excite electrons from the filled valence band (VB) to the unoccupied conduction band (CB), where the subsequent relaxation results in the emission of visible photons. At this juncture it is important to note that the *fundamental* direct band gap of a material is not always the same as its *optical* band gap. The fundamental direct band gap is defined as the smallest direct gap between the VB and the CB, whereas the optical band gap of a material is the smallest *allowed* direct transition between the VB and the CB. Frequently, fundamental band gaps taken from calculations are often compared to experimental optical measurements, often yielding questionable results. A good example of this is the difference between the fundamental band gap and optical band gap of In_2O_3. Experimentally, the optical band gap of india has been intensely investigated, and is generally found to be in the region of 3.75 eV.[?] As all of the computational studies of india had predicted the fundamental band gap to be direct at the Γ point, it was widely assumed that the optical band gap corresponded to the direct transitions from the valence band maximum (VBM) to the conduction band minimum (CBM) at Γ.[18] X-ray photoelectron spectroscopy (XPS) studies, however, reported that the VBM of In_2O_3 was only $\sim 2.9\,eV$ below the CBM. [18] This discrepancy was only resolved in 2008, when a computational study by Walsh *et al.*[18] demonstrated that the fundamental gap was in fact symmetry forbidden, and that the optical band gap originated from transitions $\sim 0.8\,eV$ below the VBM to the CBM. The fundamental band gap of india has now been *revised* to $\sim 2.9\,eV$, indicating that a successful TCO can have a fundamental band gap smaller than 3.1 eV, provided it possesses an optical band gap that is larger than 3.1 eV.

While large optical band gaps ensure transparency in *stoichiometric* TCOs, there is another electronic structure requirement to ensure concomitant high conductivity and transparency. Ideally, all n-type TCO materials should possess a large separation between the CBM and the next highest CB of at least 3.1 eV, with p-type TCOs needing the VBM to be separated from the next highest VB also by 3.1 eV.[19] These separations mean that when charge carriers are introduced into the system, which normally sit in/near the CBM (VBM) for n-type (p-type) TCOs, the optical transitions remain $\geq 3.1\,eV$, and therefore ensure transparency, even for highly defective materials, as shown in Figure 1.5. When defects form in materials that do not show these type of CBM–CBM+1/VBM–VBM-1 separations, colour centres and loss of transparency typically ensue. The majority of the high performance n-type TCOs (e.g. SnO_2, ZnO, In_2O_3) possess large CBM–CBM+1 separations, caused by the antibonding cation s and oxygen $2p$ states, which yield highly disperse lower conduction bands. p-type TCOs typically do not have large inter-band separations at the VBM, but instead maintain transparency due to disallowed transitions from $\geq 3.1\,eV$ below the VBM to the VBM [20].

Conductivity Mechanism

Stoichiometric TCOs do not behave as conductors, as their large optical band gaps preclude the excitation of electrons from the VBM to the CBM in the visible region,

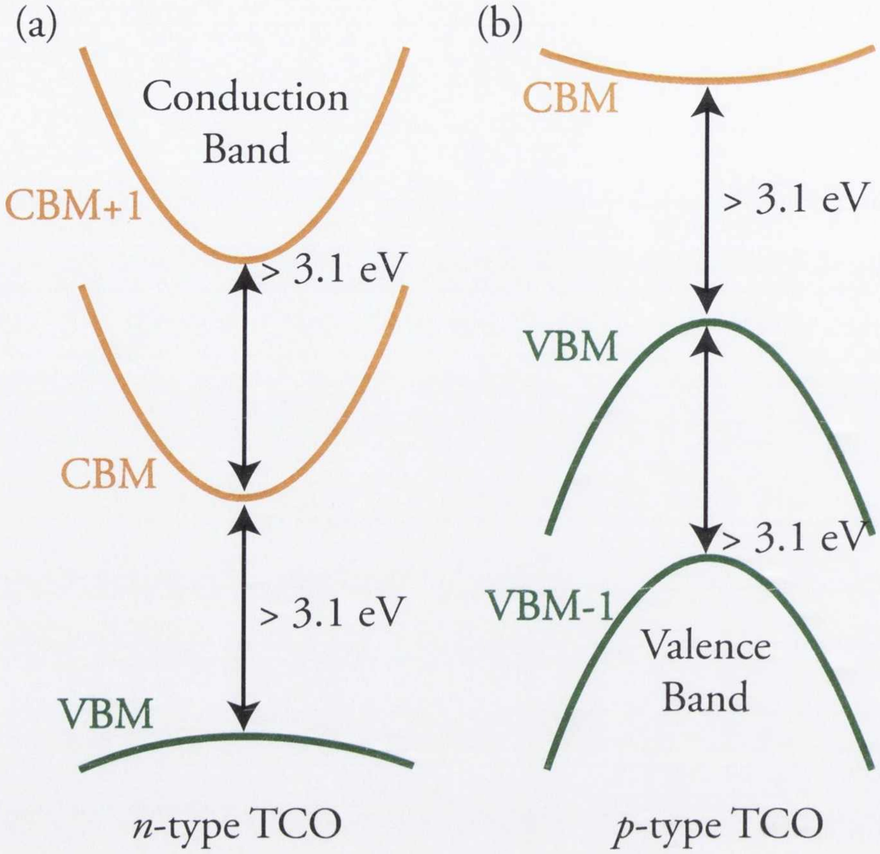

Figure 1.5: Schematic bandstructures for (a) n-type and (b) p-type TCOs, showing the requirements for maximum optical transparency. Green lines are occupied valence band states, and orange lines are unoccupied conduction band states.

meaning that stoichiometic TCOs effectively act as insulators. Conduction occurs in TCOs due to the presence of defects, be they intrinsic or extrinsic. In n-type TCOs, oxygen deficiency (in the form of oxygen vacancies or cation interstitials) or *donor* dopants (cations with a higher valence that the host cation), effectively add electrons to the system, causing occupied defect levels near the CBM, Figure 1.6 (a). In p-type TCOs, oxygen excess (in the form of cation vacancies or oxygen interstitials) and *acceptor* dopants (cations with a lower valence than that of the host), effectively reducing the number of electrons in the system, causing unoccupied "hole" states near the VBM, Figure 1.6 (b). In a good n-type TCO, donor defects should be much lower in energy than acceptor defects, meaning that the n-type conductivity can not be compensated by p-type defects. Similarly, in a good p-type TCO, acceptor defects should be much lower in energy than donor defects.

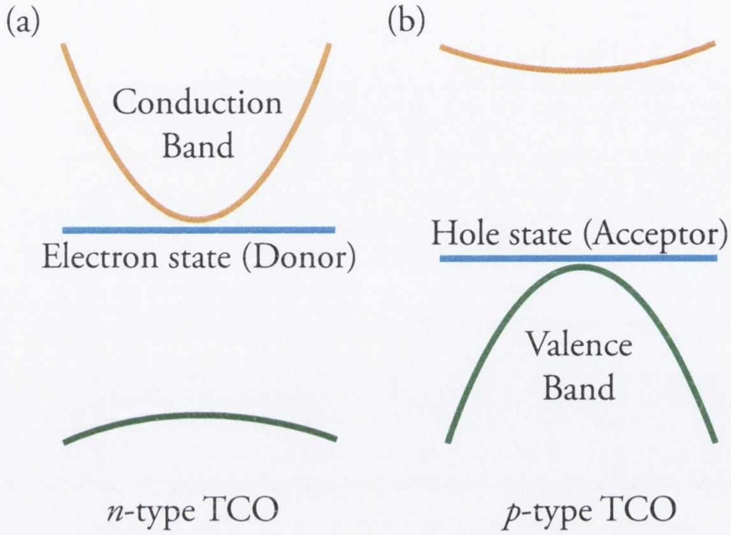

Figure 1.6: Schematic band structures outlining how defects introduce levels in the band gaps of (a) p-type and (b) n-type TCOs. Green lines are occupied valence band states, and orange lines are unoccupied conduction band states.

Excellent TCOs generally have the ability to possess a high degree of non-stoichiometry, yielding reasonable *undoped* conductivities, and are highly susceptible to extrinsic doping to yield high carrier concentrations and higher conductivities . The position of the occupied (unoccupied) defect levels within the band gap of an n-type (p-type) TCO has a huge effect on the conduction properties. To produce a high performance TCO, these defect levels should appear very close to the band edges, allowing the thermal excitation of electron or holes into the CB or VB respectively. In practice, this means a good TCO material should possess a defect level within k_BT ($\sim 30\,\text{meV}$) of the band edges at room temperature, although in the industry standard n-type TCOs the defect levels are actually resonant in the CB.[21] In an n-type TCO, the occupied defect level (donor level) can be thermally excited to the CB at room temperature, where it can freely move, causing conductivity. In a p-type TCO, hole states (unoccupied levels) are formed close to the VBM, where holes are excited to the VB, causing conductivity.

Defects with ionization levels near the band edge (within ~ 30 meV of the band edge) are called *shallow* defects, and are generally characterized by delocalized defect states. Materials that display high conductivities at room temperature (i.e. without the need for activation) are commonly called *degenerate semiconductors.* Conductivity in this type of band conducting regime is governed by:

$$\sigma = \mu n \tag{1.1}$$

where σ is the conductivity, μ is the mobility, n is the electron density and e is the electron charge. The mobility can then be calculated using:

$$\mu = \frac{e\tau}{m^*} \tag{1.2}$$

where τ is the mean time between collisions and m^* is the effective mass, which is a measure of the curvature of the bands. The more curvature (dispersion) of the CB/VB, the lower the effective mass of a material is, and therefore the higher the mobility will be. A good n-type (*p-type*) TCO should ideally possess a highly dispersed CBM (VBM). In the case of the industry standard n-type TCO materials (e.g. ZnO, In_2O_3, SnO_2), the CBM is made up of antibonding cation s and oxygen $2p$ states, where the interactions between these states produce highly disperse CBMs,[22–24] with effective masses in the range $0.1 - 0.3\,m_0$. The current p-type TCOs, however, do not possess very dispersive VBMs and as such have high effective masses in the range $0.5 - 1.0\,m_0$, meaning that they typically display lower mobilities and lower conductivities.

Defect levels that are further than ~ 30 meV away from the band edges are commonly called *deep* levels. Electrons/holes in these deep levels have to be thermally activated to conduct, with the activation energy needed increasing the further the defect level is from the band edge. Often these deep defect levels stem from more localized defect states, which are centred on a small number of atoms, sometimes causing a distinct lattice distortion (polaron formation). These type of defects can conduct through band conduction, meaning that once thermally ionized (activated), the electron/hole moves freely in the CB/VB, or alternatively can be controlled by a hopping mechanism, where electons/holes hop from one site to the next. In a polaronic hopping mechanism the conductivity is governed by:

$$\sigma \propto \exp\left(-\frac{E_a}{k_B T}\right) \tag{1.3}$$

where E_a is the hopping activation energy. From this equation it is clear that the lower the activation energy is, the higher the conductivity will be. The degree of localization of a defect is normally proportional to the distance of the defect level from the band edge. In general, materials that conduct via hopping mechanism display lower mobilities, and therefore are not ideal for TCO applications.

1.3 *n*-type TCOs

All of the industrially used TCOs (e.g. In_2O_3, SnO_2, ZnO) are n-type materials, and they all share several features in common. The cations in these materials all possess an $(n-1)d^{10}ns^0$ electronic configuration, e.g. Sn(IV):[Kr]$4d^{10}5s^05p^0$. The VBM of these materials are dominated by O $2p$ states, with the CBMs composed of antibonding cation s states and oxygen $2p$ states.[22–24]

The source of conductivity in these materials has been a contentious matter for many years. It was postulated that oxygen vacancies and cation interstitials were the intrinsic defects that cause conductivity in ZnO, In_2O_3 and SnO_2.[25] Recently however, it has been demonstrated that although the formation energies of oxygen vacancies are relatively low in these materials, the ionization levels for these defects are very deep in the band gaps.[26–28] The transition levels for cation interstitials were found to be shallow, however the formation energies were very high, indicating that they would not play a large role in any undoped conductivity.[27]

In 2000, Van de Walle demonstrated using first principles methods that interstitial hydrogen can act as a shallow donor in ZnO, and postulated that unintentional hydrogen interstitials were the source of conductivity in ZnO.[29] In a subsequent study of H in ZnO, Janotti and Van de Walle demonstrated that substitutional H on an oxygen site can also act as a donor in ZnO,[30] and this defect was used to explain the dependence of the conductivity in the partial pressure of oxygen. Subsequently it has been experimentally demonstrated that H can act as a donor in ZnO, SnO_2 and In_2O_3.[31–33]

Extrinsic doping of these n-type TCO materials has proved very successful, with ITO currently the market leader. Presently, the majority of research into the n-type TCOs is focused on the replacement of ITO as the industry standard, and the investigation of cheaper methods of TCO processing.

1.4 p-type TCOs

Although TCOs have a vast range of applications, research on active device fabrication using solely TCO materials has been very limited.[13] To fabricate a *junction device*, it is imperative that high performance p-type TCOs are available. A high figure of merit p-type TCO would open up the possibility of all oxide "invisible electronics" (alternatively know as "transparent electronics").[13] It is conceivable that a *pn* junction comprised of an n-type and p-type TCO could lead to a functional transparent window, which could allow the visible portion of the solar radiation through, but generate electricity by absorbing in the ultra violet (UV).[11]

The top of the valence band of most wide band gap binary oxides (such as In_2O_2, ZnO and SnO_2) is usually dominated by O $2p$ states, which when doped p-type, results in deep lying, strongly localized O $2p$ hole polarons, limiting any electronic conduction.[34,35] For decades research had been focused on doping the usually n-type TCO materials to make them p-type, and indeed this research is still ongoing in the case of ZnO.[36,37] Not surprisingly, all attempts to p-type dope the n-type TCOs have resulted in extremely low conductivities, and it is only recently that the computational physics community have come to realize the localized nature of p-type defects in these materials.[38]

In 1997, Kawazoe *et al.* first reported p-type conductivity and transparency in thin films of $CuAlO_2$.[12] Subsequently, Hosono and co-workers postulated that combining the valence band features of Cu_2O (a native p-type oxide with an optical band gap of $\sim$ 2.17 eV which precludes it as a TCO[39]) with the larger band gaps of other binary oxides was an appealing method of developing p-type TCOs.[40] In Cu_2O, the Cu occupied $3d$ states hybridize with the O $2p$ states in the valence band (VB), with Cu d states dominating at the top of the VB,[39] as shown in Figure 1.7. Thus, upon hole formation (due to oxygen excess), $3d^{10}$ Cu^I is oxidized to $3d^9$ Cu^{II},[39] creating holes on Cu ions. As the Cu states are hybridized with oxygen, this leads to *less* localized holes with *increased* mobility. These valence band features are still present in $CuAlO_2$, meaning $CuAlO_2$ retains the p-type features of Cu_2O,[12] and this has been shown in many previous theoretical and experimental studies on the electronic structure of Cu^I-based Delafosites.[41–43]

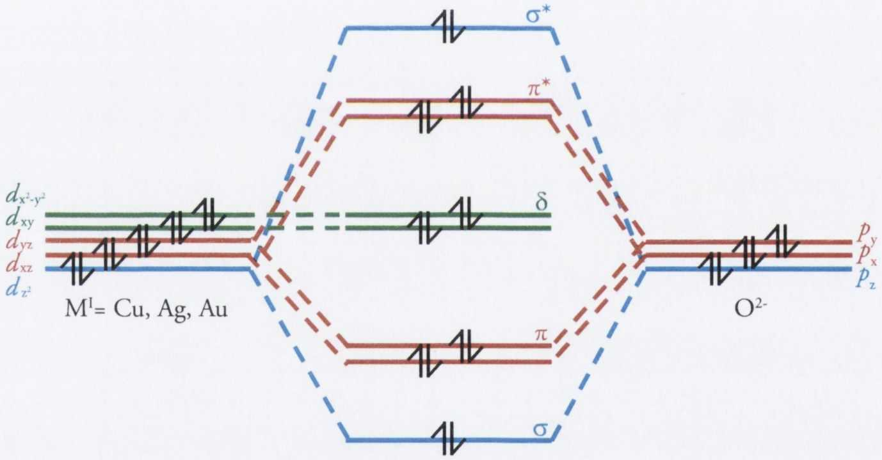

Figure 1.7: Schematic of the ideal valence band structure of a p-type TCO.

The relatively small band gap of Cu_2O is thought to be caused by the three dimensional interactions between the $3d^{10}$ electrons on neighbouring Cu^I ions.[44] These three dimensional interactions arise due to the structure of the system, which can be thought of as being made up of two inter-penetrating cristobalite lattices.[45,46] In the Cu_2O structure, each Cu atom is linearly coordinated between two oxygen atoms. In the delafossite structure (Figure 1.8) each Cu atom also is linearly coordinated with two oxygen atoms, forming O–Cu–O dumbbells parallel to the c axis. Oxygens in these O–Cu–O units are also each coordinated to three M^{III} atoms, oriented such that

M^{III}-centered octahedra form $M^{III}O_2$ layers which lie parallel to the *ab* plane. Two alternative layer stackings are possible, resulting in a hexagonal (space group $P63/mmc$) or rhombohedral (space group $R3 - mh$) unit cell[47]. Thus the delafossite structure decreases the dimensionality of the Cu–Cu interactions, usually resulting in band gaps large enough for TCO applications[48] These theories have been supported by the extensive theoretical work of Alemany and co-workers.[49,50]

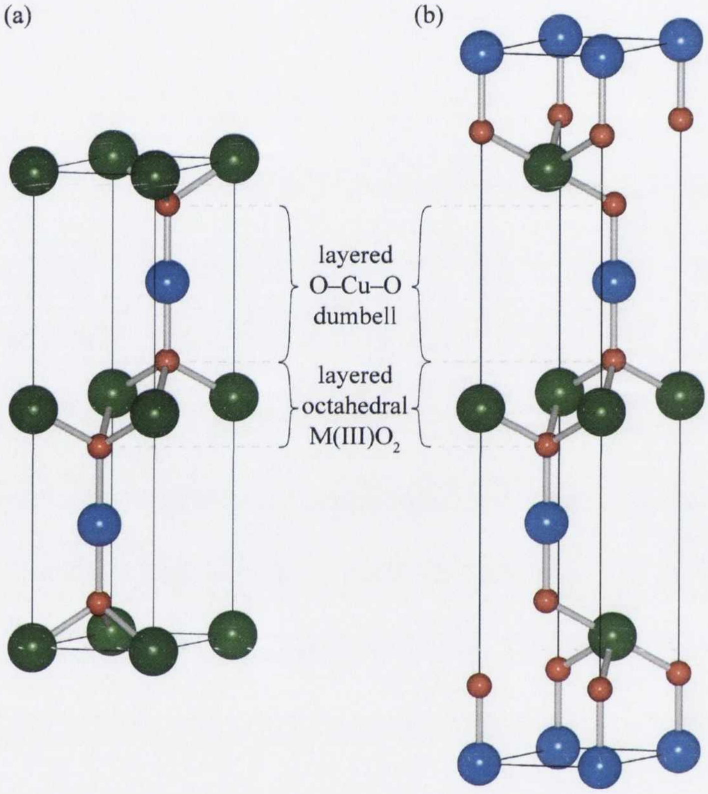

Figure 1.8: The conventional unit cell of (a) hexagonal and (b) rhombohedral $CuM^{III}O_2$. The red, blue and green spheres are oxygen, copper and M^{III} respectively.

Using the concepts developed by Hosono and co workers,[40] many Cu^I based delafossites having transparency and *p*-type conductivity have been synthesized, including $CuScO_2$, $CuYO_2$, $CuInO_2$, $CuGaO_2$ and $CuCrO_2$.[51] Indeed, other structures have been identified that combine *p*-type conductivity and optical transparency in Cu^I based materials, including $SrCu_2O_2$[52,53] and layered oxychalogenides (LaCuOS)[54], although presently the *p*-type TCO with the highest conductivity is a delafossite (Mg doped

$CuCrO_2$).[55]

To date the highest reported conductivity of a doped *p*-type TCO is 220 S cm^{-1} for Mg-doped $CuCrO_2$,[55] which is still two orders of magnitude lower than the typical *n*-type TCOs. Computationally, delafossites have been investigated to elucidate the origin of the conductivity in these materials, with the general consensus being that copper vacancies are the relevant defects.[56,57] These studies, however, predict that copper vacancies are shallow defects in these materials, and should lead to degenerate semiconducting behaviour.[56,57] *All* the previous DFT results are at variance with all experimental measurements of the activated conductivity of the delafossite materials.[58–61]

1.5 Thesis Outline

Despite the many applications and widespread interest in TCO materials, a number of unanswered questions regarding the electronic structure and defect chemistry of TCO materials exists, in particular with regard to *p*-type TCOs. The main motivation for the work presented in this thesis has been to fully understand the complex chemistry of the Cu^{I}-based delafossite oxides, and to ascertain if high performance *p*-type TCOs can be produced from these materials. In Chapter 1, a brief overview of the the history and electronic structure of TCO materials, together with some typical TCO device applications have been reported.

In Chapter 2, the computational methods used in this thesis are discussed, including the quantum theory underpinning the approaches we have utilized, together with the limitations and advantages of the various methods we have employed. In Chapter 3, the implementation of these methods within the Vienna *Ab Initio* Simulation Package (VASP), which we have utilized in all our calculations, are discussed. We outline the post-processing analysis methods utilized to gain insight into the electronic structure of each material investigated.

In Chapter 4, we examine the electronic structure of $CuM^{III}O_2$ (M^{III} = Al, Cr, Sc, Y) in an attempt to rationalize the conductivity trends reported in the literature. We will discuss the influence the electronic structure of the M^{III} ion on the valence band features of these materials, and hence on the mobility of holes in these systems. Chapter 5 investigates the latest *p*-type delafossite TCO to be discovered, and assess its reported conductivity based on its electronic structure.

In Chapter 6, the defect chemistry of Cu_2O, the parent compound to all the delafossite oxides, is addressed. We use three levels of computational complexity in a bid to rationalize the previous experimental and theoretical results, which quite clearly contradict each other. In Chapter 7 we use the understanding of the defect chemistry of Cu^{I}-based oxides gleamed from Chapter 6 to investigate the defect chemistry of the prototype Cu^{I}-based delafossite oxide, $CuAlO_2$, and of the most promising *p*-type TCO, $CuCrO_2$. This analysis will also add to the understanding of the effect of the M^{III} ion on the valence band we obtained in Chapter 4.

In Chapters 8 and 9 we investigate some novel *p*-TCO materials, and compare their TCO abilities to that of the delafossite TCOs. The two structure motifs studied are the Zn d^6 spinel oxide structure, and a novel layered oxychalcogenide $(Cu_2S_2)(Sr_3Sc_2O_5)$, which was reported to possess a large hole mobility.

Finally, in Chapter 10 we will provide a summary of all our findings, and discuss the impact of this work on the field of *p*-type TCOs. This will be followed by a brief discussion of some possible future direction for the field of *p*-type TCOs.

Chapter 2

Computational Theory

2.1 Quantum Chemistry Methods

2.1.1 Schrödinger Equation

The fundamental goal of the majority of quantum chemical approaches is the (approximate) solution of the Schrödinger equation[62] in its time independent form:

$$\hat{H}\Psi = E\Psi \tag{2.1}$$

Where E is the energy, Ψ is the wavefunction and $\hat{H}$ is the Hamiltonian, which is defined as the sum of the kinetic and potential energy operators:

$$\hat{H} = -\frac{\hbar}{2}\sum \frac{1}{\mathrm{m}_i}\nabla_i^2 + V(r) \tag{2.2}$$

Where i is the index over all the particles in the system, m_i is the mass of particle i, the Laplacian $\nabla_i^2 = \left(\frac{\delta^2}{\delta x_i^2} + \frac{\delta^2}{\delta y_i^2} + \frac{\delta^2}{\delta z_i^2}\right)$ is the kinetic energy operator, $\hbar = \frac{h}{2\pi}$ and $V(r)$ is the potential energy of the system as a function of its coordinates. The kinetic energy operator can be dissected further into the contributions to the kinetic energy from the nuclei and the electrons, with the potential energy being divided into the contributions from the nuclei–nuclei interactions , the electron–nuclei interactions, and the electron-electron interactions :

$$\hat{H} = \hat{K}_{nuc} + \hat{K}_{elec} + V_{nuc-nuc} + V_{nuc-elec} + V_{elec-elec} \tag{2.3}$$

The solution of the Schrödinger equation, which is a partial differential eigenvalue equation, would allow the calculation of the ground state energy and the wavefunction. The Hamiltonian operates on the eigenfunction (wavefunction), which yields the eigenfunction multiplied by the energy. The wavefunction produced from the Schrödinger equation has no physical meaning, but the square of this wavefunction gives the probability of finding an electron in space, i.e. the *electron density.* Unfortunately, the electron-electron interactions of Equation 2.3 are impossible to determine analytically, rendering the Schrödinger equation insolvable for systems with greater than one electron. Therefore, various approximations are a necessity to solve it for more complex systems.

2.1.2 The Born-Oppenheimer-Approximation

To aid in solving the Schrödinger equation, we can divide the wavefunction into terms that depend only on nuclear or electronic contributions:

$$\hat{H} = (\hat{K}_{nuc} + \hat{V}_{nuc-nuc}) + \hat{V}_{nuc-elec} + \hat{K}_{elec} + \hat{V}_{elec-elec} \tag{2.4}$$

The nuclei move significantly more slowly than the electrons, meaning that they can be thought of as being fixed in space relative to the electrons, an as such their kinetic energy, $\hat{K}_{nuc}$ can be ignored, and need not be calculated. This is the essence of the Born-Oppenheimer approximation, in which the nuclei are fixed in space, and have zero kinetic energy.[62] The potential energy of the nuclei-nuclei interactions, $\hat{V}_{nuc-nuc}$, is therefore a constant for a fixed set of atomic coordinates, and is added the solution of the electronic Schrödinger equation, given by:

$$\hat{H}_e \Psi_e = E_e \Psi_e \tag{2.5}$$

with $\hat{V}_{nuc-nuc}$ defined simply as :

$$\hat{V}_{nuc-nuc} = \sum_{A<B} \frac{e^2 Z_A Z_B}{r_{AB}} \tag{2.6}$$

where e is the charge of the electron, Z_A and Z_B are the nuclear charges of atoms A and B, and r_{AB} is the distance between the two nuclei. This simplification leaves the electronic Hamiltonian, $\hat{H}_e$ with just three terms to be calculated:

$$\hat{H}_e = \hat{K}_{elec} + \hat{V}_{nuc-elec} + \hat{V}_{elec-elec} \tag{2.7}$$

where $\hat{K}_{elec}$ is simply defined as:

$$\hat{K}_{elec} = -\sum_{i}^{N} \frac{1}{2} \nabla_i^2 \tag{2.8}$$

and the nuclear–electron interaction, $V_{nuc-elec}$ operates on the wavefunction:

$$\hat{V}_{nuc-elec} = -\sum_{A}^{M} \sum_{i}^{n} \frac{Z_A}{r_{iA}} \tag{2.9}$$

Both of these terms are relatively easy to calculate, however the electron–electron term, $V_{elec-elec}$, remains the most challenging part of the Schrödinger equation to solve, and must be further approximated. The Born-Oppenheimer approximation is successfully applied in the vast majority of ground state modern electronic structure methods, and only fails when dealing with the motion of extremely light particles (e.g. hydrogen), or when the correlation between electronic and ionic motion is important. In these cases, time-dependent theories are a necessity.

2.1.3 The Variational Principle

Another principle utilized to provide an approximate solution to the Schrödinger equation is the variational principle. The variational principle states that the expectation value of a Hamiltonian, $\hat{H}$, calculated using a trial wavefunction, Ψ_T, is never lower than the true ground state energy , E_0. In an ideal world, E_0 is the expectation value of $\hat{H}$ calculated using the *true* ground state wavefunction, Ψ_0, as outlined in Equation 2.10:

$$\left\langle \Psi_T \middle| \hat{H} \middle| \Psi_T \right\rangle = E_T \geq E_0 = \left\langle \Psi_0 \middle| \hat{H} \middle| \Psi_0 \right\rangle \tag{2.10}$$

The premise of this principle, is that the energies calculated from a set of trial wavefunctions can never be less than those of the true wavefunction, which means that the lowest energy trial wavefunction will be closest in energy to that of the true wavefunction, and as such, the quality of the calculation can be gradually improved by varying the wavefunction until the lowest energy solution is obtained. Unfortunately, there is no exact way of telling how close your trial wavefunction is to the true wavefunction

2.1.4 Hartree-Fock Approximation

In 1928, Hartree divided the many electron wavefunction up into the product of one electron wavefunctions, effectively using a simplification involving a one electron Hamiltonian and ignoring electron-electron interactions:

$$h(i) = -\frac{1}{2}\nabla_i^2 + \sum_A^M \frac{1}{r_{i_A}} \qquad \text{and} \qquad H = \sum_i^N h(i) \tag{2.11}$$

This equation is now solveable, and results in a series of spin orbitals which satisfy the eigenequation:

$$h(i)\chi_j(x_i) = \epsilon_j \chi_j(x_i) \tag{2.12}$$

with the interpretation that electron i occupies a spin orbital χ_j with energy ϵ_j. The resulting wavefunction is given by:

$$\Psi(x_1....x_N) = \chi_i(x_1)\chi_j(x_2)\chi_k(x_3).....\chi_n(x_N) \tag{2.13}$$

This became known as the Hartree product (HP) wavefunction, and the resulting system energy is:

$$< \Psi |H| \Psi >= \epsilon_i + \epsilon_j + \epsilon_k.......... + \epsilon_n = E \tag{2.14}$$

In the SCF approach an initial trial set of wavefunctions is chosen and for each electron the potential is calculated by its interaction with the rest of the stationary electrons in the system, therefore treating them as an average distribution in space. This is known as the mean field approach. Solving the Schrödinger equation results in a new wavefunction and hence a change in the electron distribution and thus in the potential. The procedure must thus be iterated until there is no change in the wavefunctions, or until certain convergence criteria are satisfied.

However, within Hartree's approximation, the wavefucntion is physically unrealistic. It is an independent electron model, which ignores the fact that electrons repel each other. A Russian physicist, Vladimir Fock, recognized that the Hartree wavefunction did not satisfy the Pauli exclusion principle, i.e. the wavefunction was not antisymmetric with respect to electron interchange, meaning that if you interchange two electrons in Equation 2.13, you get the exact same wavefunction.[62]

If we take a two electron example, like the wavefunction of the Helium atom we can see that the two possible Hartree wavefunctions are given by:

$$\Psi^{HP} = \chi_i(x_1)\chi_j(x_2) \qquad \text{and} \qquad \Psi^{HP} = \chi_i(x_2)\chi_j(x_1) \tag{2.15}$$

where χ_i could be the $1s\ \alpha$ and χ_j could be the $1s\ \beta$ for the ground state.

It is clear that these are not correct as one is formed from the other by swapping the electron around. Therefore swapping of an electron does not change the sign of the wavefucntion, meaning the Pauli exclusion principle is not satisfied. By inspection, we can come up with a wavefunction that does satisfy the Pauli exclusion principle:

$$\Psi = \frac{1}{\sqrt{2}}\left[\chi_i(x_1)\chi_j(x_2) - \chi_i(x_2)\chi_j(x_1)\right] \tag{2.16}$$

where the factor at the beginning is a normalisation constant. Swapping electrons 1 and 2 now yields:

$$\Psi = \frac{1}{\sqrt{2}}\left[\chi_i(x_2)\chi_j(x_1) - \chi_i(x_1)\chi_j(x_2)\right] = -\frac{1}{\sqrt{2}}\left[\chi_i(x_1)\chi_j(x_2) - \chi_i(x_2)\chi_j(x_1)\right] = -\Psi \tag{2.17}$$

This phenomenon of electron indistinguishability which leads to the anti symmetric wavefunction was not properly understood and people spoke of the "exchange" of electrons. From this, the element of the energy which directly results from this is often referred to as the exchange energy.

Subsequently, Slater determined that an antisymmetric wavefunction, Ψ could be constructed by using the determinant of the the system with N electrons and N spin orbitals, Equation 2.18. Thus in the Hartree-Fock approach the total energy is minimized with respect to the orbitals of the determinant.

$$\psi_{SD} = \frac{1}{\sqrt{N}} det \left\{ \chi_1 \left(\boldsymbol{x}_1 \right) \chi_2 \left(\boldsymbol{x}_2 \right) ....\chi_N \left(\boldsymbol{x}_N \right) \right\} \tag{2.18}$$

The Pauli principle is built into this wavefunction. If we attempt to doubly occupy a spin orbital (χ_i) by putting both electrons into it, the wavefunction disappears:

$$\Psi = \frac{1}{\sqrt{2}} \begin{vmatrix} \chi_i(x_1) & \chi_i(x_1) \\ \chi_i(x_2) & \chi_i(x_2) \end{vmatrix}$$

which is the same as:

$$\frac{1}{\sqrt{2}} \left[\chi_i(x_1)\chi_i(x_2) - \chi_i(x_2)\chi_i(x_1) \right] = 0 \tag{2.19}$$

To obtain the Hartree-Fock energy, two-electron integrals in the form shown in Equation 2.20 and Equation 2.21 below are necessary.

$$J_{ij} = \int \int \chi_i(x_1)\chi_j^*(x_2) \frac{1}{r_{12}} \chi_i(x_1)\chi_j^*(x_2) d\tau_1 d\tau_2 \tag{2.20}$$

$$K_{ij} = \int \int \chi_i(x_1)\chi_j^*(x_2) \frac{1}{r_{12}} \chi_j(x_1)\chi_i^*(x_2) d\tau_1 d\tau_2 \tag{2.21}$$

where J_{ij} represents the electrostatic repulsion between the electrons, and is known as the *Coulomb term*, and K_{ij} is a quantum mechanical effect arising from the antisymmetric wavefunction, and is known as the *exchange integral*. From the Slater determinant wavefunctions, the exchange term can only be non-zero for electrons of the same spin, making it impossible for two electrons of the same spin from occupying the same position in space. The exchange integral, K_{ij}, is a negative term which lowers the total energy of the system, and is the most computationally expensive part of a HF calculation

2.1.5 Roothan-Hall equations

For complex systems, the molecular orbitals (MOs) need to be expressed in terms of basis functions using the linear combination of atomic orbitals (LCAO) approach:

$$\chi_i = \sum_{\mu} C_{\mu}^{i} \phi_{\mu} \tag{2.22}$$

where ϕ_μ are the atomic orbital like basis functions and C_μ^i are the coefficients of the atomic orbitals μ in molecular orbital i. Roothan and Hall, while working independently, developed a set of matrix equations known as the Roothan-Hall equations.[63] This approach yielded a secular equation in the form:

$$FC = SC\epsilon \tag{2.23}$$

in which F is the Fock matrix which is constructed from the single-electron energy operators, S is the overlap matrix of basis functions, C is the matrix of coefficients C_μ^i, and ϵ is the diagonal matrix of eigenvalues ϵ_i.

2.1.6 Hartree-Fock Limitations

The HF approach is still widely used in quantum chemistry, and often yields predicted equilibrium interatomic distances and bond angles for the majority of molecules that are within a few percent of experiment. However, the HF approach suffers from a number of limitations. The very definition of the variational principle implies that the energy of the true wavefunction will *always* be lower than the energy of the HF wavefunction. This energy difference has been described by Lowdin[64] as the *correlation energy.* In HF the electrons are expressed via an antisymmetrized product, meaning that the HF approach assumes that each electron moves independently of all the other electrons in the system, with the exception of a Coulombic repulsion to the average position of all electrons. The motion of electrons is actually correlated, meaning that the electrons “avoid” each other more than HF theory suggests.

There are two types of correlation: (a) dynamical and (b) non-dynamical. Dynamical correlation can be expressed simply, i.e. for two electrons, the probability of finding one electron at a certain position depends on the position of the second electron. HF is therefore not appropriate for systems with localized electrons such as transition metals, or for metallic states, as it fails to account for collective Coulomb screening in delocalized electrons systems.[63] Non-dynamical correlation can occur in systems which are described by more than one degenerate determinant, e.g. for molecules where the highest occupied molecular orbital is comprised of two or more degenerate states. In these cases, HF populates one of the degenerate states, instead of giving them both equal weight. Dynamical correlation, however, is the largest source of correlation error in the HF approach. The correlation energy is usually only $\sim 0.1\%$ of the total energy, but due to its similar magnitude to total energy differences, large errors can occur when properties where electrons are redistributed (i.e. binding energies, reaction energies) are calculated.

HF has been implemented for periodic systems, however, the computational cost is dominated by the exchange integral. This computational expense, in conjunction with the inherent correlation problems, make HF unsuitable for large scale simulations of periodic solid systems. To achieve greater accuracy, *post* HF methods such as Møller-Plesset (MP) Perturbation Theory or Configuration Interaction (CI) can be used. Unfortunately, these methods are extremely computationally expensive (scaling up to N^7 and well beyond), and are therefore limited to relatively small systems, and are only recently being applied to the solid state. These methods are thus not suitable for large periodic supercells required for semiconductor defect calculations. One method that can handle the electron correlation problem of HF theory is density functional theory (DFT), which will be addressed in the next section.

2.1.7 Density Functional Theory

Density Functional Theory (DFT) relates the total electronic energy as a functional of the charge density. The value of a functional varies not with a single variable, but with another function (in this case the electron density). In 1964 Hohenberg and Kohn's (H-K) theorems[65] proved that the ground state energy of a system can be written as a functional of the electron density. They also proved that the information contained in the electron density function $\rho(r)$ (which depends on only three variables), could determine all ground state properties. Therefore, the problem is simplified to optimising $\rho(r)$ as opposed to solving Ψ which is a function of 3N variables (N being the number of electrons). As the total energy calculated by this density cannot be lower than the true ground state energy, the ground state density can be calculated via the variational principle. We begin by splitting the total energy into its contributions

$$E\left[\rho(r)\right] = T\left[\rho(r)\right] + E_{ee}\left[\rho(r)\right] + E_{Ne}\left[\rho(r)\right] \tag{2.24}$$

where $T\left[\rho(r)\right]$ is the kinetic energy, $E_{ee}\left[\rho(r)\right]$ is the electron–electron interactions and $E_{Ne}\left[\rho(r)\right]$ is the nuclear–electron interaction. This can be rewritten as shown in Equation 2.25, which shows the relationship between the total electronic energy $E\left[\rho(r)\right]$ and $\rho\left(r\right)$, where $F[\rho(r)]$ is known as the *Hohenberg and Kohn universal functional*, and V_{ext} is the external potential (core, external field etc.) the electrons move in.

$$E\left[\rho(r)\right] = F\left[\rho(r)\right] + \int \rho(r)\left(r\right).V_{ext}\left(r\right).dr \tag{2.25}$$

Minimising the functional $E[\rho(r)]$, using the ground state electron density ρ_0(r), gives the exact ground state electronic energy, E_0.

Kohn and Sham[66] then demonstrated how a computational scheme within the H-K formalism could be achieved with the key being the re-introduction of a wavefunction. The main problem with previous attempts was the difficulty in calculating the kinetic energy. The idea of K-S was to consider a fictitious non-interacting systems of electrons, *which has the same exact ground state density as the fully interacting system of electrons.*

$$\rho_S(r) = \sum_i \left|\rho_{KS}^2(r)\right| = \rho_{exact}(r) \tag{2.26}$$

By splitting the kinetic energy into the energy associated with non-interacting electrons ($T_S\left[\rho(r)\right]$) and a correction ($T_C\left[\rho(r)\right]$) due to electron-electron interactions, the kinetic energy can be calculated in the same way as in HF.

$$T\left[\rho(r)\right] \longrightarrow T_S\left[\rho(r)\right] + T_C\left[\rho(r)\right] \qquad \text{where} \qquad T_S\left[\rho(r)\right] = -\frac{1}{2}\sum_i \left\langle \chi_i \left|\nabla^2\right| \chi_i \right\rangle \tag{2.27}$$

The electron–electron interactions can be written using the classical Hartree energy:

$$E_{ee}\left[\rho(r)\right] = \frac{e^2}{2}\int\int \frac{\rho(r)\rho(r')}{|r-r'|}drdr' + E_{NC}\left[\rho(r)\right] \tag{2.28}$$

where the "NC" in Equation 2.28 is the non-classical part of the electron-electron interaction. From the earlier discussion of the HF method, we can say that this contains the exchange and correlation. The Hohenberg and Kohn functional is thus:

$$F\left[\rho(r)\right] = T_S\left[\rho(r)\right] + J\left[\rho(r)\right] + E_{XC}\left[\rho(r)\right] \tag{2.29}$$

in which we have denoted the classical Coulomb interaction by $J\left[\rho(r)\right]$ and the remaining non-classical part of the electron–electron interaction is now explicitly denoted by $E_{XC}\left[\rho(r)\right]$, the exchange-correlation energy and is defined as:

$$E_{XC}\left[\rho(r)\right] = \left(T\left[\rho(r)\right] - T_S\left[\rho(r)\right]\right) + \left(E_{ee}\left[\rho(r)\right] - J\left[\rho(r)\right]\right) = T_C\left[\rho(r)\right] + E_{NC}\left[\rho(r)\right] \tag{2.30}$$

Hence both exchange and correlation are built into the formalism of DFT quite naturally and there is no separation between the two effects unlike in wavefunction methods. From this we can derive the single particle Kohn-Sham equations where we are seeking a set of single particle orbitals that produce a Slater determinant which has the same density as the exact density of the real system. The total energy is now:

$$E\left[\rho(r)\right] = T_S\left[\rho(r)\right] + J\left[\rho(r)\right] + E_{XC}\left[\rho(r)\right] + E_{Ne}\left[\rho(r)\right] \tag{2.31}$$

where:

$$T_S\left[\rho(r)\right] = \sum_{i=1}^{N} \langle \chi_i \left| \nabla^2 \right| \chi_i \rangle \tag{2.32}$$

and:

$$J\left[\rho(r)\right] = \frac{1}{2}\sum_{i}^{N}\sum_{j}^{N}\int\int \left|\chi_i\right|^2 \frac{1}{r_{12}} \left|\chi_j\right|^2 dr_1 dr_2 \tag{2.33}$$

and:

$$E_{Ne}\left[\rho(r)\right] = -\sum_{i}^{N}\int\sum_{M}^{A}\frac{Z_A}{r_{1A}}\left|\chi_i\right|^2 dr_1 \tag{2.34}$$

when written in terms of the wavefunction.[67]

The variational principle is then applied to this equation, i.e. what is the best set of molecular orbitals, $\chi_i(r)$, which minimizes the energy, subject to the constraint that the orbitals are orthonormal. We attain a set of single particle equations which look similar to the HF equations. In these equations, a potential acts on the wavefunctions to produce the eigenvalues and eigenvectors.

$$\left(-\frac{1}{2}\nabla^2 + \left[\int \frac{\rho(r)}{r_{12}} dr_2 + V_{XC}(r) - \sum_A^M \frac{Z_A}{r_{1A}}\right]\right) \chi_i = \epsilon_i \chi_i \tag{2.35}$$

which gives:

$$\left(-\frac{1}{2}\nabla^2 + V_{eff}(r)\right) \chi_i = \epsilon_i \chi_i \tag{2.36}$$

This defines the Kohn-Sham (Fock-like) one electron operator for the total energy. Similar to HF, the potential V_{eff} depends on the orbitals, which we are trying to compute, and so an iterative procedure must be followed. Theoretically DFT is an exact method for finding the ground state energy, but only if the exact $E_{xc}[n]$ is known. The functional form of $E_{xc}[\rho(r)]$, however, is unknown, and must be approximated. Therefore instead of having the exact exchange and *zero* correlation of HF theory, we instead obtain *approximate* exchange and *approximate* correlation. Despite these approximations to exchange and correlation, DFT has become the method of choice in computational semiconductor research, both in physics and chemistry.

2.1.8 Exchange-Correlation Functional

The exchange-correlation functional is therefore vital to the success of the DFT method. The approach of Kohn-Sham allows for an exact description of the majority of the contributions to the electronic energy of a molecular system, with all the remaining parts gathered together into the $E_{XC}[\rho(r)]$. One reason that DFT is so appealing, is that even relatively simple approximations to $E_{XC}[\rho(r)]$ can yield reasonable results in terms of electronic structure and optimized lattice constant.

Most $E_{XC}[\rho(r)]$ functionals are predicated upon the idea of a uniform electron gas model. This model is a hypothetical system in which an almost infinite number of electrons are free to move in an electrically neutral environment, which is quite similar to the behaviour of valence electrons in an ideal metal. One of the benefits of using a model like this is that very accurate exchange and correlation energies are known for this type of system due to a series of in-depth quantum-Monte-Carlo simulations.

The dependence of $E_{XC}\left[\rho(r)\right]$ on the density can be written in terms of $\rho\left(r\right)$ and the exchange correlation energy per electron $\epsilon_{xc}\left[\rho(r)\right]$:

$$E_{xc}\left[\rho(r)\right] = \int \rho\left(r\right) \epsilon_{xc}\left[\rho\right] dr \tag{2.37}$$

The total exchange-correlation ($E_{XC}\left[\rho(r)\right]$) can therefore be evaluated by integrating $\epsilon_{xc}\left[\rho\right]$ over all points in the system. The most basic formulation for an $E_{XC}\left[\rho(r)\right]$ potential for a real system based on contributions from the uniform electron gas model is the local density approximation (LDA). The main assumption in LDA is that, at each point $\boldsymbol{r}$ in the system, ϵ_{xc}, is equal to the exchange-correlation of a homogenous electron gas with the same density. The exchange portion, ϵ_x, can be calculated from Bloch and Dirac's[68,69] equation, which expresses the exchange as a function of the density. The functional form of the correlation, ϵ_c, is unknown. This problem was successfully surpassed by Ceperley and Alder,[70] who computed the total energy of several electron gases of different densities using quantum-Monte-Carlo, and then subtracted the ϵ_x from the total energies, yielding the ϵ_c. Fits to this data were then performed by Vosko, Wilk and Nusair[71] to produce an equation for the LDA correlation energy. The biggest approximation made in the LDA is that the $E_{XC}\left[\rho(r)\right]$ depends solely on the density at point r and not how the density is changing in its local environment. In practice, the LDA works reasonably well for systems in which the electron density does not vary rapidly and thus offers comparable accuracy to the HF approach, and has become widely used in both quantum physics and quantum chemistry. However, LDA is known to suffer from a number of issues, including the overbinding of electrons, which results in the overestimation of atomisation and ionisation energies, and underestimated bond lengths.

To improve on these shortcomings, the generalized gradient approximation (GGA) was developed, and has subsequently become one of the most frequently used $E_{XC}\left[\rho(r)\right]$ functionals. Within the GGA method, an electron gas is again considered, however, in this case the $E_{XC}\left[\rho(r)\right]$ is dependent not only on the density at position $\boldsymbol{r}$, but also on the variation close to $\boldsymbol{r}$ (the gradient of the density). This approach achieves more flexibility and accuracy in determining the electrons structure of molecules and solids using DFT. The majority of GGA $E_{XC}\left[\rho(r)\right]$ functionals are essentially made up of the LDA $E_{XC}\left[\rho(r)\right]$ plus correction terms to include the gradient. Historically, there are two different classes of GGA functional. The first of these are derived by fitting to experimental data (e.g. Becke's exchange and correlation functionals,[72] and the Lee-Yang-Parr (LYP)[73] correlation functional), however these functionals are usually derived from molecules and the first few rows of the periodic table, and thus should be used with extreme caution when applied to heavier elements. The other class of GGA functional do not depend on empirical parameters, and *should* be more applicable to a wide range of chemical compounds. Example of this class is the $E_{XC}\left[\rho(r)\right]$ of Perdew and Wang (PW91),[74] and the now very popular Perdew, Burke and Ernzerhof (PBE) functional.[75] The PBE functional has been employed in all the DFT calculations presented in this thesis.

2.1.9 LDA/GGA Limitations

DFT has become the theoretical method of choice in computational solid state chemistry and physics, primarily due to its simplicity and reasonable accuracy. *Standard* DFT approaches such as the LDA or GGA, however, suffer from a number of problems, most of which stem from the fact that these methods use an approximate exchange-correlation functional. The formulation of Equation 2.33, means that the Coulomb term, $J\left[\rho(r)\right]$, includes the spurious interaction of an electron with itself, which would not occur in an exact exchange-correlation functional. This error means that each electron interacts with itself and is known as the self interaction error (SIE). The SIE causes huge problems for systems with highly localized orbitals, where the electrons are in close proximity with each other. This causes the electrons to delocalize, in a attempt to minimize the self interaction. In the case of semiconductors/insulators with localized defect states, standard DFT functionals tend to delocalize the electron or hole states over many atoms, often predicting degenerate metallic behaviour, when experiment indicates the activated deep levels. This type of behaviour is very evident in the case of CeO_2 (known as cerium dioxide or ceria), as experimentally the formation of an oxygen vacancy is known to release two electrons to the lattice, which localize on two Ce sites neighbouring the vacancy, formally reducing these sites form Ce^{IV} to Ce^{III}.[76] In Kröger-Vink notation this is:

$$O_O^x + 2Ce_{Ce}^x \rightarrow V_O^{\bullet\bullet} + 2Ce_{Ce}^{'} + \frac{1}{2}O_{2} \tag{2.38}$$

where O_O^x is a neutral oxygen on an oxygen lattice site, Ce^x is a neutral cerium in a cerium site, $V_O^{\bullet\bullet}$ is a doubly positively charged vacancy in an oxygen site and $Ce_{Ce}^{'}$ is a trivalent Ce atom in a cerium site. The previously unocupied $4f$ state is occupied for the Ce(III) ions, giving the electronic configuration Ce4f^1.[76] Ultraviolet photoelectron epectroscopy (UPS) and x-ray photoeletron spectroscopy (XPS) studies have indicated distinct reduced Ce^{III} states deep in the bandgap of reduced CeO_2.[76] Standard DFT predicts the excess electrons left over upon oxygen vacancy formation to be delocalized over all the Ce atoms neighbouring the vacacny,[77] with is completely at variance with experiment.

The other important error associated with standard DFT approaches is that the band gaps it produces for many semiconductors are often significantly smaller than their experimental values, and in some cases DFT can even predict known semiconductors to be metallic.[78] This "band gap error" is inherent to DFT due to a disconuity that occurs in the exact exchange-corelation functional.[79]

Attempts have been made to remove the SIE from DFT calculations, with probably the best known of these being the self-interaction corrected (SIC) functional developed by Perdew and Zunger,[80] which explicitly subtracts the unphysical self-interaction terms. Unfortunately the SIC of Perdew and Zunger in both its scaled and unscaled versions, has a very high cost/performance ratio,[81] and therefore is not widely used. We therefore discuss in the following sections two computationally less expensive methods of approximately correcting for some of the inherant errors of standard DFT functionals.

2.1.10 The DFT+U Approach

The so called DFT+U approach was developed for strongly correlated systems (e.g. transition metal oxides), in which the d electrons spend the majority of the time in regions near the ions. This close proximity of the electrons to each other near the ions leads to strong Coulombic repulsion, and hence *strongly correlated* motion. The term strongly correlated, in the definition of DFT+U, does not refer to the usual chemistry definition of correlation formulated by Lowdin[64]. Lowdin's definition states that the correlation energy is the difference between the exact ground state energy and the Hartree-Fock ground state energy. In DFT+U it refers to the physics term of strong Coulombic interactions resulting in localised electronic states.

Within HF theory the Coulombic interaction is correctly described because the self-interaction of the electron is cancelled by the exact exchange. In standard DFT functionals, the functional only contains approximate exchange, giving rise to the SIE [82? –84]. In the DFT+U approach, the interactions between electrons at the same atomic centre (on-site interactions) are treated using a parameterised Hamiltonian, with these interactions being included only for a specific orbital quantum number, l. In the rotationally invariant formulation of Dudarev,[83] the energy is given by:

$$E_{GGA+U} = E_{GGA} + \frac{U-J}{2}\sum_{\sigma,m}(n_{l,m,\sigma} - n_{l,m,\sigma}^2) \tag{2.39}$$

where $n_{l,m,\sigma}$ is the occupation number for an orbital with quantum number, l, magnetic quantum number, m, and a spin of σ. The parameters U and J correspond to the average Coulomb and exchange interactions between electrons of the same angular momentum on the same atom. Thus the $+U$ term can be considered as an energetic penalty to partial occupation, with the term being zero when the occupation is zero or one, and non-zero when there is fractional occupation. This has the result of encouraging the localization of electrons to atomic centres.

The DFT+U approach does not raise the computational cost compared to a GGA/LDA calculation, and as such it has become a very popular method. It does, however, possess some drawbacks, and indeed some caveats about its "proper" usage. To use the DFT+U formalism it is important to determine a suitable value of U. First principles prescriptions have been developed for this purpose[85,86]. However, U is likely to be geometry dependent, and although this is expected to be a small effect in the bulk, it could be a large factor for systems with low symmetry, such as surfaces and those containing defects[87]; different U values may in theory be required for each inequivalent site, and would vary during large structural relaxations. Also the +U value cannot be used to solve for problems that are not fully caused by the SIE, such as the band gap error. For example, employing a larger value of U to fit band gaps to experimental data rather than to correctly localise a polaronic defect state can result in defect states that are completely at variance with experimental results.[88,89] Often a pragmatic approach is adopted, based on the specific behaviour we are trying to recreate, e.g. if we are interested primarily in the description of a defect state, we select U based on the *relative* position in the band gap of the defect state energy level, compared to detailed experiment, such as XPS or UPS data. This approach has been successfully applied to highly correlated oxides such as V_2O_5,[88] MoO_3,[90] TiO_2,[91] and to our earlier example of the failings of standard DFT functionals, CeO_2.[92]

2.1.11 Hybrid DFT

Another approach to correct for the SIE is the so-called hybrid DFT approach. HF theory provides a method that does not suffer from the SIE, as it employs exact exchange, however, it lacks correlation. A mixing of the exact exchange of HF with the approximate DFT exchange-correlation functional should in essence significantly reduce the SIE and yield an improved $E_{XC}\left[\rho(r)\right]$ functional. In practice, a simple combination of HF exchange with the correlation of DFT was not very successful, however, a linear combination of the HF exchange and the DFT $E_{XC}\left[\rho(r)\right]$ functional proved more successful, and was termed *hybrid DFT* (HDFT).[93,94]

$$E_{XC}^{HDFT} = \alpha E_X^{HF} + (1-\alpha) E_{XC}^{DFT} \tag{2.40}$$

By varying the value of exact exchange, α, the amount of HF exchange included in the calculation could be varied, with α typically fit to some experimental data, e.g. electronic structure.

More advanced HDFT functionals have been developed, which are fit to experimental data, of which the B3LYP[95] functional is a good example. This functional uses Becke's[93] hybrid exchange functional with 20 % HF exhange and the Lee-Yang-Parr[73] (LYP) correlation functional and the LDA $E_{XC}\left[\rho(r)\right]$ functional:

$$E_{XC}^{B3LYP} = (1-a)E_X^{LDA} + aE_X^{HF} + bE_X^{B88} + cE_C^{LYP} + (1-c)E_C^{LDA} \tag{2.41}$$

In this formulation, the three parameters a, b, and c are fitted to the atomisation energies, ionization potentials and proton affinities for a set of compounds of the first row elements. The performance of B3LYP has been criticised recently as it is not fit for materials such as metal oxides or materials containing heavy elements, and as such should not be used to examine these materials.[96]

An alternative HDFT functional is the PBE0 functional, which has been shown to work well for metals and for a number of semiconductors.[97] PBE0 combines 25 % HF exchange with 75 % PBE exchange and 100 % PBE correlation (Equation 2.42), with these percentages derived from perturbation theory.[98]

$$E_{XC}^{PBE0} = \frac{1}{4}E_X^{HF} + \frac{3}{4}E_X^{PBE} + E_C^{PBE} \tag{2.42}$$

PBE0 has been shown to outperform B3LYP for solid state calculations,[96] but unfortunately is quite computationally expensive in a plane wave formalism. Difficulties in evaluating the Fock exchange in a real space formalism are caused by the slow decay of the exchange interaction with distance. An alternative approach is the HSE06 hybrid functional approach, in which this problem is addressed by separating the description of the exchange interaction into long and a short range parts.[99] Thus, a percentage ($\alpha =$ 25%) of exact nonlocal Fock exchange is added to the PBE functional (the choice of α is empirical and can vary from system to system[100]), and a screening of $\omega = 0.11\,\text{bohr}^{-1}$

is applied to partition the Coulomb potential into long range (LR) and short range (SR) terms. Thus the exchange and correlation terms are:

$$E_{XC}^{\mathrm{HSE06}}(\omega) = E_{X}^{\mathrm{HSE06,SR}} + E_{X}^{\mathrm{PBE,LR}} + E_{C}^{\mathrm{PBE}} \tag{2.43}$$

where

$$E_{X}^{\mathrm{HSE06,SR}} = \frac{1}{4}E_{X}^{\mathrm{Fock,SR}} + \frac{3}{4}E_{X}^{\mathrm{PBE,SR}} \tag{2.44}$$

Hartree-Fock and PBE exchange are therefore only mixed in the SR part, with the LR exchange interactions being represented by the corresponding part of the range separated PBE functional[99]. Setting $\omega = 0.00\,\mathrm{bohr}^{-1}$ yields the PBE0 functional, and setting $\omega = \infty\,\mathrm{bohr}^{-1}$ gives the PBE functional.

2.2 Solid State Simulations

2.2.1 Periodic Boundary Conditions

A direct solution of the Schrödinger equation for a macroscopic crystal is prohibited due to the large number of electrons they contain. To overcome this hurdle, the periodicity concept can be employed to take advantage of the repeating arrangement of atoms in a crystal. In this way, we can solve a Schrödinger equation for a *finite* repeating unit with special boundary conditions, instead of attempting to solve the Schrödinger equation for the infinite system. The magnitude (a, b, and c lattice vectors) and shape (α, β and γ cell angles) of the unit cell (smallest cell possible), together with the atomic positions within the unit cell, define the crystal structure. Therefore, this approach takes advantage of the space group symmetry of the unit cell under considerations. In all our calculations, the unit cell of the material being investigated is repeated periodically in all three directions, as shown in Figure 2.1

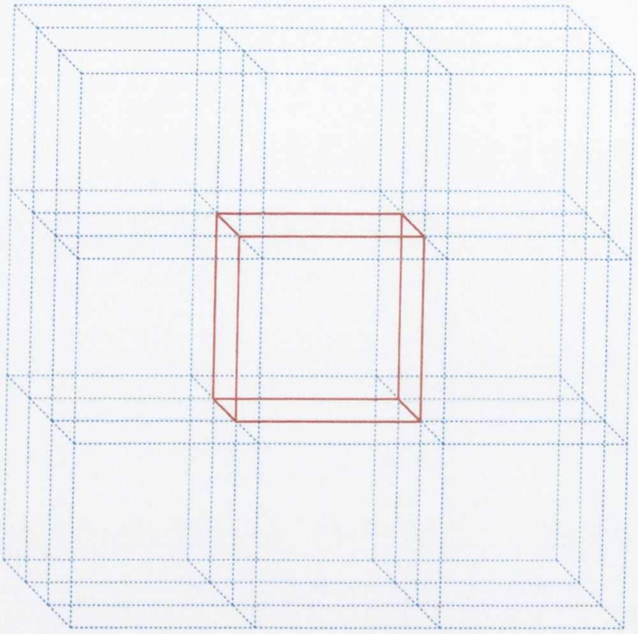

Figure 2.1: A $3 \times 3 \times 3$ expansion of a unit cell.

2.2.2 Basis Sets and Pseudopotentials

The success of any quantum chemical approach hinges on the quality of the mathematical representation of the wavefunction that is employed. These mathematical representations are usually obtained from a linear combination of functions known as *basis* functions. For periodic systems, plane waves (of the form $\exp^{ikx}$) act as a suitable basis set and offer high accuracy.[101] The advantages of a plan wave basis set is that it is not biased towards any system, and is independent of the atomic positions. The basis set is dependent on the magnitude of the simulation cell, and not the number of atoms in the cell, meaning that basis-set superpositions errors are not as big a problem as the are for localized basis sets (e.g. Gaussian functions).

The wavefunction in a plane wave approach can be expressed as a linear combination of plane waves which differ by reciprocal lattice vectors. In principle, the Fourier series needed to fully describe a given system would be infinite. As a kinetic energy term (frequency) is associated with each plane wave, this allows the implementation of an upper threshold, called the plane wave energy *cutoff*, which reduces the basis set to a finite size. Typically, a high cutoff energy is required to represent a wavefunction with rapid changes in electron density, i.e. electrons that are close to the core region of an atom. For a given system, a cutoff has to be selected that offers adequate convergence, which in practice means that for oxide materials, the cutoff is limited by the electrons of oxygen, and not the electrons of heavier cations. As the plane wave basis set can be optimized through variation of this single energy cutoff parameter, it is much more straight forward to optimize than for localized basis sets.

Normally, in planewave basis sets, only the valence electrons are represented explicitly. The major issues with representing valence electrons with planewaves is that their wavefunctions show rapid oscillations near the nuclei due to their requirements that they be orthogonal with the core electrons. This means that a large number of planewaves with high kinetic energy would be necessary to accurately model the rapidly oscillating wavefunction. To circumvent this problem, a pseudopotential is normally introduced which describes the interaction between the the valence electrons with the core electrons and the nucleus. The pseudopotential has the same shape as the valence electrons outside the core region, but has fewer nodes in the core region (Figure 2.2), which reduces the the magnitude of the planewave basis set required. Pseudopotentials are generally derived from all-electron calculations, and are parameterized to reproduce the behaviour and properties of the valence electrons. By relaxing the constraint that the real and pseudo wavefunction represent the same charge (norm conserving), Vanderbilt[102,102] demonstrated that the same accuracy can be achieved using a smoother function and therefore a smaller cutoff.

The projector augmented wave method[103] (PAW) was developed by Blöchl to accurately and efficiently calculate the electronic structure of materials within the framework of DFT. In the PAW method, localized basis sets are used to represent the core electrons, with the effect of these core states projected onto the valence electrons. This approach yields the numerical advantages of the pseudopotential calculations while retaining the physics of all-electron calculations, including the correct nodal behaviour

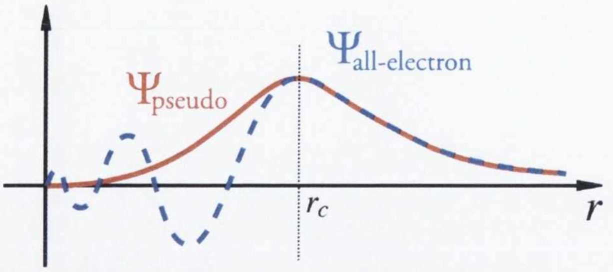

Figure 2.2: Schematic of the relationship between an all electron (blue dashed line) and a pseudopotential (red) wavefunction. The all electrons and pseudopotential wavefunctions match above the cutoff r_c.

of the valence electron wavefunctions. The PAW approach employs many of the same ideas developed by Vanderbilt and is employed in all our calculations. The PAW fixed core states are generated from all-electron scalar relativistic calculations.

2.2.3 Brillouin Zone and k-Points

By applying Bloch's theorem[104] to the wavefunctions, the use of periodic boundary conditions to simplify the calculation of the electronic structure is made possible. Bloch's theorem states that in a periodic system (e.g. an electron moving in a periodic potential of the ions in a crystal lattice) the electronic wavefunction can be written in the form

$$\Psi(x) = \exp^{ikx} u(x) \tag{2.45}$$

The exponent represents a plane wave and $u(x)$ is the periodicity of the lattice, with k being the wave vector which represents the phase relationship of the wavefunction between repeated unit cells. The Brillouin zone is the region of "k-space" in which all eigenvalues of the Hamiltonian may be labeled uniquely within any $(\frac{2\pi}{a})$ range along the k-axis, Figure 2.3.

In a DFT calculation, the electron density is calculated at each iterative step, and can be found by integrating the squares of the magnitudes of the Kohn-Sham eigen-

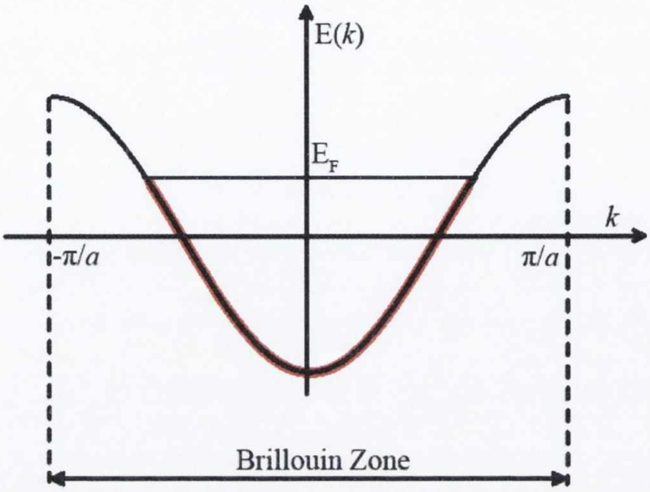

Figure 2.3: A schematic band structure (eigenvalue spectrum) in the Brilliouin zone. All states up to the Fermi level (E_F are occupied.

functions over the Brillouin zone. In practice, to minimize the computational cost, the integral must be approximated by a sum over selected k-points. As the wavefunction varies smoothly in reciprocal space, an accurate approximation to the total energy can be achieved by sampling representative points.[105] In the case of non-metallic systems only a small set of k-points is needed, however for metallic systems, a much denser set of k-points is necessary to acurately define the Fermi level. Convergence is obtained by systematically increasing the number of k-points sampled. Common k-point meshes employed are the so-called "regular" meshes, where the points are equally spaced from the origin, and the "special" k-point meshes, which offsets the regular mesh from the origin to reduce the number of k-points required. A method commonly employed is the Monkhorst and Pack[106] method which can make use of both regular (even) and special (odd) meshes.

2.2.4 Electronic Optimizations

The lattice vectors, atomic coordinates and total number of electrons of a solid are required to perform a solid state DFT calculation. The optimized electronic and geometric structures are determined through an iterative proceedure as outlined schematically in Figure 2.4. Firstly, the program begins by generating a trial charge density and wavefunction (which can be randomly generated or taken from a previous iteration). The Hamiltonian is then set up as a sum of $T[n]$, $J[n]$ and $E_{XC}[\rho(r)]$, and the iterative refinement of the wavefunction begins with the solution of the Kohn Sham equations. Diagonalisation of the Kohn-Sham matrix to obtain the eigenvalues is the most time consuming portion of the calculation, typically taking up in excess of 90% of its time. Traditional diagonalisation methods are very computer intensive, as the matrix diagonalization increase with N^3. A very large diagonalisation problem is caused by the use of plan wave basis sets, and therefore iterative diagonalisation methods are most efficient for these large problems. In our calculations the Kohn-Sham equations are solved using the iterative blocked Davidson[107] algoritmn.

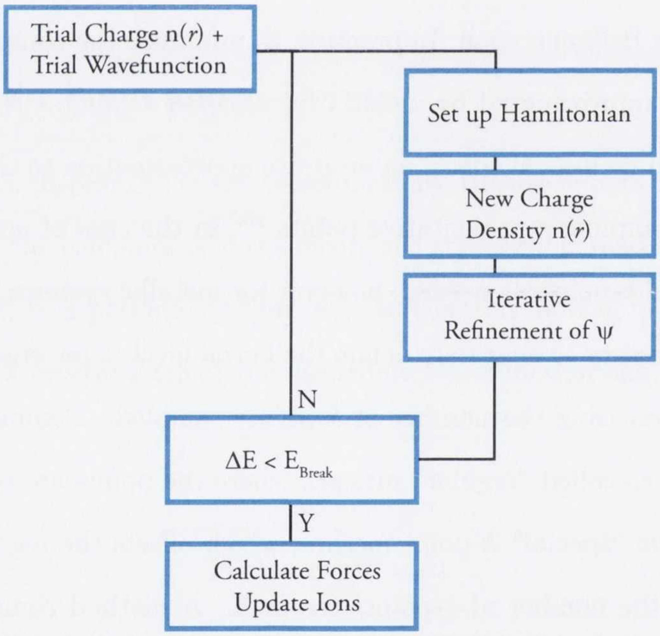

Figure 2.4: Schematic of a self consistent DFT scheme.

Once the Kohn-SHam equations are solved, we obtain a new charge density and wavefunction. If the change in energy of the new configuration is within a specified energy threshold of the starting energy, then the new wavefunction is accepted, and it is used to calculate the forces and update ion positions. If it is not accepted, the new charge density and wavefunction are used as the initial input and the proceedure is repeated self consistently until the convergence criteria are finally met.

2.2.5 Force Model and Geometry Optimization

The forces on the ions are calculated using the Hellmann-Feynman theorem.[108] Classically, force is defined as the derivative of energy with respect to position. The easiest way to estimate the force on an ion, is to calculate it is to move the ion in all directions and calculate it numerically. Therefore, for a system with N ions, this will need 6N calculations of energy. The Hellmann-Feynman theorem speeds this process up considerably as its allows all forces (acting on all the ions) to be calculated by calling the energy sub-routine only once. The theorem states that the force on any fixed nucleus in a system of nuclei and electrons is just the classical electrostatic attraction felt by the nucleus. This allows the force to be estimated directly from the wavefunction which has been previously calculated.

The one drawback of this approach is that a term to represent the derivative of the basis set with respect to the position of the ion, is neglected. This contribution to the force on the ion is called the Pulay force(commonly called the Pulay stress).[109] Therefore, if the value of the Pulay force is not calculated, there is an error in the value of the Hellmann-Feynman force. Pulay forces *must* always be considered when using localized basis sets. In a plane wave basis set regime, the complications from Pulay stress have been shown to be substantially reduced, but must be properly treated for the case of volume relaxations.

Once there are zero net forces on each ion, the minimim energy ionic configuration has been reached. The calculated forces are used to perform Quasi-Newton relaxations, which instead of obtaining an estimate of the Hessian matrix (the square matrix of second partial derivatives) at a single point, gradually builds up an approximate Hessian matrix by using gradient information from some of the previous iterates, until the forces on the atoms have reached a certain convergence criterion.

Chapter 3

Computational Methodology

3.1 Vienna *Ab Initio* Simulation Package (VASP)

All calculations in this thesis were performed using the Vienna *Ab Initio* Simulation Package (VASP).[110–112] VASP is a quantum mechanical code that is widely used in both the computational chemistry and computational physics communities for electronic structure calculations. The wide popularity of VASP stems from the fact that it contains its own set of optimized PAW pseudopotentials for each element, and has DFT, DFT+U, HF and Hybrid-DFT methods implemented in it, making it an extremely flexible code. Once the initial unit cell is specified, periodic boundary conditions are used to repeat the unit cell in three directions to represent an infinite lattice. Full electronic and geometric relaxations (optimisations) are then carried out for the material under investigation. Subsequently, further calculations can then be performed to determine properties such as band structures, density of states and optical analysis. The calculations in this thesis were performed on three different compute cluster within the Trinity Centre for High Performance Computing: (i) the IITAC supercomputer, which is an Opteron 2.40 GHz chip, 712 core machine with a Voltaire infiniband interconnect, (ii) The Lonsdale supercomputer, which is an Opteron 2.30 GHz chip, 1232 core machine with infiniband interconnect, and (iii) the Crusher supercomputer, which is an Intel 2.50 GHz chip, 144 core machine with infiniband interconnect.

3.2 Structural Optimization and Convergence

There are three major factors that determine the precision of self-consistent calculations on solid state systems; (i) resolution of the basis set, (ii) the k-point sampling density, and (ii) adequate optimization of the geometry. In all our calculations, the convergence for each system is checked rigorously in relation to both plane wave cutoff energy and k-point mesh density. The frozen core approximation in the PAW pseudopotential reduces the number of plane waves required in our calculations. As all of the materials investigated in this thesis contain oxygen, which is a lighter anion where the valence electrons vary more rapidly, relatively high values of cutoffs are needed. The minimum cut off that was found to be sufficient for most of our calculations is 400 eV, however for the relatively computationally inexpensive PBE and PBE+U calculations, a cutoff of 500 eV is utilized. For all systems investigated, tests were carried out to ensure convergence of at least 0.01 eV/formulae unit.

Through years of experience of electronic structure calculations within the Watson research group, it has been demonstrated that a k-point sampling density of approximately 0.04 Å^{-1} results in acceptable convergence for most non-metallic systems. Table 3.1 shows a simple convergence table between lattice vector magnitude, k-point sampling density and the number of k-points. The number of k-points is taken as a whole integer, and is rounded to the nearest even number for continuity in the convergence. To ensure that convergence is obtained, calculations were performed with a k-point density above and below 0.04 Å^{-1}, checking that the total energies remain within at least 0.01 eV/formulae unit.

We can determine the equilibrium structure of a system quite conveniently using total energy calculations. Using the variational principle, which tells us that the ground state of a system possesses the lowest energy, we can compare the total energy for different configurations of a system and determine the lowest energy configuration. In all the materials studied in this thesis, optimization at a series of volumes was performed for each structure, allowing the atomic positions, the lattice vectors and

Table 3.1: Relationship between of the magnitude of the lattice vector and the k-point density, with a sampling rate of 0.04 Å^{-1}.

Lattice Vector (Å)	LV^{-1}	LV^{-1}/0.04	k-point Density
2.00	0.5000	12.50	12
4.00	0.2500	6.26	6
6.00	0.1667	4.17	4
8.00	0.1250	3.13	4
10.00	0.1000	2.5	2
12.00	0.0834	2.09	2

the cell angles to relax within a constrained total volume. The energy-volume curves obtained from this approach were then fitted to the Murnaghan equation of state[113] to obtain the equilibrium cell volume, which is then optimized. This approach is taken to avoid the problem of the Pulay stress and changes in the effective basis set and its cutoff that occur in plane wave calculations on volume changes.[?]

Figure 3.1 shows a graph of the PBE+U calculated energy-volume data points and the fitted Murnaghan equation of state curve for Cu_2O, calculated using a 500 eV cutoff. The results for three k-point sampling densities are shown. For a $4 \times 4 \times 4$ k-point density the calculation is quite well converged (within 0.05 eV/Cu), and is chosen for the computationally expensive Hybrid calculations. However, the $6 \times 6 \times 6$ is chosen for the computationally inexpensive PBE and PBE+U calculations as it offered a convergence up to the fourth decimal place per Cu with only a moderate addition in computational burden, Chapter 6.

For each system studied, we must provide an initial estimate of the volume. Therefore we use the experimentally determined lattice constant, or if one is not available, we make initial estimates based on similar materials. The volume is then adjusted systematically until the data set brackets a minimum. Upon obtaining a minimum volume from the Murnaghan equation of state, a final geometry relaxation calculation

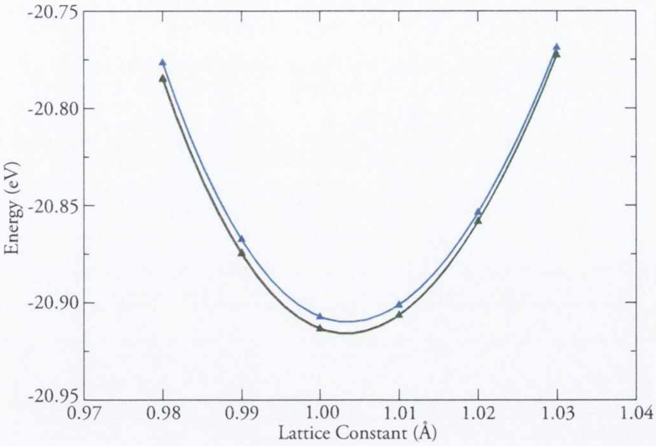

Figure 3.1: Murnaghan equation of state fit (lines) to the energy-volume data (triangles) obtained for Cu_2O. Gamma centred k-point meshes of $4 \times 4 \times 4$, $6 \times 6 \times 6$, and $8 \times 8 \times 8$ are represented by the blue, red, and green colours.

is performed at this volume, yielding the optimized structure. This procedure is shown schematically in Figure 3.2, which illustrates the process of structural optimization, plane wave and k-point convergence calculations. A comprehensive optimization of each system requires nine series of volume optimization calculations to be performed, with each one resulting in a final equilibrium calculation. From these results the optimal configuration is chosen and the electronic structure is then analysed.

3.3 Electronic Structure Calculations

3.3.1 Band Structures

We can gain information about the electronic structure of a material by using the Kohn-Sham eigenvalues extracted from the DFT calculation to determine the band structure of a system, which is the energy of the eigenvalues plotted as a function of k. If we examine the positions of the valence band maximum and the conduction band minimum within the band structure, the magnitude and nature of the band gap can be determined. The dispersion (curvature) of a band allows the strength of an interaction between atomic orbitals to be identified with a more disperse band indicating a stronger

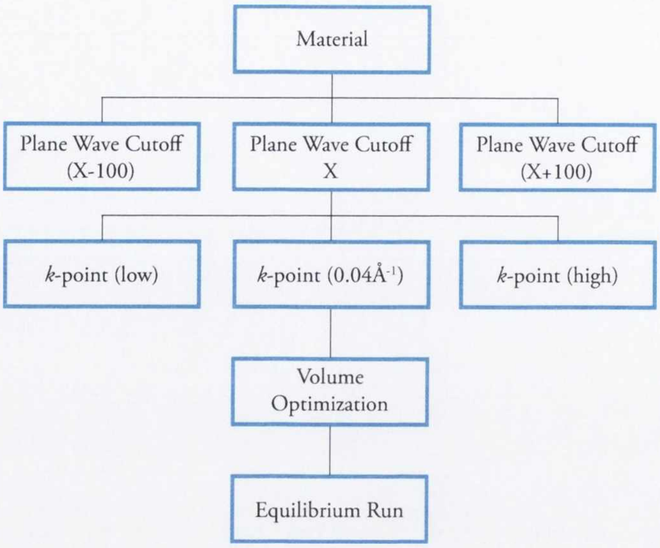

Figure 3.2: Schematic flow chart of structural optimization and convergence calculations.

interaction while a flat non-disperse bands indicates weak interactions between atomic orbitals. For example, metal *s*–*s* interactions tend to be very strong due to the overlap caused by the disperse nature of *s*. In many TCOs such as In_2O_3, with conduction bands predominately made up of cation *s* states, the CBM shows a high dispersion at the Γ point. However for compounds with a *d*-orbital based conduction band such as the Zn d^6 spinels that will be discussed in Chapter 8 the dispersion is much less.

A band structure calculation is performed in VASP by firstly self-consistently calculating an accurate charge density and wavefunction using a homogeneous k-point mesh. The next step is to perform a non self consistent calculation with the charge density held constant, to evaluate the eigenvalues as each of the k-points on the high symmetry lines of the reciprocal cell. The eigenvalues can then be plotted against k-points to give the band structure.

Choosing *k*-points for Band Structures

It is not feasible to plot the bands at all possible k-points, as plotting the energy over all k-points would require an infinite number of vectors. The general approach is to show the evolution of the band energy across certain lines of the Brillouin zone unique to the crystal class. The Brillouin Zone is specific to the space group of the particular material being studied. For example, the high symmetry points within the Brillouin Zone for a rhombohedral delafossite (space group #166) are shown in Figure 3.3. The coordinates of the high symmetry points used in all our calculations are taken from Bradley and Cracknell.[114] The energy can be plotted over a path which visits each of these points (e.g. $\Gamma \longrightarrow$ F $\longrightarrow$ L $\longrightarrow$ Z $\longrightarrow$ Γ, as illustrated in Figure 7.2.

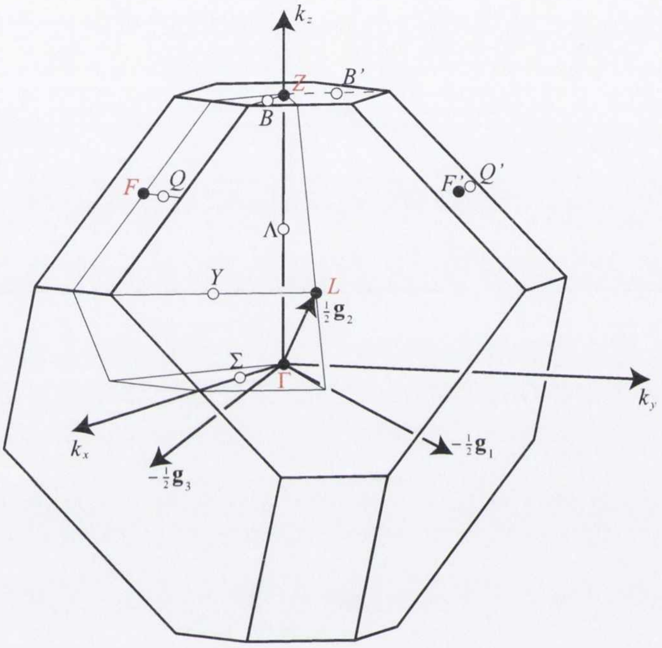

Figure 3.3: The Brilliuin Zone of space group #166 taken from Bradley and Cracknell [114]. $\Gamma = (0,0,0)$; $Z = (\frac{1}{2},\frac{1}{2},\frac{1}{2})$, $L = (0,\frac{1}{2},0)$ and $F = (\frac{1}{2},\frac{1}{2},0)$.

3.3.2 Electronic Density of States

Another way of displaying information about the electronic structure of a material is the electronic density of states (EDOS). The total EDOS shows the density of eigenvalues as a function of energy, meaning it is essentially an integrated band structure. Although the total EDOS can provide information about the total electronic structure, it can not tell the viewer to which ion or orbitals these states belong. To clarify the interpretation of the electronic structure, it is possible to calculate the partial (ion and l and m decomposed) electronic density of states (PEDOS). The wavefunctions are projected onto spherical harmonics within spheres of a certain radius around each ion. In order to accurately reflect the electron density surrounding each ion, this radius can be determined by examining the charge density surrounding each atom. The ratio between projection radii can be worked out by plotting the charge density map and measuring the radius of the charge density sphere surrounding each atom. The ratio between the atomic radii is then calculated and the size of the radii (in Å) is then varied, whilst keeping the ratio fixed, until the correct numbers of electrons are reached in the calculation. As it is impossible to account for the charge density using non-overlapping spheres the projection spheres normally overlap. In the case of hybrid DFT calculations, however, the computational cost of checking the radius is excessive, so the PAW projection radii as specified in the VASP pseudopotentials are used.

3.3.3 Effective Mass

In semiconductor physics, a common method used to estimate the conductive ability of a material is to calculate the transport effective mass of the band edges. In principle, a good *n*-type material should have a low electron effective mass at the CBM and similarly a good *p*-type conductor should have a low hole effective mass at the VBM. Bands with a low effective mass are characterized by a high degree of curvature (dispersion), while bands with high effective masses are generally flat and non-disperse. Highly dispersed bands lead to a high degree of electron/hole delocalization which results in high mobility and hence high conductivity, whilst flat bands result in localized electrons/holes which are not very mobile. In our calculations the transport effective mass (m^*_T) is calculated using:

$$\frac{1}{m^*_T(\mathrm{E})} = \frac{1}{\hbar^2 k}\frac{dE}{dk} \tag{3.1}$$

where $E(k)$ is the band edge energy as a function of wave vector k, obtained directly from the calculations.[115] The premise of effective mass theory relies on parabolic bands at the band edges. However, for most of the materials investigated in this thesis, the band edges are far from parabolic, and thus are not expected to be well described under a typical semiconductor effective mass approximation.[115] Despite this, we report the effective masses of the VBMs for some of the materials as a rough guide to the conduction properties.

3.3.4 Optical Absorption Calculations

As mentioned earlier in Section 1.2.4, the fundamental band gap of a material can be very different to the *optical* band gap. In order to accurately compare our calculations with experiments, we have computed the optical absorption spectrum for some of the materials studied in this thesis. Both the optical transition matrix elements and the optical absorption spectrum are calculated within the transversal approximation and PAW method.[116].

In this approach, the optical transition matrix elements, $\left\langle \psi_i \middle| \widehat{\mathrm{P}}_\alpha \middle| \psi_f \right\rangle$, between states i and f (with $\widehat{\mathrm{P}}_\alpha$ being the momentum operator with polarization α, and the PAW all electron wave function denoted ψ) are calculated using the method devised by Adolph *et al.*[117] The imaginary part of the dielectric function can be derived from the transition matrix elements using:

$$\mathrm{Im}\,\epsilon_{\alpha\beta}(\omega) = \left(\frac{2\pi e}{m\omega}\right)^2 \sum_{if} \int d(\mathbf{k}) \left\langle \psi_i \middle| \widehat{\mathrm{P}}_\alpha \middle| \psi_f \right\rangle \left\langle \psi_f \middle| \widehat{\mathrm{P}}_\beta \middle| \psi_i \right\rangle \delta(E_f(\mathbf{k}) - E_i(\mathbf{k}) - \hbar\omega) \tag{3.2}$$

with the integration performed using the tetrahedron method[118] and a fine k-point mesh (in our calculations $10 \times 10 \times 10$ is a sufficiently fine mesh). The real part of the dielectric function, $\mathrm{Re}\,\epsilon_{\alpha\beta}(\omega)$, can be obtained from the imaginary part using the Kramers-Kronig relations[119]. The absorption coefficient is then calculated using:

$$A_{\alpha\alpha}(\omega) = \frac{\sqrt{2\left[|\epsilon_{\alpha\alpha}(\omega)| - \mathrm{Re}\,\epsilon_{\alpha\alpha}(\omega)\right]}}{c} \tag{3.3}$$

In this methodology, the adsorption spectra is summed over all direct VB to conduction band (CB) transitions and therefore ignores indirect and intraband adsorptions. [117]. Within this framework of single particle transitions, the electron-hole correlations are not treated, and so would require treatment by higher order electronic structure methods.[120,121]. Nevertheless, this method has been previously shown to provide reasonable optical absorption spectra.[122–124]

3.3.5 Valence Band Alignment

It has become popular amongst the theoretical physics community to calculate the "natural" valence band alignments of different materials and thus rank them according to the doping limit rule[125,126]. In this thesis we calculate the valence band alignments according to the method developed by Wei and Zunger[127,128], which does not take into account the deformation potentials.[129,130] To align the valence band of two notional oxides AO and BO, we construct a heterostructure of 1 × 1 × 8 in the [001] direction, yielding superlattices made up of a fifty-fifty mix of AO/BO. The lattice constants of AO and BO are averaged and used as the lattice constant of the superlattice. All the atoms in the heterostructure are relaxed until the forces on each atom are less than $0.01\,\mathrm{eV}\,\AA^{-1}$.

The valence band offsets are thus given by:

$$\begin{aligned} \Delta E_{\mathrm{V}}^{\mathrm{AO/BO}} &= \Delta E_{\mathrm{VBM-CL}}^{\mathrm{AO}} - \Delta E_{\mathrm{VBM-CL}}^{\mathrm{BO}} \\ &\quad + \Delta E_{\mathrm{CL_A-CL_B}}^{\mathrm{AO/BO}} \end{aligned} \tag{3.4}$$

where $\Delta E_{\mathrm{VBM-CL}}^{\mathrm{AO}} = E_{\mathrm{VBM}}^{\mathrm{AO}} - E_{\mathrm{CL}}^{\mathrm{AO}}$ and $\Delta E_{\mathrm{VBM-CL}}^{\mathrm{BO}} = E_{\mathrm{VBM}}^{\mathrm{BO}} - E_{\mathrm{CL}}^{\mathrm{BO}}$. These are the core-level (CL) to VBM separations for pure AO and BO at their equilibrium lattice constants. $\Delta E_{\mathrm{CL_A-CL_B}}^{\mathrm{AO/BO}} = E_{\mathrm{CL_A}}^{\mathrm{AO/BO}} - E_{\mathrm{CL_B}}^{\mathrm{AO/BO}}$ is the difference in core-level binding between the core levels in the constituent halves of the heterostructure.

3.3.6 Bader Charge Analysis

Quantum chemical theory does not directly define atomic charges in molecules or solids. DFT outputs the electron density, which in the framework of a plane wave basis set scheme, makes determining how the electrons should be partitioned quite difficult.

In quantum chemistry, the most commonly used partioning scheme is the Mulliken analysis, but this approach is predicated on localized basis sets, and therefore in not appropriate for our DFT systems. Instead we use the Bader[131] charge analysis method (Atoms in Molecules, AIM), using the program developed by Henkelman *et al.*[132] In this scheme, we define an atomic volume as that region of space, including the nucleus, which lies within all zero flux surfaces surrounding the nucleus. This essentially that we start at a maximum in the electron density (at the nucleus) and work outwards (opposite direction to density gradient) until the gradient reaches zero and starts to rise again. At the zero point, we have a bond between two atoms. In AIM theory, the partial atomic charge is the difference between the nuclear charge and the number of electrons residing within an atomic basin (number of electrons is the integral of the density over space):

$$q_k = Z_k - \int\limits_{\Omega_k} \rho(r) dr \tag{3.5}$$

where the volume of the atomic basin (the zero flux surface) is given by Ω_k.

3.4 Defect Calculations

The properties of materials are often controlled by defects or impurities. In a crystalline solid, defects are typically randomly distributed throughout the material, and often at very low concentrations. Simulation of defects in a single unit cell are therefore not feasible, and instead the unit cell is expanded in all direction to form a supercell, which itself is treated within periodic boundary conditions. Provided the impurities are sufficiently well separated from their periodic images (larger enough supercells), the properties of individual isolated impurities can be derived. In practice, however, the size of the supercell used is often limited by the complexity of the computational method employed, and also the computational resources available. In this section we outline the methodology we employ in the calculation of defects in supercells.

3.4.1 Formation Enthalpy of a Neutral Defect

The formation enthalpy of a neutral defect is calculated from

$$\Delta H_{\mathrm{f}}(\mathrm{D},0) = \left(E^{\mathrm{D},0} - E^{\mathrm{H}}\right) + \sum_i n_i(E_i + \mu_i) \tag{3.6}$$

where E^{H} is the total energy of the stoichiometric host supercell and $E(\mathrm{D},0)$ is the total energy of the neutral (charge state 0) defective cell. Calculations on the constituent elements of the material in their standard states, (e.g in the case of $\mathrm{Cu_2O}$, this would be $\mathrm{O_2}$ and Cu metal) give the elemental energies, E_i, with n being positive or negative if an atom is added to or removed from an external reservoir. μ_i is the chemical potential of the element being added to or removed from an external reservoir, and can be used to approximate typical growth conditions. Choosing chemical potential limits is discussed further in Section 3.4.5.

3.4.2 Formation Enthalpy of Charged Defects

Most defects and impurities can occur in multiple charge states. The formation enthalpy of a defect in a charge state q is given by:

$$\Delta H_{\mathrm{f}}(\mathrm{D},q) = \left(E^{\mathrm{D},q} - E^{\mathrm{H}}\right) + \sum_i n_i(E_i + \mu_i) + q\left(E_{\mathrm{Fermi}} + \epsilon^{\mathrm{H}}_{\mathrm{VBM}}\right) + E_{\mathrm{corr}} \tag{3.7}$$

where $E^{\mathrm{D},q}$ is the total energy of the defective cell. E_{Fermi} ranges from the VBM ($E_{\mathrm{Fermi}} = 0\,\mathrm{eV}$) to the CBM ($E_{\mathrm{Fermi}} = \mathrm{CBM}\,\mathrm{eV}$). $\epsilon^{\mathrm{H}}_{\mathrm{VBM}}$ is the VBM eigenvalue of the host bulk. E_{corr} are necessary corrections to the formation energies to account for finite cell size considerations and valence band alignments, and will be discussed in more detail later in this section.

Correction Method 1

The first correction the used is the alignment of the VBM in the defective supercell with the stoichiometric supercell, which changes Equation 3.7 to:

$$\Delta H_{\mathrm{f}}(\mathrm{D},q) = \left(E^{\mathrm{D},q} - E^{\mathrm{H}}\right) + \sum_i n_i(E_i + \mu_i) + q\left(E_{\mathrm{Fermi}} + \epsilon^{\mathrm{H}}_{\mathrm{VBM}}\right) + q\Delta v(\mathrm{D}) \qquad (3.8)$$

This alignment correction, Δ_v, is necessary as $\epsilon^{\mathrm{H}}_{\mathrm{VBM}}$ for the stoichiometric supercell cannot be directly applied to the defective supercell. This is due to the long range nature of the Coulombic potential and the periodic boundary conditions of the supercell approach.[133] This is addressed by inspecting a core level (in this case the O 1s core states) in the supercell far away from the impurity and aligning it with the core level in the stoichiometric supercell, to define the shift in the reference level, given by

$$\Delta v(\mathrm{D}) = \epsilon^{\mathrm{far}}_{\mathrm{core,1s}}(\mathrm{D},\mathrm{q}) - \epsilon^{\mathrm{H}}_{\mathrm{core,1s}},$$

where $\epsilon^{\mathrm{far}}_{\mathrm{core,1s}}(\mathrm{D},\mathrm{q})$ is the O 1s core energy level of the furthest O atom from the defect location, and $\epsilon^{\mathrm{H}}_{\mathrm{core,1s}}$ is the O 1s core energy level of the bulk host.

Correction Method 2

During the course of this work, a new correction scheme was proposed by Freysoldt, Neugebauer, and Van de Walle,[134] which cancels the interaction of the defect with its periodic images in the supercell approach and aligns the electrostatic potential to the bulk material. It is implemented in a simple program called "sxdefectalign" and can be adopted to work with a VASP output. Using this new correction scheme, Equation 3.7 becomes:

$$\Delta H_{\mathrm{f}}(\mathrm{D},q) = \left(E^{\mathrm{D},q} - E^{\mathrm{H}}\right) + \sum_i n_i(E_i + \mu_i) + q\left(E_{\mathrm{Fermi}} + \epsilon^{\mathrm{H}}_{\mathrm{VBM}}\right) + E_{\mathrm{align}}\left[q\right]. \qquad (3.9)$$

where $E_{\mathrm{align}}\left[q\right]$ is the correction term that accounts for (i) accounts for the proper alignment of the VBM between the bulk and the defective supercells and (ii) corrects for the finite-size-cell effects in the calculations of charged impurities.[134] The one extra parameter that need to be input in the program is that of the dielectric constant. This can be caclulated withing VASP for DFT and DFT+U, but not for HSE06 calculations. In the case of HSE06 calculations, we use the experimentally determined dielectric constant of the materials being investigated.

3.4.3 Thermodynamic Transition levels

Point defects and impurities often introduce defect levels into the band gap of a material. Experimentally these defect levels can be detected, and used to identify the nature of the defect or impurity, although sometimes identification of these levels experimentally can amount to guesswork. Computational identification of these defect levels is becoming an increasingly utilized tool in both the physics and chemistry communities. The experimental levels that are of interest nearly always involve transitions from one charge state to another of a defect centre. This means that the single particle levels (SPLs), which are the raw eigenvalues (Kohn Sham states) of the defect states in band structure, cannot be directly compared with any relevant experimentally measurable levels.[133]

Thermodynamic ionization (transition) levels of a given defect, $\epsilon_{\mathrm{D}}(q/q')$, are defined as the Fermi-level for which the charge states q and q' have equal total energy. These transition levels can be calculated using

$$\epsilon_{\mathrm{D}}(q/q') = \frac{\Delta H^{\mathrm{f}}(\mathrm{D},\mathrm{q}) - \Delta H^{\mathrm{f}}(\mathrm{D},\mathrm{q}')}{q'-q}, \tag{3.10}$$

and can be directly compared to the trap levels reported in experiments where the final charge state can relax to its equilibrium configuration after the transition, such as deep level transient spectroscopy (DLTS).[135]

3.4.4 Optical Transition Levels

The optical transition level (OTL), $\epsilon_{\mathrm{opt}}(q/q')$, associated with a transition between charge states q and q' is defined just as in Equation 3.10, with the exception being that energy of the final state of q' is calculated at the atomic configuration of initial state q. These optical levels would only be observed in experiments where the final charge state cannot relax to its equilibrium configuration after the transition (a vertical transition), [133] such as photoluminescence (PL) experiments. The difference in energy between the unrelaxed configuration and the relaxed equilibrium configuration is the relaxation energy, E_{rel} (the Franck-Condon shift).

3.4.5 Chemical Potential Limits

The chemical potentials depend on the experimental growth conditions, and in the case of oxides can be metal-rich or oxygen-rich, and anything in between. In principle they should be treated as a variable in this formalism of Equations 3.6 and 3.7, but in practice, firm boundaries are normally placed on the chemical potentials. Varying the chemical potentials, μ_i of each species can reflect specific equilibrium growth conditions, within the global constraint of the calculated enthalpy of the host. In the following discussion we use Cu_2O as our example of a host oxide (all energies quoted are taken from PBE+U calculations, as outlined in Chapter 6), and this yields:

$$2\mu_{\mathrm{Cu}} + \mu_{\mathrm{O}} = \Delta H_{\mathrm{f}}^{\mathrm{Cu_2O}} = -1.55\,\mathrm{eV}. \tag{3.11}$$

The lower limit of μ_O, which would indicate a *Cu-rich/O-poor* environment is limited by Cu metal formation:

$$\Delta\mu_{\mathrm{Cu}} = 0\,\mathrm{eV}, \qquad \rightarrow \qquad \Delta\mu_{\mathrm{O}} = -1.55\,\mathrm{eV}.$$

The upper bound of μ_O (*Cu-poor/O-rich*) is limited by CuO formation:

$$\mu_{\mathrm{Cu}} + \mu_{\mathrm{O}} \leq \Delta H_{\mathrm{f}}^{\mathrm{CuO}} = -1.36\,\mathrm{eV}, \tag{3.12}$$

Solving Equations 3.11 and 3.12 simultaneously yields:

$$\Delta\mu_{\mathrm{Cu}} = -0.19\,\mathrm{eV}, \qquad \textit{and} \qquad \Delta\mu_{\mathrm{O}} = -1.17\,\mathrm{eV}.$$

Identifying chemical potential limits becomes more challenging as you move towards ternary and quaternary compounds. We discuss the approach to identifying chemical potential limits for ternary delafossites $CuAlO_2$ and $CuCrO_2$ in Chapter 7.

3.4.6 Transition Level Diagrams

Plotting the formation energy of defects as a function of Fermi level (a transition level diagram) has become standard practice in the computational semiconductor physics community, with these diagrams typically displaying a plethora of information on the one diagram. Understanding a transition level diagram, however, is quite challenging . Generally, the approach taken is to plot the formation energy against E_{Fermi} at a constant chemical potential. Quite often two plots are presented, one at cation-rich conditions, and one at anion-rich conditions, as shown in Figure 3.4. Each defect usually possesses many different charge states, plotted as the blue and red dashed lines in Figure 3.4, but normally only the most stable charge state at each E_{Fermi} is plotted (full lines in Figure 3.4. Not all charge states are necessarily stable across the fermi level of a material, and in the case of the anion vacancy in our example, the +1 charge state is not stable, and therefore will not be seen experimentally. Such a defect is called a negative U defect.[26]

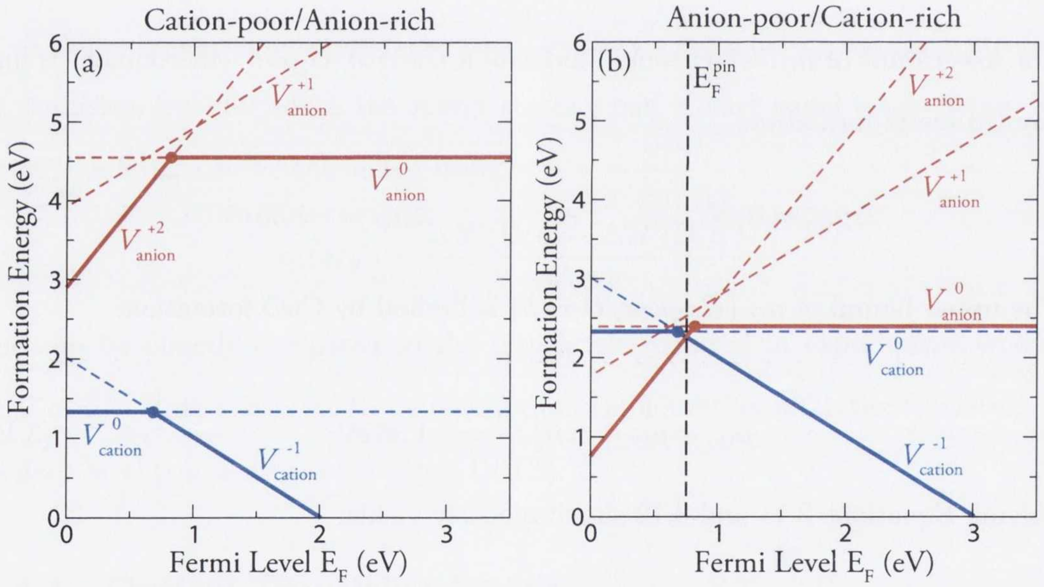

Figure 3.4: Sample transition level diagram for a notional binary material under (a) cation-poor/anion-rich conditions, and (b) anion-poor/cation-rich conditions. Blue denotes p-type defects, red denotes n-type defects. The solid dots denote the transition levels $\epsilon(q/q')$. The black vertical dashed line in (b) denotes the Fermi pinning energy.

In these diagrams, the n-type defect charge states slope upwards from left to right (positive slope), indicating the ionization of electrons from the donor states into the CB, whereas the p-type defect charge states slope downwards from left to right, indicating the ionization of electrons from the VB into the hole state. The transition levels (ionization levels) are usually marked with a solid sphere on these diagrams, and are the point where one charge state is in equilibrium with another, as defined in Equation 3.10. If a transition level (TL) of a p-type defect is within $0.03\,\text{eV}$ of the VBM, then this would indicate a good p-type conductor, with *shallow* acceptor levels, allowing the easy promotion of an electron and the formation of a hole in the VB.

We can assume therefore from Figure 3.4 that this notional material is p-type under cation-poor conditions as the formation energy of the cation vacancy is much lower that than of the anion vacancy, meaning that anion vacancies cannot compensate for the lower energy cation vacancies. We can also tell from the position of the transition levels of the cation vacancy that p-type conductivity in this material is *activated*, as the TL is quite deep in the band gap, away from the VBM. This indicates that this materials will not will not be a degenerate p-type semiconductor. The TL for the anion vacancy is extremely deep with respect to the CBM, meaning that n-type conductivity in this material is highly unlikely. If two charge states from acceptor and donor levels cross, this pins the Fermi level at this point, as shown in Figure 3.4 (b), meaning that as you move left or right on the diagram, the electronic behaviour of the system changes to reflect the lowest energy defect at each E_{Fermi}.

Chapter 4

Conductivity anomalies in Cu^{I}-based delafossite TCOs

4.1 Introduction

The development of "Transparent Electronics" is a much sought after goal for materials scientists.[13] Key materials in this quest are transparent conducting oxides (TCOs), which combine both electrical conductivity and optical transparency in a single material, usually possessing optical bandgaps greater than 3 eV and carrier concentrations of at least $10^{20}\,\mathrm{cm}^{-3}$.[6] The ultimate aim is the fabrication of functional p-n junctions using these TCOs, which would open up pathways to a myriad of possible transparent electronic devices.[11]

n-type TCOs (In_2O_3[18], ZnO[136], SnO_2[137]) are currently utilized in a number of commercial applications[9]. Previous efforts to produce p-type TCOs had centered on doping the usually n-type TCOs to make them p-type, particularly ZnO[36,37]. The top of the valence band of most wide band gap binary oxides usually is dominated by O $2p$ states, which when doped p-type, results in deep lying, *localized* O $2p$ holes (polarons), which are coupled to strong lattice distortions.[34] These oxygen holes severely limit any electronic conduction.[34,35]

p-type TCOs have only been a reality since 1997 when Hosono and co-workers first reported the optical and electrical properties of copper aluminate ($CuAlO_2$)[12], which crystalizes in the delafossite structure ($Cu^IM^{III}O_2$). This sparked an explosion of interest in developing *p*-type TCOs, using Hosono's "Chemical Modulation of the Valence Band" to combine the *p*-type conductivity of Cu_2O and with the larger band gaps of other binary oxides.[40] Cu_2O is a a native *p*-type semiconducting oxide, with a band gap of 2.17 eV which precludes it from TCO applications[39]. Ternary Cu based delafossite materials retain the valence band features of Cu_2O, with the Cu states dominating the top of the valence band, while extending the band gap by alloying with the wide band gap trivalent binary oxide. Although other Cu^I-based structures have been identified that display *p*-type conduction, e.g. $SrCu_2O_2$[52,53] and layered oxychalogenides ($LaCuOS$[54,138], $[Cu_2S_2][Sr_3Sc_2O_5]$[139,140] etc.), to date the *p*-type TCO with the highest conductivity is a delafossite (Mg doped $CuCrO_2$).[55]

It is well known that doping the trivalent metal site with a divalent dopant significantly improves the conductivity[13], but the trends seen for different trivalent metal cations from Al to Cr to Sc to Y (in increasing ionic radius) remains a mystery. Nagarajan *et al.* attempt to explain the trend in increasing conductivity of $CuY_{1-x}Ca_xO_2$ to $CuSc_{1-x}Mg_xO_2$ to $CuCr_{1-x}Mg_xO_2$ by noting that the increasing conductivity tracks a decreasing ionic radius of the M^{III} cation, and hence a decreasing lattice parameter in the Cu ion plane.[55] They suggest that this leads to increased Cu *d* orbital overlap and as a result better hole mobility. The authors also cite the need for detailed band structure calculations to examine the effect of the different M^{III} cation *d* orbitals on the valance band stucture.[55] This size dependence theory can possibly be ruled out by the observed conductivity of $CuAl_{1-x}Mg_xO_2$, which at $4\,\text{x}\,10^{-4}\,\text{S}\,\text{cm}^{-1}$ has a much lower conductivity than that of $CuCr_{1-x}Mg_xO_2$ ($220\,\text{S}\,\text{cm}^{-1}$), despite the ionic radius of Al being smaller than Cr.[51]

Sleight and co-workers discuss the effect of the M^{III} ion on the mobility of holes in *p*-type delafossites.[141] The authors suggest that the lower hole mobilities in *p*-type delafossites relative to Cu_2O may be caused by the lack of Cu–O–Cu linkages as seen in Cu_2O. In the delafossite structure there are only Cu–O–M^{III}–O–Cu linkages. They suggest the higher conductivities observed for $CuCrO_2$ and $CuFeO_2$ may be due to favourable mixing with the *3d* states on the M^{III} cation in the Cu–O–M^{III}–O–Cu linkages.[141]

Recently copper delafossites have been the recipient of a lot of theoretical analysis, but this has focused on band gap features, defect energetics and the effect of doping on the band structure, and to a certain extent has neglected to look at the detailed electronic structure of these materials. Being the prototypical copper delafossite TCO, $CuAlO_2$ has received most of the attention. This has included investigating the band gap[122,142], intrinsic defects[143], doping to form acceptor levels[144], and doping for dilute magnetic semiconductor applications (both in the Cu position and the Al position[145]). $CuAlO_2$ was investigated by Nie *et al.*[122] , along with $CuInO_2$ and $CuGaO_2$, using local density approximation (LDA) within the linearized augmented-plane wave (LAPW) method, reporting an indirect band-gap for all three materials. An indirect band gap was also reported by Robertson and co-workers[142], who investigated the hexagonal cell of $CuAlO_2$ using LDA. The layer stacking has little effect on the minimum gap, with an indirect gap of 2.1 eV predicted for both the hexagonal and rhombohedral sequences.

An LDA study of native defects in $CuAlO_2$ was also carried out by Hamada *et al.* [143] which postulated that copper vacancies and oxygen interstitials are the relevant defects, and that control of the copper and oxygen partial pressures is essential for the fabrication of low-resistivity $CuAlO_2$. The effects of Cu and Al vacancies, and Be, Mg and Ca dopants on the electronic structure of $CuAlO_2$ have also been investigated using LDA based LAPW calculations[144], with the results showing that the most promising defects for improving *p*-type conductivity are Cu vacancies and Be doping at Al sites.

$CuScO_2$ and $CuYO_2$ have received sparse attention, with only a handful of theoretical investigations in the literature[146–149]. Gilliland *et al.* have studied the bandstructure of $CuScO_2$ using LDA[146]. They report a direct band gap at L, but do not report the band gap magnitude.[146] Shi and co-workers have studied intrinsic[147] and extrinsic[148] defects in $CuScO_2$ and $CuYO_2$. They report the copper vacancies and oxygen interstitials have relatively low formation energies in these materials, and that under oxygen rich conditions, the oxygen antisite becomes an important acceptor[147]. Mg and Ca dopants are found to be the most prominent extrinsic defects.[148]. A recent study by Li and co-workers investigated the band edge features of $CuM^{III}O_2$ (M^{III} = Al, Y, Sc) and calculated the valence band alignment of these materials to ascertain why $CuScO_2$ shows the best conductivity of the three[149]. They find that $CuScO_2$ has the lowest hole effective mass and the highest VBM relative to the vacuum of all three, and conclude that these factors make $CuScO_2$ the most conductive.[149]

Very recently Eyert and co-workers have investigated the electronic structure of $CuCrO_2$ using GGA within the augmented spherical wave (ASW) method.[150] The authors present spin polarized PEDOS for the rhombohedral representation of the $CuCrO_2$ cell. This 4 atom cell cannot therefore take into account the antiferromagnetic nature of $CuCrO_2$,[151] and hence this study is restricted to the higher energy ferromagnetic configuration.[150] The PEDOS reports that Cr $3d$ t_{2g}^3 states dominate at the top of the valence band, $\sim$ 1.5 eV above the Cu $3d$ peak,[150] although this is inconsistent with high resolution XPS studies which show that Cu states dominate at the VBM.[152]

In this chapter, we systematically study the effect of the M^{III} cation on the electronic structure and chemical bonding of $CuM^{III}O_2$ (M^{III} = Al, Y, Sc, Cr). We demonstrate the importance of the increased covalency between the M^{III} states and oxygen as we move from Al to Y to Sc to Cr. We will also discuss the experimentally seen conductivity trends in doped Cu-based TCOs using the doping limit rule, effective mass theory and our knowledge of the detailed electronic structure of the materials.

4.2 Calculation Methodology

Structural optimizations were performed on the hexagonal $CuM^{III}O_2$ (space group P63/mmc) cells using density functional theory (DFT)[65,66] as implemented in the VASP[112,153] code. Exchange and correlation were described using the generalized gradient approximation (GGA), within the Perdew-Burke-Ernzerhof (PBE)[75] formalism.

The core electrons (Cu:[Ar], Al:[Ne], Y:[Ar], Sc:[Ne], Cr:[Ar], O:[He]) were treated within the projector augmented (PAW) Method[103].In each case the the atomic positions, lattice vectors and cell angles were allowed to relax, while the total volume was held constant. The resulting energy volume curves were fitted to the Murnaghan equation of state to obtain the equilibrium bulk cell volume.[113] Convergence with respect to k-point sampling and plane wave energy cut off was checked, and for all systems a Monkhorst Pack k-point grid of $4 \times 4 \times 1$ and a plane-wave cutoff of 500 eV were found to be sufficient. Calculations were carried out at a $9 \times 9 \times 5$ k-point grid to provide accurate density of states. Calculations were performed using DFT corrected for on-site Coulombic interactions GGA + U[83] to overcome the errors associated with the DFT self-interaction. GGA typically underbinds localised orbitals such as metal d states, and the $+U$ modification provides an approximate correction for this shortcoming[154].

The U value chosen for the Cu d was 5.2 eV; which closely reproduces features of the experimental x-ray photoemission spectroscopy (XPS) spectra for Cu_2O (specifically the position of the Cu $3d$ peaks as shown in Figure 4.1), and has been shown to reproduce the valence band features of both $CuAlO_2$[155] and $CuCrO_2$[152]. This U is also similar to the U values used by Raebiger *et al.* of 5 eV (which was also chosen to reproduce features of a Cu_2O XPS valence band spectra[156]), and the value of 6 eV chosen by Huda *et al.* to account for the correlation in narrow $3d$-bands.[157]. A U value of 4 eV for the Cr d states, which has been shown to reproduce the valence band features of Cr_2O_3.[158] All the Calculations of $CuCrO_2$ which contains open-d shells Cr atoms were spin polarized. Calculations were deemed to be converged when the forces on all the atoms were less than 0.001 eV $\AA^{-1}$. Structure visualization and analysis were performed using VESTA[159].

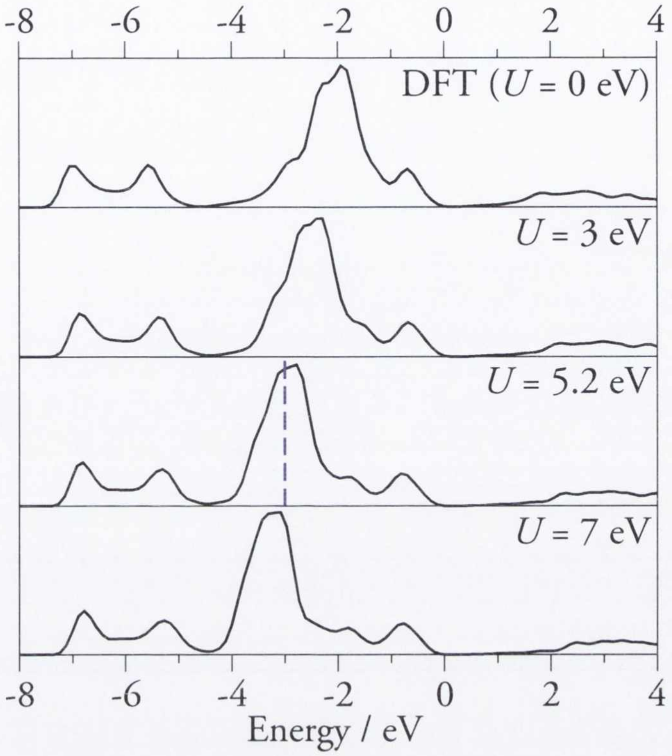

Figure 4.1: The valence band of Cu_2O as calculated with $U = 0\,\text{eV}$, $3\,\text{eV}$, $5.2\,\text{eV}$ and $7\,\text{eV}$. The experimental position of the $3d$ peak taken from the XPS study of Hu *et al.* [39], is indicated by a purple, vertical dashed line.

4.3 Results

4.3.1 Structure

The optimized structural parameters of $CuM^{III}O_2$ (M^{III} = Al, Y, Sc, Cr) are shown in Table 7.2. In all our delafossites, the calculated lattice constants are slightly overestimated, but this is a known overestimation associated with GGA calculations. The calculated bond lengths for each material are in good agreement with experimentally determined measurements.[47,160? ,161] The lattice parameter a increases for Al–Cr–Sc–Y, consistent with the trend in cation M^{III} sizes. It has been suggested that the larger M^{III}-cations can improve the capacity of a material for extrinsic doping on the M^{III}-site, which can result in high hole concentrations[149], and this has been used to explain the more promising p-type conductivity of doped $CuScO_2$ and $CuYO_2$ compared to that of the smallest cation $CuAlO_2$. This however does not explain the much higher p-type conductivity of Mg doped $CuCrO_2$, considering it has a smaller M^{III} cation size than both $CuYO_2$ and $CuScO_2$. Nagarajan *et al.* suggested that a decrease in the cation M^{III} size, increases the Cu d–d overlap, resulting in greater conductivity.[55] This would explain the trend in increasing conductivity for $CuYO_2$ to $CuSc_2$ to $CuCrO_2$, but cannot explain the poor conductivity observed for $CuAlO_2$.

	$CuAlO_2$	$CuCrO_2$	$CuScO_2$	$CuYO_2$
Volume	81.79	92.50	104.47	125.90
a	2.885 (+0.7%)	3.055 (+2.9%)	3.248 (+0.7%)	3.562 (+1.1%)
c	11.340 (+0.2%)	11.416 (+0.1%)	11.429 (+0.1%)	11.454 (+0.1%)
Cu–O	1.866	1.844	1.832	1.821
M^{III}–O	1.928	2.032	2.138	2.306

Table 4.1: Structural data and nearest-neighbour interatomic distances for the optimized $CuM^{III}O_2$ (M^{III} = Al, Cr, Sc, Y) structures. Percentage errors with respect to experimental data ($CuAlO_2$[47], $CuCrO_2$[?], $CuScO_2$[160], $CuYO_2$[161]) are given in parenthesis. Volumes are given in Å^3 and lattice dimensions and interatomic distances in Å.

4.3.2 Electronic Structure

$CuAlO_2$

The calculated bandstructure of $CuAlO_2$ is shown in Figure 4.2. The conduction band minimum is positioned at Γ and a broad, flat valence band maximum (VBM) is found along the H-K line and extends past K in the K-Γ direction. This is in good agreement with previous calculations[122], but is at variance with the study by Robertson *et al.* which predicted that the VBM is situated at L.[142]. In our present study, the highest occupied band at the L k–vector is 0.1 eV below the VBM. This results in an indirect band gap of 2.2 eV. Although this is an overestimation compared to the value of 1.8 eV obtained from optical-absorption experiments[44], it has been proposed that intrinsic defect levels decrease the experimental value.[142] A direct band gap of 3.1 eV is found at Γ, compared to 3.5 eV found by experiment.[44]

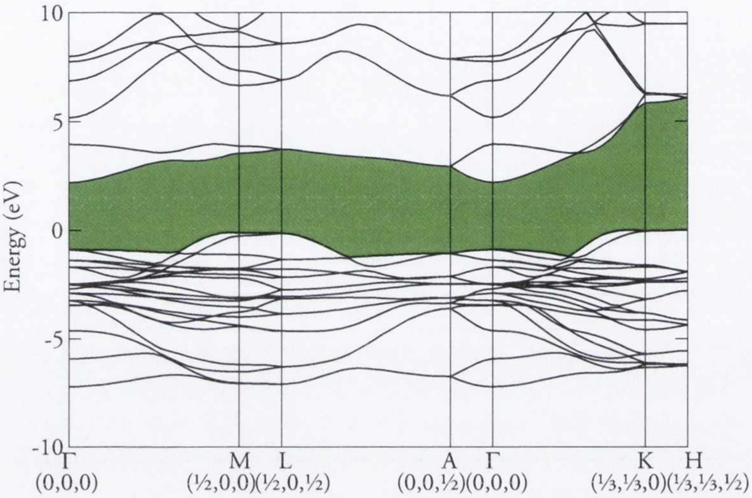

Figure 4.2: The electronic band structure of $CuAlO_2$ along the high symmetry points, plotted with reference to the top of the valence band at 0 eV. The green shaded area denotes the band gap.

Figure 4.3 shows the calculated total and partial (ion decomposed) electronic densities of states (EDOS/PEDOS) for $CuAlO_2$. Four distinct peaks are found in the valence band, consistent with a recent XPS study reported by Aston *et al.*[43] The conduction band consists of a narrow peak (labeled V) between 2 and 4 eV and a second broader peak above 6 eV.

The Cu PEDOS is dominated by 3d states between −4 and −1 eV, corresponding to peaks III and IV in the EDOS. There are also Cu 3d states between −9 eV and −4 eV, indicating a degree of covalent bonding with oxygen. The Al PEDOS shows a small valence band contribution concentrated between −9 eV and −4 eV which consists of a mixture of 3*s*, 3*p* and 3*d* states. In the conduction band the onset of Al states does not occur until +5 eV. The Al contributions to the EDOS are small, as is expected for an atom which is often well described by a fully ionized +3 oxidation state, and Al makes a minimal contribution to the states determining the electronic conduction

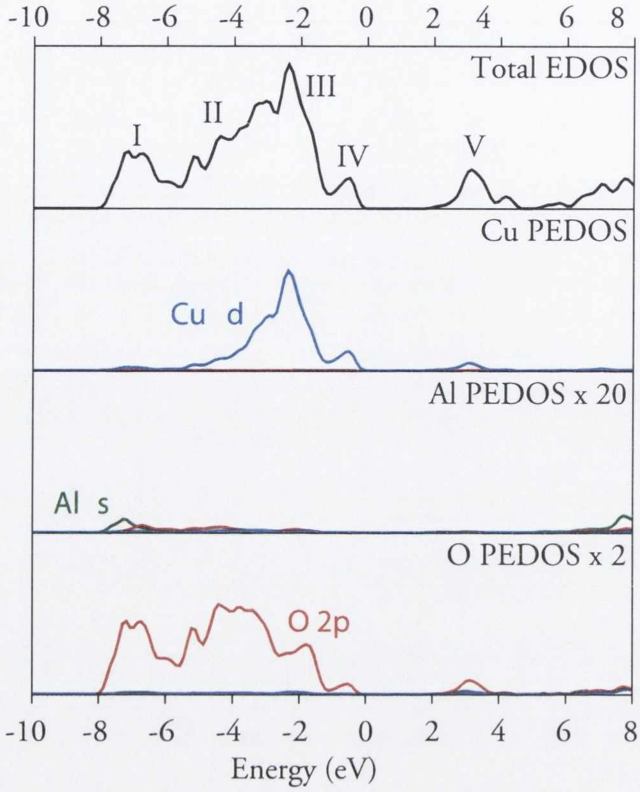

Figure 4.3: The electronic density of states for $CuAlO_2$. (*a*) Total EDOS, (*b*) Cu PEDOS, (*c*) Al PEDOS and (*d*) O PEDOS. The blue lines represent *d* states, green *s* states and red *p* states.

properties. The O PEDOS displays all four peaks observed in the EDOS. Peak I is O 2*p* in nature with a minor contribution from Al 3*s* and 3*p* states. Peak II is mainly O 2*p* although Cu 3*d* states are also present. Peak III is mostly Cu 3*d* with some O 2*p* contribution.The bottom of the conduction band (Peak V) and top of the valence band (Peak IV) both consist of states derived from a mixture of Cu 3*d* and O 2*p*.

$CuCrO_2$

The bandstructure (Figure 4.4) for $CuCrO_2$ exhibits an indirect band gap of 2.04 eV, with a direct gap measuring 2.55 eV found near M along M–Γ. For $CuCrO_2$ there is an experimentally demonstrated redshift in the experimental optical absorption relative to $CuAlO_2$. The CBM is centered between L and A and the VBM is situated at M. This was also found to be the case for 50% Cr doped $CuAlO_2$[155]. The presence of two

Cr sites introduces the possibility of magnetic ordering within the periodicity of the simulated unit cell. Due to the t_{2g}^3 configuration, antiferromagnetic (AF) interactions are stabilized, while ferromagnetic (FM) interactions result in no net energy gain. The calculated energy difference between the AF and FM configurations is small at 20 meV/f.u. which is consistent with the low Curie temperature that has been noted in experiment.[162]

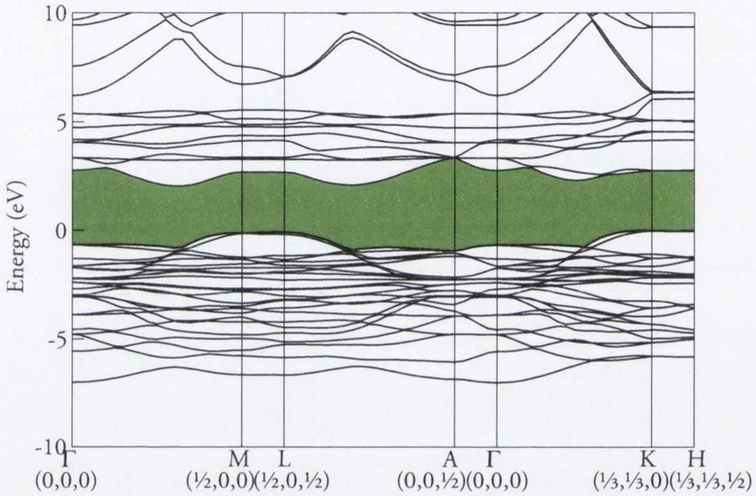

Figure 4.4: The electronic band structure of $CuCrO_2$ along the high symmetry points, plotted with reference to the top of the valence band at 0 eV. The green shaded area denotes the band gap.

The EDOS of $CuCrO_2$ is shown in Figure 4.5. The valence band features are very similar to those reported by Arnold *et al.* in a recent XPS study.[152]. These features are different from those of $CuAlO_2$, with a significant shoulder appearing on the higher energy side of the main peak (peak III) at ~ -1.5 eV. In the Cu PEDOS, the Cu peak shape is also affected: the shoulder to the left of the maximum just below -2 eV is less pronounced, and a second shoulder now appears to the high energy side of the main peak. The Cr states appear along the entirety of the valence band, with a significant peak at ~ -2.5 eV, and with the Cr contribution to peak IV increasing the density of states at the top of the valence band relative to that of $CuAlO_2$. The O $2p$ states dominate the lower valence band, with peaks I and II being made up mainly of O $2p$

states, but with significant contributions from Cu *d* and Cr *d* states. The bottom of the conduction band is predominantly Cr in nature, with the contribution from O 2*p* states now extending up to ~ 5 eV due to increased interaction with the Cr 3*d*. This increased Cr–O interaction compared to Al–O in $CuAlO_2$ is likely to be responsible for the change in the k-vector of the CBM away from Γ.

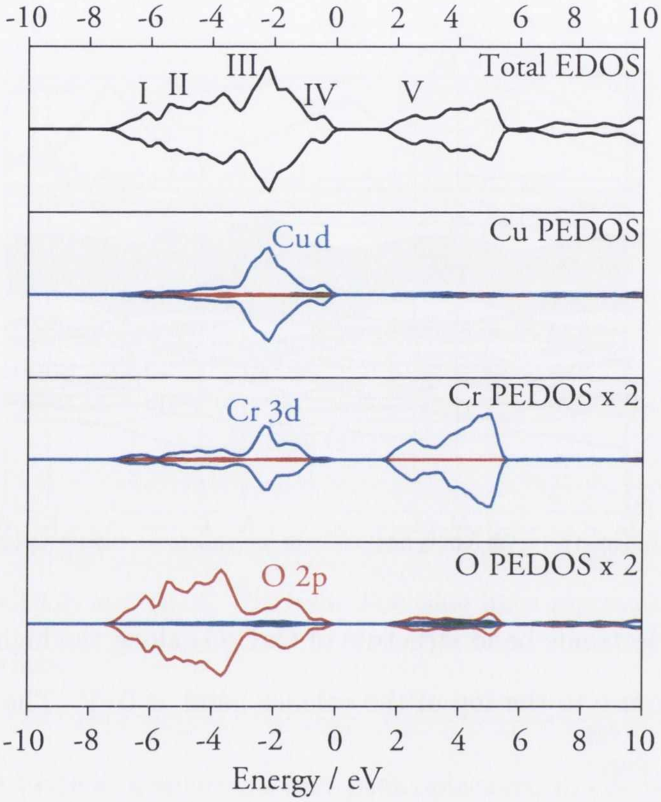

Figure 4.5: The electronic density of states for $CuCrO_2$. (*a*) Total EDOS, (*b*) Cu PEDOS, (*c*) Cr PEDOS and (*d*) O PEDOS. The blue lines represent *d* states, green *s* states and red *p* states.

$CuScO_2$

The bandstructure of $CuScO_2$ is shown in Figure 4.6. The VBM is situated at H, with the CBM lying at Γ. Previous studies by Shi *et al.*[149] and Gilliland *et al.*[146] have reported a direct band gap for $CuScO_2$, but these studies were carried out using the smaller rhombehedral cell, although it has been shown that $CuScO_2$ forms preferentially in the hexagonal structure.[157] The indirect band gap measures 2.88 eV with the smallest direct band gap measuring 2.98 eV at the M point. Experiment reports the band gap of $CuScO_2$ to be 3.3 eV.[163]

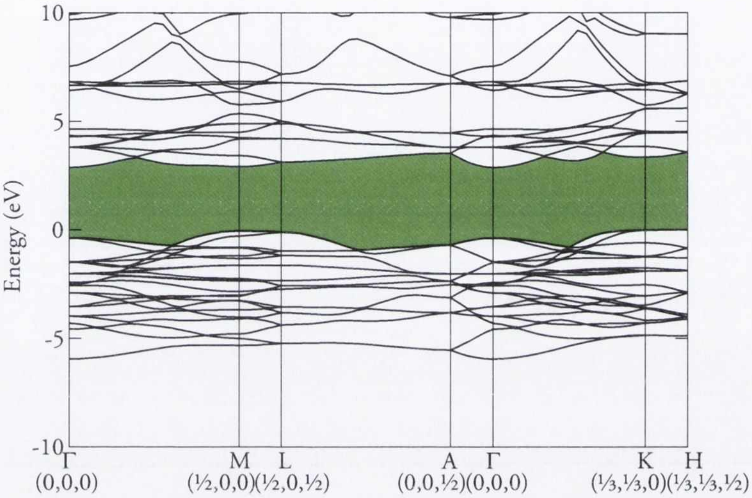

Figure 4.6: The electronic band structure of $CuScO_2$ along the high symmetry points, plotted with reference to the top of the valence band at 0 eV. The green shaded area denotes the band gap.

Figure 4.7 shows the calculated total and partial EDOS for $CuScO_2$. The valence band consists of 6 distinct peaks (labeled I-VI) with the conduction band consisting of two large peaks (VII, VIII). The Cu PEDOS is dominated by $3d$ states between −4 eV to 0 eV, but also features some $3d$ states between −6 eV to −4 eV, indicating some covalency with the oxygen states. The Sc PEDOS shows a very minor valence band contribution. However the conduction band is dominated by Sc d states, which make up the vast majority of peaks VII and VIII. As is the case for Al in $CuAlO_2$, the Sc states in $CuScO_2$ are not expected to have a significant contribution to the states determining the electronic conduction properties. The O PEDOS shows that O plays a dominant role in three of the peaks at the lower end of the valence band spectrum, and a significant role in peak V. Peak I and II are primarily O $2p$ in nature with some interaction with Cu $3d$, Peak III is of mainly O $2p$ character with some significant Cu $3d$ hybridization. Peaks IV, V and VI are dominated by Cu $3d$ states with some significantly O $2p$ contibution to peak V. The conduction band make-up (Peak VII and VIII is dominated by Sc d states , with some slight mixing of O $2p$ states, indicating some M^{III}–O interaction, which was not present in CuAlO$_2$

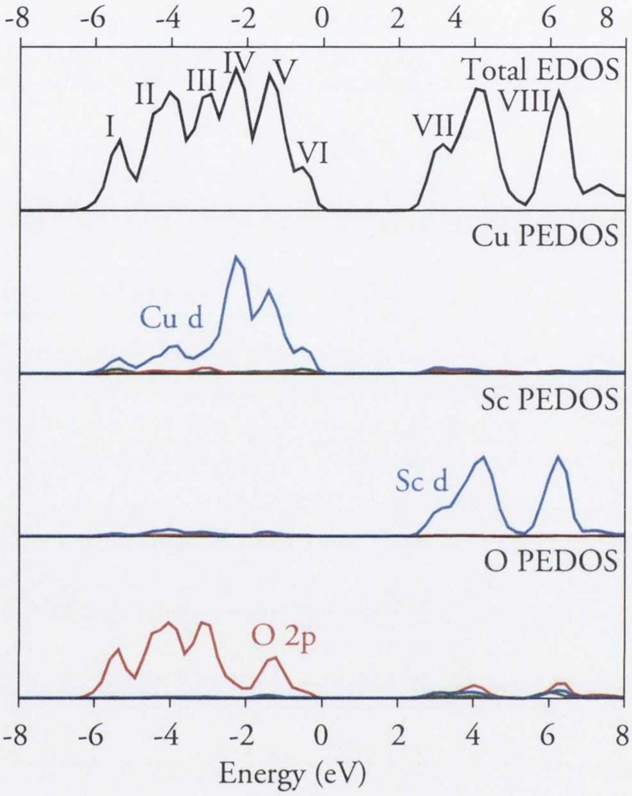

Figure 4.7: The electronic density of states for CuScO$_2$. (*a*) Total EDOS, (*b*) Cu PEDOS, (*c*) Sc PEDOS and (*d*) O PEDOS. The blue lines represent d states, green s states and red p states.

CuYO$_2$

The calculated bandstructure for CuYO$_2$ is shown in Figure 4.8. The VBM is situated at H, similar to the bandstructure for CuScO$_2$. The CBM is located at Γ, giving an indirect band gap of 2.93 eV, which is consistent with the work of Shi *et al.*, which also reported an indirect band gap for CuYO$_2$ [149]. They reported a calculated indirect band gap of 2.63 eV, which is an underestimation compared to our calculated value. This is to be expected, as we have used GGA + U, which although not a method to be used for absolute band gap correction, does often result in better descriptions of band gaps than GGA.[154] The smallest direct gap is located at Γ, and measures 3.15 eV, compared to the experimentally reported band gap of ~ 3.5 eV.[164]

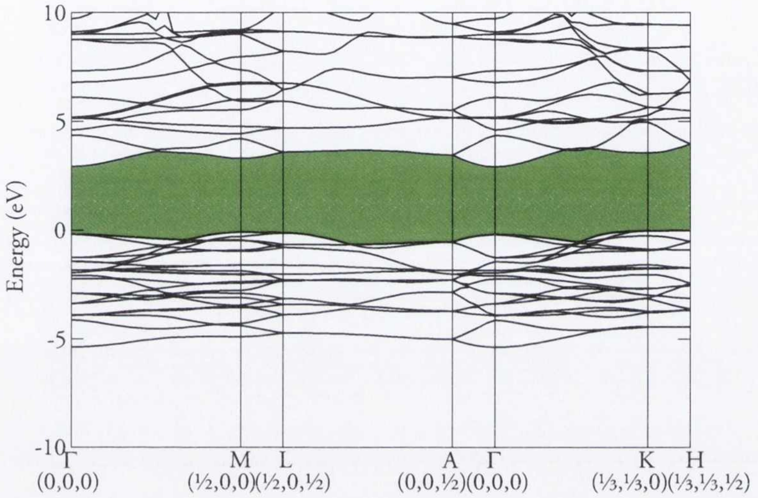

Figure 4.8: The electronic band structure of $CuYO_2$ along the high symmetry points, plotted with reference to the top of the valence band at 0 eV. The green shaded area denotes the band gap.

The calculated total and partial EDOS for $CuYO_2$ is displayed in Figure 4.9. The valence band shows five distinctive peaks (labeled I to V), with two peaks present in the conduction band (VI, VII). Similar to $CuScO_2$, the Cu PEDOS is dominated by Cu *d* states between -3 eV and the VBM, but there are some significant Cu *d* states between -6 eV and -3 eV. The Y PEDOS valence band features are also similar to that of $CuScO_2$, with the Y *d* and *p* states only having a small contribution. However the Y *d* states dominate the conduction band of the Y PEDOS, corresponding to peaks VI and VII on the total EDOS. The oxygen PEDOS shows us that peaks I, II and III in the total EDOS are primarily of O 2*p* character, with some Cu *d* mixing and some very minor contributions from Y states. Peaks IV and V are made up of Cu *d* states, with some significant mixing with O 2*p* states. Some small O 2*p* contributions are noted in the conduction band, indicating a degree of interaction between the yttrium and oxygen, similar to $CuScO_2$.

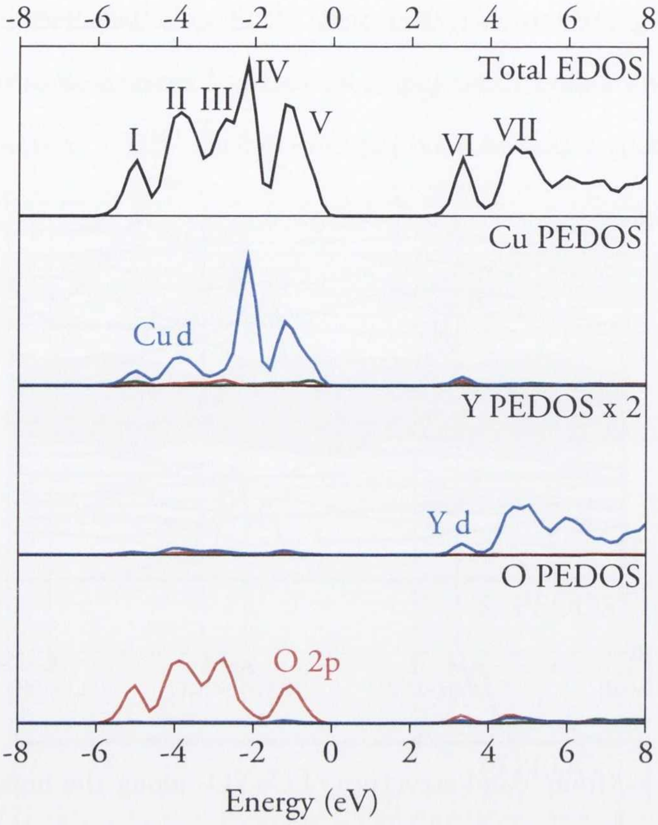

Figure 4.9: The electronic density of states for CuYO$_2$. (*a*) Total EDOS, (*b*) Cu PEDOS, (*c*) Y PEDOS and (*d*) O PEDOS. The blue lines represent *d* states, green *s* states and red *p* states.

4.3.3 Bader Analysis

It is clear from the analysis of the valence band features of the four delafossites that the greatest interaction between M^{III} states and the valence band is seen for CuCrO$_2$. While Sc states in CuScO$_2$, and Y states in CuYO$_2$ both appear to interact with the O 2p states in the conduction band (more than the O 2p states interact with Al states in the conduction band of CuAlO$_2$), they have no major interactions with the states that will determine the p-type conduction properties of these materials, at the top of the valence band. It is instructive at this point to quantify how the distribution of charge changes as we vary the M^{III} cation from Al–Cr–Sc–Y, using Bader[131] partial charge analysis.

The calculated Bader charges are listed in Table 4.2. Al has a charge of +2.48 e in $CuAlO_2$, in comparison to a formally ionic state of +3 e. This results highlights the ionicity of Al in this system. The charges for Cu (+0.50 e) and O (−1.49 e) are less than would be expected from the purely ionic model, but are consistent with the calculated densities of states, which show significant covalent mixing between the Cu and O in the valence band states.

	$CuAlO_2$	$CuCrO_2$	$CuScO_2$	$CuYO_2$
Cu	+0.52	+0.52	+0.52	+0.51
M^{III}	+2.48	+1.68	+2.03	+2.18
O	-1.50	-1.10	-1.27	-1.34

Table 4.2: Bader partial electron charges for $CuAlO_2$, $CuCrO_2$, $CuScO_2$ and $CuYO_2$

Analysis of $CuCrO_2$ gives charges of +0.52 e for Cu, +1.68 e for Cr and −1.10 e for O, which indicates covalent mixing between all three species. All three ions are significantly less ionic than their formal oxidation states suggest, and indeed O is considerably less ionic than it is in $CuAlO_2$. This indicates partial charge transfer from O to Cr and that the amount of charge transfer from O to Cu is not affected. This supports the interpretation of the PEDOS that Cr contributes significantly to the top of the valence band and bottom of the conduction band.

For $CuScO_2$ charges of +0.52 e for Cu, +2.03 e for Sc and −1.27 e for O are found, again indicating valence charge being distributed between the three species. The fact that the O and Sc results are slightly more ionic than O and Cr in $CuCrO_2$ indicates that there are definitely less covalent interactions in $CuScO_2$ than $CuCrO_2$, as is evidenced by the PEDOS, where Sc states do not play a major role in the valence band makeup.

The results for $CuYO_2$ are similar to $CuScO_2$, with charges of +0.51 e for Cu, +2.18 e for Y and −1.34 e for O being found. This again indicates that the covalent interactions are smaller in this system between the O and Y states, with both being more ionic than Sc and O in $CuScO_2$. This again is similar to the analysis of the

EDOS/PEDOS which shows some covalency between Y d states and O $2p$ in the conduction band, but virtually none in the valence band, leading to a more ionic description of Y and O states in $CuYO_2$ when compared to $CuScO_2$ and $CuCrO_2$.

4.3.4 Effective Hole Masses of the VBM

A common method used to determine the conductive ability of a material is to calculate the effective mass of the band edges. In the case of p-type TCOs, the hole effective mass at the VBM should indicate the p-type conduction properties of a material. The effective masses of $CuM^{III}O_2$ (M^{III} = Al, Cr, Sc, Y) were calculated using the method outlined in Section 3.3.3. The premise of effective mass theory relies on parabolic bands at the band edges. Although there is some slight curvature at the VBM for the four delafossites examined in this study, the high densities of states around the VB maxima means that the bands are far from parabolic, and thus are not expected to be well described under a typical semiconductor effective mass approximation.[115] Despite this, we report the effective masses of the VBMs for each material as a rough guide to the conduction properties of each material. We also report the effective masses calculated using spin orbit coupling, as this has been shown previously to split the doublet VBMs of other copper based p-type TCOs, and to have a big effect on the corresponding effective masses.[165]

Table 4.3 shows the calculated effective hole masses for the four delafossites involved in this study. The effective masses in the [100] and [010] directions are isotropic, which is to be expected for the hexagonal representation of the delafossite structure. A recent study by Shi *et al.* using the rhombohedral cell, found the effective masses to be anisotropic in three directions.[149] They noted the smallest effective masses were in the [001] direction, which they stated was due to the O–Cu–O chain along that direction offering a channel for hole transfer.[149] In our results we find that effective masses are largest in the [001] direction, with the effective mass of $CuAlO_2$ in the [001] being a rather large $58.43\,m_O$. This indicates a virtually flat band, which agrees with analysis of the bandstructure of $CuAlO_2$ at the valence band edge. Surprisingly the delafossite with the smallest effective mass in the [001] direction is $CuYO_2$. This is at variance with the results of Shi *et al.*, who found that the effective masses of $CuScO_2$ were lower than both $CuYO_2$ and $CuAlO_2$. This however is based on the average of the effective masses in the three directions[149]. Indeed the effective mass of $CuYO_2$ in the [001] direction is found to be lower than that for $CuScO_2$ and $CuAlO_2$, meaning $CuYO_2$ should find it easiest to conduct along the O-Cu-O channels.[149]It is clear from the results that we have obtained that applying effective mass theory to this type of material is not accurate. These systems to not have parabolic bands, and have been shown experimentally in the cases of $CuAlO_2$[60], $CuScO_2$[61] and $CuYO_2$[61] to conduct via polaronic hopping mechanisms, which are not well described by effective mass theory. As the holes are expected to hop from Cu to Cu,[166] it is not surprising that the effective masses in the [100] and [010] directions are lowest, indicating that conduction in delafossites will most likely take place in the *ab* Cu-Cu plane, and not in the [001] plane through the $M^{III}O_2$ layers. Thus we tentatively suggest that all we can really take from these calculations is that on average, the effective mass of holes at the VBMs of $CuYO_2$, $CuScO_2$ and $CuCrO_2$ are smaller than that of $CuAlO_2$, and that on average, the effective masses for $CuCrO_2$ are lowest.

	GGA + U			GGA + U + SO		
	m_{100}	m_{010}	m_{001}	m_{100}	m_{010}	m_{001}
$CuAlO_2$	2.60	2.60	58.43	2.60	2.60	38.95
$CuCrO_2$	2.96	2.96	7.21	4.53	4.53	6.07
$CuScO_2$	4.00	4.00	8.22	4.00	4.00	8.22
$CuYO_2$	4.21	4.21	7.16	3.72	3.72	7.64

Table 4.3: Table showing the effective masses (in units of free electron mass, m_O) for $CuAlO_2$, $CuCrO_2$, $CuScO_2$ and $CuYO_2$, calculated using GGA + U and GGA + U with spin-orbit coupling. m_{100}, m_{010}, m_{001} are the effective masses in the [100], [010] and [001] directions respectively.

4.3.5 Valence Band Alignments

It has become popular amongst the theoretical physics community to calculate the "natural" valence band alignments of different materials and thus rank them according to the doping limit rule[125,126]. This type of analysis has previously been carried out for $\mathrm{Cu(Al/In/Ga)O_2}$[122] and for $\mathrm{Cu(Al/Sc/Y)O_2}$[149]. Although these are separate studies from different authors, the authors of the latter study use the approximate transitivity of the of band offsets[127] to compare the alignments in both studies. They conclude that $\mathrm{CuScO_2}$ has the highest VBM of the five delafossites, and therefore is easier to dope *p*-type, according to the doping limit rule[149].

We calculate the valence band alignments according to the method developed by Wei and Zunger[127,128], which does not take into account the deformation potentials. [129,130] Heterostructures of 1 × 1 × 8 were constructed in the [001] direction, resulting in 48 and 64 atom superlattices made up of a fifty-fifty mix of $\mathrm{CuAO_2/CuBO_2}$. The lattice constants of $\mathrm{CuAO_2}$ and $\mathrm{CuBO_2}$ are averaged and used as the lattice constant of the superlattice. All the atoms in the heterostructure are relaxed until the forces on each atom are less than $0.01\,\mathrm{eV}\,\mathring{A}^{-1}$.

The valence band offsets are thus given by:

$$\begin{aligned}\Delta E_{\mathrm{V}}^{\mathrm{CuA/BO_2}} &= \Delta E_{\mathrm{VBM-CL}}^{\mathrm{CuAO_2}} - \Delta E_{\mathrm{VBM-CL}}^{\mathrm{CuBO_2}} \\ &\quad + \Delta E_{\mathrm{CL_A-CL_B}}^{\mathrm{CuA/BO_2}} \qquad (4.1)\end{aligned}$$

where $\Delta E_{\mathrm{VBM-CL}}^{\mathrm{CuAO_2}} = E_{\mathrm{VBM}}^{\mathrm{CuAO_2}} - E_{\mathrm{CL}}^{\mathrm{CuAO_2}}$ and $\Delta E_{\mathrm{VBM-CL}}^{\mathrm{CuBO_2}} = E_{\mathrm{VBM}}^{\mathrm{CuBO_2}} - E_{\mathrm{CL}}^{\mathrm{CuBO_2}}$. These are the core-level (CL) to VBM separations for pure $\mathrm{CuAO_2}$ and $\mathrm{CuBO_2}$ at their equilibrium lattice constants. $\Delta E_{\mathrm{CL_A-CL_B}}^{\mathrm{CuA/BO_2}} = E_{\mathrm{CL_A}}^{\mathrm{CuA/BO_2}} - E_{\mathrm{CL_B}}^{\mathrm{CuA/BO_2}}$ is the difference in core-level binding between the core levels in the constituent halves of the heterostructure.

As different studies have used different representative core levels, we have calculated the alignments in three ways; using the O 1*s* levels, using the Cu 1*s* levels; using the $\mathrm{M^{III}}$ 1*s* levels and using the average energy of the 1*s* levels of Cu, $\mathrm{M^{III}}$ and O as the energy of the core level. The calculated alignment results for the four different methodologies are shown in Table 4.4. It is clear for the calculated alignments that the choice of core-level has a big influence on the resultant alignment, with all four methods showing vastly different trends. Considering that the original study on $Cu(Al/In/Ga)O_2$ used core levels which they did not specify[122] and the study of $Cu(Al/Sc/Y)O_2$ used the average of the the $1s$ levels of Cu, M^{III} and O[149], we would have to question the accuracy of applying the approximate transitivity of band offsets between alignment studies using different core-levels when you take into account the difference the choice of core-levels has on the alignment. Using the M^{III} $1s$ states, on their own, or as part of an average, definitely distorts the alignment hugely compared to the alignments from the Cu $1s$ states or the O $1s$ states. None of the alignment methodologies used are consistent with the observed experimental conductivity trends, which would suggest that the trend should be Cr–Sc–Y–A in the order of highest VBM to lowest VBM. In fact, the difference in trends between the different core-level choices must call into question the use of this method to calculate alignments for copper based ternary oxides. It should also be noted that the errors associated with this method can be rectified by calculating the absolute deformation potential of these materials, which should in principle account for variations in the core levels, but is too expensive and time consuming to calculate for non-cubic systems[167]

	O $1s$	Cu $1s$	M^{III} $1s$	$\langle 1s \rangle$
$CuAlO_2$	-0.01	+0.29	-1.52	-0.41
$CuCrO_2$	+0.07	+0.22	-0.63	-0.11
$CuScO_2$	0.00	0.00	0.00	0.00
$CuYO_2$	-.016	-0.19	+1.05	+0.23

Table 4.4: The GGA + U natural band alignments of $CuM^{III}O_2$ (M^{III} = Al, Sc, Cr, Y) calculated using the O $1s$ states; the Cu $1s$ states; the M^{III} $1s$ and the average of the Cu $1s$, O $1s$ and M^{III} $1s$ states as the core levels (denoted $\langle 1s \rangle$). $CuScO_2$ is taken as the reference level in all four alignments.

4.4 Discussion

Since the first report of p-type transparent conductivity in the $CuM^{III}O_2$ structure in 1997, interest in these materials has been intense. Despite the repeated findings of poor conductivity compared to their n-type TCO counterparts, $CuM^{III}O_2$ TCOs retain popularity as a viable platform for future high performance p-type TCO applications. [168,169] In addition, delafossite structured materials have started to receive attention as potential electrodes in photoelectrochemical (PEC) water splitting,[170–178] in spite of the fact that in many cases their band gaps are far in excess of the optimal range for PEC applications (1.7–2.2 eV).[124]

It is clear from our results that due to the polaronic nature of these Cu^{I} oxides. [58,60,61], effective mass theory is not an ideal way to rank the conductivity properties of delafossite materials. Further to this, calculating the natural valence band offsets for these ternary copper materials using the Wei and Zunger approach[127,128] does not yield any worthwhile information, and we have demonstrated that the trends are extremely sensitive to the choice of core level used in the analysis. Although these methods have been used quite successfully for simple binary materials,[125,126] accurate band offsets for ternary delafossites do not seem possible using this method.

As delafossites and Cu^{I} oxides in general are reported to be polaronic,[58–61,166,179–187] it is expected that the Cu–Cu distances should play a part in any conductivity, as holes are expected to hop from Cu to Cu.[166] The Cu–Cu distance (equal to the a/b lattice constant) is determined by the size of the M^{III} ion, which suggests that the conductivity will increase as the size of the M^{III} ion decreases. This would also explain why undoped $CuAlO_2$ has been reported to have a higher conductivity than both non-doped $CuScO_2$ and $CuYO_2$.[51]

The size of the M^{III} cation also determines the amount of oxygen interstitials that these materials can maintain.[141,188] Increasing the number of oxygen interstitials increases the number of charge carriers into the system, and this argument has been used to explain why $CuYO_2$[141] is reported to have a higher non-doped conductivity than $CuScO_2$[189]. This premise fails, however, to explain why $CuCrO_2$ has a higher undoped conductivity even than $CuAlO_2$.[51] It is also reported that as the size of the M^{III}, there is a corresponding increase in the ability to dope these materials.[149] It is known that there is a very limited range for Mg^{II} substitution in $CuCrO_2$, with $x = 0.05$ being the limit for $CuCr_{1-x}Mg_xO_2$.[150] Despite this, the conductivity of $CuCrO_2$:Mg is much higher than that of $CuScO_2$:Mg and $CuYO_2Ca$, which can contain a much higher dopant concentration. It is therefore clear that the electronic structure of the M^{III} ion must therefore also play a key role in conductivity.

If we analyse the Bader charges for the four delafossites studied we can see that the trend of M^{III} ion covalency with oxygen follows Cr>Sc>Y>Al, with Cr having the largest covalent interaction. This follows exactly the experimentally known conductivity trend for the doped delafossites. This is not unexpected, as elementary chemical intuition tells us that a more delocalized, covalent valence band would be optimal for hole mobility enhancement.

It is clear from these results that conductivity in these systems is a competition between both size and electronic structure of the M^{III} ions. The important requirements for good conductivity would seem to be (i) the M^{III} ion not being overly large, and thus not limiting the hole hopping, leading to good non-doped conductivity; (ii) the M^{III} ion having a favourable electronic structure, which can enhance the mobility of holes and (iii) the M^{III} ion not being too small and limiting the dopability of the material and hence allowing a high charge carrier concentration. Finding a compromise between these three factors is the key, and might plausibly explain why $CuCrO_2$ is currently the leading material, possessing a favourable electronic structure, and an M^{III} ion big enough to allow doping and small enough not to limit hopping.

4.5 Conclusion

In this chapter, the electronic structure and geometry of $CuM^{III}O_2$ (M^{III} = Al, Y, Sc Cr) have been calculated using GGA + U. Calculated band structures, and atom decomposed densities of states have been reported. The influence of the *d* states of Y, Sc and Cr on the density of states was investigated, with the Cr *d* states of $CuCrO_2$ found to have the greatest influence on the valence band makeup of the delafossites. Bader analysis indicated that the covalent interactions between the trivalent metal and oxygen follows the trend Cr>Sc>Y>Al with Cr having the greatest covalent interaction with oxygen. This trend follows the experimental trend of conductivity in doped delafossites. Thus we conclude that favourable cation size *and* favourable mixing between the *d* states of the M^{III} ion and the O $2p$ states, are likely to determine mobility and conduction in these delafossite type materials.

Chapter 5

$CuBO_2$: The newest delafossite TCO?

5.1 Introduction

Since the discovery of p-type conductivity in $CuAlO_2$, many Cu(I) based delafossites having transparency and p-type conductivity have been synthesized, including $CuScO_2$, $CuYO_2$, $CuInO_2$, $CuGaO_2$ and $CuCrO_2$[51]. Indeed, other structures have been identified that combine p-type conductivity and optical transparency in Cu(I) based materials, including $SrCu_2O_2$[52,53] and layered oxychalogenides (LaCuOS)[54], although to date the p-type TCO with the highest conductivity is a delafossite (Mg doped $CuCrO_2$).[55]

Until 2002, the behaviour of the group 13 (group IIIA) delafossites (Al, Ga, In) was not well understood, with apparent band gap anomalies and the issue of bipolar doping proving very puzzling.[12,44,190,191] Group 13 semiconductors are known to have direct band gaps that decrease as the atomic number of the group 13 element increases,[192] e.g. $CuMS_2$ and MAs (M = Al, Ga, In). In group 13 delafossites the trend was thought to be reversed, with optically measured bandgaps that increased as the atomic number increased going down the group.[12,44,190,191] Wei and co-workers used first principles methods to investigate the electronic structure of these materials, showing that these materials did obey the trends seen in other group 13 containing semiconductors.[122]

They found using LDA that *both* the calculated indirect band gap and direct band gaps *do* decrease as the atomic number increases.[122] The optically measured band gap anomalies were thus explained by examining the calculated absorption spectra, which showed trends in keeping with experiment, with the optical band gap *increasing* with increasing atomic number, due to direct transitions at Γ being symmetry disallowed. [122]

Recently, a study by Snure and Tiwari has identified a new group 13 delafossite, $CuBO_2$, as a new p-type TCO[168]. Thin films of $CuBO_2$ display a remarkable room temperature electrical conductivity of 1.65 S cm^{-1}[168], which is, to the best of our knowledge, the highest intrinsic conductivity reported of all the delafosites. A fit to their optical absorption data produces an indirect band gap of 2.2 eV and a direct optical band gap of 4.5 eV. The a and c lattice vectors have been reported as 2.84 Å and 16.52 Å respectively, on the basis of X-ray diffraction (XRD) of the films, although the thin film nature may affect these properties.

In this chapter we present a density functional theory (DFT) study, examining the detailed electronic structure of $CuBO_2$. We show conclusively that (i) the lattice parameters reported by Snure and Tiwari[168] are not consistent with previous experimental trends, and need to be re-investigated, (ii) the valence band features of $CuBO_2$ are consistent with other delafossite p-type TCOs, (iii) the effective hole masses of the valence band maximum (VBM) are consistent with the reported good conductivity and (iv) the predicted indirect band gap and optical band gap of $CuBO_2$ are 3.21 eV and $\sim$ 5.1 eV respectively. The reason for the enhanced conductivity is discussed in relation to other delafossite TCOs.

5.2 Calculation Methodology

The periodic DFT code VASP[112,153] was employed for all our calculations, in which a plane wave basis set describes the valence electronic states. In all our calculations, the Perdew-Burke-Ernzerhof[193] (PBE) gradient corrected functional was used to treat the exchange and correlation. Interactions between the cores (Cu:[Ar], B[He] and O:[He]) and the valence electrons were described using the projector-augmented wave [103,111] (PAW) method. Calculations were performed using DFT corrected for on-site Coulombic interactions GGA + U[83] and the hybrid density functional (HSE06)[99]

Structural optimizations of bulk $3R$ $CuBO_2$ were performed using GGA + U and HSE06 at a series of volumes in order to calculate the equilibrium lattice parameters. In each case the the atomic positions, lattice vector and cell angle were allowed to relax, while the total volume was held constant. The resulting energy volume curves were fitted to the Murnaghan equation of state to obtain the equilibrium bulk cell volume. [113] Convergence with respect to k-point sampling and plane wave energy cut off was checked, and for both systems a cutoff of 500 eV and a k-point sampling of $10 \times 10 \times 10$ were found to be sufficient. Calculations were deemed to be converged when the forces on all the atoms were less than 0.001 eV Å^{-1}.

5.3 Results

To the best of our knowledge, there has been no complete crystallographic structural data reported for $CuBO_2$. The only reported estimation of the lattice constants of $CuBO_2$ are reported for thin films of $CuBO_2$, taken from the study undertaken by Snure and Tiwari.[168] Therefore we have adopted two approaches to find the minimum GGA structure for $CuBO_2$; (a) perform a constant volume structural optimization from the estimated lattice constants taken from Snure and Tiwari's study[168] and (b) perform a constant volume structural optimization from a known delafossite structure, closest in magnitude to the proposed structure, which in this case is $CuAlO_2$.

Approaches (a) and (b) both converged to the same structure and produced the calculated structural data shown in Table 5.1 and Table 5.2. It is clear that the a lattice vectors obtained from our GGA + U calculations (2.53 Å) are significantly smaller than those obtained experimentally for the $CuBO_2$ thin films (2.84 Å).

To test the validity of our prediction, the experimental trend of the a vector against

	GGA + U	HSE06	Experiment[168]
Volume	30.76	29.42	38.46
a	2.53	2.49	2.84
c	16.58	16.43	16.52

Table 5.1: Structural data for the GGA + U and HSE06 optimized $CuBO_2$ and the experimental data from the work of Snure and Tiwari.[168] Volumes are given in Å^3 and lattice dimensions and in Å.

	$CuBO_2$ GGA+U	$CuBO_2$ HSE06	$CuAlO_2$[160]	$CuGaO_2$[160]	$CuInO_2$[194]
Cu–O	1.889	1.875	1.864	1.848	1.845
M^{III}–O	1.703	1.677	1.910	1.996	2.173

Table 5.2: Cu–O and M^{III}–O nearest-neighbour interatomic distances for the GGA + U and HSE06 optimized $CuBO_2$ and the experimentally reported bond lengths of $CuAlO_2$, $CuGaO_2$ and $CuInO_2$. All interatomic distances are given in Å.

ionic radii for some known delafossite structures is shown in Figure 5.1. The experimental lattice parameter reported for $CuBO_2$ is a considerable distance away from the experimental trend of the a lattice parameter against ionic radii. Our GGA + U calculated a value is slightly overestimated compared to the experimental trend line, as is expected from a GGA calculation, but overall is much closer fit to the experimental trend line. The GGA + U result are slightly overestimated compared with the GGA+ U calculated lattice parameter trend for $CuAlO_2$, $CuGaO_2$ and $CuInO_2$, although this is probably a consequence of the small ionic radius of B. Minimization at the HSE06 level results in lattice parameters of $a = 2.49$ Å and $c = 16.42$ Å . The a lattice parameter from our HSE06 calculation is even closer to the experimental trend line in Figure 5.1. This is to be expected, as HSE06 is known to produce improved lattice parameters compared to GGA[195], which typically overestimates by 1–2%. The HSE06 calculated a lattice parameters for $CuAlO_2$, $CuGaO_2$ and $CuInO_2$[196] are also displayed in 5.1, to highlight the small deviations from the experimental trend that usually occur using this method. Similar to the GGA + U result, the HSE06 result for $CuBO_2$ slightly deviates from the previous HSE06 trend, but is still in much greater agreement with the experimental trend than the data from Snure and Tiwari.[168] This further indicates that the a lattice parameter taken from the work of Snure and Tiwari is severely overestimated,[168] by as much a 0.4 Å.

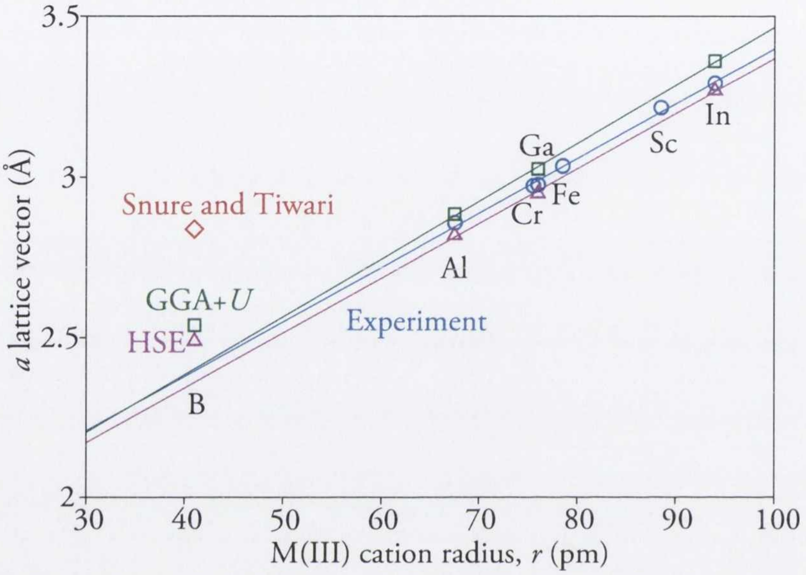

Figure 5.1: Plot of a lattice parameter versus ionic radii for some common Cu based delafossites. The blue circles signify experimental a lattice parameters for known delafossites[51], the red diamond is the lattice parameter for $CuBO_2$ proposed by Snure and Tiwari[168], the green squares signify the GGA + U calculated a lattice parameters and the pink triangles are the HSE06 calculated a lattice parameters for $CuBO_2$, $CuAlO_2$, $CuGaO_2$ and $CuInO_2$.

The GGA + U calculated bandstructure of $CuBO_2$ along the high symmetry lines taken from Bradley and Cracknell[114] is shown in Figure 5.2. The VBM is situated at the F point, while the conduction band minimum (CBM) lies at Γ, giving an indirect band gap of 1.94 eV, with the smallest direct band gap situated at Γ and measuring 3.21 eV. This cannot be viewed as a prediction of the absolute value of the indirect or direct band gaps, as GGA + U calculations are known to produce underestimated band gaps.[155] Direct band gaps at similar energy differences are found at L (3.24 eV) and F (3.24 eV). The positioning of the VBM is a deviation from the behaviour of the other group 13 delafossites predicted from LDA calculations, as $CuAlO_2$, $CuGaO_2$ and $CuInO_2$ all have VBMs situated on the line from F–Γ near F.[122]

To verify if the band gap trends observed in other group 13 delafossites are maintained, we compare the indirect and direct bandgaps for $CuBO_2$ with the previous theoretical results.[155] The other known group 13 delafossites show a trend of decreasing indirect band gap as the group 13 cation increases in atomic number, with LDA calculated indirect gaps decreasing from 1.97 eV ($CuAlO_2$) to 0.95 eV ($CuGaO_2$) to 0.43 eV ($CuInO_2$).[122] Similarly the direct band gap trends show a decrease in magnitude of the gap as the atomic number of the group 13 ion increases, with the LDA calculated direct band gaps decreasing from 2.93 eV ($CuAlO_2$) to 1.63 eV ($CuGaO_2$) to 0.73 eV ($CuInO_2$).[122] For these trends to be maintained, it would have been expected that the indirect and direct band gaps of $CuBO_2$ would be greater than those of $CuAlO_2$. As it would be remiss of us to directly compare GGA + U band gaps to the LDA calculated bandgaps taken from the study of Wei and co workers[122], we instead compare with previous GGA + U results for $CuAlO_2$.[155] The indirect and direct band gaps for $CuAlO_2$ calculated at the GGA + U level are 2.2 eV and 3.1 eV respectively. [155] As our calculated fundamental indirect band gap for $CuBO_2$ (1.94 eV) is smaller than that of $CuAlO_2$, $CuBO_2$ does not seem to follow the same trends as the other group 13 delafossites. The direct band gap however does follow the trend, with the direct band gap of $CuBO_2$ (3.21 eV) being larger than that of $CuAlO_2$ (3.1 eV).[155]

Our HSE06 calculated indirect and direct band gaps measure 3.08 eV (between F and Γ) and 3.59 eV (at F) respectively. The value of the indirect band gap is clearly larger than that reported by Snure and Tiwari[168] of 2.2 eV and the value of the direct band gap is clearly smaller than the 4.5 eV proposed in the literature[168], although it would be foolhardy to compare the calculated direct band gap with an optically measured band gap[122]. The HSE06 functional is expected to predict band gaps that are closer to experiment than those of LDA/GGA/GGA + U methods[123,195,197–199], and so as large a difference as the difference reported here between experiment and calculation is unusual. This difference between the calculated indirect band gap and the experimentally measured indirect band gap, allied to the apparent anomaly in the structural data reported from the $CuBO_2$ thin films, is another indicator that an experimental re-investigation of the structure and properties of $CuBO_2$ is warranted.

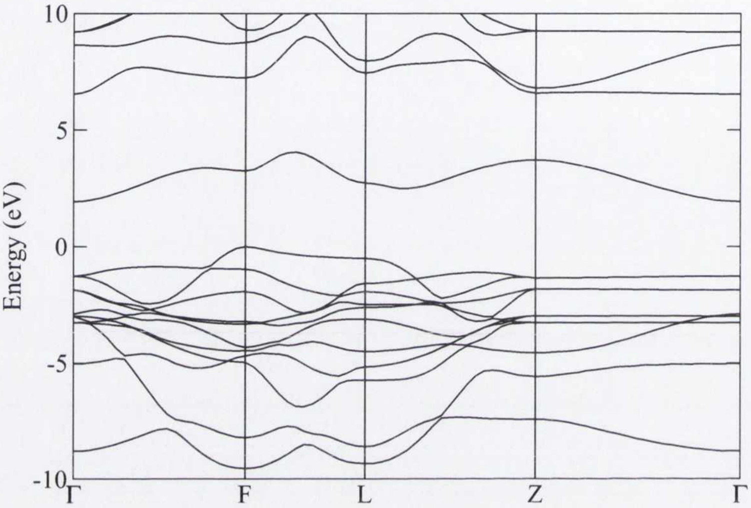

Figure 5.2: GGA + U calculated bandstructure of $CuBO_2$. The top of the valence band is set to 0 eV.

Figure 5.3 (a-d) shows the calculated total and partial (ion decomposed) electronic densities of states (EDOS/PEDOS) for $CuBO_2$. The PEDOS were calculated by projecting wavefunctions onto atom-centered spherical harmonics, with radii of 1.4 Å for Cu, 1.1 Å for B and 1.4 Å for O. These radii reproduce the correct number of electrons in the system, and their ratios are consistent with the positions of minima observed between the atoms in valence-charge density plots. The valence band (VB) can be split up into four distinguishable regions (labelled I to IV), with the conduction band considered in two sections (V and VI).

Region I spans from -10 eV to -8 eV, and is composed mainly of O $2p$ states, with some mixing of B s and p states. It is noticeable that the s states of B are ~ 2 eV lower in energy than the s states of Al in $CuAlO_2$, as seen in Chapter 4. Region II (between -8 eV and -6.5 eV) is again dominated by O $2p$ states, with some minor mixing with Cu $3d$ and B p states. Between -6.5 eV and -2 eV (Region III), Cu $3d$

states dominate, with significant O 2*p* hybridization and some minor B *p* interaction. At the top of the VB, Region IV, Cu *d* states are dominant, as is to be expected from a Cu(I) oxide, with some mixing with O 2*p* states. The bottom of the CB consists of a mix of Cu 3*d* states and O 2*p* states, similar again to $CuAlO_2$[155].

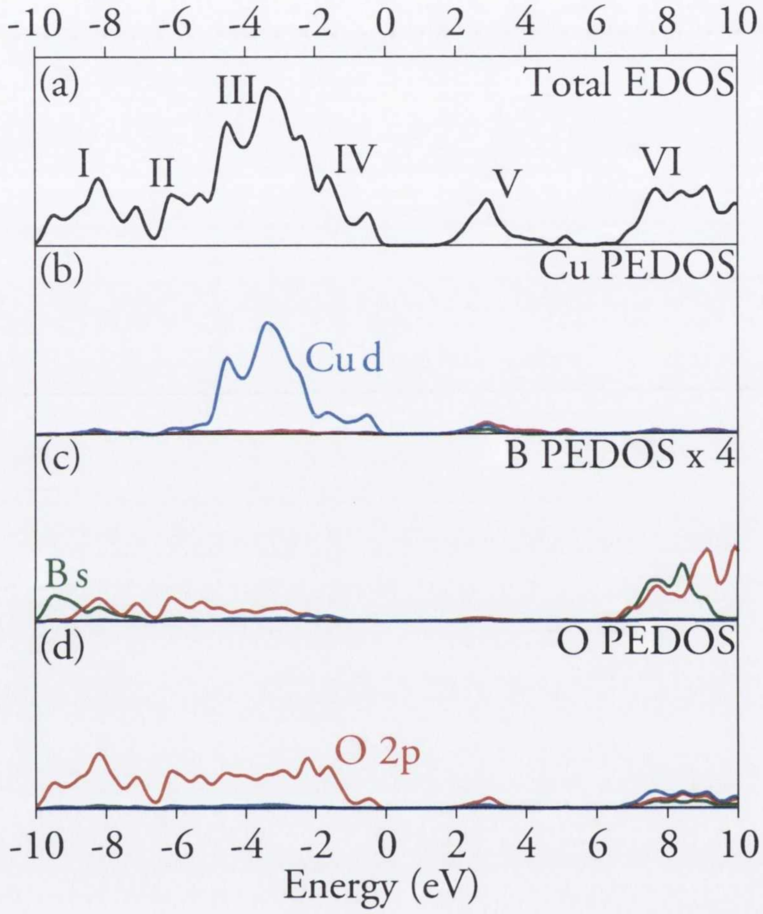

Figure 5.3: The electronic density of states for $CuBO_2$.(a) Total EDOS, (b) Cu PEDOS, (c) B PEDOS and (d) O PEDOS. The blue lines represent *d* states, green *s* states and red *p* states.

In order to gain a deeper understanding of the band structure features, we have plotted projections of the charge density for the VBM at F and the CBM at the Γ point through a (001) plane containing both Cu, B and O atoms, labeled (b) and (c) in Figure 5.4. A numerical breakdown of the states at the VBM shows that it contains ~ 67% Cu *d* character and ~ 31% oxygen *p* character, with B states effectively playing no role in the VBM makeup at F. This is further evidenced by the charge density plot of the VBM (5.4 (b)) which clearly shows d like orbitals on the Cu ions and p like orbitals on the O ions, with the absence of any density on the B states. A similar numerical analysis of the CBM at Γ finds it to be composed of $\sim 39\%$ Cu d, $\sim 21\%$ Cu s, $\sim 34\%$ O s and only $\sim 5\%$ B s. Analysis of the charge density plot of the CBM (Figure 5.4 (c)) visibly shows the mixed s and d states on the Cu ions, and the s like nature of the density on the oxygen ions, with the B s states just visible.

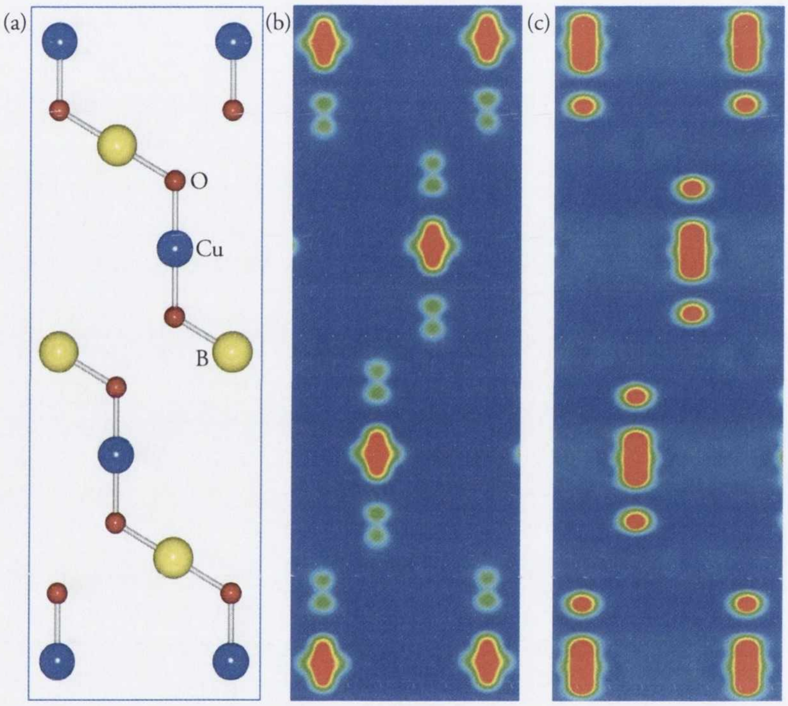

Figure 5.4: Charge density contour plots showing the band edges of $CuBO_2$ through a (001) plane. (a) is the structure of the cell in the (001) plane, (b) is the charge density of the VBM at F and (c) is the charge density of the CBM at Γ, plotted from 0 eV (blue) to 0.003 eV (red) e.Å^{-3}.

The corresponding GGA + U and HSE06 calculated optical absorption spectra are shown in Figure 5.5. For $CuBO_2$, we find that fundamental band-edge transitions at the Γ and Z points are symmetry disallowed, with absorption beginning at 3.25 eV for GGA + U and 3.59 eV for HSE06. This is consistent with the findings of Nie *et al.*, who found that the VBM and the CBM at Γ and Z have the same (even) parity for $CuMO_2$ (M = Al, Ga, In), resulting in zero dipolar optical absorption[122]. Their calculated matrix elements show that increases in the optical spectrum only occur close to the direct transition at the L and F points, which is consistent with our $CuBO_2$ results.

For the GGA + U calculated spectrum, this results in a peak centered around 5.5 eV which decreases and then subsequently ascends after 8 eV to shorter photon wavelengths. A similar pattern is seen for the HSE06 spectrum, with the peak centered at 7 eV. The HSE06 spectrum is essentially blue shifted, with a reduction in intensity. This reduction in intensity is required by the f−sum rule.[200] The increase in width of the peak at 7 eV, and the new sharper peak at 6 eV are a consequence of the different effects the GGA + U and HSE06 approaches will have on individual bands.[200] These spectra show very similar features to those calculated for other group 13 delafossites ($CuMO_2$, M = Al, Ga, In) with LDA.[122] In each case the spectra featured abrupt absorption edges, although like $CuAlO_2$ and unlike $CuGaO_2$ and $CuInO_2$, $CuBO_2$ does not have a small tail below the absorption edge. Our calculations indicate that $CuBO_2$ is indeed transparent.

In an attempt to quantify the electronic conduction properties of $CuBO_2$, we calculate the hole effective mass at the VBM and CBM. Cu-based p-type TCOs are reported to conduct through a polaronic hopping mechanism[60,61], and the bands at the top of the VB are clearly not parabolic, so we do not expect $CuBO_2$ to be well described under a typical semiconductor effective mass approximation; nevertheless, the calculated effective masses serve as a rough guide of the conduction properties. At the VBM, the effective masses in the [100] and [010] directions are isotropic, measuring 1.71 m_e, with a calculated effective mass in the [001] direction of 0.45 m_e.

The effective masses of the CBM are isotropic in all three directions, with an effective mass of 1.58 m_e. Our calculated effective masses for the VBM are larger than those reported for $CuMO_2$ (M = Al, Sc, Y) but this study used the LDA functional[149], which results in underestimated lattice parameters, smaller band gaps and therefore lower effective masses. Recently, masses of the magnitude of 16 m_e have been reported

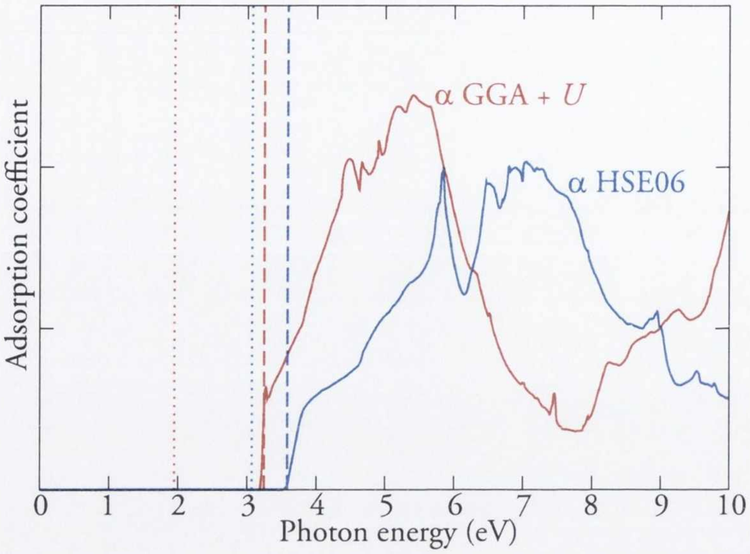

Figure 5.5: Calculated optical absorption spectrum of $CuBO_2$ summed over all possible direct valence to conduction band transitions. GGA + U (red) and HSE06 (blue). The dotted lines represent the fundamental indirect band gaps, the dashed lines represent the magnitude of the *optical* band gap.

for the VB and $0.24\,m_e$ for the CB of In_2O_3[21], indicative of good n-type ability and bad p-type ability. This highlights that strong mixing of low binding energy cation states (here Cu d) with O $2p$ is required to provide valence band dispersion. Taking into account the known disproportion between the n-type ability of one of the current industry standards and the relatively bad performance of current p-type TCOs, our calculated effective masses suggest good potential for enhanced p-type performance.

5.4 Discussion

It is clear that the calculations at the GGA + U and HSE06 level bring into doubt the formation of delafossite $CuBO_2$ in the work of Snure and Tiwari.[168] Investigation of the $\Delta H_f^{CuBO_2}$ at the HSE06 level, given by:

$$\mu_{Cu} + \mu_O + \mu_B = \Delta H_f^{CuBO_2} = -4.22\,\mathrm{eV}$$

tells us that the material is stable with respect to dissociation. However, the material is not stable with respect to its binary oxides, Cu_2O and B_2O_3 ($\Delta H_f^{CuBO_2} = \sim 0.4$ eV. This type of behaviour has been noted previously for other multiternary compounds,[201] but this does not preclude their formation. Boron does not typically adopt octahedral coordination environments, but it has been found to be octahedrally coordinated in some ternary systems[202], so it is not unreasonable that it could form delafossite $CuBO_2$. What is certain is that there is a pressing need for a re-examination of the crystal structure of $CuBO_2$.

At this point it is instructive to rationalize why the potential delafossite $CuBO_2$ displays better intrinsic conductivity than other Cu based TCOs. The B states do not contribute to the states that control conduction in the valence band, with the Cu *d* states dominating with some minor contributions from the O 2*p* states at the top of the VBM. In fact, it could be argued that B disrupts the VB features of the parent compound, Cu_2O, the least amount of all the M^{III} cations, meaning that the p-type conduction properties are the most similar to that of Cu_2O. In such a case, the B ions simply serve to reduce the dimensionality of the system, making the band gap bigger by disrupting the three dimensional interactions between the $3d^{10}$ electrons on neighbouring Cu^I ions in Cu_2O.[44] This view is further evidenced by the absence of any charge density on the B atoms when examining the wavefunctions at the VBM and CBM. This is not the case for $CuAlO_2$, $CuCrO_2$, $CuScO_2$ or $CuYO_2$ where the M^{III} cation can be seen from previous calculations to play some role (however small) in the states that make up the VBM[58,149], as seen in Chapter 4.

The *a* lattice parameter could also play a key role in the higher intrinsic conductivity of $CuBO_2$ in comparison to undoped $CuAlO_2$, $CuCrO_2$, $CuYO_2$ etc. As conduction in delafossites is thought to be governed by polaronic hopping mechanisms[60,61], it is to be expected that the decrease in the *a* parameter would directly correlate to an increase in the rate of hopping. Hopping of holes from Cu to Cu has long been thought to be the p-type conduction mechanism in these materials[166], with the distances between Cu sites being a limiting factor. With the predicted Cu–Cu distance in $CuBO_2$ being 2.49 Å , and the next smallest Cu–Cu distance being in $CuAlO_2$ (2.86 Å), one can assume that the smaller Cu–Cu distance in $CuBO_2$ is responsible for its increased intrinsic conductivity. As the size of the M^{III} ion increases, the Cu–Cu distances increase, presumably making hopping more difficult. Unfortunately as the size of the M^{III} ion increases, so too does the ability to dope the material[149]. By this rationale, extrinsic doping of $CuBO_2$ to increase carrier concentrations and lower the Fermi level could, for instance, be substantially more difficult than doping $CuInO_2$.

5.5 Conclusion

In this chapter, we have calculated the geometry and electronic structure of the delafossite TCO $CuBO_2$ using GGA $+U$ and HSE06 density functionals. The lattice parameters reported from experiment are shown to be highly questionable, with the GGA $+ U$ and HSE06 calculated lattice parameters comparing excellently with known experimental trends. $CuBO_2$ is predicted to possess a fundamental indirect band gap of ~ 3.1 eV and with a predicted optical band gap of ~ 3.6 eV, which are an underestimation and overestimation, respectively, of previous experimental absorption data. Analysis of the band extrema shows that B plays virtually no role in the states that govern conduction. Calculated effective masses of the band edges predict good *p*-type conductivity, consistent with experiment. This increased intrinsic conductivity relative to other delafossite TCOs is attributed to the Cu–Cu distances in $CuBO_2$ being smaller than in any other delafossite.

Chapter 6

Defect Chemistry of Cu_2O

6.1 Introduction

Cu_2O is a natively *p*-type semiconductor with many applications such as in catalysis, gas sensing, dilute magnetic semiconductors, and photovoltaics (PV).[203,204] It possesses a direct band gap of 2.17 eV, making it a good candidate for photo-electrochemical water splitting,[204] and solar cell applications.[205] In addition, Cu_2O satisfies the economical and environmental requirement necessary for large scale applications, as it is an abundant, low-cost and non-toxic material.[206] The recent explosion of interest in *p*-type TCOs such as $CuM^{III}O_2$ (M^{III} = Al, Cr, B, Ga, In)[51] and $SrCu_2O_2$[52] has also re-focused attention on the chemistry of Cu^I oxides, as the *p*-type properties of these materials are thought to be similar.[39]

6.2 *p*-type defect chemistry of Cu_2O

P-type conduction in Cu_2O is caused by oxygen excess, which results in the formation of hole (acceptor) states above the valence band.[39] The valence bands of most wide band gap metal oxides are composed of O 2*p* states, leading *p*-type doping to often result in localized oxygen holes deep in the band gap, associated with poor *p*-type conduction. In Cu_2O, the top of the valence band is dominated by Cu 3*d* states, with some O 2*p* mixing.[207] Upon hole formation, oxidation of $3d^{10}$ Cu^I to $3d^9$ Cu^{II} is thought to occur, with the corresponding acceptor levels being formed primarily on the Cu *d* states.[13]

The bandgap of Cu_2O is not sufficiently large for transparency in the visible spectrum, making Cu_2O itself unsuitable for TCO applications. The small band gap is thought to be due to the three-dimensional interactions between $3d^{10}$ electrons on neighbouring Cu^{I} ions.[44] These three-dimensional interactions are a consequence of the crystal structure, which can be thought of as two interpenetrating cristobalite lattices,[45,46] as shown in Figure 6.1. It was proposed by Kawazoe *et al.* that maintaining the *p*-type nature of Cu_2O is necessary for the development of Cu-based *p*-type TCOs, and this was incorporated in a set of design rules for TCOs, called the "Chemical Modulation of the Valence Band".[40] This approach aims to maintain the valence band properties of Cu_2O, while increasing the band gap by alloying with other oxides, such as Al_2O_3 or SrO, to form $CuAlO_2$ or $SrCu_2O_2$ respectively. These ternary oxides decrease the dimensionality of the Cu–Cu interactions, yielding band gaps large enough for TCO applications.[48,50,52] The defect chemistry of Cu_2O and these technologically useful daughter compounds is expected to be similar, thus developing an understanding of the *p*-type behaviour of Cu_2O is an important step towards understanding the chemistry of Cu-based TCOs.

Although the *p*-type conduction properties of Cu_2O have been studied extensively for decades,[182–184,208,209] the exact nature of the hole states found in the band gap of Cu_2O has been a source of much controversy, with acceptor like states being reported in the range 0.12–0.70 eV.[210–217] Deep level transient spectroscopy (DLTS) has shown the presence of hole traps 0.40–0.55 eV above the top of the valence band maximum (VBM).[216,218] These hole traps have been attributed to structural anomalies such as CuO "islands".[216] Similar conclusions were reached regarding the acceptor levels in DLTS study of Cd-doped Cu_2O[219]

A recent DLTS study, with a broader temperature range of 100 K to 350 K, reported two trap levels.[217] The first trap at 0.45 eV above the VBM was attributed to copper vacancies, while a second trap at 0.25 eV was tentatively assigned as a Cu-divacancy.

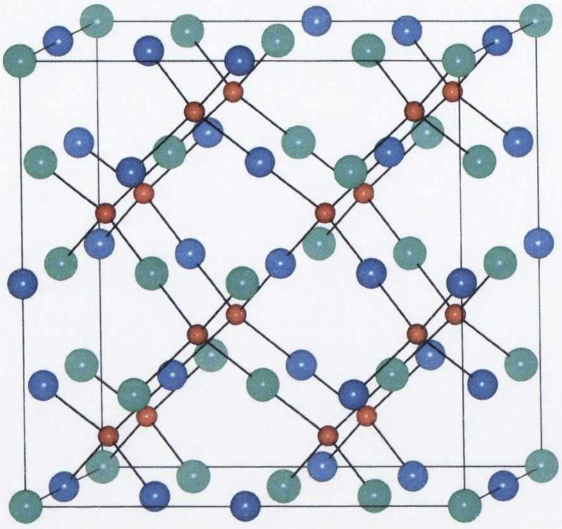

Figure 6.1: A $3\times3\times3$ supercell of cubic Cu_2O showing the two inter-penetrating cristobalite-like structures. Dark blue and light blue spheres indicate the copper atoms associated with the different cristobalite sublattices, and the red spheres are oxygen.

The trap at 0.25 eV becomes the dominant feature with increasing oxygen flow rate, possibly indicating that the formation of Cu-divacancies is facilitated by increasing Cu mono-vacancy formation. The authors excluded the possibility of the trap at 0.25 eV being due to oxygen interstitials, as they reasoned interstitial oxygen would be unlikely to act as an acceptor.

Deep acceptor states are also observed with photo-induced current transient spectroscopy (PICT), with the defect states having activation energies ranging 0.12–0.63 eV above the VBM.[215] The acceptor state at 0.63 eV was assigned as a copper vacancy defect with an acceptor-type charge state. None of the other defects levels were assigned.

The presence of more than one acceptor level has also been noted by Pollack *et al.*[210] Samples of cuprous oxide were prepared using a high-temperature equilibration and quenching technique designed to "freeze in" any non-stoichiometry. For a sample equilibrated at 1373 K at an oxygen partial pressure placing its composition in a region near the CuO–Cu_2O phase boundary, an acceptor level at 0.4 eV was found, but the relevant defect was not assigned.[210] Another sample was equilibrated at 1373 K, at an oxygen partial pressure placing it near the Cu–Cu_2O phase boundary, and two acceptor levels found. Only one could be accurately resolved at 0.16 eV above the VBM.[210] The nature of this defect level was again not assigned.

An acceptor defect level at 0.16 eV has also been reported in a photoluminescence study of polycrystalline *n*-type Cu_2O, but this defect level was not assigned since previous studies had shown copper vacancies give much deeper acceptor levels.[213]

The existence of multiple acceptor levels was given further support in a study of the Poole-Frenkel (P-F) conduction mechanism of Mo–Cu_2O–Au thin film structures, [212] which suggested P-F conduction is governed by two temperature dependent mechanisms. In the low-temperature range 78–230 K, conduction is due to a field assisted lowering of the ionization energy of an acceptor level 0.12 eV above the VBM, and in the range 231–321 K conduction is related to an acceptor level at 0.70 eV.[212] The nature of these distinct acceptor levels was not discussed.

Additional studies include those of Peterson *et al.*[208] and Porat and Reiss[220]. In the former, a defect model involving copper vacancies, holes, and singly ionized oxygen interstitials was obtained by fitting to tracer difusion data and the conductivity data of Maluenda *et al.*[183] combined with the stoichiometry data of O'Keefe and Moore.[208,221] Porat and Reiss studied the defect chemistry of $Cu_{2-y}O$ at elevated temperatures and suggested that above 1150 K the dominant ionic defect is the doubly charged oxygen interstitial, whereas at temperatures below 950 K the singly charged copper vacancy dominates.[220]

The existence of defect levels in Cu_2O systems is therefore not in doubt, although the source of these acceptor levels still remains uncertain. It has been known for decades that Cu_2O conducts via a polaronic, hole-hopping mechanism,[179–181] which is governed by an activated Arrhenius-type behaviour.[182–185] This type of conductivity is consistent with localized single particle levels (SPL or raw eigenvalues of the hole states) deep in the band gap of the material.

Cu vacancies in Cu_2O have not received much theoretical attention[222–225]. Wright *et al.* studied the energetics of Cu vacancies in Cu_2O using DFT-LDA, finding that a "simple" vacancy, V_{Cu} (written in typical solid state physics format, not in Kroger-Vink format), in which one Cu is removed leaving two three-coordinate oxygen atoms, is less stable than a "split" vacancy, $V_{\mathrm{Cu}}^{\mathrm{split}}$, where one remaining Cu moves toward the "simple" vacancy, and into a tetrahedrally coordinated site.[222] Divacancies were also examined, but only to compensate the substitution of Al or In into a Cu position, and the electronic structure of these defects was not analysed.[222]

Cu vacancies were also studied by Nolan *et al.* using density functional theory within the generalised gradient approximation (GGA) and with GGA supplemented by an on-site Coulomb correction(GGA+U).[223] For both GGA and GGA+U (where a U of 7 eV was applied to the Cu d states), a delocalized state was reported for the simple vacancy, with the defect band crossing the Fermi level, giving a metallic system. Based on the equivalence of the GGA and GGA+U results for the simple vacancy it was argued that GGA+U is unnecessary for modeling Cu vacancies in Cu_2O. The split vacancy was also described as corresponding to a delocalized state, although no detailed analysis of the electronic structure was presented. The simple vacancy was 0.06 eV more favourable than the split vacancy. The authors interpreted their results as showing the presence of an acceptor level at 0.2 eV above the VBM, and this was suggested to be consistent with the hole traps seen at 0.45 – 0.55 eV in DLTS experiments.[216,219] Transition levels were not calculated, however, and the presented band structures show a spin-paired system with the Fermi level 0.2 eV below the top of the VBM, with no empty states in the gap. It appears that this analysis compares a calculated SPL to the experimental transition level, even though they are distinctly different properties. [226] The formation of oxygen interstitials was not considered in this work.

Raebiger and co-workers employed GGA, with a GGA+U correction to the energetics, to study Cu vacancies in Cu_2O.[224] They proposed cation vacancies as the most likely cause of p-type conduction due to the preferential formation of this defect. The calculated transition level for the simple V_{Cu} was $\sim$ 0.28 eV, which compares well to the trap at 0.25 eV in the DLTS study of Paul *et al.*[217] It should be noted however that these calculated levels are subject to a rigid shift of 0.32 eV applied to the VBM of the

GGA calculation. This shift is derived from a reference bulk calculation using GGA+U with $U = 5\,\text{eV}$ applied to the Cu d states, without which the transition levels would be resonant in the valence band. It was postulated that the most probable explanation for the deep hole trap levels reported in the literature is the presence of interstitial oxygen. Detailed electronic structures were not reported for the simple and split vacancies or for the oxygen interstitial.

Soon *et al.* used GGA to study the formation of defects in the bulk and on the surfaces of Cu_2O.[225] In the bulk, the formation of Cu vacancies was favourable under all conditions but the calculated transitions levels for the Cu vacancy and the split vacancy were in the valence band. The same shift of 0.32 eV was applied to the transition levels as used in the study by Raebiger *et al.*[224] making their transition levels appear in the band gap. This study did not consider CuO formation as the limit of Cu-poor/O-rich growth conditions, and thus the Cu-poor/O-rich results are probably for an unphysical composition.[225]

From both the previous experimental and theoretical work, it is clear that there is a pressing need for a re-examination of these defect levels within the bandgap of Cu_2O. In this chapter we attempt to answer three questions: (i) can PBE or PBE+U reproduce the polaronic nature of defective Cu_2O, with distinct localized defect SPL?, (ii) can either method successfully reproduce deep acceptor levels seen experimentally, and thus elucidate the nature of these levels? and (iii) is a hybrid DFT method necessary in situations where the VBM of a material is made up of strong mixing between cation and anion states. We present a comprehensive first principles examination of the electronic structure and geometry of acceptor-level–forming defects in Cu_2O using PBE and PBE+U and HSE06. We find: (i) for the first time in a DFT based study of Cu_2O distinct acceptor level bands split off from the valence band for the split vacancy and oxygen interstitials using PBE+U and HSE, thus reproducing the expected polaronic nature of the system, (ii) the application of a rigid shift to the PBE calculated transition levels is not equivalent to the application of a +U correction in all calculations, and its use therefore is not justified, (iii) the positioning of calculated transition levels for the defects investigated using both PBE and PBE+U cannot reproduce the experimentally seen hole trap positions, due to the partially delocalized nature of these defect states, and hence neither PBE or PBE+U are sufficient to model these acceptor like states in Cu_2O. A hybrid DFT methods is shown to be necessary when dealing with materials with cation and anion states mixing strongly at the VBM.

6.3 Theoretical Methods

The periodic DFT code VASP[112,153] was employed for all our calculations. The Perdew-Burke-Ernzerhof[193] (PBE) gradient corrected functional was used to treat exchange and correlation. Interactions between the cores (Cu:[Ar] and O:[He]) and the valence electrons were described using the projector-augmented wave[103] (PAW) method. The defect calculations were fully spin polarized to describe the unpaired electrons produced upon defect formation.

Structural optimizations of bulk Cu_2O were performed using PBE and PBE+U and HSE at a series of volumes to calculate the equilibrium lattice parameters. The U value applied to the Cu d states was 5.2 eV, which closely reproduces the XPS valence band features of Cu_2O,[39,227] and has also acccurately reproduced the valence band features of $CuM^{III}O_2$ (M^{III} = Al, Cr) as shown in Section 4 The value of exact non-local exchange (α) chosen for the HSE06 calculations was 27.5%, which yielded a bandgap of 2.12 eV, in excellent agreement with the experimentally measured band gap of 2.17 eV.[45]

In each case the atomic positions, lattice vectors and cell angles were allowed to relax, while the total volume was held constant. The resulting energy–volume curves were fitted to the Murnaghan equation of state to obtain the equilibrium bulk cell volume.[113] Convergence with respect to k-point sampling and plane wave energy cutoff were checked, and a cutoff of 500 eV and a k-point sampling of $8 \times 8 \times 8$ was used for the PBE and PBE+U calculations, with a cutoff of 400 eV utilized for the HSE06 calculations. Structural optimizations were deemed to be converged when the force on every ion was less than 0.01 eVÅ^{-1}. The minimum lattice parameters for PBE and PBE+U and HSE were then used for all subsequent supercell system calculations, with the same calculation parameters and convergence criteria. Supercells of 162 atoms were used in all PBE and PBE+U defect calculations, with a $3\times3\times3$ k-point mesh, centred at the Γ point. A 48 atom supercell was utilized for the more computationally expensive HSE calculations. The defects considered are copper vacancies in both the simple and split configurations; V_{Cu} and $V_{\mathrm{Cu}}^{\mathrm{split}}$; and oxygen interstitials in octahedral and tetrahedral sites; $\mathrm{O}_{\mathrm{i}}^{\mathrm{oct}}$ and $\mathrm{O}_{\mathrm{i}}^{\mathrm{tet}}$.

So that consistent energies could be used in the calculation of defect formation energies, PBE and HSE calculations were performed on molecular oxygen, and PBE+U and PBE and HSE calculations were performed on Cu metal and CuO using equivalent convergence criteria and calculation parameters.

The formation energies of defect in this chapter are calculated using the approach as outlined in Correction Method 1 in Chapter 3. We have not explicitly corrected the formation energies to account for spurious image charge corrections, due to the fact that at the time these calculations were carried out, none of the correction methods in the literature had proved satisfactory.[228] Instead, we checked supercell size convergence in supercells of 48, 162, and 384 atoms, finding that the formation energies of the defects changed by a maximum of 0.08 eV, and that transition levels only changed by 0.09 eV. Therefore we conclude that any changes to the defect energetics and transition levels reported in this chapter, due to finite size effects will not change any of the conclusions. Using the apporach outlined in Section 3.4.5, the PBE, PBE+U and HSE calculated chemical potentials for Cu_2O are given in Table 6.1.

	PBE		PBE+U		HSE	
	Cu	O	Cu	O	Cu	O
Cu-poor/O-rich	-0.08	-1.07	-0.19	-1.17	-0.13	-1.34
Cu-rich/O-poor	0	-1.23	0	-1.55	0	-1.59

Table 6.1: PBE, PBE+U and HSE calculated chemical potential limits for Cu_2O

6.4 Bulk Equilibrium Structures

Table 6.2 lists the calculated lattice parameters, equilibrium Cu–O bond distances and fundamental band gaps for the stoichiometric bulk Cu_2O using PBE and PBE+U and HSE. The PBE, PBE+U and HSE lattice parameters and bond lengths are in good agreement with previous PBE results[223] and with known experimental values.[229] The PBE band gap (0.44 eV) is severely underestimated compared to experiment (2.17 eV), [39] but this is a known feature of PBE/LDA functionals.[155] Although the addition of the +U correction increases the band gap (to 0.67 eV), it is still severely underestimated. This is to be expected as PBE+U should not be used to fit to band gaps, except in the case where the VBM and CBM are of the same localized orbitals, as in the case of Mott insulators.[154] HSE ($\alpha = 27.5\,\%$) yields a band gap of 2.12 eV, which compares very well with the experimental band gap of 2.17 eV.

Table 6.2: Comparison of the lattice constant a, Cu–O bond lengths, and fundamental band gaps (E_g) of bulk Cu_2O from previous theoretical and experimental studies and those from the current PBE, PBE+U and HSE calculations. Bond distances and lattice parameters are given in Å, E_g is measured in eV.

	a	Cu–O	E_g
LDA[222]	4.18	-	-
GGA-PBE[223]	4.29	1.86	0.47
GGA-PBE[225]	4.32	-	0.46
GGA-PBE[224]	4.31	-	0.43
GGA-PBE (this study)	4.31	1.86	0.44
GGA-PBE+U (this study)	4.28	1.85	0.67
HSE (this study)	4.28	1.85	2.12
Expt[229]	4.27	1.85	2.17

6.5 PBE *p*-type defects

6.5.1 Single Particle levels

The single particle level offsets from the highest occupied state (figure 6.2) for both V_{Cu} and $V_{\mathrm{Cu}}^{\mathrm{split}}$ show no distinct acceptor bands in the band gap. For both vacancies the defect levels cross the Fermi level, giving semi-metallic defect complexes. Raebiger *et al.* have suggested that this delocalization of defect states is the main difference between hole states in Cu(I) based materials and hole states in native *n*-type materials.[224]

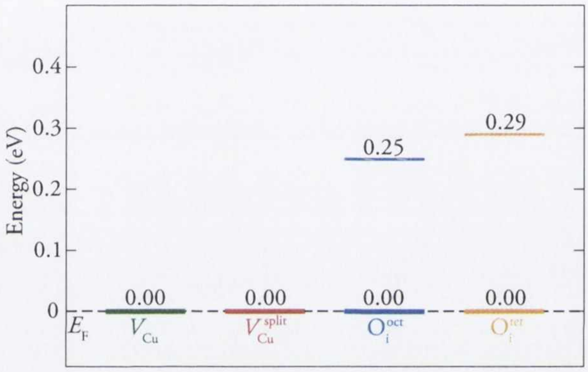

Figure 6.2: Offsets of the hole SPL from the Fermi energy for the *p*-type defects studied using PBE. The Fermi energy does not represent the VBM in the cases of the oxygen interstitials.

In typical *n*-type oxides such as ZnO, the O(p) dangling bond states of V_{Zn} occur deep in the band gap. In contrast, the delocalized nature of the PBE single particle levels for V_{Cu} has been interpreted by Raebiger *et al.* as holes residing in "delocalized, valence-band-like perturbed-host states" (PHS) and not as split off "defect-localized" states.[224] It was reported that the dangling bond states of the unrelaxed V_{Cu} are 4 eV below the VB, and "float up" to occupy a delocalized PHS just above the VBM, thus giving rise to p type conductivity. Nolan and Elliot[223] also found delocalized hole states predicted by their PBE calculations, and similarly suggested this explains the *p*-type conductivity in Cu_2O. Delocalized SPL levels were also described by Soon *et al.*[225] This description of metallic defect-derived conductivity in Cu_2O, however, is in apparent contradiction to the activated, polaronic, hopping mechanism identified experimentally.[180,181] The relatively high resistivity observed for bulk Cu_2O of 35 Ω cm, [230] is also atypical for metallic type conduction, and suggests caution in interpreting the delocalised electronic states predicted with PBE as the source of *p*-type conductivity.

For an interstitial in an octahedral site, $\mathrm{O_i^{oct}}$, PBE predicts that one defect band crosses the Fermi level and one distinct acceptor level lies 0.25 eV above the VBM. For an interstitial in a tetrahedral site, $\mathrm{O_i^{tet}}$, one defect band crosses the Fermi level, and one acceptor level lies 0.29 eV above the VBM. These results are again at variance with the known polaronic nature of conductivity in Cu_2O, as the description of the electronic structure of both oxygen interstitials using PBE indicates semi-metallic conductivity.

6.5.2 Energetics and Transition levels

Figure 6.3 shows the calculated formation enthalpies of all the intrinsic *p*-type defects for different charge states calculated with PBE, under Cu-rich/O-poor conditions. V_{Cu} has the lowest formation enthalpy; $\Delta H^{\mathrm{f}}(V_{\mathrm{Cu}}, 0) = 0.41\,\mathrm{eV}$. The formation energy of $V_{\mathrm{Cu}}^{\mathrm{split}}$ is considerably higher with $\Delta H^{\mathrm{f}}(V_{\mathrm{Cu}}^{\mathrm{split}}, 0) = 1.24\,\mathrm{eV}$. This is significantly different to the results of Nolan and Elliott,[223] who found V_{Cu} to be only 0.06 eV more favourable than $V_{\mathrm{Cu}}^{\mathrm{split}}$, and to those of Raebiger *et al.* and Soon *et al.* who found V_{Cu} to be 0.30 eV and 0.31 eV more stable than $V_{\mathrm{Cu}}^{\mathrm{split}}$ respectively.[224,225] It should be noted that the calculations performed by Nolan and Elliot[223] were carried out in a 48 atom supercell, whereas our calculations were performed in a 162 atom supercell. The formation enthalpies of $\mathrm{O_i^{oct}}$ and $\mathrm{O_i^{tet}}$ are 1.36 eV and 1.65 eV, and as such are considerably higher in energy than the V_{Cu}. This trend is maintained under Cu-poor/O-rich conditions as the range of chemical potential in quite narrow. The formation enthalpy of all defects is lowered, but V_{Cu} and $V_{\mathrm{Cu}}^{\mathrm{split}}$ remain more stable than the $\mathrm{O_{int}}$. This is consistent with the results of Raebiger *et al.* and Soon *et al.*[224,225] It should be noted however, that neglecting the formation of CuO when defining the limiting chemical potential means Soon *et al.* predicted that under Cu-poor/O-rich conditions the formation energy of V_{Cu} is exothermic, indicating V_{Cu} would form spontaneously.

[225] This is unsurprising since Cu_2O is chemically unstable with respect to CuO under these conditions, and the formation of copper vacancies drives the system towards the more stable CuO phase. These results clearly show that the defect chemistry of Cu_2O will be dominated by copper vacancies, this change in the formation energy of the oxygen interstitials is irrelevant.

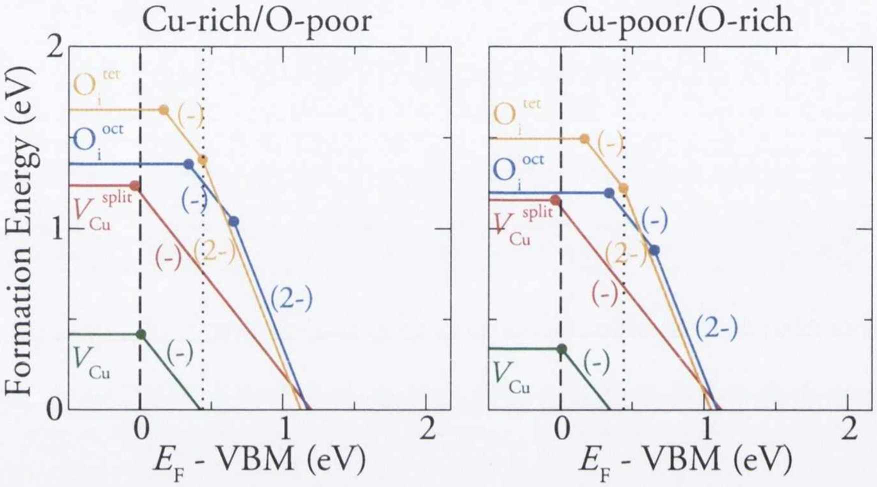

Figure 6.3: Formation energies for intrinsic p-type defects in Cu_2O in Cu-rich/O-poor conditions (left hand panel) and Cu-poor/O-rich conditions (right hand panel) calculated using PBE. The solid dots denote the transition levels $\epsilon(q/q')$. The dashed and the dotted lines indicate the position of the VBM and the CBM respectively.

The calculated ϵ(0/-) transition levels for V_{Cu} (0.01 eV) and for V_{Cu}^{split} (−0.04 eV) are not consistent with the trap levels reported in the DLTS study of Paul *et al.* which are 0.25 eV and 0.45 eV above the VBM.[217] Such shallow ϵ(0/-) transition levels would be indicative of a degenerate semiconductor, and is not consistent with the known activated nature of conduction in Cu_2O.[182–185] The transition levels for the oxygen interstitials are deep in the band gap, with the ϵ(0/-) transition levels at 0.16 eV and 0.34 eV, and the ϵ(-/-2) transition levels 0.43 eV and 0.65 eV above the VBM for O_i^{oct} and O_i^{tet} respectively. Raebiger *et al.* have suggested that the deeper trap levels (0.45 eV) as seen in DLTS experiments can be explained by the ϵ(0/-) transition levels of the O_{int}.[224]

6.6 PBE+U p-type defects

6.6.1 Single Particle levels

The PBE+U description of V_{Cu} is similar to that for PBE, Figure 6.4 The defect SPL again crosses the Fermi energy, producing a semi-metallic defect complex, as noted previously by Nolan and Elliott.[223] The PBE+U description of $V_{\mathrm{Cu}}^{\mathrm{split}}$, however, is notably different to the PBE description. The defect SPL for $V_{\mathrm{Cu}}^{\mathrm{split}}$ is split off from the VBM by 0.04 eV, indicative of a polaronic defect centre, and in better agreement with the activated conduction behaviour seen experimentally. Interestingly, Nolan and Elliot reported PBE and PBE+U both predicted a *delocalized* description for $V_{\mathrm{Cu}}^{\mathrm{split}}$.[223] Their use of a larger value of U of 7 eV than the present study, however, would suggest that the defect state ought to be more split off than described here.

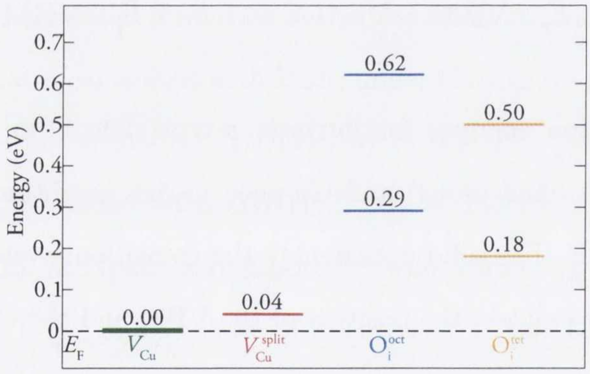

Figure 6.4: Offsets of the hole SPL from the Fermi energy for the p-type defects studied using PBE+U. The Fermi energy does not represent the VBM for the oxygen interstitials

Both $\mathrm{O}_{\mathrm{i}}^{\mathrm{oct}}$ and $\mathrm{O}_{\mathrm{i}}^{\mathrm{tet}}$ produce two distinct acceptor SPL above the VBM, with one positioned deep in the bandgap and one in the conduction band. This is again more consistent with an activated, polaronic conduction mechanism than the PBE description. The position of the higher SPL bands in the conduction band for both $\mathrm{O}_{\mathrm{i}}^{\mathrm{oct}}$ and $\mathrm{O}_{\mathrm{i}}^{\mathrm{tet}}$ is possibly an artifact of the underestimated band gap typical of PBE/PBE+U calculations.

6.6.2 Energetics and Transition levels

The PBE+U calculated formation enthalpies of the defects for Cu-rich/O-poor conditions are shown in Figure 6.5. V_{Cu} again has the lowest formation energy of $\Delta H^{\mathrm{f}}(V_{\mathrm{Cu}}, 0) = 0.92\,\mathrm{eV}$. The formation energy of $V_{\mathrm{Cu}}^{\mathrm{split}}$ is $\Delta H^{\mathrm{f}}(V_{\mathrm{Cu}}^{\mathrm{split}}, 0) = 1.66\,\mathrm{eV}$, which significantly higher than the energy predicted using PBE. This is in contrast to the previous LDA study of Wright *et al.*[222] and the PBE/PBE+U study of Nolan and Elliott.[223] $\mathrm{O}_{\mathrm{i}}^{\mathrm{tet}}$ and $\mathrm{O}_{\mathrm{i}}^{\mathrm{oct}}$ have formation energies of 1.97 eV and 2.07 eV respectively. Under Cu-poor/O-rich conditions, the formation energy of the V_{Cu} and $V_{\mathrm{Cu}}^{\mathrm{split}}$ are lowered to 0.73 eV and 1.47 eV, with the oxygen interstitial formation energies shifted downwards to 1.59 eV and 1.69 eV for $\mathrm{O}_{\mathrm{i}}^{\mathrm{tet}}$ and $\mathrm{O}_{\mathrm{i}}^{\mathrm{oct}}$ respectively.

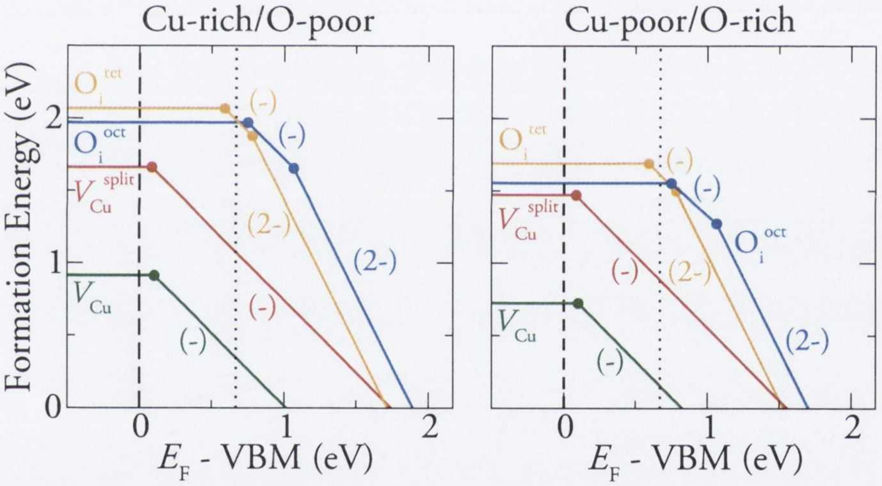

Figure 6.5: Formation energies for intrinsic p-type defects in Cu_2O in Cu-rich/O-poor conditions (left hand panel) and Cu-poor/O-rich conditions (right hand panel) calculated using PBE+U. The solid dots denote the transition levels $\epsilon(q/q')$. The dashed and the dotted lines indicate the position of the VBM and the CBM respectively.

The calculated $\epsilon(0/\text{-})$ transition levels for $V_{\mathrm{Cu}}^{\mathrm{split}}$ and V_{Cu} are 0.10 eV and 0.08 eV. Again, these transition levels are not in agreement with the two trap levels reported from recent DLTS studies.[217] The $\epsilon(0/\text{-})$ transition levels of $\mathrm{O}_{\mathrm{i}}^{\mathrm{oct}}$ and $\mathrm{O}_{\mathrm{i}}^{\mathrm{tet}}$ are 0.59 eV and 0.75 eV, and the $\epsilon(\text{-}/\text{-}2)$ transition levels are 0.77 eV and 1.06 eV. We find the difference in transition levels between PBE and PBE+U is not well represented by a rigid shift, particularly when comparing calculated levels for oxygen interstitials with those for copper vacancies (Table 6.3). The transition levels for the oxygen interstitials are too deep to be associated with the hole traps observed at 0.45 eV in the DLTS studies,[217] at variance with conclusions of Raebiger *et al.*[224].

Table 6.3: PBE and PBE+U calculated acceptor transition levels, $\epsilon_{\mathrm{A}}(q/q')$, for the p-type defects investigated. ΔE is the shift of the PBE+U transition level relative to the PBE transition level; $\Delta E = \epsilon_{\mathrm{D}}^{\mathrm{PBE}+U}(q/q')$ - $\epsilon_{\mathrm{D}}^{\mathrm{PBE}}(q/q')$.

	V_{Cu}	V_{split}	$\mathrm{O}_{\mathrm{i}}^{\mathrm{oct}}$		$\mathrm{O}_{\mathrm{i}}^{\mathrm{tet}}$	
	$\epsilon_{\mathrm{A}}(0/-)$	$\epsilon_{\mathrm{A}}(0/-)$	$\epsilon_{\mathrm{A}}(0/-)$	$\epsilon_{\mathrm{A}}(-/-2)$	$\epsilon_{\mathrm{A}}(0/-)$	$\epsilon_{\mathrm{A}}(-/-2)$
PBE	0.01	-0.04	0.16	0.43	0.34	0.65
PBE+U	0.10	0.08	0.59	0.77	0.75	1.06
ΔE	0.09	0.12	0.43	0.34	0.31	0.41

6.7 HSE p-type defects

6.7.1 Single Particle levels

All the defects display acceptor SPL deep in the band gap (Figure 6.6 and Table 6.4), as expected for a polaronic system, and thus in agreement with experimental data. This is in contrast to the delocalized defect states predicted by previous calculations performed with standard PBE functionals[223–225]. Raebiger *et al.* proposed p-type conductivity in Cu_2O is due to holes produced by V_{Cu}, which reside in "delocalized, valence-band–like perturbed-host states" and not split off "defect-localized" states[224]. Such a description is however at variance with the experimentally known activated, polaronic, hopping mechanism[180,181]. It is noteworthy that the typical resistivity of Cu_2O is 35 Ω cm [230], which is considerably higher than the resistivities expected for classical band-conducting semiconductors, but which is in keeping with our calculated SPL being deep in the band gap.

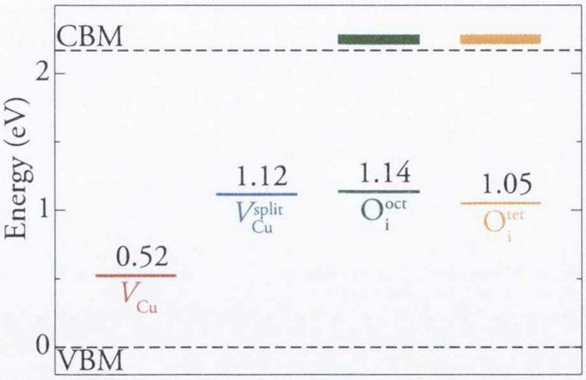

Figure 6.6: HSE single-particle level offsets from the VBM of V_{Cu}, V_{Cu}^{split}, O_i^{oct}, and O_i^{tet}.

Analysis of the hole charge densities associated with these defects reveals distinct *polaronic centres*. The hole state for V_{Cu} is localized on the six copper ions bonded to the two three coordinate oxygens, with some hole density residing on the two oxygens themselves. The V_{Cu}^{split} hole state is strongly localized on the copper that moves towards the vacancy, and has Cu *d* character, with some mixing with the $2p$ states on the four coordination oxygens; Figure 6.7. The hole states for both O_i^{oct} and O_i^{tet} are localized mainly on the interstitial oxygen and the surrounding Cu ions. In all cases, the defect centres are localized polarons, in contrast to the delocalized hole states predicted by PBE calculations[223,224].

6.7.2 Energetics and Transition levels

Figure 6.8(a) and Table 6.4 give the calculated formation enthalpies of all the intrinsic *p*-type defects calculated for Cu_2O in different charge states for Cu-rich/O-poor conditions. Under Cu-rich conditions V_{Cu}^{split} has the lowest formation enthalpy of all the defects investigated, with the formation energy of V_{Cu} only 0.01 eV greater. This agrees with the LDA study of Wright *et al.* who found V_{Cu}^{split} to be most stable[222], and is at variance with all previous PBE calculations[223–225]. Formation enthalpies for both V_{Cu} and O_i are lowered under Cu-poor/O-rich conditions (Figure 6.8(b)), with the trend in formation energies unchanged. Copper vacancies (V_{Cu} and V_{Cu}^{split}) have the

Table 6.4: Formation energies $\Delta H_f(D, 0)$ in Cu-rich/O-poor conditions, single particle (eigenvalue) levels for the hole states, and acceptor transition levels, $\epsilon_D(0/\text{-}1)$ for the four calculated *p*-type defects in Cu_2O.

	$\Delta H_f(D)$ (eV)				Single particle level (eV)				$\epsilon_D(0/-1)$ (eV)			
	V_{Cu}	V_{Cu}^{split}	O_i^{oct}	O_i^{tet}	V_{Cu}	V_{Cu}^{split}	O_i^{oct}	O_i^{tet}	V_{Cu}	V_{Cu}^{split}	O_i^{oct}	O_i^{tet}
This work	1.15	1.14	1.94	1.87	0.52	1.11	1.13	1.05	0.23	0.47	1.08	1.27
PBE[223]	0.41	0.47	-	-	0.00	-	-	-	-	-	-	-
PBE[224]	0.70	1.00	1.80	1.30	0.00	-	-	-	0.28	0.29	0.66	0.78
PBE[225]	0.47	0.78	1.90	1.47	0.00	-	-	-	0.18	0.20	0.45	0.65

lowest formation energies under all conditions and are therefore the likely cause of hole carriers in Cu_2O.

The calculated $\epsilon(0/\text{-})$ transition levels for V_{split} (0.47 eV) and for V_{Cu} (0.22 eV) are in excellent agreement with the trap levels reported in the DLTS study of Paul *et al.*[231] at 0.45 eV and 0.25 eV above the VBM, and with those in a more recent DLTS study of Cu_2O by the same authors that finds trap levels at 0.5 eV and 0.21 eV[232]. That two distinct hole traps are found in DLTS spectra is explained by the similar formation energies of the V_{split} and V_{Cu} and their differing transition levels. The calculated transition levels of the oxygen interstitials are ultra deep, with the $\epsilon(0/\text{-})$ transition levels at 1.08 eV and 1.28 eV, and the $\epsilon(\text{-}/\text{-}2)$ transition levels are 1.36 eV and 1.98 eV above the VBM for the O_i^{oct} and O_i^{tet} respectively. The suggestion by Raebiger *et al.* that O_i could be the source of the deeper trap levels (0.45 eV) is shown to be an artifact of the inability of PBE to describe the polaronic states of Cu_2O properly[224], and we conclude that oxygen interstitials do not contribute to *p*-type conductivity in Cu_2O, as defect formation is energetically disfavoured and the transition levels are too deep.

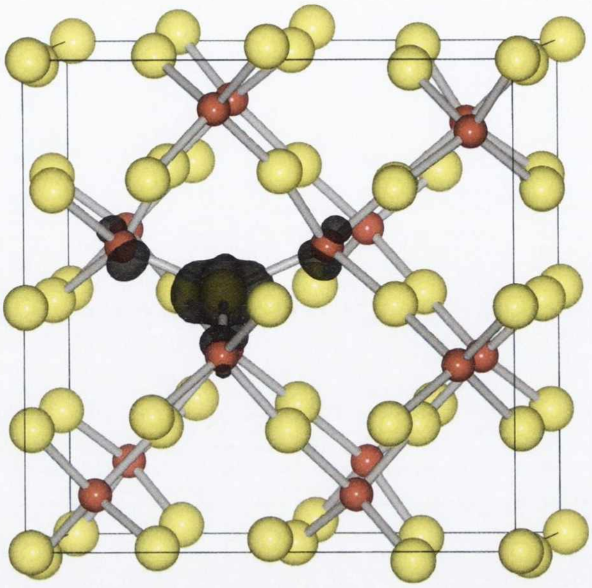

Figure 6.7: HSE (α = 27.5%) hole density for $V_{\mathrm{Cu}}^{\mathrm{split}}$ in Cu_2O. The red and yellow spheres denote O and Cu respectively. The blue isosurface is shown at $0.05\,\mathrm{e}\,\text{Å}^{-3}$

6.8 *n*-type Defect Chemistry of Cu_2O

We have now established from Sections 6.7.1 and 6.7.2 that the defect chemistry of Cu_2O is polaronic in nature, and is caused by cation deficiency, with copper vacancies (V_{Cu}) dominating under all growth conditions. To date the best conversion efficiency reported for a cuprous oxide based PV device is $\sim 2\%$,[233] which is an order of magnitude lower than its theoretical efficiency. This low efficiency has been attributed to the reliance on Schottky junctions and p-n heterojunctions in Cu_2O PV devices, mainly due to the non-existence of *n*-type Cu_2O.[234] The development of *n*-type Cu_2O has therefore become an important research goal, and is vital for the realization of high efficiency PV devices based on homo-junctions of Cu_2O.

Surprisingly, electro-deposited *undoped* thin films of Cu_2O displaying *n*-type conductivity have been reported.[235–239] The origin of the *n*-type conductivity in these films is still a matter of debate, with oxygen vacancies[238] (V_{O}) and copper antisites ($\mathrm{Cu_O}$),[240] being suggested as the source of donors. It has also been postulated that varying the pH of the sample during electro-deposition can control the polarity of the conductivity

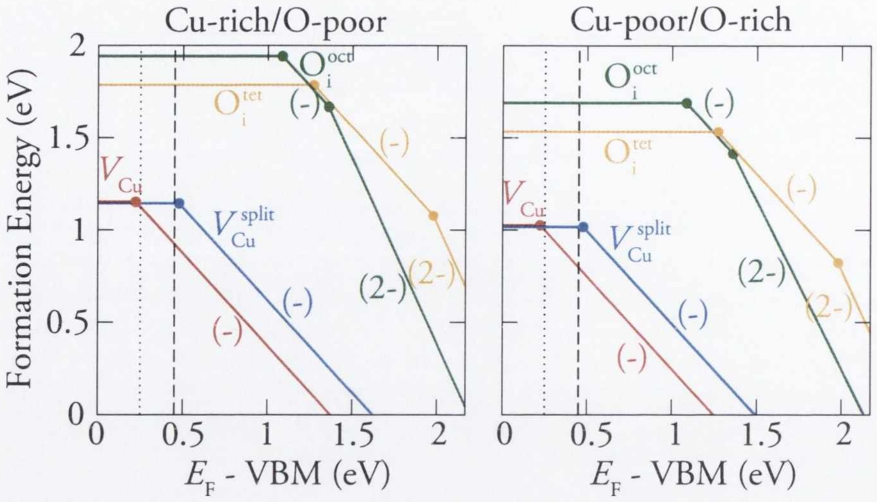

Figure 6.8: Formation energies for intrinsic p-type defects in Cu_2O in Cu-rich/O-poor conditions (left and panel) and (b) Cu-poor/O-rich conditions (right hand panel). The solid dots denote the transition levels $\epsilon(q/q')$. The dotted and the dashed lines indicate the position of traps A and B from the DLTS study of Paul *et al.*[231]

in Cu_2O thin films.[239]

Another posible source of n-type conductivity in Cu_2O could be adventitious hydrogen. The behaviour of hydrogen in semiconductors has been investigated for decades. [241] It was thought that interstitial hydrogen behaved only as an *amphoteric* impurity in semiconductors, acting as a donor in p-type materials and as an acceptor in n-type materials.[242] However, in 2000, Van de Walle demonstrated using first-principles methods that hydrogen could act as a shallow donor in wide band gap n-type ZnO.[29] This was subsequently verified by many experimental studies, e.g. Cox *et al.*[31], and it has been demonstrated that hydrogen can act as a shallow donor *and* is a source of n-type conductivity in other wide band gap n-type oxide semiconductors.[33,243] The behaviour of hydrogen in p-type oxides, however, has not been elucidated. A recent muon spectroscopy study has indicated that hydrogen in Cu_2O has *"quasi-atomic"* character and causes an electrically active level $\sim$ 1 eV above the valence band maximum (VBM).[32] However, this study could not identify if the transition level represents hole or electron ionization, and could not infer any site identification.[32]

In this section we investigate the interplay of intrinsic p-type and n-type defects in Cu_2O. As we have now established the need for hybrid DFT when describing p-type defects in Cu_2O, we use the screened hybrid density functional as proposed by Heyd, Scuseria and Ernzerhof (HSE)[99] in the rest of our defect analysis. We confirm that V_{O} and Cu_i *cannot* act as donors in Cu_2O. Furthermore, we show that the transitions levels of the $(V_{\mathrm{O}} - V_{\mathrm{Cu}})$ complex are very deep in the band gap, and are unlikely to contribute to any n-type conductivity. P-type conductivity is predicted to dominate under all growth conditions. In light of these results we discuss the previous experimental findings. We also present an examination of the geometry and electronic structure of hydrogen in Cu_2O and compare the calculated transition levels to the levels for intrinsic n- and p-type defects. We show (i) in stoichiometric Cu_2O, hydrogen preferentially occupies the tetrahedral interstitial position, explaining for the first time the quasi-atomic nature of hydrogen in Cu_2O as indicated by Muon spectroscopy, (ii) hydrogen acts as an amphoteric defect in stoichiometric Cu_2O, and is *not* a cause of n-type conductivity, and (iii) hydrogen will bind into any V_{Cu} in the system and *passivate* p-type conductivity. In light of these results we discuss strategies to remove hydrogen from the system and increase Cu_2O device performance.

6.8.1 Intrinsic n-type defects

To examine *all* the possible intrinsic defects in Cu_2O, we have considered the formation of oxygen vacancies (V_{O}), copper vacancies (V_{Cu}), copper interstitials (Cu_i) and oxygen interstitials (O_i) in the octahedral and tetrahedral interstitial positions within the Cu_2O lattice, Figure 6.9. We have not considered the formation of $\mathrm{Cu_O}$, as Soon *et al* have previously shown it to have an extremely high formation energy using GGA ($\sim 4-6\,\mathrm{eV}$),[225] and it is unlikely that HSE calculations will lower this formation energy enough to make it competitive with the other native defects. In addition we examined the formation of a complex $(V_{\mathrm{O}} - V_{\mathrm{Cu}})$ formed between V_{Cu} and V_{O}, as this has been suggested as a source of the persistent photo conductivity (PPC) observed in Cu_2O samples,[244] and is expected to behave as a one electron donor.

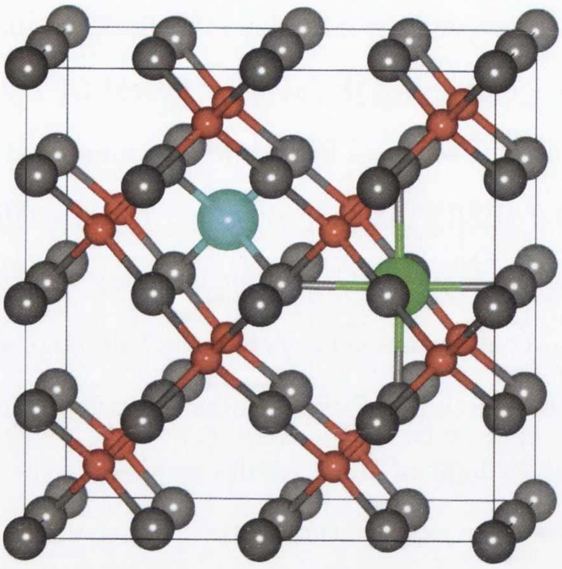

Figure 6.9: Octahedral (green sphere) and tetrahedral (turquoise sphere) interstitial positions in Cu_2O. The grey and red spheres are Cu and O respectively.

6.8.2 Single particle levels of the donor states

We have previously demonstrated that the single particle levels (SPLs, raw eigenvalues of the defect states) for p-type defects in Cu_2O are deep in the band gap as shown in Section 6.7.1. As Cu_2O does not possess the characteristic metal s dominated conduction band minima (CBM) of the well known n-type degenerate semiconducting oxides (e.g. In_2O_3, CdO, SnO_2 etc.), n-type defects in Cu_2O are not expected to be shallow donors. The SPL for n-type defects in Cu_2O are shown in Figure 6.10. The excess electrons left behind upon V_O formation are so deep that they are resonant in the VB, while the SPLs of Cu_i^{oct} and Cu_i^{tet} are 1.18 eV and 1.23 eV below the CBM respectively. The SPL for the $(V_O - V_{Cu})$ complex is also resonant in the VB. It is unlikely that any of the considered n-type defects will lead to high levels of n-type conductivity, as these defects are very deep, and are deeper even that the SPL for the polaronic p-type defects.

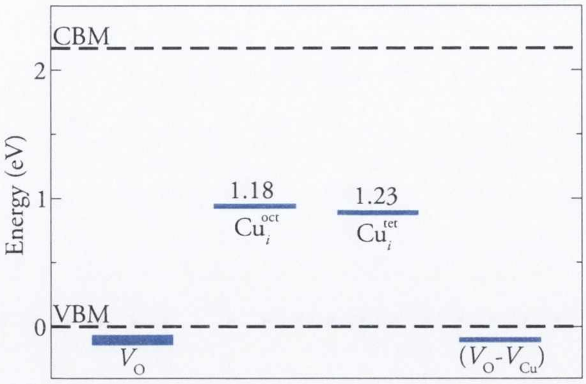

Figure 6.10: HSE single-particle level offsets of donor states from the CBM of V_O, Cu_i^{oct}, Cu_i^{tet} and the $(V_{Cu} - V_O)$ complex.

6.8.3 Defect energetics and transition levels

The HSE calculated formation enthalpies of the intrinsic n- and p-type defects in different charge states and under both Cu-rich/O-poor conditions and O-rich/Cu-poor are given in Figure 6.11. Under both sets of conditions V_{Cu} and V_{Cu}^{split} have the lowest formation enthalpy, with the formation enthalpy of V_O very close in energy under Cu-rich conditions. The formation energy of the n-type defects are lowered relative to the p-type defects under Cu-rich conditions, with the reverse occurring under Cu-poor conditions. Under all conditions, and based on formation enthalpies alone, cation and anion vacancies are likely to dominate the defect chemistry of Cu_2O.

It is important to bear in mind that a good n-type (p-type) semi-conductor should possess shallow donors (acceptors), meaning that the $\epsilon(+x/0)$ ($\epsilon(0/-x)$) transitions are within $\sim 0.03\,\text{eV}$ (kT) of the CBM (VBM), or indeed inside the CB (VB).The further an ionization level is from the band edge, the worse the conductivity will be. In agreement with previous GGA studies,[225,245] V_O does not have a transition level in the band gap, meaning it is stable only in the charge-neutral state and will not compensate acceptor formation, and does not operate as a donor. Cu_i^{oct} and Cu_i^{tet} are both found to be *amphoteric* defects, having both $\epsilon(0/-)$ and $\epsilon(+/0)$ transitions in the band gap, and are found to be prohibitively high in energy under all growth conditions. Thus even if Cu_i could form, it would not contribute to any n-type conductivity, as it

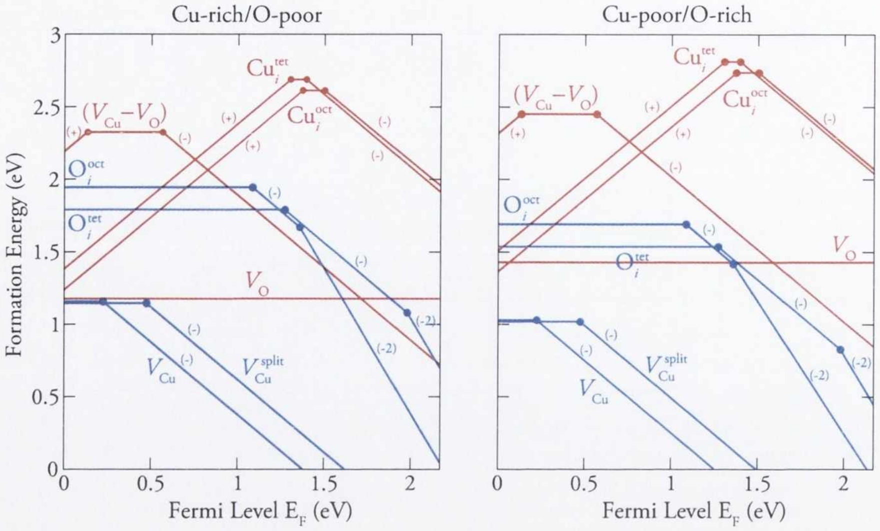

Figure 6.11: HSE calculated formation energies for intrinsic p-type (blue) and n-type defects in Cu_2O as a function of Fermi energy in: Cu-rich/O-poor conditions (left hand panel) and Cu-poor/O-rich conditions (right hand panel). The solid dots denote the transition levels $\epsilon(q/q')$.

would behave like an acceptor under typical n-type conditions, and as a donor under p-type conditions. The $(V_O - V_{Cu})$ complex has a high formation enthalpy, with a very deep $\epsilon(+/0)$ transition 0.13 eV above the VBM (2.04 eV from the CBM), *and* a $\epsilon(0/\text{-})$ at 0.56 eV above the VBM, meaning it will not be a source of n-type conductivity. Thus, based on our HSE calculations, we find that under all growth conditions, p-type conductivity stemming from V_{Cu}^{split} and V_{Cu} will dominate. As all n-type defects in Cu_2O are found to be incapable of behaving as (relatively) shallow donors or even compensating p-type conductivity, the repeated tantalizing reports of n-type samples are quite puzzling.

6.8.4 Behaviour of H in Cu_2O

We have examined the stability of interstitial hydrogen, H_i, in stoichiometric Cu_2O in both the tetrahedral, H_i^{tet}, and octahedral, H_i^{oct}, interstitial positions, in the so called bond centre (H_i^{BC}) position and in two anion anti-bonding configurations (H_i^{AB1} and

H_i^{AB2}), as shown in Figure 6.12. From the formation energies listed in Table 6.5, it is clear that the most favourable position for H_i in Cu_2O is the H_i^{tet} position. This is surprising, as in many oxides and nitrides,[29,246,247] H preferentially occupies a position next to the anions in either a bond centre or anion anti-bonding configuration. This result explains the uncertainty about the preferred lattice site for H in Cu_2O found in the Muon study by Cox *et al.* Analyzing the charge density distribution of the H_i^{tet}, Figure 6.13, we can see that the electron from the interstitial hydrogen is donated to the four cation nearest neighbours and to the interstitial itself, in a "quasi-atomic" manner. The tetrahedral interstitial position was first proposed by Cox *et al.* as a possible explanation for their experimental results.[32] This view was recently supported by the GGA calculations of Catlow *et al.*,[248] where GGA calculations did not find the H_i^{tet} to be the lowest energy configuration, but it was proposed as the mimimum energy structure based on *a posteriori* corrections.

When examining the interaction of H with defective Cu_2O, we have only considered H interacting with V_{Cu} and V_O, as the formation energy of the both anion and cation interstitials are very high.[245] We tested H on both the perfect Cu and O crystallographic sites, and then offset from these sites, finding that for H_O, hydrogen sits on the perfect lattice site. For H interacting with a V_{Cu}, H wanted to distort from the perfect Cu site and move towards one of the two three-coordinate oxygens left behind upon V_{Cu} formation, forming an O–H bond. The energy to form the resulting $(H - V_{Cu})$ complex was found to be only 0.17 eV, making it the most stable defect considered, Table 6.5.

6.8.5 Defect energetics and transition levels.

Figure 6.14 shows a plot of formation energy as a function of Fermi-level position for all intrinsic defects and H related impurities for both Cu-rich/O-poor and Cu-poor/O-rich regimes. For most of the H related defects, all three charge states (-, 0 and +) are stable within the band gap. This type of behaviour has not been reported thus far for H in oxides. *All* H_i defects act as *amphoteric* impurities under both sets of conditions, meaning that H_i will effectively kill both *p*-type and *n*-type conductivity

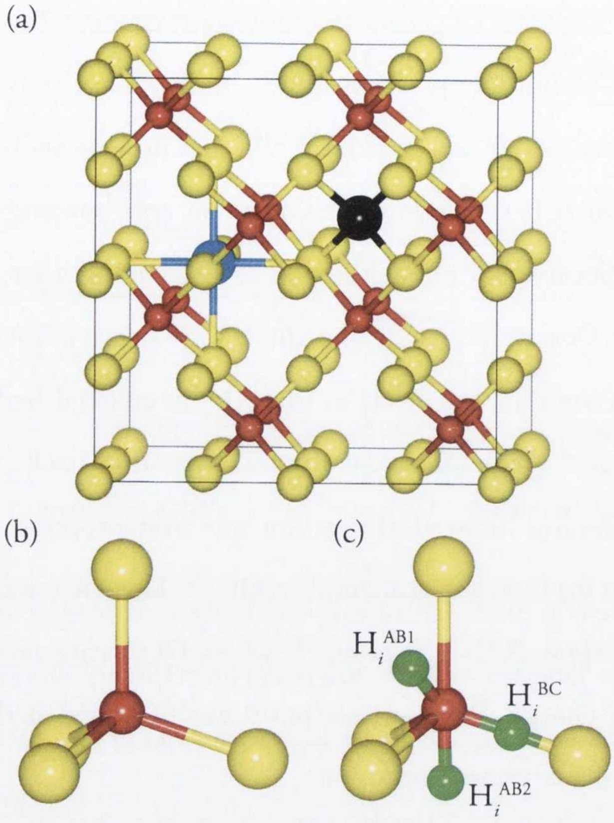

Figure 6.12: (a) Octahedral (blue sphere) and tetrahedral (black sphere) interstitial positions in Cu_2O, (b) coordination around an O atom in Cu_2O and (c) possible sites for interstitial H (H_i^{BC}, H_i^{AB1} and H_i^{AB2}) around the tetrahedral O in Cu_2O .

in the system. H_O is also an amphoteric defect, with a larger formation energy than all the H interstitials. This behaviour is very different to the behaviour of H_O in other wide-band-gap n-type oxides, where is its found to act as a shallow donor.[30]

It is likely that the transition level seen by Cox *et al.* is actually the 0/- transition, for the $(H - V_{Cu})$ defect, which occurs at $\sim 1.15\,\text{eV}$ above the VBM. Thus we have identified that the level seen in muon spectroscopy most likely represents hole ionization. The already deep transitions levels of V_{Cu} are thus passivated, with the transition level for $(H - V_{Cu})$ being *ultra* deep in the band gap, severely affecting the p-type ability of Cu_2O under all growth conditions.

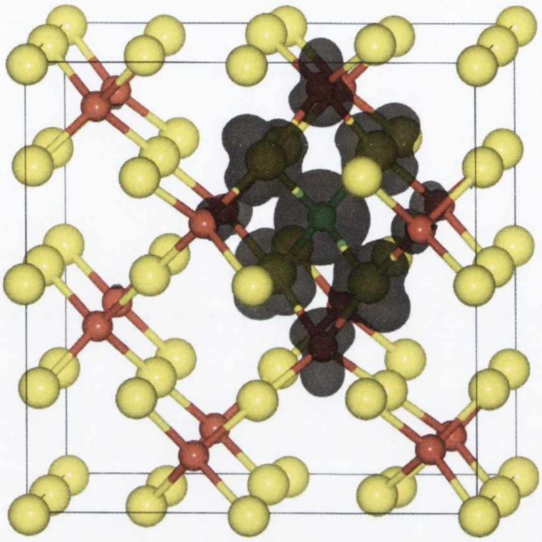

Figure 6.13: HSE ($\alpha = 27.5\%$) spin density density for H_i^{tet} in Cu_2O. The red, yellow and green spheres denote O and Cu and H respectively. The black isosurface is shown at $0.01\,\mathrm{e\,\mathring{A}}^{-3}$.

6.8.6 Acceptor Reactivation

The calculated binding energy of the $(\mathrm{H}_i - V_{\mathrm{Cu}})$ complex is given by:

$$E_b = \Delta H_{\mathrm{f}}\left[(V_{\mathrm{Cu}}), 0\right] + \Delta H_{\mathrm{f}}\left[(\mathrm{H}_i), 0\right] - \Delta H_{\mathrm{f}}\left[(\mathrm{H}_i - V_{\mathrm{Cu}}), 0\right], \tag{6.1}$$

where $\Delta H_{\mathrm{f}}\left[(\mathrm{H}_i - V_{\mathrm{Cu}}), 0\right]$ is the formation energy of the complex in the neutral charge state. A positive E_b indicates that the complex $(\mathrm{H}_i - V_{\mathrm{Cu}})$ is lower in energy than the isolated H_i and V_{Cu}. We obtain an E_b of 2.62eV, which is very large when compared with the binding energy for other hydrogen-acceptor complexes, e.g. in SnO_2:IIIA[249] (0.22 – 0.53 eV) or in GaN:Mg[250] (0.7 eV). The high binding energy is most likely due to the fact that in Cu_2O, H actually binds into a *vacancy*, whereas in SnO_2 and GaN H binds onto anions neighbouring the acceptor dopants.

Using the nudged elastic band (NEB) method we have calculated the migration barrier for H_i in Cu_2O to be $\sim 0.18\,\mathrm{eV}$, which is very low compared to the calculated migration barriers in other oxides, e.g. SnO_2 (0.57 eV).[28] In other oxides and nitrides, H_i exists as H_i^+, bonded to the anions.[29,247] The reason for this low migration barrier is that as H_i is most stable in the $\mathrm{H}_i^{\mathrm{tet}}$ position, and not in an AB or BC configuration,

Table 6.5: HSE calculated formation energies in the neutral charge state, $\Delta H_\mathrm{f}\,[(\mathrm{D}),0]$, for H defects in Cu_2O in Cu-rich/O-poor conditions. O–H and Cu–H bond lengths are given where appropriate.

Defect	$\Delta H_\mathrm{f}\,[(\mathrm{D}),0]$ (eV)	$d_\mathrm{O-H}$ (Å)	$d_\mathrm{Cu-H}$ (Å)
$\mathrm{H}_i^\mathrm{oct}$	2.21	2.37	1.76
$\mathrm{H}_i^\mathrm{tet}$	1.64	2.47	1.80
H_i^BC	1.98	0.99	–
$\mathrm{H}_i^\mathrm{AB1}$	2.32	0.98	–
$\mathrm{H}_i^\mathrm{AB2}$	1.93	0.98	–
H_O	2.26	–	1.66
$(\mathrm{H}_2)_i^\mathrm{oct}$	2.41	–	–
$(\mathrm{H}_2)_i^\mathrm{tet}$	2.25	–	–
$(\mathrm{H}_i - V_\mathrm{Cu})$	0.17	0.98	–

it does not have to break any strong O–H bonds, and is free to move from tetrahedral hole to tetrahedral hole. Cox *et al.* have also noted that muonium can diffuse quite easily in Cu_2O, with a hop rate activation energy of $\sim 0.1\,\mathrm{eV}$,[32] which is in reasonable agreement with our migration barrier of $\sim 0.18\,\mathrm{eV}$.

Experimentally the removal of hydrogen and reactivation of acceptors in GaN:Mg is possible with thermal annealing.[251] This begs the question: can H be annealed out of Cu_2O to reactivate the intrinsic acceptors and increase p-type conductivity? Based on our results for the migration barrier of H_i, we can calculate the temperatures at which we expect H_i to become mobile using transition state theory as outlined by Van de Walle and co-workers.[26,252] Transition state theory[253] tells us that an interstitial can jump to the next interstitial site over an migration barrier, E_m with a frequency

$$\Gamma = \Gamma_0 \exp\left(-\frac{E_m}{k_\mathrm{B}T}\right), \tag{6.2}$$

where Γ_0 is the ratio of the vibrational frequencies at the starting configuration to the frequencies at the saddle point, k_B is the Boltzmann constant and T is the temperature.

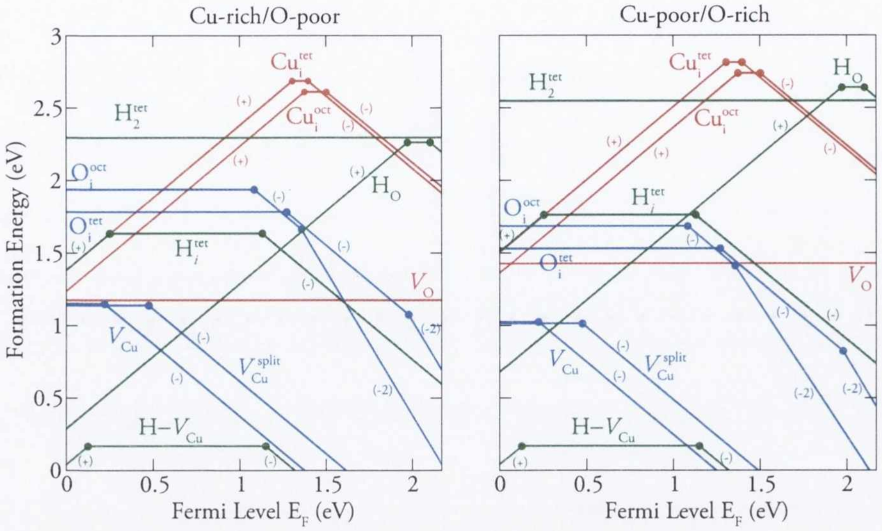

Figure 6.14: HSE ($\alpha = 27.5\%$) calculated formation energies for intrinsic p-type (blue), n-type (red), and hydrogen impurity (green) defects in Cu_2O in Cu-rich/O-poor conditions (left hand panel) and Cu-poor/O-rich conditions (right hand panel). The solid dots denote the transition levels $\epsilon(q/q')$

Van de Walle and co-workers have shown that using a typical phonon frequency of $10^{13}\,s^{-1}$ for Γ_0, and setting $\Gamma = 1\,s^{-1}$ (taking the normal definition of of activation temperature, i.e. T for which the jump rate Γ is 1/s), can yield reasonable annealing temperatures.[26,252] From this analysis we define an annealing temperature T, which is the T at which the H jump rate is 1/s. This yields an annealing temperature for H_i of 72 K, which indicates that H_i will be annealed out well below room temperature.

However, H trapped in a V_{Cu} will be much more difficult to remove. Approximating the activation energy for dissociation of the $(H_i - V_{Cu})$ complex to be equal to the binding energy for the complex (2.62eV), we can estimate an annealing temperature for the removal of all H from the system of 943 K. This result gives good agreement with experiment, as the disappearance of the muonium signal in Cu_2O was noted to occur at around 900 K.[32]

6.9 Discussion

p-type defects With both PBE and PBE+U, V_{Cu} is the most energetically favourable p-type defect in Cu_2O under all growth conditions, and is therefore predicted to be the most likely source of hole carriers in Cu_2O. $V_{\mathrm{Cu}}^{\mathrm{split}}$ is considerably higher in energy with both methods, and $\mathrm{O}_{\mathrm{i}}^{\mathrm{oct}}$ and $\mathrm{O}_{\mathrm{i}}^{\mathrm{tet}}$ are unfavoured under all conditions, and are therefore unlikely to be the source of any conductivity. HSE, however, predicts that the $V_{\mathrm{Cu}}^{\mathrm{split}}$ and V_{Cu} are very close in energy, with the $V_{\mathrm{Cu}}^{\mathrm{split}}$ slightly more stable. The HSE formation energies of both $\mathrm{O}_{\mathrm{i}}^{\mathrm{oct}}$ and $\mathrm{O}_{\mathrm{i}}^{\mathrm{tet}}$ are found to be very high, indicating that they will not play a large role in conductivity.

The magnitude of the formation energy of the various defects increases dramatically from PBE to PBE+U to HSE. Our PBE calculated formation energy for V_{Cu} is 0.41 eV, which is close to the PBE result of Nolan and Elliott of 0.34 eV[223](162 atom cell). The PBE formation energy of the $V_{\mathrm{Cu}}^{\mathrm{split}}$ was found to be 1.24 eV, which is considerably higher than that of the V_{Cu}. Nolan and Elliott had reported that $V_{\mathrm{Cu}}^{\mathrm{split}}$ was only 0.06 eV less stable than V_{Cu} in a 48 atom cell.[223] They do not however report the formation energy for $V_{\mathrm{Cu}}^{\mathrm{split}}$ in a 162 atom cell, but the recent study conducted by Soon *et al.* reported that $V_{\mathrm{Cu}}^{\mathrm{split}}$ is as much as 0.31 eV less stable than V_{Cu} in a 48 atom cell also using PBE.[225] This situation is reversed for our HSE calculations, which predicts that $V_{\mathrm{Cu}}^{\mathrm{split}}$ is slighlty more stable than V_{Cu}. The PBE+U calculated formation energy for V_{Cu} is found to be 0.92 eV, and for $V_{\mathrm{Cu}}^{\mathrm{split}}$ is found to be 1.66 eV. Previous PBE+U ($U = 7$ eV) calculations[223] had also found that the energy to form both V_{Cu} and $V_{\mathrm{Cu}}^{\mathrm{split}}$ *increases* as you move from PBE to PBE+U. The magnitude of both vacancies from our work is less than in that study, although this is probably a consequence of the larger simulation cell used in our work, and the differing U values utilised.

Neither PBE or PBE+U give SPL and $\epsilon(0/-)$ transition levels that can be interpreted as being in good agreement with experiment. The polaronic nature of Cu_2O is not correctly described by PBE for any of the p-type defects investigated; all the SPL indicate semi-metallic behaviour. Indeed the weak localization effects of V_{Cu} using both PBE and PBE+U are shown in Table 6.6, which lists the spin populations on the nearest neighbour atoms, from which it is clear that V_{Cu} does not represent a localized polaron in either methodology. The calculated transition levels for $V_{\mathrm{Cu}}^{\mathrm{split}}$ are in the valence band, and for V_{Cu} are so shallow as to be thermally ionized at room temperature. This is inconsistent with the deep ionization levels seen experimentally.[216,217,219] The PBE+U description of V_{Cu} is similarly inconsistent with the polaronic nature of Cu_2O, predicting a SPL that crosses the Fermi energy at the top of the valence band. PBE+U predicts that $V_{\mathrm{Cu}}^{\mathrm{split}}$ and both $\mathrm{O}_\mathrm{i}^{\mathrm{tet}}$ and $\mathrm{O}_\mathrm{i}^{\mathrm{oct}}$ have distinct hole SPL in the band gap. Although this is consistent with the experimentally noted polaronic, activated conduction,[182–185] the calculated transition levels do not agree with the positions of the deep levels seen in DLTS experiments.[217]

Table 6.6: Localization of hole spin states on ions neighbouring the copper vacancies calculated using PBE and PBE+U. For V_{Cu} this is the total spin on the six copper ions coordinated to the three coordinate oxygens, for the V_{split} this corresponds to the spin on the tetrahedrally coordinated copper, with the spins on the four oxygens coordinated to this in parentheses.

	PBE	PBE+U	HSE
V_{Cu}	0.01	0.03	0.12
V_{split}	0.17 (0.02)	0.46 (0.05)	0.69 (0.05)

Comparison of the $\epsilon(0/-)$ transition levels calculated using PBE and PBE+U shows that the PBE+U results are not equivalent to the PBE transition levels plus a rigid shift, particularly when comparing oxygen interstitials with copper vacancies. This suggests that caution should be taken when interpreting results obtained from applying compensatory shifts to PBE transition levels in systems where defect states are thought to be polaronic.

A higher value of U might be expected to split off these levels even further from the VBM. As the value of U of 5.2 eV employed here closely reproduces valence band features of Cu_2O and $CuM^{III}O_2$ (as seen in Section 4), it is likely that applying such a correction to the Cu 3*d* states would only be an unphysical attempt to compensate for other shortcomings in the PBE+U description for this system, and would be unjustified.

By applying a hybrid functional to investigate these defects, we find a correct description of the activated deep defects associated with polaronic Cu_2O, with our calculated transition levels in excellent agreement with recent DLTS experiments.[231] HSE yields relatively localized defects as shown in Table 6.6, which is more consistent with the view that Cu_2O is polaronic, and SPLs deep in the band gap. The success of the hybrid functional approach stems from the fact that they allow a degree of exact exchange to be applied to every species, and not just to the Cu *d* states as for PBE+U. This allows an improved description of the mixed Cu *d*/O *p* VBM, and thus more accurately describes the polaronic nature of defective Cu_2O.

n-type defects It is interesting to address some of the donor states reported in *undoped* Cu_2O samples. In 1958, Bloem studied the effect of oxygen partial pressure during preparation of Cu_2O using photoluminescence (PL) experiments, reporting two donor states attributed to singly and doubly ionized V_O.[254] This study was unable, however, to report the energy levels of these donor states. In 1972, Schick and Trivich identified two donor states in Cu_2O samples, at 1.34 eV and 1.03 eV below the CBM. [255] The source of these donor states was not elucidated, but it was postulated that these levels could be attributed to the donor levels proposed by Bloem's earlier work. Rakhshani reported a donor level at 0.92 eV below the CBM, although the source of this donor level was not identified, and the energy level was derived from approximations to the space-charge-limited-current (SCLC) theory.[211]

In a more recent study, a donor state has been noted at 0.38 eV below the CBM, which was attributed to V_O from PL experiments.[238] This donor state is considerably *shallower* than those reported in earlier studies, and notably comes from an *electrodeposited* sample. Our analysis, and the previous GGA results[225,245] strongly suggest that V_O cannot be the source of these reported donor levels. It is possible, however, that the extremely deep donor states seen experimentally could be the $\epsilon(+/0)$ states of Cu_i^{tet} (0.87 eV below the CBM) and Cu_i^{oct} (0.80 eV below the CBM). With the exception of the 0.38 eV donor level reported by Rakhshani,[211], all reported donor levels are extremely deep, and would not be expected to lead to good *n*-type conductivity.

An explanation for the reported dependence of conductivity polarity upon pH was very recently offered by Tao and co-workers.[240] Using LDA-DFT, the authors attempt to calculate the formation of intrinsic defects under "vacuum-based" and "solution-based" growth environments by setting the chemical potential limits using the formation energy of Cu_2O formation for the vacuum-based and the energies of OH and H_2O as chemical potential limits for the solution-based environments.[240] This analysis yields the conclusion that the antisite defect, Cu_O, is the most stable defect under extremely acidic conditions, existing only in the Cu_O^+ state, and acting as a shallow donor.[240] *Unfortunately* this study is flawed, as it does not take into account the formation of CuO as a chemical potential limit of Cu-poor/O-rich growth conditions, and thus the Cu-poor/O-rich results are probably for an unphysical Cu_2O composition (Under these conditions CuO would be formed rather than Cu_2O). In addition, using OH and H_2O as chemical potential limits actually sets the Cu potential even further outside the chemical limit set by CuO formation, making the results highly questionable. Further to this, the study also predicts V_{Cu} to be a shallow acceptor,[240] which is completely at variance with experiment, as *p*-type Cu_2O is known to be polaronic, with deep acceptor levels[231]

H in Cu_2O Our calculations show that H does not cause shallow donor behaviour in Cu_2O as it does in many *n*-type oxides. We have, however, revealed that H in fact acts as a hole killer in Cu_2O, binding strongly into any copper vacacnies in the system, and killing any *p*-type conductivity. In the literature, annealing studies on Cu_2O samples have resulted in remarkable decreases in resistivity.[205,256] Annealing thin films of Cu_2O at 623 K has been reported to result in a decrease in resistivity by *four orders of magnitude* compared to as prepared films.[205] This decrease in resisitivity is attributed to increased crystallinity from the annealing process.[205] Onimisi has reported a decrease in resistivity of Cu_2O solar cell samples by $\sim$ 36% upon annealing at 773 K, and the higher output performance of annealed Cu_2O solar cells over that of unannealed samples.[256] Similarly $CuAlO_2$, a wide band gap transparent conducting oxide (TCO) whose defect chemistry is very similar to that of Cu_2O,[257] experiences a decrease in resistivity of three orders of magnitude upon post annealing.[258] $SrCu_2O_2$, another p-type TCO, also experiences a decrease in resistivty upon post annealing.[259]

It is surprising that these reported increases in conductivity upon post annealing have not been linked to the possible removal of H, and subsequent reactivation of acceptors in these systems, especially since H is ubiquitous in most materials. In fact H is known to passivate p-type defects in $CuInSe_2$ and $CuGaSe_2$ solar cell absorbers,[260] and can even reverse the polarity of conductivity in $CuInSe_2$.[261] In light of our results, we propose that post annealing be adopted to increase Cu_2O's p-type conductivity, as any H in the Cu_2O system will effectively act as *hole killers*, and impair device performance.

Having ruled out all the intrinsic n-type defects and the possibility of adventitious hydrogen doping as the source of n-type conductivity in Cu_2O, we must now pose the question: What is causing the n-type reports? Perhaps the best explanation for the observed n-type films of electrodeposited Cu_2O comes from an X-ray absorption fine structure (XAFS), ultraviolet spectroscopy (UPS), and Mott-Schottky electochemical impedance analysis study performed by Nian *et al.*[262] In this study, the authors found that based on the structural features obtained for their films, that strong Cu^{2+} absorption occurs on the unstable Cu deficient surface states , leading to the formation of an inversion layer which displays n-type conductivity,[262] although CuO is known to also be p-type.[230] The authors also report that *intact* Cu_2O films are p-type.[262] This theory might also explain the discrepancy between the shallower donor level reported by Garuthara and Siripala,[238] and the very deep levels seen previously.[254,255] The shallower donor level could arise from the inversion layer caused during electrodeposition.

6.10 Conclusion

In this chapter we have investigated p-type defects in Cu_2O using both PBE, PBE+U and HSE and find that copper vacancies are the most stable defects under all conditions with all three methods. Neither PBE or PBE+U can accurately reproduce the polaronic nature of defects Cu_2O, with the single particle levels for V_{Cu} delocalized and crossing the Fermi level using both methods, inconsistent with the experimentally known activated hopping mechanism. PBE and PBE+U calculated transition levels for all the p-type defects investigated cannot reproduce the deep hole trap levels as seen in previous DLTS experiments. While the PBE+U description of the single particle levels for V_{Cu}^{split}, O_i^{tet} and O_i^{oct} are improved compared to the PBE descriptions, the calculated transition levels are not in keeping with experimental results. We conclude that both PBE and PBE+U are unsuitable methods for modeling p-type defects in Cu_2O. Using the HSE screened hybrid functional, we assign the two trap levels reported in DLTS studies of Cu_2O to the $\epsilon(0/-)$ transition levels of V_{Cu} and V_{split}. The polaronic nature of Cu_2O is correctly described for the first time in a DFT study, with relatively deep single-particle levels found for *all* p-type defects. This can help explain the poor performance of Cu_2O thin-film solar cells; these deep acceptor levels will pin the Fermi level in the band gap, resulting in the extremely low open circuit voltages of 0.0–0.4 eV observed[263,264].

Hybrid DFT thus reveals a qualitatively different description for defect properties in Cu_2O compared to PBE and PBE+U, which fully explains the nature of the experimentally observed hole traps. Furthermore, since conduction in Cu^I-based TCOs is thought to be similarly polaronic[60,61,166], it is likely that hybrid functionals will be necessary for modeling these materials. This new understanding of localized behaviour in these Cu^I-based materials should serve as a guide to theoreticians and experimentalists alike who treat Cu^I-based oxide materials as classical semiconductors.

In Section 6.8 we have demonstrated that intrinsic donor defects and unintentional hydrogen incorporation *cannot* be the source of n-type conductivity in *undoped* Cu_2O

thin films. It is likely that the *n*-type conductivity reported in the literature stems from an inversion layer formed during electrodeposition, or from some external impurity (e.g. Cl doping[265]). If increased efficiency Cu_2O homojunctions for widespread PV applications are to be realized, it is clear that extensive research into the defect chemistry of these reported *n*-type samples is warranted. A thorough understanding of these surface modifications could be used to overcome intrinsic conductivity limits.

We have also revealed the quasi-atomic nature of H_i^{tet} in the Cu_2O crystal structure, and that contrary to most oxides and nitrides, H_i in stoichiometric Cu_2O does not favour formation of a H–anion bond. H passivates V_{Cu} under all growth conditions, and will therefore kill *p*-type conductivity. As H is an ever-present impurity in oxide materials, we propose that post annealing will be necessary to improve *p*-type performance of Cu_2O samples. As the defect chemistry of the Cu^{I}-based TCOs are similar to that of Cu_2O, it is expected that H will behave similarly in these materials. Thus post annealing to remove H in these materials will be necessary for increased performance.

Chapter 7

Defect chemistry of $CuAlO_2$ and $CuCrO_2$

In this chapter we examine the defect chemistry of the first reported delafossite *p*-type TCO, $CuAlO_2$ and the delafossite with the highest reported conductivity, $CuCrO_2$. For $CuAlO_2$, the differences between the experimentally observed activated conductivity and the theoretically predicted degenerate semiconducting behaviour are examined. For $CuCrO_2$ we focus on the question of the nature of the band gap, and the origin of its improved conductivity relative to other delafossite oxides.

7.1 Defect Chemistry of $CuAlO_2$

Although $CuAlO_2$ is the prototype *p*-type TCO, and is by far the most studied of the delafossite materials, some critical questions about the band structure and conductivity of this material remain unanswered. The transparency of the group 13 (B, Al, Ga, In) delafossites is made possible by forbidden transitions at the Γ and Z points, with allowed transitions only occurring at the F and L points.[122] with the optically allowed direct band gap (E_g^{dir}) for $CuAlO_2$ at the L point. Experimentally, the *optical* band gap of $CuAlO_2$ has been reported in the range 3.3 – 4.2 eV[12,266,267], however, the main source of controversy in the literature has been the positioning of the indirect band gap (E_g^{ind}), with different studies proposing E_g^{ind} in the range 1.65 – 2.99 eV.[267,268] It has recently been postulated that the reported E_g^{ind} in the range $1.65 - 2.10\,\mathrm{eV}$ are not E_g^{ind} at all, but are actually signals from defects.[267,268] The absorptions commonly attributed to these E_g^{ind} possess optical absorption coefficients that are in excess of two orders of magnitude larger than typical indirect absorption edges.[267] Most theoretical studies predict the E_g^{ind} to be much less than $1\,\mathrm{eV}$ smaller than that of the E_g^{dir} at L, [269] and not $\sim 1.40 - 1.85\,\mathrm{eV}$ smaller as some experiments have observed.

The source of hole carriers in $CuAlO_2$, and indeed the conductivity mechanism itself is also a matter of much debate. Many theoretical studies have been undertaken to understand defects and conductivity in delafossite materials.[57,270] However, in *all* of these studies the GGA or LDA methodologies have been used, which have been shown to be unable to accurately model *p*-type defects in $\mathrm{Cu^{I}}$-based oxide materials, Chapter 6 In *all* cases Cu vacancies (V_{Cu}) were reported to be the defect with the lowest formation energy, and therefore linked to any intrinsic conductivity in these systems. [57,270] Tellingly, these GGA/LDA studies[57,270] found that the formation of V_{Cu} in these systems was *spontaneous* (with energies $\Delta H_{\mathrm{f}}(\mathrm{D}, 0) < 0\,\mathrm{eV}$), and with transition levels (TLs) *inside* the valence band, indicating degenerate semiconducting behaviour. This is clearly at variance with experimental observations that delafossite materials conduct through activated *polaronic* hopping mechanisms,[60,61,166] or through activated band conduction from a deep TL 700 meV above the VBM.[268]

The general consensus from both experiment and theory has been that V_{Cu} is the dominant defect, followed by oxygen interstitials, $\mathrm{O_i}$.[57,270] Intriguingly, Mason and co-workers have postulated that the defect responsible for conductivity at high temperature in $CuAlO_2$ is not V_{Cu}, but a defect cluster of an Al on a Cu site bound to two oxygen interstitials, $[\mathrm{Al}_{\mathrm{Cu}}^{\bullet\bullet} + 2\mathrm{O}_{\mathrm{i}}'']''$.[60] This defect has *never* been investigated theoretically.

In this section, we present a hybrid-DFT examination of the electronic structure and energetics of intrinsic defects in $CuAlO_2$. We report: (i) the dominant defects under all growth condition are $\mathrm{Cu_{Al}}$ and V_{Cu}, and not $[\mathrm{Al}_{\mathrm{Cu}}^{\bullet\bullet} + 2\mathrm{O}_{\mathrm{i}}'']''$, (ii) we find deep TLs for all *p*-type defects, consistent with the experimentally known activated conductivity and (iii) we identify the defect that give rise to the signals often mistaken as the E_g^{ind} of $CuAlO_2$.

7.1.1 Theoretical Section

All calculations in this section were performed using HSE06[99] within the VASP code.[271] Interactions between the cores (Cu:[Ar], Al:[Ne] and O:[He]) and the valence electrons were described using the PAW method[110]. A planewave cutoff of 500 eV and *k*-point sampling of 8×8×8 for rhombohedral $CuAlO_2$ were used, and the structure was deemed to be converged when the forces on all the atoms were less than 0.01 eV Å^{-1}. Defects were calculated in a 3×3×1 (108 atom) expansion of the twelve atom hexagonal representation of the rhombohedral unit cell, all calculations were spin polarized. Corrections to the defect formation energies to take account of finite size effects were performed using the approach of Freysoldt *et al.*[134], as outlined in Correction method 2 of Section 3.4.2

7.1.2 Thermodynamic stability of $CuAlO_2$.

Varying the chemical potentials, μ_i in Equation 3.9, relates to varying the partial pressures experimentally. They can thus be used to set the different conditions under which $CuAlO_2$ may form, and determine the optimum conditions for defect formation, within the global constraint of the calculated enthalpy of the host, in this instance $CuAlO_2$: $\mu_{\mathrm{Cu}} + \mu_{\mathrm{Al}} + 2\mu_{\mathrm{O}} = \Delta H_{\mathrm{f}}^{\mathrm{CuAlO_2}} = -8.92\,\mathrm{eV}$. To avoid precipitation into solid elemental Cu, Al and O_2 gas we also require: $\mu_{\mathrm{Cu}} \leq 0$, $\mu_{\mathrm{Al}} \leq 0$, and $\mu_{\mathrm{O}} \leq 0$. The chemical potentials are further constrained by the decomposition of $CuAlO_2$ into binary compounds: $\mu_{Cu}+\mu_O \leq \Delta H_{\mathrm{f}}^{\mathrm{CuO}} = -1.40\,\mathrm{eV}$, $2\mu_{Cu}+\mu_O \leq \Delta H_{\mathrm{f}}^{\mathrm{Cu_2O}} = -1.55\,\mathrm{eV}$ and $2\mu_{Al} + 3\mu_O \leq \Delta H_{\mathrm{f}}^{\mathrm{Al_2O_3}} = -16.09\,\mathrm{eV}$, and the competing ternary phase $CuAl_2O_4$: $\mu_{\mathrm{Cu}} + 2\mu_{\mathrm{Al}} + 4\mu_{\mathrm{O}} \leq \Delta H_{\mathrm{f}}^{\mathrm{CuAl_2O_4}} = -16.74\,\mathrm{eV}$. Previous DFT defect studies of the delafossites have failed to take the formation of CuO into account, meaning their Cu-poor regimes were probably for an unphysical composition.[57,270,272]

The HSE06 calculated accessible range of chemical potentials for $CuAlO_2$ is illustrated in Figure 7.1, in a two-dimensional (μ_{Al}, μ_{Cu}) plane, following the approach of Walsh *et al.*[273] and Person *et al.*[274] The vertices of the stability triangle are formed from the host condition ($\mu_{\mathrm{Cu}} + \mu_{\mathrm{Al}} + 2\mu_{\mathrm{Al}} = \Delta H_{\mathrm{f}}^{\mathrm{CuAlO_2}}$), giving the limits of Cu/Al rich, Cu poor and Al poor environments. Taking into account the constraints imposed by the competing binary oxides, and the spinel $\Delta H_{\mathrm{f}}^{\mathrm{CuAl_2O_4}}$ phase, the stable range of μ_{Al}, μ_{Cu} for $CuAlO_2$ is shaded grey in Figure 7.1. The region under which $CuAlO_2$ forms corresponds to relatively Cu-rich, Al-poor and O-rich conditions.

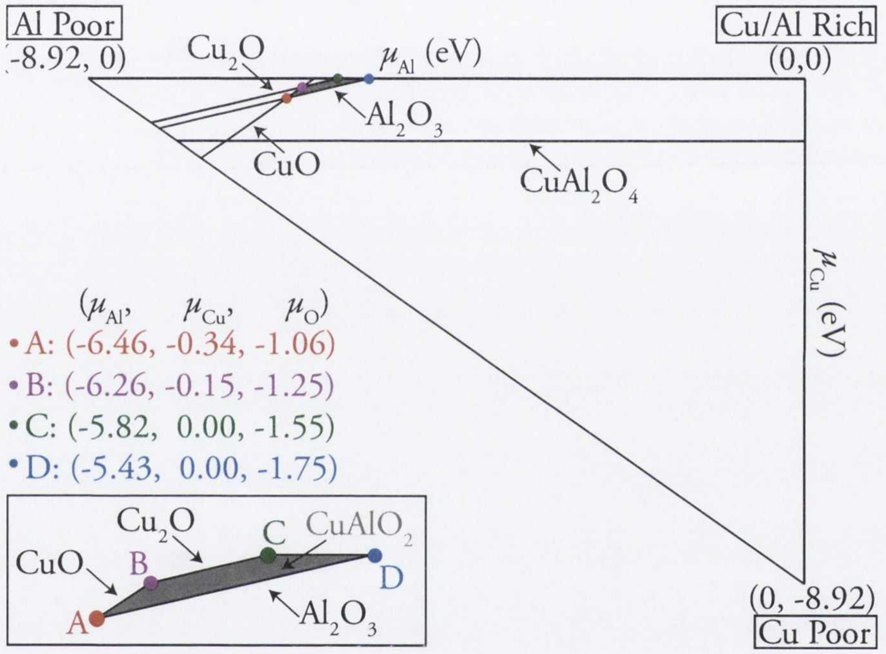

Figure 7.1: Illustration of the accessible (μ_{Al}, μ_{Cu}) chemical potential range. The triangle vertices are determined by the formation enthalpy of $CuAlO_2$. Limits imposed by the formation of competing binary oxides result in the stable region shaded grey. The chosen environments are indicated by the red, pink, green and blue spheres respectively.

Within these boundaries, we considered four environments, A to D as indicated on Figure 7.1. Condition A corresponds to Al-poor, Cu-poor and O-rich conditions. Environment B is at the Al-poor limit, with μ_{Cu} and μ_{O} having mid-range values, with condition C corresponding to the Cu-rich limit of the stability region, with a mid range μ_{Al} and a relatively low μ_{O}. Lastly, environment D represents Al-rich, O-poor and Cu-rich limits, which should favour the formation of oxygen poor (or n-type) defects.

7.1.3 Band structure features.

The HSE06 calculated band structure is shown in Figure 7.2, and possesses features consistent with previous theoretical bandstructures.[58] The CBM occurs at the Γ point, with the VBM situated at F. The $\mathrm{E}_g^{\mathrm{dir}}$ at the L point is 4.08 eV, while the corresponding $\mathrm{E}_g^{\mathrm{ind}}$ is 3.52 eV. Therefore our calculated $\mathrm{E}_g^{\mathrm{dir}}$ is within the experimental range of optical band gaps, and is consistent with previous HSE06 calculations.[269] Our HSE06 bandgap is however much larger than the PBE+U calculated band gap for $2H$ $CuAlO_2$, which yielded an $\mathrm{E}_g^{\mathrm{dir}}$ of 3.10 eV and an $\mathrm{E}_g^{\mathrm{dir}}$ of 2.20 eV (Chapter 4). The difference between the $\mathrm{E}_g^{\mathrm{dir}}$ and $\mathrm{E}_g^{\mathrm{ind}}$ is for our HSE06 calculated band structure is only 0.56 eV. It has been noted previously that as the level of theory utilized to compute the band gap of $CuAlO_2$ is increased, $E_g^{\mathrm{dir}} - E_g^{\mathrm{ind}}$ decreases,[269] and this trend matches our results on going from PBE+U to HSE06. Our HSE06 calculated results, in agreement with previous theory results, indicate that the absorption signals assumed to be $\mathrm{E}_g^{\mathrm{ind}}$ in the range 1.65 – 2.10 eV are unlikely to be a property of *stoichiometric* $CuAlO_2$, and may stem from defect signals.

7.1.4 Defect energetics and ionization levels.

The formation energies in the neutral charge state ($\Delta H_{\mathrm{f}}(\mathrm{D}, 0)$) of the intrinsic defects investigated in $CuAlO_2$ at the four different environments are shown in Table 7.1. It is clear that environment A (Cu-poor/Al-poor/O-rich) is the most favourable for p-type defect formation, as the lowest energy for p-type defects such as V_{Cu}, $\mathrm{Cu}_{\mathrm{Al}}$ and O_i occur in this environment, and therefore should be adopted to maximise the intrinsic p-type nature of these materials. It is also interesting to note that V_{Cu} and $\mathrm{Cu}_{\mathrm{Al}}$ will dominate under all growth conditions, and that the defect complex proposed by Mason and co-workers[60] possesses a large formation energy under all conditions, making it unlikely

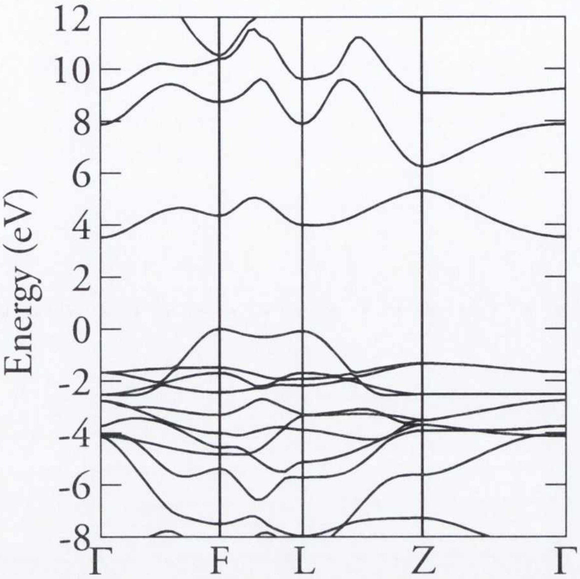

Figure 7.2: HSE calculated band structure of rhombohedral $CuAlO_2$.

to play any part in *p*-type conductivity in this system.

In their study of both high-temperature solid state (SS) synthesized and low-temperature hydrothermally (HT) synthesized $CuAlO_2$, Mason and co-workers[60] found the ratio of Cu/Al to be 0.96 for the SS and 0.86 for the HT, meaning that Al was in excess. The authors performed structure refinements using XRD and concluded that the model that produced the best fit to their experiments was Al substitution at Cu sites and oxygen interstitials. From the fact that Al_{Cu} is a donor defect (and the samples were *p*-type), and that Al prefers a higher coordination than the linear coordination of the Cu site, the authors proposed a defect complex of Al_{Cu} with two oxygen interstitials bound to it in a pseudo-tetrahedral manner. Figure 7.3 illustrates the lowest energy configuration for $[Al_{Cu}^{\bullet\bullet} + 2O_i'']''$ as calculated using HSE06, and shows the two bound hole states which are localized mainly on the four Cu atoms bonded to the two oxygen interstitials. The holes are mainly composed of Cu 3*d* states. Our calculations indicate that the formation energy for such a complex is very large (6.06 eV), but the binding energy for the complex (the difference between the formation energies of $[Al_{Cu}^{\bullet\bullet} + 2O_i'']''$ and the formation energies of the constituent defects Al_{Cu} + $2O_i$) is also very large at 7.45 eV, indicating that O_i would be attracted to Al_{Cu} if it forms. It is thus plausible

Table 7.1: HSE06 calculated formation energy of intrinsic defects $CuAlO_2$ at the four environments specified in 7.1 All energies are quoted in eV.

Defect	A	B	C	D
V_{Cu}	1.33	1.52	1.67	1.67
V_{O}	4.45	3.73	4.20	3.85
V_{Al}	4.13	4.33	4.77	5.16
$\mathrm{Cu}_{\mathrm{Al}}$	1.25	1.25	1.55	1.94
$\mathrm{Al}_{\mathrm{Cu}}$	7.33	7.33	7.03	6.65
O_i	3.09	3.29	3.44	3.78
Cu_i	5.25	5.06	4.91	4.91
$[\mathrm{Al}_{\mathrm{Cu}}^{\bullet\bullet} + 2\mathrm{O}_{\mathrm{i}}'']''$	6.06	6.45	6.93	6.74

that this defect complex could form during synthesis and be trapped due to its high binding energy.

A plot of formation energy as a function of Fermi-level position is shown in Figure 7.4 for all intrinsic defects in the Cu-poor/Al-poor regime. The first point to note is that the formation energy of V_{Cu} and the $\mathrm{Cu}_{\mathrm{Al}}$ antisite are substantially lower in energy than all other defects, with the $\mathrm{Cu}_{\mathrm{Al}}$ slightly more energetically favourable. The (0/-1) TL for V_{Cu} at 0.68 eV is in excellent agreement with the experimentally reported TL of 0.70 eV[268], and is a significant improvement on previous GGA/LDA TLs (-0.33eV and -0.40eV).[57,270] O_i and V_{Al} are much higher in energy, and possess deeper TLs than V_{Cu}, indicating that they will not play a major role in any conductivity. The formation energy of the $[\mathrm{Al}_{\mathrm{Cu}}^{\bullet\bullet} + 2\mathrm{O}_{\mathrm{i}}'']''$ defect complex as proposed by Mason and co-workers[60] is 6.06 eV, and its (0/-1) TL is 1.83 eV above the VBM, meaning it is unlikely to ever be a source of conductivity in $CuAlO_2$.

The formation energies of compensating *n*-type defects are also very high, with V_{O} being stable only in the neutral and +2 charge states (making it a negative U type defect), with the (+2/0) TL very deep (2.70 eV below the CBM). Cu_i has a large

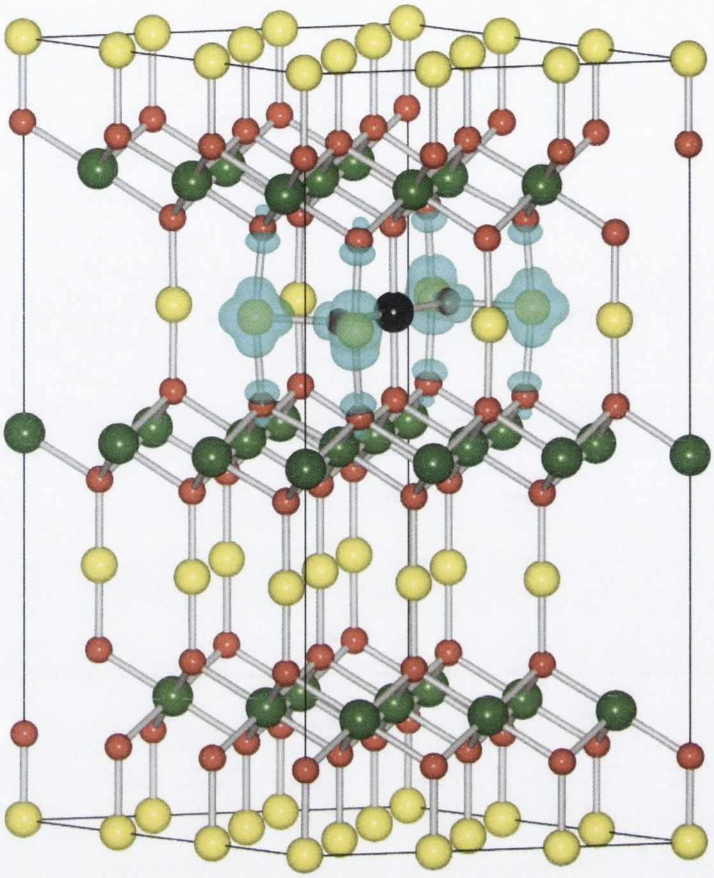

Figure 7.3: The lowest energy $[\mathrm{Al}^{\bullet\bullet}_{\mathrm{Cu}} + 2\mathrm{O}''_{\mathrm{i}}]''$ cluster configuration calculated with HSE06. Yellow, green and red spheres indicate copper, aluminium and oxygen atoms respectively. The Al on a Cu site is indicated with a black sphere, and is in its "pseudo-tetrahedra" coordination. The spin density isosurface is set to $0.05\,\mathrm{e\,\AA}^{-3}$..

formation energy with relatively deep (+1/0) TL, and the formation energy of the $\mathrm{Al_{Cu}}$ antisite is extremely high in energy. These results indicate that *p*-type defects will dominate under Cu-poor/Al-poor conditions, and indeed under all growth conditions (see Supporting Information).

7.1.5 Optical Transition Levels

In Figure 7.5 we compare the experimentally reported optical absorptions signals and proposed E_g^{ind} signals to the HSE06 calculated optical transition levels (OTLs) as calculated using the formalism as outlined in Section 3.4.4. The calculated (0/-1) OTL

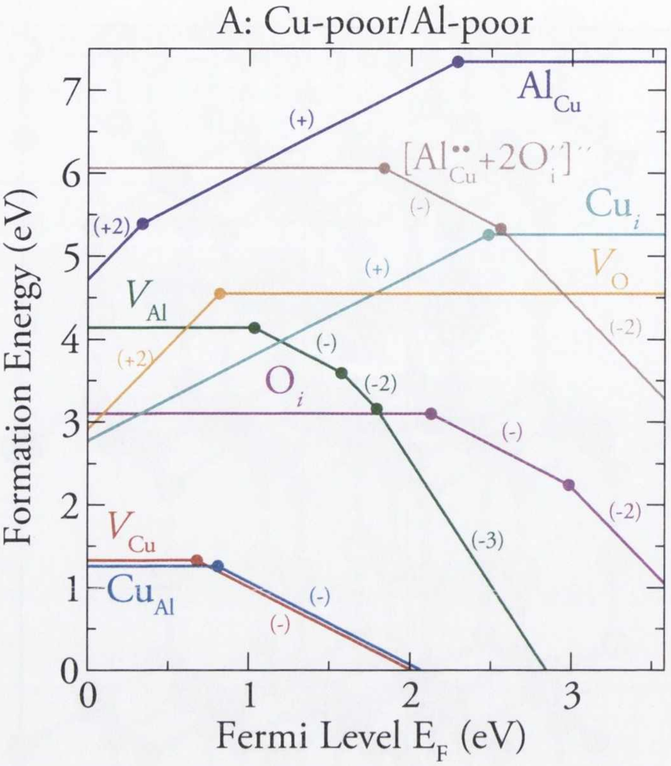

Figure 7.4: HSE06 calculated formation energies for intrinsic defects in $CuAlO_2$ as a function of Fermi energy under Cu-poor/Al-poor conditions. The solid dots denote the transition levels $\epsilon(q/q')$.

for V_{Cu} is found to be 0.87 eV, with the (0/-1) OTL for $\mathrm{Cu}_{\mathrm{Al}}$ at 1.73 eV, which are the two defects with the lowest formation energies, and therefore the defects most likely to be observed in optical absorption experiments. The weak absorptions noted in the most recent study by Tate *et al.*[268] at 0.85 eV and 1.75 eV, and in the study by Pellicer-Porres *et al.*[267] at 0.9 eV and 1.8 eV, are in excellent agreement with the (0/-1) OTL of V_{Cu} and the (0/-1) OTL for $\mathrm{Cu}_{\mathrm{Al}}$. The (0/-1) OTL of $\mathrm{Cu}_{\mathrm{Al}}$ is significantly deeper than its (0/-1) TL, as the adiabatic TL includes lattice relaxation, which in this case is large. V_{Cu}, however, does not experience a large relaxation, and thus the OTL and TLs for V_{Cu} are much closer in energy. As regards the often quoted indirect band gaps ranging from 1.65 – 2.10 eV, the only calculated optical signals in that region are the (0/-1) OTL of $\mathrm{Cu}_{\mathrm{Al}}$. Therefore we tentatively assign the reported indirect band gaps in this range to the (0/-1) $\mathrm{Cu}_{\mathrm{Al}}$ OTL. The 0TLs for the $[\mathrm{Al}_{\mathrm{Cu}}^{\bullet\bullet}+2\mathrm{O}_{\mathrm{i}}'']''$ should appear at

1.83 eV and 2.56 eV, but as the formation energy of this cluster is so high, it is unlikley they would be observed.

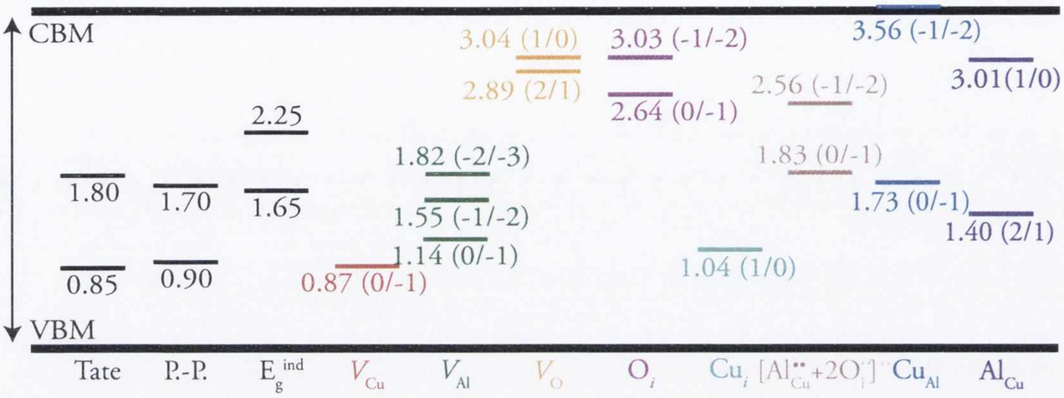

Figure 7.5: HSE06 calculated optical transition levels for native defects in $CuAlO_2$.

7.2 p-type Defects in $CuCrO_2$

It is well known that doping the trivalent metal site in the delafossite structure with a divalent dopant significantly improves the conductivity[13], but the conductivity trends seen for different trivalent metal cations have remained contentious. Nagarajan *et al.* attempted to explain the trend in increasing conductivity of $CuY_{1-x}Ca_xO_2$ to $CuSc_{1-x}Mg_xO_2$ to $CuCr_{1-x}Mg_xO_2$ by noting that the increasing conductivity tracks a decreasing ionic radius of the M^{III} cation, and hence a decreasing lattice paramater in the Cu ion plane.[55] They suggest that this leads to increased Cu *d* orbital overlap and as a result better hole mobility. This size dependence theory can effectively be ruled out by the observed conductivity of $CuAl_{1-x}Mg_xO_2$, which at $4\,x\,10^{-4}\,S\,cm^{-1}$ has a much lower conductivity than that of $CuCr_{1-x}Mg_xO_2$ ($220\,S\,cm^{-1}$), despite the ionic radius of Al being smaller than Cr.[51]

Sleight and co-workers have discussed the effect of the M^{III} ion on the mobility of holes in p-type delafossites.[141] The authors suggest that the lower hole mobilities in p-type delafossites relative to Cu_2O may be caused by the lack of Cu–O–Cu linkages as seen in Cu_2O. In the delafossite structure there are only Cu–O–M^{III}–O–Cu linkages.

The authors suggest that the higher conductivities observed for $CuCrO_2$ and $CuFeO_2$ may be due to favourable mixing with the *3d* states on the M^{III} cation in the Cu–O–M^{III}–O–Cu linkages.[141] In Chapter 4 we proposed that in $CuCrO_2$, the Cr 3*d* states appear in the valence band and mix with the O 2*p*, and that this increased covalency in the system leads to increased hole mobility.

Very recently, $CuCrO_2$ has attracted attention for a range of applications other than TCO applications. In the condensed matter physics community, $CuCrO_2$ has been investigated for its unusual magnetic properties, due to its frustrated antiferromagnetic ordering and multiferroic properties.[151,275–284] It has generated interest due to its catalytic abilities in hydrogenation reactions,[285] its ozone sensing properties,[286,287] and as a possible thermoelectric material.[288,289] $CuCrO_2$ has also been identified as a possible photocatalyst for hydrogen evolution,[290] NO_2^-[291] and NO_3^-[292] removal, and removal of M^{2+} cations (M = Ni, Cu, Zn, Cd, Hg).[293]

The nature of the band gap of $CuCrO_2$ has been a source of controversy in the literature, with some experimental studies reporting an indirect band gap,[294–296] and others finding $CuCrO_2$ to be a direct band gap semiconductor.[297] The earliest recorded measurement of the band gap of $CuCrO_2$ was carried out by Benko and Koffyberg,[294] who found that it possessed an indirect band gap of 1.28 eV, with an indirect *allowed* transition at 3.08 eV and a direct allowed transition at 3.35 eV. A further interband transition at $\sim$ 2.20 eV was noted, although the authors were not able to determine the transition type.[294] In general, recent optical measurements have found the *direct* optical band gap to be in the range 2.95 – 3.30 eV, meaning $CuCrO_2$ is transparent to visible light.[55,298–303]

Rastogi *et al.* have recently reported for 155 nm (305 nm) thick, spray deposited thin films for Mg-doped $CuCrO_2$, indirect band gaps of 2.58 eV (2.79 eV) and direct band gap of 3.08 eV (3.14 eV).[295] Mahapattra and Shivashanhar have also reported thin films of $CuCrO_2$ formed using chemical vapour deposition to possess an indirect band gap of 2.63 eV and a direct band gap of 3.08 eV.[296] Conversely, Li *et al.* have reported that no indirect band gap exists in their $CuCrO_2$ thin films prepared by pulsed laser deposition, with the *fundamental* band gap being direct and measuring 3.20 eV.[297]

Undoped $CuCrO_2$ is a semi-conductor with a high resistivity (although its resistivity is lower than that of $CuAlO_2$), however, substitution of divalent dopants (e.g. Mg, Ca, Ni) for trivalent Cr in this system leads to a marked increase in conductivity. [55,275,276,284,289,299,304] This increase in conductivity has been linked to both Cu^{I}/Cu^{II}, [162,305] and to Cr^{III}/Cr^{IV} hole mechanisms.[288] All other delafossites are thought to conduct via the Cu^{I}/Cu^{II} mechanism[58–61,166,294,306], and recent high resolution x-ray photoelectron spectroscopy (XPS) studies in conjunction with GGA+U calculations have shown that Cu states dominate at the VBM, indicating the likelihood of a copper hole mechanisms.[152] GGA calculations have, however, indicated that Cr states dominate at the VBM, and in conjuction with magnetoresistance studies, this was reported to indicate a Cr^{III}/Cr^{IV} mechanism.[150]

In this section we address two main questions about the fundamental chemistry/physics of $CuCrO_2$: (a) What is the nature of the band gap of $CuCrO_2$?, and (b) what is the conductivity mechanism of $CuCrO_2$, do holes exist on the Cu or the Cr states? Using PBE, PBE+U and the screened hybrid functional HSE06, we investigated the band structure of $CuCrO_2$, and investigate three p-type defects in $CuCrO_2$, namely copper vacancies (V_{Cu}), oxygen interstitials (O_i), and Mg dopants on a Cr lattice site (Mg_{Cr}). We show: (i) PBE+U and HSE06 predict that the states that dominate at the VBM are Cu 3d states, consistent with previous XPS experiments,[152] with GGA providing a very poor description of the location of both the Cu and Cr 3d levels, (ii) with all three approaches, $CuCrO_2$ is found to possess an indirect band gap, (iii) V_{Cu} is the dominant *intrinsic* p-type defect in $CuCrO_2$, (iv) Mg_{Cr} defect formation energies are lower than intrinsic p-type defect energies under all growth conditions, and (v) acceptor defects in $CuCrO_2$ form holes on the Cu d states, and not on the Cr d states as had previously been proposed. In light of these results we discuss the increased conductivity of $CuCrO_2$ relative to other delafossite TCOs.

7.2.1 Theoretical Methods

All calculations were performed using the VASP code,[153] with the projector augmented wave (PAW) approach.[111] The calculations were performed using PBE, PBE+U (U_{Cu_d} = 5.2 eV, U_{Cr_d} = 4.0 eV), and HSE06. Interactions between the cores (Cu:[Ar], Cr:[Ar] and O:[He]) and the valence electrons were described using the PAW method[110]. While the exotic magnetic interactions in $CuCrO_2$ are of much interest,[151,275–284] reproducing these interactions is not feasible with the large supercells and computationally expensive methods used in this study. Therefore, we employed a simplified antiferromagentic (AF) ordering for our calculations, consisting of planes of ferromagnetically ordered Cr states, with AF layer–layer interactions (taken from PBE+U test calculations). We considered only the hexagonal (Space group $P_{63}mmc$, #194) polymorph of $CuCrO_2$ to allow us to simulate the known AF ordering within the unit cell.

In each method we minimized the bulk $CuCrO_2$ using the constant volume approach, as outlined in Section 3.2. A plane wave cutoff of 400 eV and k-point sampling of $4\times4\times1$ found to be sufficient for each method, however we have used a k-point sampling of 9×9×5 for our density of states calculations . The structure was deemed to be converged when the forces on all the atoms were less than 0.01 eV Å^{-1}. As $CuCrO_2$ contains open-d shells Cr atoms, all calculations were spin polarized. Defects were calculated in a $4\times4\times1$ (128 atom) supercell, and structure visualization and analysis were performed using VESTA[159]. Defect energetics were calculated using the same approach used for the $CuAlO_2$ defects in the preceeding section.

Equilibrium Structures

The PBE, PBE+U and HSE06 calculated structures for hexagonal $CuCrO_2$ are shown in Table 7.2. The PBE calculated lattice parameters are overestimated compared to experiment, but this is a known overestimation of the GGA method.[307] PBE+U overestimates the a lattice parameter by more than the PBE, but has an improved c parameter. Minimization with HSE06 yields a c parameter that is in excellent agreement with experiment,[308], but with an overestimated a parameter. Overall, HSE06 yields the closest lattice parameters to experiment, which is not surprising, as the HSE06 functional regularly yields structural information that is more accurate than standard DFT methods.

Table 7.2: Structural data and nearest-neighbour interatomic distances for the optimized PBE, PBE+U and HSE06 optimized $CuCrO_2$ structures, compared to experimental data.[?] . Volumes are given in Å^3 and lattice dimensions and interatomic distances in Å.

	PBE	PBE+U	HSE06	Expt.[308]
a	3.01	3.05	3.01	2.97
c	11.47	11.42	11.40	11.40
Volume	90.04	92.25	89.73	87.32
$d_{\mathrm{Cr-O}}$	2.01	2.03	2.01	1.99
$d_{\mathrm{Cu-O}}$	1.86	1.84	1.86	1.85

7.2.2 Electronic Structure

The PBE, PBE+U and HSE06 calculated band structures for hexagonal $CuCrO_2$ are shown in Figure 7.6. For all three methods, the VBM is located on the K to Γ line, near K, with the CBM found on the M-Γ line, indicating that $CuCrO_2$ is an *indirect* band gap material, and not a direct band gap materials as had been suggested previously.[297] The calculated indirect band gaps are 1.06 eV, 2.06 eV and 3.09 eV using PBE, PBE+U and HSE06 respectively. The PBE calculated band structure features are visibly different to those of the PBE+U and HSE06 band structure, possessing a much less dispersive valence band.

Upon analysis of the PBE, PBE+U and HSE06 calculated total and partial (ion decomposed) electronic densities of states (EDOS/PEDOS) for $CuCrO_2$, Figure 7.7, the reason for the flatter band structure features for the PBE band structure become apparent. In the PBE EDOS/PEDOS, the Cr 3d states dominate at the VBM and the

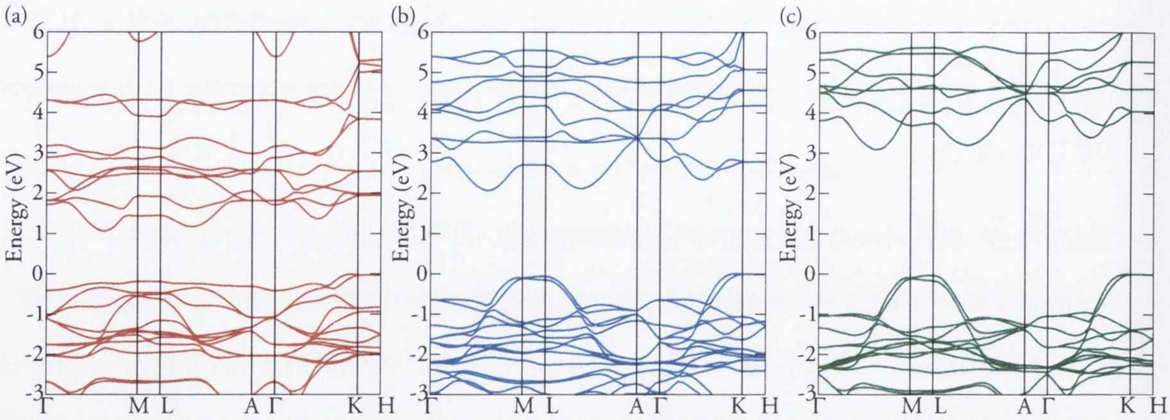

Figure 7.6: (a) PBE, (b) PBE+U and (c) HSE06 calculated band structures for $CuCrO_2$

CBM, whereas in the PBE+U and HSE06 EDOS/PEDOS, the Cr 3d states are pushed to lower energies relative to the VBM, with Cu 3d states dominating at the VBM in both cases, making the valence band visibly more disperse in the band structures, Figure 7.6. The Cu 3d peak positions for both the PBE+U and the HSE06 PEDOS are situated at ~ -2.1 eV, with the Cu 3d peaks centered at ~ -1.75 eV using PBE. High resolution XPS studies have placed the Cu 3d peak at ~ -2.1 eV,[152] indicating that the HSE06 and PBE+U treatment of the known self interaction error of the Cu 3d states is probably satisfactory, but is not satisfied at all in the case of PBE. The Cr d–d splitting is appreciably increased in the PBE+U and HSE06 calculations compared to the PBE.

7.2.3 Optical analysis

The optical absorption spectra for $CuCrO_2$, calculated using PBE, PBE+U and HSE06, are shown in Figure 8.7. With PBE, and using the Tauc relation ($E_g \propto \alpha^2$), the onset of optical absorption begins at ~ 1.5 eV, which is considerably underestimated compared to the experimental range of 2.95 – 3.30 eV.[55,298–303] PBE+U provides an improved description of the optical band gap compared to experiments, with a calculated optical band gap of ~ 2.7 eV, however, this *direct* band gap is only in the range of the *indirect* band gaps reported in experiment. The HSE06 optical band gap is calculated to be

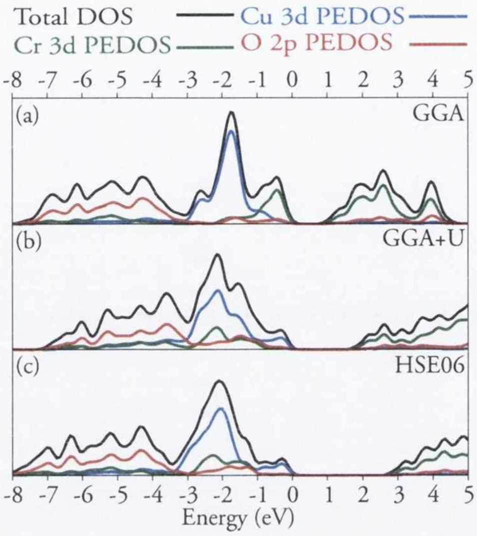

Figure 7.7: Electronic density of states for $CuCrO_2$ calculated using (a) PBE, (b) PBE+U and (c) HSE06. The total DOS, Cu d, Cr d and O $2p$ states are colored black blue, green and red, respectively.

$\sim$ 3.75 eV, which is an overestimation of $\sim$ 0.45 eV over the largest experimentally reported optical band gaps for $CuCrO_2$. In line with these findings, hybrid functionals has been shown recently to overestimate the band gaps of some transition metal containing ternary oxide systems.[100]

Fitting exchange to the band gap is an often-used correction when the hybrid function of choice does not yield the expected band gap,[186,249] however, in this case there are too many uncertainties about the exact indirect and direct band gaps of $CuCrO_2$, so we have not attempted any "exchange fitting" in this case. The earliest study of the opto-electronic properties of $CuCrO_2$ by Benko and Koffyberg[294] had reported an indirect band gap of only 1.28 eV. The same authors also studied $CuAlO_2$,[306] and consistent with many other studies[267] reported an indirect band gap of 1.65 eV for $CuAlO_2$. Recent experiments[267,268] and calculations[269,309] have called into question the validity of these "indirect band gap" signals in $CuAlO_2$, and postulate that they stem from defect absorptions, as the absorptions commonly attributed to these E_g^{ind} possess optical absorption coefficients that are in excess of two orders of magnitude larger than typical indirect absorption edges.[267] A thorough re-investigation of the exact nature of the band gap of $CuCrO_2$ is thus warranted.

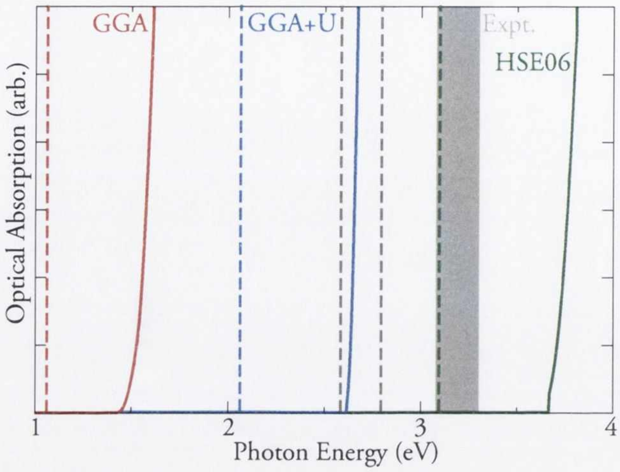

Figure 7.8: Calculated optical absorption spectra of $CuCrO_2$ summed over all possible direct valence to conduction band transitions. PBE (red) PBE*U* (blue), HSE06 (green) and Experiment (grey). Dashed lines indicate indirect band gaps, solid lines indicate optical absorptions.

7.2.4 Thermodynamic stability of $CuCrO_2$

By varying the chemical potentials, μ_i, we can simulate the effect of varying the partial pressures experimentally, setting the conditions under which $CuCrO_2$ forms. In this way, we can determine the optimum conditions for *p*-type defect formation, within the constraint of the calculated enthalpy of the host: $\mu_{\mathrm{Cu}}+\mu_{\mathrm{Cr}}+2\mu_{\mathrm{O}} = \Delta H_{\mathrm{f}}^{\mathrm{CuCrO_2}}$. To avoid precipitation into solid elemental Cu, Cr and O_2 gas we also require: $\mu_{\mathrm{Cu}} \leq 0, \mu_{\mathrm{Cr}} \leq 0, \mu_{\mathrm{O}} \leq 0$. The chemical potentials are further constrained by the decomposition of $CuCrO_2$ into binary compounds: $\mu_{Cu} + \mu_{O} \leq \Delta H_{\mathrm{f}}^{\mathrm{CuO}}$, $2\mu_{Cu} + \mu_{O} \leq \Delta H_{\mathrm{f}}^{\mathrm{Cu_2O}}$ and $2\mu_{Cr} + 3\mu_{O} \leq \Delta H_{\mathrm{f}}^{\mathrm{Cr_2O_3}}$. A boundary is also imposed when Mg doping, as we want to avoid the formation of MgO: $\mu_{Mg} + \mu_{O} \leq \Delta H_{\mathrm{f}}^{\mathrm{MgO}}$. The PBE, PBE+U and HSE06 calculated formation energies of the oxides considered are given in Table 7.3.

The phase diagram for $CuCrO_2$ can be drawn up as in Figure 7.9 which indicates the range of chemical potentials under which $CuCrO_2$ forms, calculated using

Table 7.3: Formation enthalpies of $CuCrO_2$ and the relevant binaries calculated using PBE, PBE+U and HSE06 and comparison with experiment. Formation energies are given in eV/formula unit

Structure	PBE	PBE+U	HSE06	Expt.[310]
Cu_2O	-1.23	-1.55	-1.55	-1.73
CuO	-1.18	-1.36	-1.40	-1.61
Cr_2O_3	-9.99	-10.64	-11.64	-11.69
MgO	-3.97	-5.51	-5.74	-6.24
$CuCrO_2$	-5.70	-6.33	-6.85	–

HSE06. The triangle vertices correspond to Cr/O-rich conditions ($\mu_{Cr} = \mu_O = 0.00$, $\mu_{Cu} = -6.85$), Cu/O-rich conditions ($\mu_{Cr} = -6.85$, $\mu_{Cu} = \mu_O = 0.00$) and Cu/Cr-rich conditions ($\mu_{Cr} = \mu_{Cu} = 0.00$ $\mu_O = -3.43$) and are calculated directly from $\mu_{\mathrm{Cu}} + \mu_{\mathrm{Cr}} + 2\mu_{\mathrm{O}} = \Delta H_{\mathrm{f}}^{\mathrm{CuCrO_2}} = -6.85\,\mathrm{eV}$. The boundaries for binary phase formation are then calculated from the binary equations. This results in a narrow range of chemical potentials under which $CuCrO_2$ is thermodynamically stable. Within these boundaries we explicitly consider four conditions, as marked in Figure 7.9. Enviornment A in Figure 7.9, corresponds to Cr-poor, Cu-poor and O-rich conditions. Environment B is at the Cr-poor limit, with μ_{Cu} and μ_{O} having mid-range values, with condition C corresponding to the Cu-rich limit of the stability region, with a mid range $\mu_{\mathrm{Cr}}$and a relatively low μ_{O}. Lastly, environment D represents Cr-rich, O-poor and Cu-rich limits, which should favour the formation of oxygen poor (or n-type) defects. This analysis was repeated using PBE and PBE+U, with the corresponding chemical potential limits for each method in each environment shown in Table 7.4.

7.2.5 Defect energetics and transition levels.

Table 7.5 lists the neutral formation energies of the different p-type defects under the four differing growth conditions for PBE, PBE+U and HSE06. It is clear that the

	PBE			PBE + U			HSE06		
	μ_{Cr}	μ_{Cu}	μ_O	μ_{Cr}	μ_{Cu}	μ_O	μ_{Cr}	μ_{Cu}	μ_O
A	-3.65	-0.34	-0.86	-4.24	-0.65	-0.71	-4.72	-0.67	-0.73
B	-3.39	-0.06	-1.23	-3.79	-0.19	-1.17	-4.20	-0.15	-1.25
C	-3.24	0.00	-1.23	-3.22	0.00	-1.55	-3.75	0.00	-1.55
D	-2.66	0.00	-1.52	-2.29	0.00	-2.02	-2.72	0.00	-2.07

Table 7.4: The PBE, PBE+U and HSE06 calculated chemical potentials at the four chemical potential limits imposed by the formation of competing binary oxides for $CuCrO_2$, as indicated in 7.9. All energies are given in eV.

formation energies are lowest for environment A (Cu-poor/Cr-poor/O-rich), and as such these conditions should be enforced to maximise p-type performance of undoped and acceptor doped $CuCrO_2$ samples.

	PBE			PBE + U			HSE06		
	V_{Cu}	O_i	Mg_{Cr}	V_{Cu}	O_i	Mg_{Cr}	V_{Cu}	O_i	Mg_{Cr}
A	0.16	1.27	-0.54	0.95	1.38	0.46	1.45	1.63	0.62
B	0.45	1.54	-0.54	1.41	1.85	0.46	1.97	2.15	0.62
C	0.50	1.65	-0.50	1.60	2.23	0.65	2.12	2.45	0.77
D	0.50	1.94	-0.21	1.60	2.69	1.11	2.12	2.96	1.29

Table 7.5: The PBE, PBE+U and HSE06 calculated neutral defect formation energies for V_{Cu}, O_i and Mg_{Cr} at the four chemical potential limits imposed by the formation of competing binary oxides for $CuCrO_2$, as indicated in 7.9. All energies are given in eV.

Figure 7.10 displays a plot of the formation energy of p-type defects in $CuCrO_2$ (copper vacancies V_{Cu} , oxygen interstitials O_i, and Mg-dopants Mg_{Cr}) under *Cu-poor/Al-poor* conditions as a function of Fermi-level position, calculated using PBE, PBE+U and HSE06. First, there are some very evident trends in formation energies.

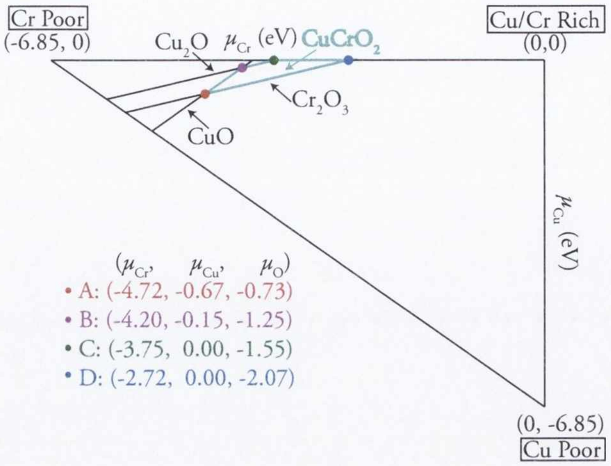

Figure 7.9: Illustration of the accessible (μ_{Cu}, μ_{Cr} chemical potential range for $CuCrO_2$ calculated using HSE06.

The formation energy of *all* three defects considered increases as the complexity of the theoretical method utilized is increased, i.e. PBE < PBE+U < HSE06. We noted a similar trend previously in studies of p-type defects in Cu_2O, Chapter 6.

Secondly, for each method the formation energy of Mg_{Cr} is lower than the formation energy of V_{Cu}. GGA predicts the formation energy of Mg_{Cr} to be *spontaneous* with a formation energy of -0.53 eV, and predicts the formation energy of V_{Cu} to be only 0.16 eV. PBE+U predicts that the formation energy of Mg_{Cr} *costs* energy (0.46 eV), with HSE06 predicting the formation energy to be 0.62 eV. The results of the *higher* complexity calculations are very different, and highlight the need for caution when interpreting defect formation energies calculated using standard DFT functionals, such as GGA or LDA. The GGA results can serve only as an indicator of the energetic trends in formation energy, but cannot reveal any quantitative information about formation energies.

The HSE06 formation energy of V_{Cu} (1.45 eV) is close to that of the HSE06 calculated formation energy for V_{Cu} in $CuAlO_2$ (1.33 eV), as seen in the Section 7.1. The HSE06 calculated formation energy for an O_i in $CuCrO_2$ is 1.63 eV, however, which is considerably lower than the HSE06 calculated formation energy of an O_i in $CuAlO_2$ (3.10 eV). This difference can be explained by the larger lattice parameters of $CuCrO_2$,

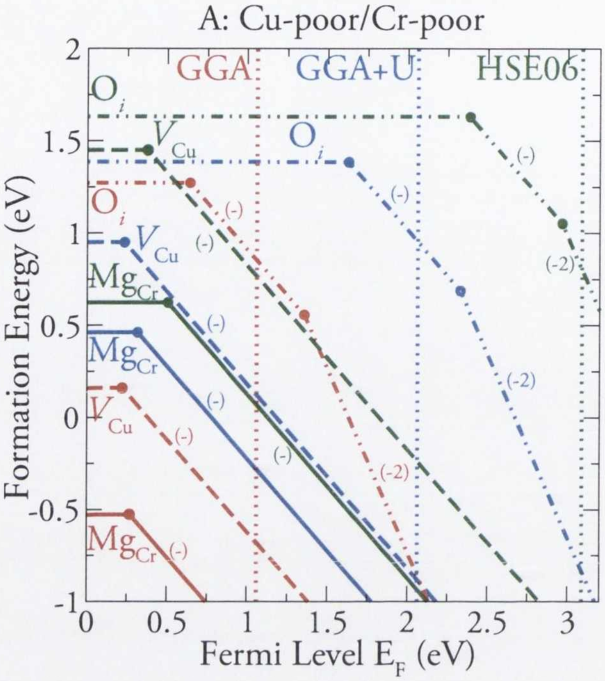

Figure 7.10: PBE (red), PBE+U (blue) and HSE06 (red) calculated formation energies for p-type defects in $CuCrO_2$ as a function of Fermi energy under Cu-poor/Cr-poor conditions. The solid lines denote Mg_{Cr}, the dashed lines denote V_{Cu}, and the dot-dot-dash lines denote O_i for each method. The vertical dotted lines denote the calculated CBM for each method, and the solid dots denote the transition levels $\epsilon(q/q')$.

which gives rise to a larger interstitial site for O_i to form.

For all three methods employed, activated conductivity is predicted, although it should be noted that, without the explicit inclusion of a correction for finite size effects and valence band alignment,[134] the PBE transition levels for V_{Cu} and Mg_{Cr} are actually resonant in the valence band. Previous standard DFT studies of the defect chemistry/physics of delafossites have neglected to deal with finite size effects and valence band alignments, and as such the incorrect prediction of degenerate conductivity for $CuAlO_2$ for example,[57,270] is not surprising.

The transition levels for all three defects get deeper as you move from PBE to PBE+U to HSE06. The (0/-1) transition level for the V_{Cu} with HSE06 is 0.37 eV, which is considerably shallower than the HSE06 calculated transition levels for $CuAlO_2$ at 0.68 eV. This is consistent with that fact that $CuCrO_2$ displays a higher undoped conductivity than $CuAlO_2$.[51] The experimentally reported acceptor level for $CuAlO_2$ is 0.70 eV,[268] which is possibly a good indicator of the reliability of the HSE06 transition levels for delafossite systems.

7.2.6 Hole localization/delocalization

To elucidate the mechanism of hole formation in $CuCrO_2$, we have plotted the spin density (difference between the alpha and beta spin) for the V_{Cu} in $CuCrO_2$, with the results displayed in Figure 7.11. Upon examination of the spin density for the PBE V_{Cu}, it becomes apparent that no hole density is present on the Cu atoms, with all the hole density mixed in with the Cr spins. This is not surprising, as the Cr states dominate at the VBM in the PBE description, and as such holes would be expected to form on Cr states. This situation changes when we move to PBE+U, with the hole density now delocalized over all the Cu atoms in the cell, with no change in the Cr spin density. Using HSE06, the hole density is only situated on the Cu atoms near the vacancy, but not in the neighbouring Cu layers. It is therefore apparent that the higher levels of theory predict that hole formation will be centered on the Cu atoms, and that a $\mathrm{Cr^{III}}/\mathrm{Cr^{IV}}$ hole mechanism is unlikely. HSE06 predicts the holes on the Cu sites to be less localized than holes formed from a V_{Cu} in $CuAlO_2$.

7.3 Discussion

While many studies have suggested that delafossite oxides conduct via a polaronic hopping mechanism,[60,61,166] a recent study by Tate *et al.* reported that p-type conductivity in $CuAlO_2$ is governed by band conduction, with the holes thermally activated from acceptor levels 700meV above the VBM.[268] This study was carried out on single-crystals of $CuAlO_2$, without the influence of grain boundaries, and strain effects of the previous thin film and bulk measurements.[268] Whilst a direct clarification of the conductivity

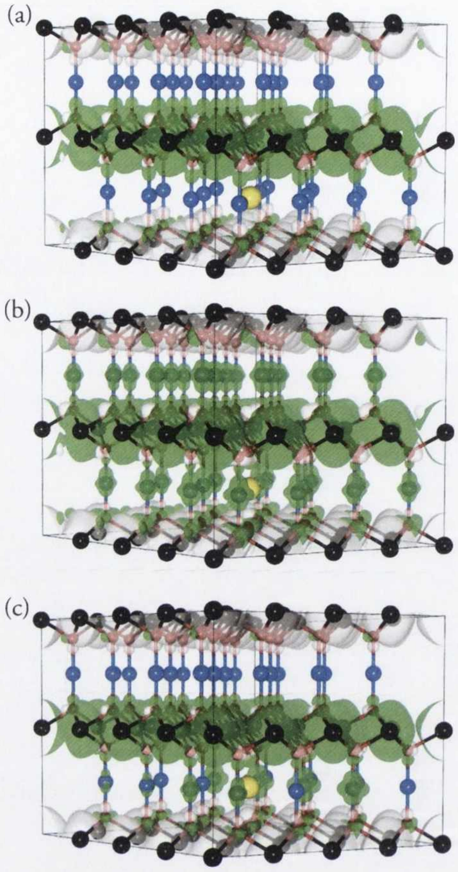

Figure 7.11: Spin density (alpha spin (green) - beta spin (white)) plot for $CuCrO_2$ calculated using (a) PBE, (b) PBE+U and (c) $CuCrO_2$. Blue, Black and red spheres denote Cu, Cr and O atoms respectively. The green/white isosurface is shown at $0.05\,\mathrm{e}\,\text{Å}^{-3}$.

mechanism is beyond the scope of this study, we can investigate the nature of geometry and electronic structure of V_{Cu} in $CuAlO_2$, and find out if it causes a polaronic distortion.

Upon formation of a V_{Cu}, the two oxygen atoms that made up the O–Cu–O dumbbell are left under-coordinated and move away from the vacancy by 0.05 Å while the six Cu ions surrounding the vacancy move inwards by $\sim$ 0.01 Å, as shown in Figure 7.12. These small perturbations of the geometry are atypical of the large distortions usually associated with small polarons.[311] Analysis of the associated spin density of the hole state, 7.12, shows that the excess spin is localized mainly on the six Cu atoms neighbouring the vacancy with *d* orbital character, which is indicative of a reasonably localized polaron.

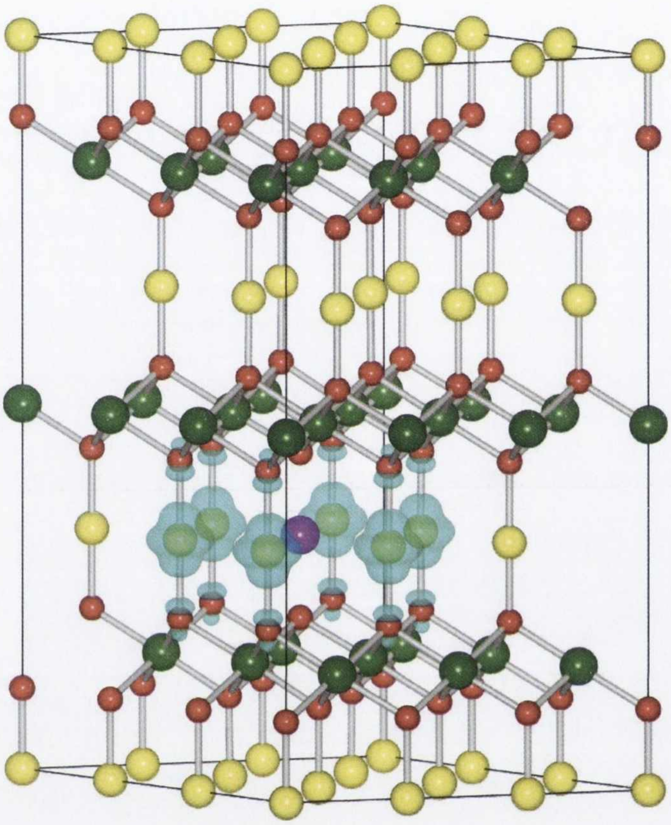

Figure 7.12: Structure and spin density of V_{Cu} in $CuAlO_2$. Yellow, red, and green spheres represent Cu, O and Al respectively. The vacancy position is indicated with a pink sphere. The blue isosurface is shown at $0.05\,\mathrm{e}\,\mathrm{\AA}^{-3}$.

The localization of hole density in $CuAlO_2$ upon V_{Cu} in $CuAlO_2$ formation can probably be taken as a sign of a polaron. As discussed previously in Chapter 4, delafossites and $\mathrm{Cu^I}$ oxides in general are considered to be polaronic,[58–61,166,179–187,312] and as such it is expected that the Cu–Cu distances should play a part in any conductivity, with holes expected to hop from Cu to Cu.[166] The Cu–Cu distance (equal to the *a*/*b* lattice constant) is determined by the size of the $\mathrm{M^{III}}$ ion, which suggests that the conductivity will increase as the size of the $\mathrm{M^{III}}$ ion decreases. In fact this seems to be true for $CuBO_2$, which has the smallest Cu–Cu distance of all delafossites, and is reported to have the highest non-doped conductivity.[168] This would also explain why undoped $CuAlO_2$ has been reported to have a higher conductivity than both undoped $CuScO_2$ and $CuYO_2$.[51]

However, conduction in these systems cannot be as simple as stating that conductivity is inversely proportional to M^{III} radii size. The number of hole carriers (introduced by intrinsic or extrinsic defects) in the system is also very important, with size of the M^{III} again thought to play an important role. The size of the M^{III} may determine the non-doped conductivity of these materials, as the larger the M^{III} ion, the more oxygen interstitials the material can contain.[141,188] This is consistent with the the reported undoped conductivity of $CuYO_2$[141] being higher a higher than $CuScO_2$[189]. It cannot, however, explain why $CuCrO_2$ has a higher undoped conductivity even than $CuAlO_2$. [51]

As the size of the trivalent ion increases, It is postulated that the ability to dope the material also increases.[149] By this rationale, extrinsic doping of $CuAlO_2$ to increase carrier concentrations and lower the Fermi level could be substantially more difficult than doping $CuYO_2$ for instance. This does not take into account, however, that suitably sized dopants for most trivalent cations can be found. It is known that there is a very limited range for Mg^{II} substitution in $CuCrO_2$, with $x = 0.05$ being the limit for $CuCr_{1-x}Mg_xO_2$,[150] as above this percentage the spinel impurity $MgCr_2O_4$ has been reported. Despite this, the conductivity of $CuCrO_2$:Mg is much higher than that of $CuScO_2$:Mg and $CuYO_2Ca$, which should be able to contain a much higher dopant concentration. Therefore, the electronic structure of the M^{III} ion must also play a prominent role in conductivity. Although our calculated TLs for Mg doped $CuCrO_2$ are slightly deeper than those of V_{Cu} (from all three levels of theory), the low formation energy means that the material is easy to dope until the solubility limit is reached. Such favourable doping energies will considerably increase the number of charge carriers in the system.

Upon analysis of our calculated density of states for $CuCrO_2$, it is clear that the higher levels of theory (PBE+U and HSE06) predict that the VBM of $CuCrO_2$ is dominated by Cu 3*d* states, with our subsequent analysis of the hole localization showing that holes are formed on the Cu atoms with these methods. HSE06 predicts that the holes are quite localized on the Cu atoms neighbouring a copper vacancy, but are not as localized as they are in $CuAlO_2$.[309] This "delocalization" of the hole state in $CuCrO_2$ compared to $CuAlO_2$ is most likely due to the increased covalency of the $CuCrO_2$ system, with the Cr 3*d* states mixing with the O 2*p* states along the entire width of the valence band. This theory is also supported by our recent examination of the bader charges of $CuM^{III}O_2$ (M^{III} = Al, Cr, Sc, Y) (Chapter 4) which revealed that the trend of M^{III} ion covalency with oxygen follows Cr>Sc>Y>Al, with Cr having the largest covalent interaction. This trend follows exactly the experimentally known conductivity trend for the doped delafossite. This is not unexpected, as elementary chemical intuition tells us that a more delocalized, covalent valence band should improve hole mobility.

It is clear from these results that conductivity in delafossites is a synergy between both size and electronic structure of the M^{III} ions. The necessary requirements for good conductivity would appear to be (a) the M^{III} ion not being overly large, and thus not limiting the hole hopping, leading to good non-doped conductivity; (b) the M^{III} ion having a favourable electronic structure, which can enhance the mobility of holes (delocalize holes states) and (c) the M^{III} ion not being too small and limiting the dopability of the material and hence allowing a high charge carrier concentration. Finding a compromise between these three factors is the key, and might plausibly explain why $CuCrO_2$ is currently the leading material, possessing a favourable electronic structure, and an M^{III} ion big enough to allow doping and small enough not to limit hopping.

7.4 Conclusion

In this chapter, We have shown that Cu_{Al} *and* V_{Cu} formation will dominate the conductivity of $CuAlO_2$, and not $[Al_{Cu}^{\bullet\bullet} + 2O_i'']''$ as had previously been proposed. The TLs of all *p*-type defects are found to be deep in the band gap, consistent with experiment, with our calculated TL for V_{Cu} at 0.68 eV in excellent agreement with a recent experimental report of an acceptor level at 0.70 eV.[268] We have identified that the indirect band gaps in the 1.65 – 2.10 eV range, reported from optical experiments, are most likely due to the (0/-1) OTL for $\mathrm{Cu_{Al}}$. $CuAlO_2$ will always be dominated by deep defect levels, meaning that high performance *p*-type $CuAlO_2$ will not be achievable. This is expected to be general for all $\mathrm{Cu^{I}}$-based delafossites.

We have also investigated the electronic structure and *p*-type defect chemistry of $CuCrO_2$ using PBE, PBE+U and HSE06. We find that the fundamental band gap of $CuCrO_2$ is indirect with all three methods, with PBE and PBE+U underestimating and HSE06 overestimating the experimentally observed range of optical band gaps. PBE suggests that Cr *d* states will dominate at the VBM, with PBE+U and HSE06 indicating that Cu *d* states will dominate at the top of the valence band, consistent with the majority of other copper-based delafossites and recent high resolution XPS studies. Mg doping on the Cr site is found to be energetically more favourable than intrinsic *p*-type defect formation, with all of the *p*-type defects considered yielding ionization levels deep in the band gap. Cu-poor/Cr-poor/O-rich conditions are found to be optimal for both intrinsic *p*-type defect formation *and* acceptor doping, and these growth conditions should be adopted to maximize performance. Both of the higher levels of theory (PBE+U and HSE06) predict that $CuCrO_2$ conducts through a $\mathrm{Cu^{I}/Cu^{II}}$ hole mechanism, and not via a $\mathrm{Cr^{III}/Cr^{IV}}$ hole mechanism as has been previously suggested. The higher conductivities of $CuCrO_2$ compared to other delafossites is attributed to favourable mixing of Cr *d* states with O 2*p* states in the valence band, producing shallower transition levels for the Cu-based holes.

Chapter 8

Spinel TCOs?

8.1 Introduction

In 2002, Hosono and co-workers first demonstrated that the normal spinel $ZnRh_2O_4$, with Zn occupying the tetrahedral sites and Rh occupying the octahedral sites (Figure 8.1) was a *p*-type wide band gap semiconductor.[313] It was reported to possess a band gap of 2.1 eV, and to display an electrical conductivity of $0.7\,S\,cm^{-1}$ at 300 K with no intentional doping.[313] The authors concluded that the magnitude of the bandgap was mainly composed of the ligand field splitting of the occupied t_{2g}^6 and unoccupied e_g^0 levels of octahedrally coordinated Rh^{III}.[313] $ZnRh_2O_4$ has also generated interest due to its possible thermoelectric properties,[314] potential photoelectrochemical applications, [315] and its ability to be synthesized as an amorphous material.[316] Unlike Cu-based *p*-type TCOs, which cannot retain their O–Cu–O linear coordination whilst amorphous, the O–Rh–O octahedral network of $ZnRh_2O_4$ is preserved in an amorphous state.[316,317] Heteroepitaxial pn junctions of crystalline $ZnRh_2O_4/ZnO$,[318] and amorphous $ZnRh_2O_4/InGaZnO_4$[317] have been subsequently demonstrated.

A very recent investigation of the transport properties of $ZnRh_2O_4$ by Mason and co-workers has concluded that the conductivity in this material is governed by activated, small *polaron* conductivity, with a hopping energy of 0.25 eV.[319] This study also reported a band gap of 2.2 eV, consistent with the results of Hosono and co-workers,

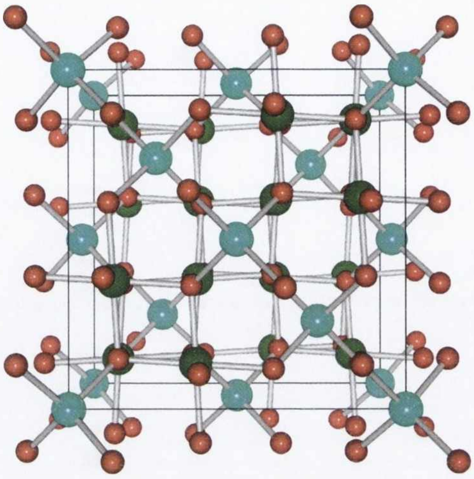

Figure 8.1: Cubic spinel structure of $ZnM^{III}_2O_4$ (M^{III} = Co, Rh, Ir). The Zn atoms (turquoise) occupy tetrahedral sites and the M^{III} atoms (green) occupy octahedral sites within an fcc oxygen (red) sublattice .

[313] and *not* big enough for TCO applications.[319]

Dekkers *et al.* reported the growth of *p*-type $ZnM^{III}_2O_4$ (M^{III} = Co, Rh, Ir) spinel thin films.[320] Based on ligand field theory they argue that the band gaps of the spinels should increase as the principal quantum number of the d^6 element increases, meaning that band gaps will increase in the order Co $3d$ < Rh $4d$ < Ir $5d$. [321] From optical absorption data, the authors report that the band gaps of $ZnCo_2O_4$, $ZnRh_2O_4$, and $ZnIr_2O_4$ are 2.26 eV, 2.74 eV, and 2.97 eV, which conforms to their expected trends.[320] Conductivities of $0.39\,\mathrm{S\,cm^{-1}}(0.61\,\mathrm{S\,cm^{-1}})$, $2.75\,\mathrm{S\,cm^{-1}}(2.83\,\mathrm{S\,cm^{-1}})$ and $3.39\,\mathrm{S\,cm^{-1}}(2.09\,\mathrm{S\,cm^{-1}})$ are reported for polycrystaline (epitaxial) films of $ZnCo_2O_4$, $ZnRh_2O_4$, and $ZnIr_2O_4$ respectively. In each case the conductivity displays Arrhenius-type behaviour, but with activation energies of less than 0.47 meV. To date, this is the only known report of the TCO $ZnIr_2O_4$.[320]

$ZnCo_2O_4$ is probably the most studied of the the $ZnM^{III}_2O_4$ spinels, with much interest generated due to its possible applications in gas sensing,[322,323] electrocatalysis, [324] supercapacitors[325], Li ion batteries,[326–328] and in dilute magnetic semiconductors. [329] Kim *et al.* reported $ZnCo_2O_4$ to possess an optical band gap of 2.63 eV, and to show both *p*- and *n*-type conductivity depending on the oxygen partial pressure.[330] Both *p*- and *n*-type samples were governed by an Arrhenius behaviour, with activations energies of only 41 meV and 45 meV respectively.[330] Samanta *et al.* found that the optical band gap of $ZnCo_2O_4$ was 2.80 eV, and interestingly was of *p*-*d* charge transfer nature.[331]

In this chapter, we investigate the electronic structure of $ZnM_2^{III}O_4$ (M^{III} = Co, Rh, Ir) spinels using the PBE generalized gradient approximation approach and the state-of-the-art screened hybrid density functional, HSE06. We find that the band gap trends obtained from both the PBE and the HSE06 calculations are *not* consistent with the trend expected from ligand field theory or from the sole experimental study containing all three materials. The suitability of these Zn *d*6 spinels as *p*-type TCOs or even as *p*-type semiconductors is discussed in light of their valence band features.

8.2 Calculation Methodology

All DFT calculations were performed using the VASP code,[153] with the projector augmented wave (PAW)[111] approach used to describe the interactions between the core and the valence electrons. The calculations were performed using GGA of Perdew, Burke and Ernzerhoff[75] (PBE) and the screened hybrid functional as proposed by Heyd, Scuseria, and Ernzerhof[99] (HSE06) in which a percentage of the exact nonlocal Fock exchange ($\alpha = 25\%$) is added to the PBE functional with a screening of $\omega = 0.11$ bohr^{-1} applied to partition the Coulomb potential into long range and short range terms.

Structural optimizations of the 14 atom primitive cell of the $ZnM_2^{III}O_4$ (M^{III} = Co, Rh, Ir) spinels were performed using PBE and HSE06 at a series of volumes in order to calculate the equilibrium lattice parameters. In each case the the atomic positions, lattice vector and cell angle were allowed to relax, while the total volume was held constant. The resulting energy volume curves were fitted to the Murnaghan equation of state to obtain the equilibrium bulk cell volume.[113] Convergence with respect to *k*-point sampling and plane wave energy cut off was checked, and for both systems a cutoff of 400 eV and a *k*-point sampling of 10 × 10 × 10 were found to be sufficient.

Calculations were deemed to be converged when the forces on all the atoms were less than 0.01 eV Å^{-1}.

8.3 Results

8.3.1 Structure

The PBE and HSE06 calculated structural paramaters for $ZnM_2^{III}O_4$ (M^{III} = Co, Rh, Ir) are given in Table 8.1. For $ZnCo_2O_4$ and $ZnRh_2O_4$, the PBE calculated lattice parameters are all overestimated compared to the experimental values, whereas the HSE06 lattice parameters are underestimated. This overestimation by PBE is well known.[154] HSE06 usually predicts structural data that is more consistent with experimental values than the GGA/LDA approaches, and has been shown previously to result in underestimated lattice parameters.[140] The bond distances for $ZnRh_2O_4$ show good agreement with experimental values.[332]

	$ZnCo_2O_4$			$ZnRh_2O_4$			$ZnIr_2O_4$		
	PBE	HSE06	Expt[333]	PBE	HSE06	Expt[332]	PBE	HSE06	Expt[320]
a	8.17	8.01	8.10	8.57	8.48	8.54	8.75	8.59	8.51
Volume	546.1	514.5	531.4	631.2	611.7	622.8	671.1	634.3	615.6
Zn–O	1.98	1.94	–	2.00	1.98	2.05	2.07	2.01	–
d^6–O	1.93	1.89	–	2.01	2.04	2.03	2.09	2.06	–

Table 8.1: Table comparing the PBE and HSE06 calculated lattice parameters, volume, Zn–O and d^6–O interatomic distances with experimental results. Volumes are given in Å^3 and lattice dimensions and interatomic distances in Å.

The lattice parameters are seen to increase as the principal quantum number of the d^6 element increases, for both PBE and HSE06. This is to be expected when one considers the ionic radius of the d^6 cations involved, e.g. Co (68.5 pm) < Rh (80.5 pm) < Ir (82 pm).[334] The HSE06 calculations predict the lattice parameter of $ZnIr_2O_4$ to be 8.59 Å, which is larger than that proposed by Dekkers *et al.* for $ZnIr_2O_4$ thin films grown on Al_2O_3 (8.50 Å) or on Quartz (8.51 Å).[320] The study by Dekkers *et al.* [320], however, reports lattice vectors for $ZnCo_2O_4$ (8.08 Å) and $ZnRh_2O_4$(8.48 Å) that are underestimated compared to other experimental values,[332,333] indicating that our HSE06 predicted value for $ZnIr_2O_4$ is reasonable.

8.3.2 PBE calculated electronic structure

The PBE calculated band structures of $ZnM^{III}_2O_4$ (M^{III} = Co, Rh, Ir) along the high symmetry lines taken from Bradley and Cracknell[114] are shown in Figure 8.2 (a-c). The valence band maximum (VBM) for all three spinels is located at the X point. The conduction band minimum (CBM) for $ZnCo_2O_4$ and $ZnRh_2O_4$ is located near the X point, on the line from X to Γ. Previous LDA and LDA+U calculations of $ZnRh_2O_4$ have also found that the CBM is displaced from X in the X–Γ direction,[315,319] in good agreement with the present calculations. The VBM, however, was found to be located close by the X position, shifted along the X–Γ direction using LDA+U,[319] but LDA calculations placed the VBM at the X point,[315] consistent with our PBE calculations. In contrast to this, the CBM for $ZnIr_2O_4$ is located at Γ, and is actually found to be made up of by Ir *s* and Zn *s* states. We have illustrated the positioning of the M^{III} *s* states in all three spinels in Figure 8.3, which shows that *s* states dominate at the CBM of $ZnIr_2O_4$ and not Ir 5*d* states as predicted by ligand field theory. Figure 8.3 clearly shows the positioning of the M^{III} *s* states in the conduction band, with the M^{III} *s* states becoming lower in energy as you go down the group. This explains the discrepancy of the CBM position for $ZnIr_2O_4$ compared to the other two materials.

The fundamental band gaps for all three materials are indirect, measuring 0.57 eV, 0.80 eV and 0.48 eV for $ZnCo_2O_4$, $ZnRh_2O_4$ and $ZnIr_2O_4$ respectively. The calculated fundamental indirect band gaps reported for $ZnRh_2O_4$ in the literature are 0.65 eV (LDA)[315], 0.81 eV (GGA)[315] and 1.65 eV (LDA+U)[319]. The GGA indirect band gap reported by Singh *et al.* is 0.01 eV bigger than our calculated band gap, but this slight discrepancy can be accounted for by the fact that *all* previous calculations of

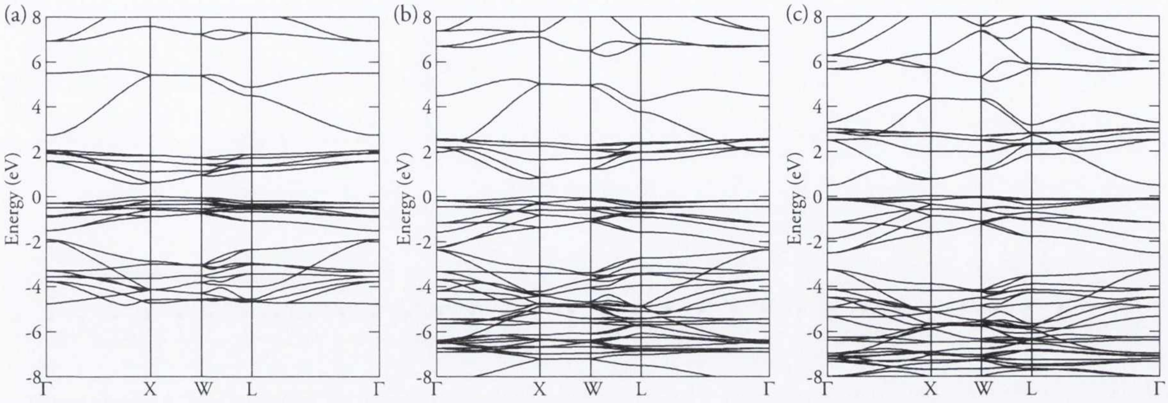

Figure 8.2: PBE calculated band structures for (a) $ZnCo_2O_4$, (b) $ZnRh_2O_4$, and (c) $ZnIr_2O_4$. The VBM is set to 0 eV in each case.

the $ZnRh_2O_4$ spinel have been performed at the *experimental* lattice parameters, and not at the calculated equilibrium structures as is the case in the present study. It is interesting to note the flat (non-disperse) nature of the bands around the VBM for all the spinels (Figure 8.2), which is not indicative of good *p*-type conduction.[319]

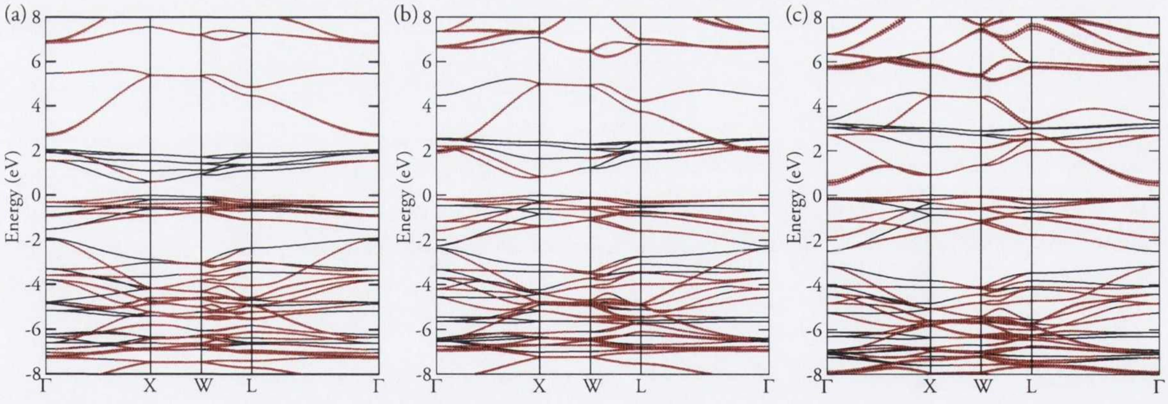

Figure 8.3: PBE calculated fat band analysis for (a) $ZnCo_2O_4$, (b) $ZnRh_2O_4$, and (c) $ZnIr_2O_4$, showing the contributions of the M^{III} *s* states to the band structure. The VBM is set to 0 eV in each case.

Figure 8.4 (a-c) shows the PBE calculated total and partial (ion decomposed) electronic densities of states (EDOS/PEDOS) for $ZnM^{III}_2O_4$ (M^{III} = Co, Rh, Ir). The main valence band features of all three of the spinels are broadly similar to available XPS/PES studies in the literature,[320] although the width of the PBE calculated valence bands is smaller than those seen experrimentally, which is a known PBE underestimation.[152,307,335–337] In each case three distinct regions are noticeable in the valence band, region I (-9 to -6 eV), region II (-6 to -2 eV) and region III (-2 to 0 eV), Figure 8.4 (a-c). Region IV represents the lower conduction band.

Region I in each spinel is dominated by Zn d states with significant mixing with O $2p$ states. Region II is mainly comprised of O $2p$ states with some minor contributions from M^{III} d and Zn $3d$ states. Region III is seen to be split-off from the lower valence band, and is clearly dominated by M^{III} d states, with a small oxygen contribution. The M^{III} peaks are centered at ~ -0.8 eV, ~ 0.7 eV and ~ -0.5 eV for $ZnCo_2O_4$, $ZnRh_2O_4$ and $ZnIr_2O_4$ respectively. The lower conduction band (Region IV) is also dominated by M^{III} d states with the main peak centered at ~ 1 eV, ~ 1.8 eV and ~ 2.2 eV for $ZnCo_2O_4$, $ZnRh_2O_4$ and $ZnIr_2O_4$ respectively.

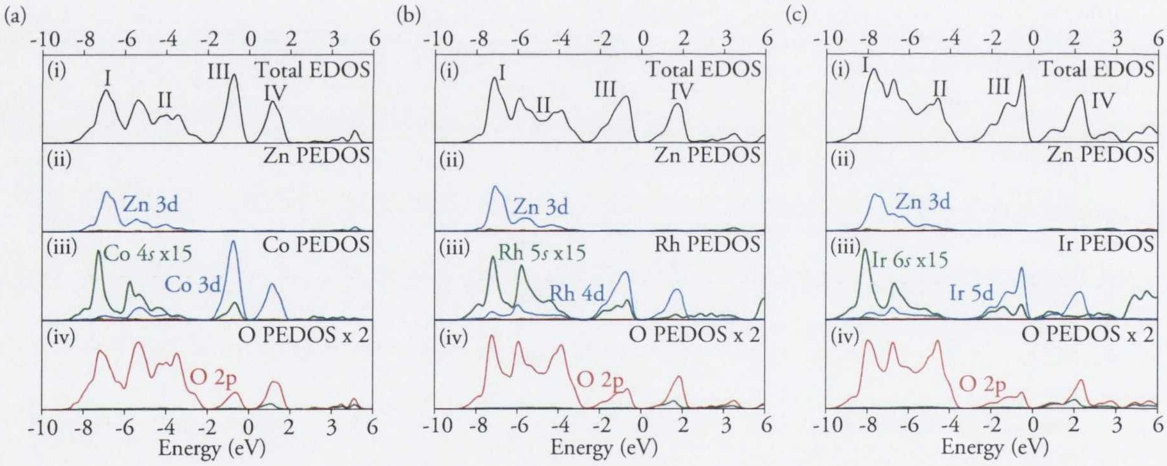

Figure 8.4: The PBE electronic density of states for (a) $ZnCo_2O_4$, (b) $ZnRh_2O_4$ and (c) $ZnIr_2O_4$. (*i*) Total EDOS, (*ii*) Zn PEDOS, (*iii*) M^{III} PEDOS and (*iv*) O PEDOS. The blue lines represent d states, green s states and red p states.

8.3.3 HSE06 calculated electronic structure

Figure 8.5 shows the HSE06 calculated band structure of $ZnM^{III}_2O_4$ (M^{III} = Co, Rh, Ir). The VBM of $ZnCo_2O_4$ is situated near W in the W–L direction, which is different to the PBE VBM positioning at the X point. The VBM of $ZnRh_2O_4$ and $ZnIr_2O_4$ are found to be at X and Γ respectively, which is consistent with the PBE positioning. The CBM of $ZnCo_2O_4$ and $ZnRh_2O_4$ are situated near X on the X–Γ line, with the CBM of $ZnIr_2O_4$ situated at Γ, similar to the PBE calculations, and is again found to be made up of Ir *s* and Zn *s* states, similar to the PBE calculations.

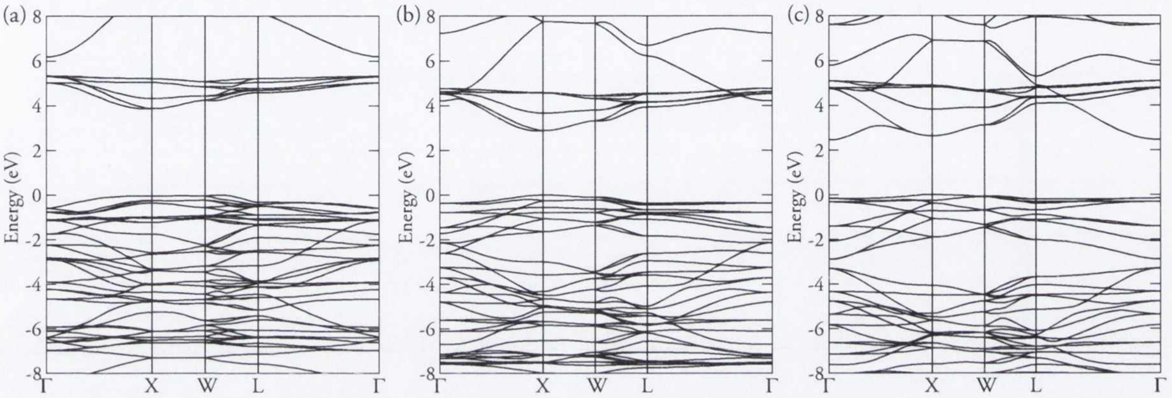

Figure 8.5: HSE06 calculated band structures for (a) $ZnCo_2O_4$, (b) $ZnRh_2O_4$, and (c) $ZnIr_2O_4$. The VBM is set to 0 eV in each case.

In agreement with the PBE calculations, the fundamental band gaps of all three spinels are found to be indirect, and measure 3.86 eV, 2.87 eV and 2.45 eV for $ZnCo_2O_4$, $ZnRh_2O_4$ and $ZnIr_2O_4$ respectively. The main features of the bandstructure are largely unchanged, except for the much larger splitting between the valence band and conduction band. The bands at the VBM still have very little dispersion, indication poor *p*-type ability.

The HSE06 calculated total and partial (ion decomposed) electronic densities of states (EDOS/PEDOS) for $ZnM^{III}_2O_4$ (M^{III} = Co, Rh, Ir) are shown in Figure 8.6(a-c). The EDOS and PEDOS of the individual spinels are very similar to those obtained with the PBE functional. The major differences are (i) the peak positioning in Region I, where the Zn *d* states are pushed to lower energies relative to the VBM than in the PBE PEDOS, and (ii) the splitting of the occupied and unoccupied manifolds of the M^{III} states is appreciably increased. Overall the shapes of the peaks remain unchanged.

Comparing the HSE06 valence band features with the PES data from the literature, it is noticeable that the peak associated with the Zn d states is closer to the experimental position than that obtained using PBE. Experimentally, the Zn 3d peaks are reported to occur at ~ -8.8 eV, ~ -9.2 eV and ~ -9.5 eV for $ZnCo_2O_4$, $ZnRh_2O_4$ and $ZnIr_2O_4$ respectively.[320] The HSE06 calculations place these peaks at ~ -6.8 eV, ~ -7.8 eV and ~ -9 eV for $ZnCo_2O_4$, $ZnRh_2O_4$ and $ZnIr_2O_4$ respectively. The corresponding PBE peak positions are ~ -7 eV, ~ -7.2 eV and ~ -7.8 eV respectively, Figure 8.4 (a-c). GGA has long been known to incorrectly position occupied Zn d states compared to experiment[26] due to the inherent self interaction error, with HSE06 on average improving the positioning of these states.

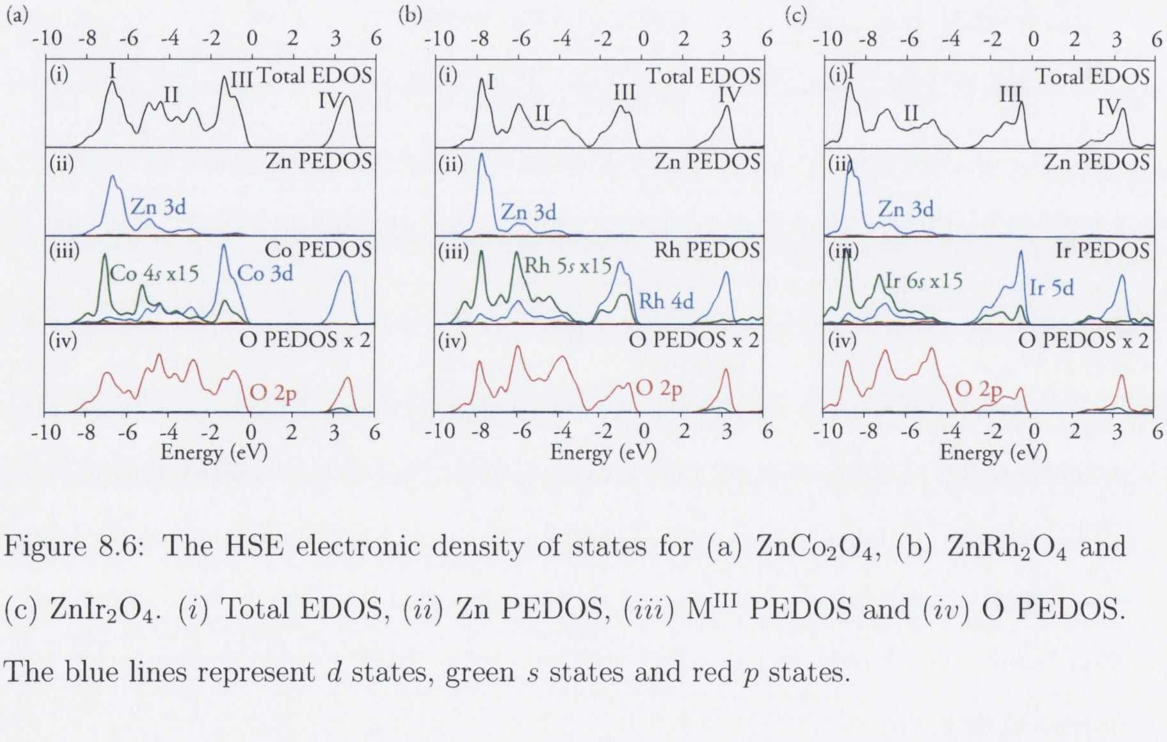

Figure 8.6: The HSE electronic density of states for (a) $ZnCo_2O_4$, (b) $ZnRh_2O_4$ and (c) $ZnIr_2O_4$. (*i*) Total EDOS, (*ii*) Zn PEDOS, (*iii*) M^{III} PEDOS and (*iv*) O PEDOS. The blue lines represent d states, green s states and red p states.

8.4 Discussion

The PBE fundamental band gap trend of $ZnRh_2O_4$ (0.80 eV) > $ZnCo_2O_4$ (0.57 eV) > $ZnIr_2O_4$ (0.48 eV) is *not* the trend expected from ligand field theory.[321] The splitting of the occupied t_{2g}^6 and unoccupied e_g^0 states in an octahedral field is expected to increase on going down the group,[321] and as the M^{III} d manifolds are expected to dominate the top of the VB and the bottom of the CB, the band gaps of these spinels are expected to follow this trend.[320] The HSE06 calculations indicate that the fundamental band gaps of $ZnCo_2O_4$, $ZnRh_2O_4$ and $ZnIr_2O_4$ are 3.86 eV, 2.87 eV and 2.45 eV respectively, which are a complete reverse of the expected trend.

The PBE (HSE06) calculated fundamental band gaps for $ZnM_2^{III}O_4$ (M^{III} = Co, Rh, Ir) are significantly smaller (larger) than those expected based on optical absorption data from the literature.[320] As we have pointed out earlier, *fundamental* band gaps are not always equivalent to *optical* band gaps. To fully understand the optical band gaps of these spinel materials, we have calculated the optical absorption spectra for the three materials using PBE and HSE06, with the resulting spectra displayed in Figure 8.7. Analysis of the optical transitions occuring in $ZnM_2^{III}O_4$ using PBE and HSE06 reveal that the lowest *direct* transitions occur at the X point for $ZnCo_2O_4$ and $ZnRh_2O_4$, with the lowest transition in $ZnIr_2O_4$ occuring at the Γ point, with transitions from highest VB to lowest CB being symmetry allowed. The PBE trend in order of increasing optical band gaps is $ZnCo_2O_4 < ZnIr_2O_4 < ZnRh_2O_4$, which does not follow the experimentally expected trend of $ZnCo_2O_4 < ZnRh_2O_4 < ZnIr_2O_4$. HSE06 completely reverses the expected trend, producing a trend of $ZnCo_2O_4 > ZnRh_2O_4 > ZnIr_2O_4$.

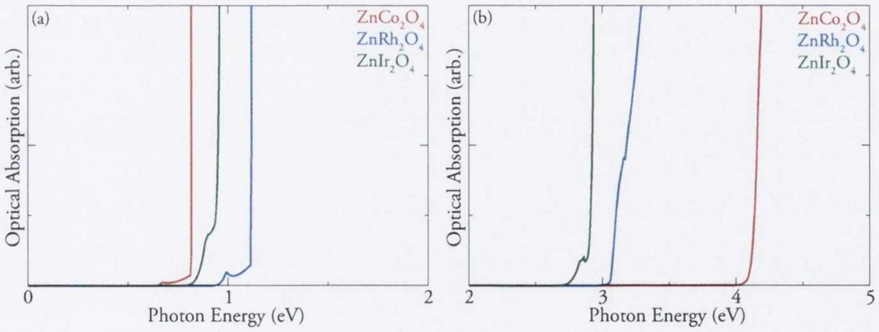

Figure 8.7: (a) PBE and (b) HSE06 calculated optical absorption spectrum of $ZnM_2^{III}O_4$ (M^{III} = Co, Rh, Ir) summed over all possible direct valence to conduction band transitions. In both figures, $ZnCo_2O_4$ is red, $ZnRh_2O_4$ is blue and $ZnIr_2O_4$ is green.

In fact, the optical band gap trend expected from ligand field theory has only ever been realised in the study by Dekkers *et al.*[320] Previous experimental measurements have in fact suggested that the *optical* band gap of $ZnCo_2O_4$[330,331] is actually larger that those of $ZnRh_2O_4$.[313,319] Singh *et al.* have even predicted the band gap of $ZnRh_2O_4$ to be only $\sim 1.2\,\mathrm{eV}$.[315] Indeed the band gaps measured by Dekkers *et al.* are at variance with *all* other measurements for $ZnCo_2O_4$ and $ZnRh_2O_4$.

It is instructive to note that the performance of hybrid functionals in describing the positioning of Co 3*d* states in Co doped ZnO has been called into question by Walsh *et al.*[100] They noted that calculations using the PBE0 hybrid functional resulted in the Co *d*–*d* splitting being overestimated by as much as 300% compared to experiment.[100] The authors analysis showed that while 25% exchange was necessary to reproduce the experimental band gap of ZnO, less than 5% exchange was adequate for Co_3O_4.

To further test the applicability of PBE and HSE06 for the description of M^{III} d^6 low spin octahedral splitting, we have also calculated the t_{2g}^6–e_g^0 splitting for $\left[M^{III}\,(NH_3)_6\right]^{3+}$ (M^{III} = Co, Rh, Ir) octahedral complexes, Table 8.2. PBE underestimates the splitting for all three complexes, but maintains the experimentally reported trend of increased splitting as the principal quantum number of the M^{III} ion increases. HSE06, however, completely reverses the expected trend, and also hugely overestimates the splitting. We have also tested the ability of Hartree-Fock (HF) to describe this splitting (Table 8.2), and we found that it wildly overestimates the splitting of the *d* states, but also completely reverses the experimentally expected trend. The HF results are very informative, as it indicates that HF itself cannot adequately describe the splitting trend for low spin d^6 ions in an octahedral field, and it is therefore unsurprising that HSE06 cannot describe this trend.

Material	PBE	HSE06	HF	Expt.[338]
$[Co\,(NH_3)_6]^{3+}$	2.61	6.24	24.51	2.85
$[Rh\,(NH_3)_6]^{3+}$	3.73	6.10	17.20	4.22
$[Ir\,(NH_3)_6]^{3+}$	4.36	6.45	16.74	5.08

Table 8.2: Table comparing the GGA, HSE06 and HF calculated t_{2g}^6–e_g^0 splitting for $\left[M^{III}\,(NH_3)_6\right]^{3+}$ (M^{III} = Co, Rh, Ir) octahedral complexes with their experimental values. All splittings are given in eV.

Although there have been arguments that GGA/LDA should describe the natural octahedral *d* orbital splitting of these materials quite well,[315] our results indicate that PBE significantly underestimates the splitting for these spinel materials. These tests also confirm that HSE06 should be utilized with *extreme* caution when calculating binary or multiternary materials involving low spin d^6 $\mathrm{M^{III}}$ cations, as the accepted value of exact exchange ($\alpha = 25\%$) grossly overestimates the t_{2g}^6–e_g^0 splitting.

Although the t_{2g}^6–e_g^0 splittings are underestimated (overestimated) with PBE (HSE), both approaches produce similar EDOS/PEDOS. There is no significant curvature at the VBM of any of the spinels, meaning that the states at the VBM are not well suited to high hole conductivity. Indeed, as the bands are clearly *not* parabolic in nature, it would not even be useful to calculate the effective hole mass of the VB. The main features of the spinels are maintained with both approaches: low lying Zn 3*d* states, with the $\mathrm{M^{III}}d$ states dominating at the top and bottom of the valence band and conduction band respectively. As the bands are flat at the VB maxima of $\mathrm{ZnRh_2O_4}$, it is not surprising that Mason and co-workers have found that conductivity in $\mathrm{ZnRh_2O_4}$ is polaronic in nature, with a hopping energy of 0.25 eV.[319] This is consistent with other spinels with low spin d^6 metals in the octahedral holes, which also display polaronic conductivity, e.g. $\mathrm{NiCo_2O_4}$[339] and $\mathrm{Co_3O_4}$.[340] Thus it is likely that $\mathrm{ZnCo_2O_4}$ and $\mathrm{ZnIr_2O_4}$ will also conduct with a polaronic mechanism, which is not ideal for TCO applications.

It is thus clear that the undoped $\mathrm{ZnM_2^{III}O_4}$ ($\mathrm{M^{III}}$ = Co, Rh, Ir) spinels will *always* be limited by activated conductivity, and if they are to become successfull *p*-type semiconductors, a change in mechanism from small polaron transort to degenerate semiconducting behaviour is necessary.[319] Allied to these intrinsic conductivity limits, the experimental uncertainty about the band gaps of these materials continues, and the nature and size of the fundamental band gap of $\mathrm{ZnIr_2O_4}$ remains uncertain. Whether $\mathrm{ZnIr_2O_4}$ is actually a TCO or not is still uncertain, although calculations indicate that the nature of the band gap is not solely determined by $d - d$ splitting, as the CBM at the Γ point is found to be of distinct Ir *s* and Zn *s* character using both PBE and

HSE06. A reinvestigation of the optical band gaps of these spinel materials is thus warranted.

8.5 Conclusion

The geometry and electronic structure of $ZnM^{III}_2O_4$ (M^{III} = Co, Rh, Ir) spinels have been investigated using GGA and HSE06 functionals. GGA is found to underestimate the experimental band gap compared to experiment, wheras HSE06 is found to severly overestimate the octahedral M^{III} t^6_{2g}–e^0_g splitting compared to experiment. The exact band gap trend expected for these materials based on ligand field theory is not recreated by either method. In the case of $ZnIr_2O_4$, both GGA and HSE06 indicate that the fundamental band gap is not controlled by *d*–*d* splitting as was expected, but instead is *d*–$M^{III}s$. This finding calls into question the expectation that the band gap of $ZnIr_2O_4$ will be the largest of the spinels, and also the view that $ZnIr_2O_4$ is a TCO. The lack of dispersion at the VBMs of all three spinels indicates that these materials will be dominated by polaronic conductivity, and will *never* be a suitable *p*-type alternative to the industry standard *n*-type TCOs.

Chapter 9

$(Cu_2S_2)(Sr_3Sc_2O_5)$– a new structural motif for *p*-type TCOs?

9.1 Introduction

Since Hosono's pioneering study in 1997, an aggressive research drive has been focused on developing other Cu^I based TCOs using the principles of "*chemical modulation of the valence band*".[51] This has resulted in the identification of other copper Delafossite materials with *p*-type TCO properties, including $CuInO_2$[341], $CuScO_2$[163], $CuCrO_2$[55], $CuGaO_2$[342], $CuYO_2$[141] and most recently $CuBO_2$.[168,169] As these materials are all either limited by an indirect band gap or low conductivity, or both, alternative Cu^I-based materials have been investigated. $SrCu_2O_2$ was also found to have *p*-type ability and transparency, even having a direct band gap, but with lower conductivities even than the delafossites.[52] To date the *p*-type TCO with the highest conductivity is a delafossite (Mg doped $CuCrO_2$),[55] which has a conductivity of 220 S cm^{-1}, which is an order of magnitude lower than the *n*-types.

These band-engineering concepts are not solely centered on materials with oxygen as the anion, and can also be applied to chalcogenides such as sulphides and selenides. [343] Chalcogenides however, suffer from much narrower band-gaps than oxides,[344] but have greater hole mobility due to stronger hybridization of the chalcogens with the Cu

$3d$ states at the VBM. Layered oxychalcogenides on the other hand, can maintain the wide band-gaps of the oxides, allied with the increased hybridization of the chalcogen, Ch p^6 (Ch = S, Se, Te) and Cu $3d^{10}$ states at the VBM. These materials have common $[Cu_2Ch_2]^{2-}$ layers between oxide layers with ionic cations (e.g. La, Sr etc.), with the Cu–Ch bonds forming VBMs with increased hybridization relative to the Cu–O VBMs in Cu^I based TCOs.[345]

LaCuOS was first identified by Hosono and co-workers as a *p*-type TCO in 2000.[54] This layered oxysulfide possessed a band-gap of 3.1 eV and when Sr doped showed *p*-type conductivity of $2.6 \times 10^{-1}\,\mathrm{S\,cm^{-1}}$.[346] Replacing the chalcogen in the structure with Se results in a *p*-type material with increased conductivity, but a decreased bandgap.[347] In fact Mg-doped LaCuOSe displayed a very promising conductivity of $910\,\mathrm{S\,cm^{-1}}$, a hole concentration greater than $10^{21}\,\mathrm{cm^{-3}}$ and a hole mobilities as high as $3.5\,\mathrm{cm^2V^{-1}s^{-1}}$.[348] However the optical band-gap of this material is only 2.8 eV, effectively ruling it out as a possible TCO.[348] This illustrates however the ability of chalcogen anions, allied with Cu^I cations to be good candidate p-type materials. The challenge remains to engineer a layered oxychalcogenide with sufficient *p*-type conductivity and better transparency, to equal the performance of the *n*-type TCOs.

Recently, Liu *et al.* have synthesized $[Cu_2S_2][Sr_3Sc_2O_5]$ (denoted SCSOS from now on), a very promising layered *p*-type transparent conducting oxychalcogenide, 9.1.[139] This oxysulfide is composed of layers of $[Cu_2S_2]^{2-}$, as seen in LaCuOS and $BaCu_2S_2$, but sandwiched between perovskite like $[Sr_3Sc_2O_5]^{2+}$ layers.[139] The highly ionic components of the perovskite like layer are thought to be responsible for the optical band-gap of 3.1 eV. The *p*-type conductivity of the undoped material was measured at $2.8\,\mathrm{S\,cm^{-1}}$, which is higher than the highest undoped conductivity of all the delafossite system ($CuBO_2$, $1.65\,\mathrm{S\,cm^{-1}}$),[168] and is two orders of magnitude higher than the undoped conductivity of LaCuOS ($0.01 - 0.1\,\mathrm{S\,cm^{-1}}$.[139] This relatively high undoped conductivity relative to other Cu^I materials is quite remarkable as the carrier concentration in undoped SCSOS is relatively low at $1 \times 10^{17}\,\mathrm{cm^{-3}}$.[139] One explanation for this is the *extremely* high hole mobility of SCSOS, which at $150\,\mathrm{cm^2V^{-1}s^{-1}}$ at room temperature, is the *highest* hole mobility of *any* *p*-type TCO, and *also* is *higher* than the highest mobility reported for *n*-type TCOs (In_2O_3:Mo, 130 cm^{2}V^{-1}s^{-1}).[139]

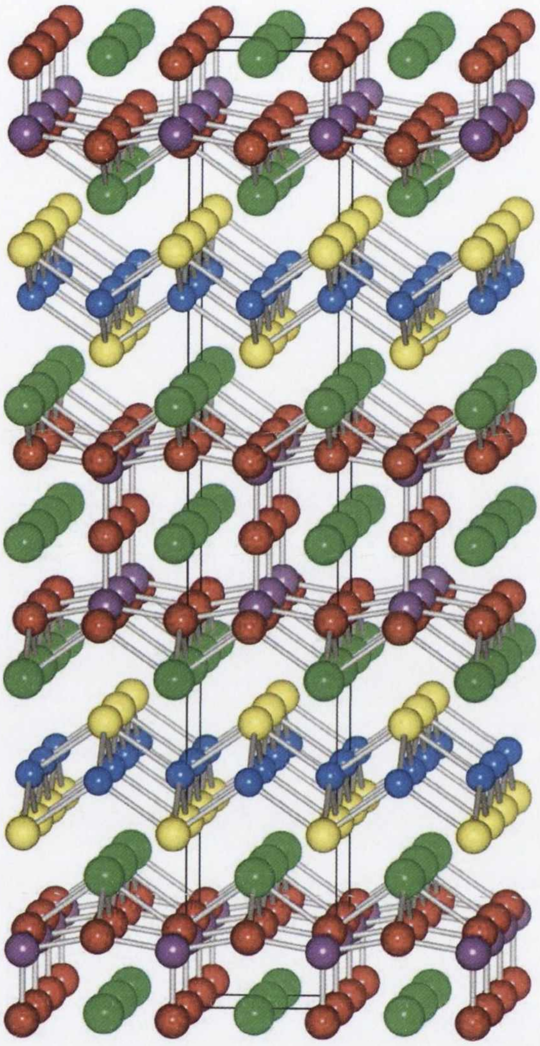

Figure 9.1: The layered structure of $[Cu_2S_2][Sr_3Sc_2O_5]$. The red, blue, yellow, purple and green balls are oxygen, copper, sulfur, scandium and strontium respectively. The unit cell is indicated by the black box.

In this chapter we use density functional theory (GGA+U and HSE06) to investigate the geometry and electronic structure of SCSOS. We show conclusively that (i) The VB features of SCSOS are consistent with other Cu^{I} based layered oxysulfides, (ii) the dispersion and effective hole masses at the VBM are consistent with the high reported conductivity of SCSOS and (iii) that the minimum optical band-gap is direct, making it potentially more useful in optoelectronic devices than indirect band-gap materials. The enhanced conductivity and hole mobility of SCSOS compared to other Cu^I based materials are discussed and strategies to improve this conductivity are formulated.

9.2 Calculation Methodology

All calculations were performed using the periodic DFT code VASP,[112,153]. The Perdew-Burke-Ernzerhof[193] (PBE) gradient corrected functional was used to treat the exchange and correlation, with the projector-augmented wave[103,111] (PAW) method was used to describe the interactions between the cores (Cu:[Ar], Sc:[Ne], Sr:[Ar], S:[Ne] and O:[He]) and the valence electrons. To counteract the errors associated with the DFT self-interaction,[154] calculations were performed using DFT corrected for on-site Coulombic interactions GGA+U[83] and a hybrid density functional (HSE06).[99] The value of U (applied to the Cu d states) used in this study was 5.2 eV. The value (α) of exact exchange used in the HSE06 calculations was 25$.

Structural optimizations of bulk SCSOS were performed using GGA+U and HSE06 at a series of volumes in order to calculate the equilibrium lattice parameters. In each case the the atomic positions, lattice vector and cell angle were allowed to relax, while the total volume was held constant. The resulting energy volume curves were fitted to the Murnaghan equation of state to obtain the equilibrium bulk cell volume.[113] Convergence with respect to k-point sampling and plane wave energy cut off were checked, and for GGA+U a cutoff of 500 eV and for HSE06 a cutoff of 400 eV were found to be sufficient. In both cases a k-point sampling of $6 \times 6 \times 1$ were found to be sufficient. Calculations were deemed to be converged when the forces on all the atoms were less than 0.01 eV Å^{-1}. Structure and charge density visualization and analysis were performed using VESTA[159].

9.3 Results

SCSOS crystallizes in the I4/mmm space group, with anti-PbO (litharge[349]) structured layers of $[Cu_2S_2]^{2-}$ alternating with perovskite like layers of $[Sr_3Sc_2O_5]^{2+}$, 9.1. [139] The GGA + *U* and HSE06 calculated lattice parameters and inter-atomic bond distances for SCSOS are shown in 9.1. The GGA + *U* results slightly overestimate the lattice constants, as is to be expected from a GGA calculation,[155] but are within 0.7% of the experimental values. The HSE06 calculations produced lattice constants slightly underestimated compared to the experimental data. Interestingly the Cu–Cu distances in SCSOS are 2.882 Å , which are longer than the Cu–Cu distances in LaCuOSe (2.876 Å) and virtually equivalent to the Cu–Cu distances in LaCuOS (2.8826 Å). [138] This result is quite surprising, as the Cu–Cu distances in copper delafossites can be a limiting factor in *p*-type conduction, as delafossites are governed by a polaronic hole hopping conduction mechanism.[58,60,61,166] In delafossite materials, the hole hops from Cu to Cu, making a shorter Cu–Cu distance extremely beneficial for good undoped conductivity.[166]. The conductivity of undoped SCSOS is know to be higher than that of LaCuOS and LaCuOSe,[139] so it would appear that the Cu–Cu distances do not have as significant an effect on conductivities in these layered oxychalcogenides.

The GGA + *U* calculated band structure of SCSOS along the high symmetry lines taken from Bradley and Cracknell[114] is shown in Figure 9.2. Both the VBM and the conduction band minimum (CBM) are situated at the Γ point, indicating that SCSOS is a direct band gap material. LaCuOS and LaCuOSe are also direct band gap materials, although BiCuOS and BiCuOSe are both indirect band gap materials, showing the sensitivity of the electronic structure of these layered materials to the choice of ionic cation in the non-$[Cu_2S_2]^{2-}$ layer.[351] The VBM at Γ displays promising dispersion, especially in the Γ–M direction, which can be viewed as being indicative of good *p*-type ability. This VB dispersion is visibly larger than that of any of the Cu^I based delafossites we have examined in Chapters 4 and 5 or of $SrCu_2O_2$.[53]

The GGA + *U* direct band gap, measured at the Γ point, is 2.12 eV. This is an

	GGA + U	HSE06	Experiment[350]
Volume	440.86	424.05	431.67
a	4.10	4.06	4.08
c	26.18	25.74	25.99
Cu–S	2.443	2.429	2.489
	2.554	2.520	2.515
Sr–O	2.901	2.870	2.882
	3.058	3.012	3.046
Sc–O	2.069	2.045	2.070
	1.997	1.972	1.903
Cu–Cu	2.901	2.873	2.882

Table 9.1: Structural data and nearest-neighbour interatomic distances for the GGA + U and HSE06 optimized [Cu_2S_2][$Sr_3Sc_2O_5$] and the experimental data from the work of Otzschi *et al.*[350] Volumes are given in Å^3 and lattice dimensions and interatomic distances in Å.

underestimation of the experimentally measured optical band gap of 3.1 eV, but is to be expected as GGA + U calculations are known to produce underestimated band gaps.[155] The HSE06 calculated direct band gap at the Γ point is 3.19 eV, which is in excellent agreement with the experimental value. HSE06 is expected to predict band gaps that are more consistent with experiment than those of LDA/GGA/GGA + U methods.[123,195,197–199]

The calculated total and partial (ion decomposed) electronic densities of states (EDOS/PEDOS) for SCSOS is shown in Figure 9.3 (a-f). The PEDOS were calculated by projecting wavefunctions onto atom centered spherical harmonics, with radii of 1.45 Å for Cu, 1.1 Å for Sr, 1.1 Å for Sc, 1.1 Å for S and 1.5 Å for O. The correct number of electrons are reproduced by these radii, and their ratios are consistent with the positions of charge density minima observed in valence-charge density plots. For

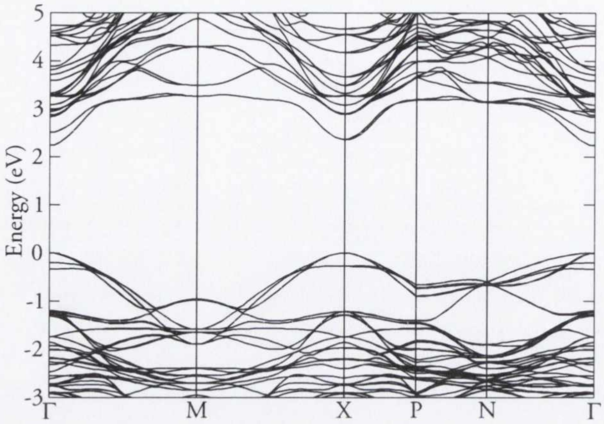

Figure 9.2: GGA + *U* calculated band structure of $[Cu_2S_2][Sr_3Sc_2O_5]$. The top of the valence band is set to 0 eV.

discussion, the VB is split into four regions (labeled I to IV), with the conduction band split into two regions (V and VI).

Region I lies between −6 eV and −4.5 eV and is composed mainly of sulfur 3*p* states with some minor mixing of Cu 3*d* and O 2*p*. Region II (between −4.5 eV and −3 eV) is dominated by O 2*p* and S 2*p* states, with the large peak at −3.8 eV in the EDOS being composed mainly of S 3*p*, O 2*p* with some mixing with Cu 3*d* states, and very minor contributions from Sc 3*d* states. Between −3 eV and −1 eV (Region III), Cu 3*d* states dominate with significant mixing with O 2*p* states and some minor interactions with with Sc 3*d* and S 3*p*. Region IV (−1 eV to the VBM), is dominated by hybridized Cu 3*d* and S 3*p* states, with very small contribution from O 2*p*. This is in contrast with the VBM features of most Cu^I based delafossites, which have Cu 3*d* states interacting strongly with O 2*p* states at the VBM.[152] Similar VBM features to those of SCSOS have been seen for LaCuOCh (Ch = S, Se, Te).[347] The bottom of the conduction band (Region V) is dominated by Sr 4*d* with some mixing with Sc 3*d* and O and S *s* states. Region VI (from 4 eV to 8, eV) is predominantly Sr 4*d* hybridized with Sc 3*d* states, with some minor mixing with O 2*p* states.

In an effort to gain insight into the band edge features of SCSOS (the states that will control any conduction), we have plotted the projections of the densities for both

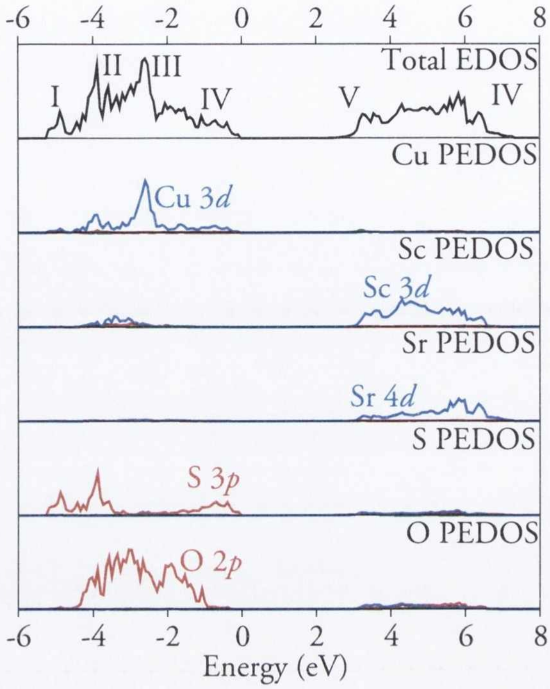

Figure 9.3: The electronic density of states for $[Cu_2S_2][Sr_3Sc_2O_5]$.(a) Total EDOS, (b) Cu PEDOS, (c) Sc PEDOS, (d) Sr PEDOS, (e) S PEDOS and (f) O PEDOS. The black lines represent total EDOS, blue lines represent *d* states, green *s* states and red *p* states.

the VBM and the CBM at the Γ point through a (010) plane containing Cu, S, Sc, Sr and O atoms, labeled (b) and (c) in Figure 9.4. It is clear from analysis of the VBM, Figure 9.4 (b), that the vast majority of the density resides in the $[Cu_2S_2]^{2-}$ layers, with the density on the S ions having *p* orbital character and the density on the Cu states having *d* orbital character. A numerical analysis of the states at the VBM shows that it consists of $\sim$ 49% Sulfur p_x and $\sim$ 39% copper d_{xy} states. The absence of any significant density on the oxygen ions indicates that oxygen states do not contribute to the *p*-type conductivity of this layered material.

A similar numerical breakdown of the states at the CBM at Γ reveals that it is composed of $\sim$ 43% sulfur *s* and p_z states, with $\sim$ 39% Sr *s* states and $\sim$ 12% O p_x states. This is further evidenced by the charge density plot of the CBM, 9.4 (c), which clearly shows the polarized *s* and p_z states on the sulfur, and the *s* states of Sr and O

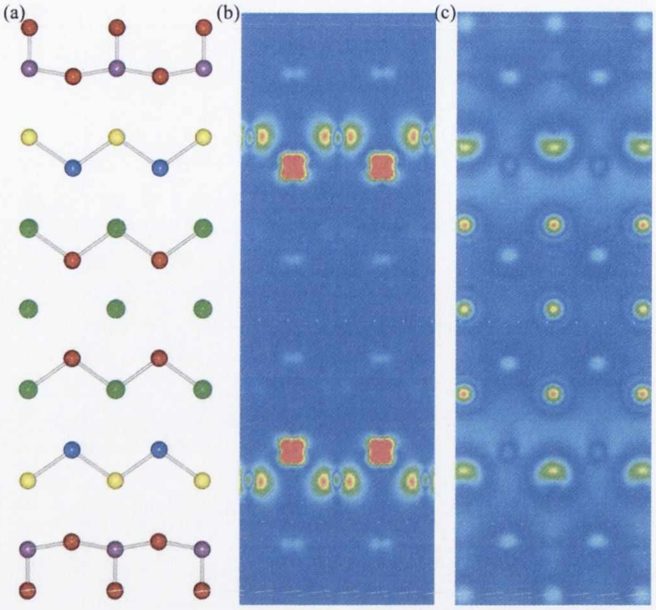

Figure 9.4: Charge density contour plots showing the band edges of $[Cu_2S_2][Sr_3Sc_2O_5]$ through a (010) plane. (a) is the structure of the cell in the (010) plane, (b) is the charge density of the VBM at Γ and (c) is the charge density of the CBM at Γ, plotted from 0 eV (blue) to 0.003 eV (red) e.$Å^{-3}$

are visible, with a distinct absence of density on the Sc and Cu states.

The optical absorption spectra for SCSOS, calculated using GGA+U and HSE06, is shown in Fugure 9.5. For SCSOS we find that fundamental band-edge transitions at the Γ point *are* symmetry allowed, with absorption beginning at 2.12 eV for GGA+U and 3.19 eV for HSE06. Using the Tauc relation ($E_g \propto \alpha^2$), we predict the optical band gaps of SCSOS to be 2.41 eV and 3.48 eV using GGA+U and HSE06 respectively. The HSE06 calculated absorption spectra are in good agreement with the absorption spectra reported from experiment.[139]

While a large optical band gap is vital for a material to be transparent, *p*-TCO materials should also have no visible light absorption between the bands below the VBM and the VBM itself (or a hole state near the VBM).[20] Similarly for *n*-type TCOs, there should be no absorption between the CBM and the conduction bands above.[19] For *p*-type (*n*-type) TCOs, it is necessary to avoid transitions between unoccupied

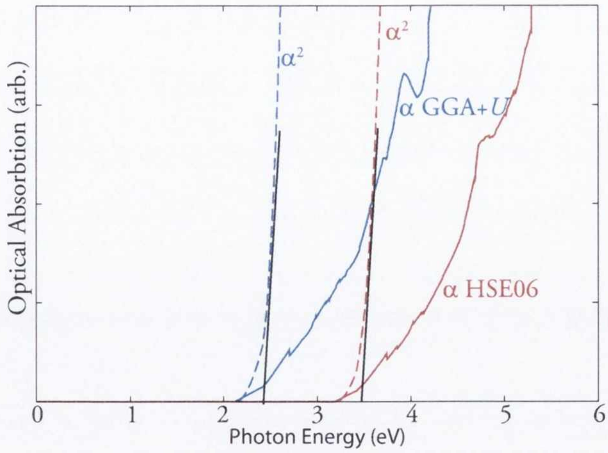

Figure 9.5: Calculated optical absorption spectrum of $[Cu_2S_2][Sr_3Sc_2O_5]$ summed over all possible direct valence to conduction band transitions. GGA + U (blue) and HSE06 (red).

(occupied) defect bands and the bands within 3.1 eV of the VBM (CBM), meaning that the defective systems are still transparent to visible light.[19] We have tested the VB-VBM transitions in SCSOS by calculating the dipole transition matrix elements between the VBM and the other VB states at Γ. This analysis revealed that the dipole transition probabilities are negligible between the VBM and states within 3.3 eV below the VBM. This is to be expected, as on-site transitions between states of the same angular momentum (e.g. O p to O p and Cu d to Cu d) are forbidden due to the classical selection rule.[20] The experimental samples of SCSOS examined by Liu et al. were known to contain intrinsic defects,[139] yet still report a band gap of 3.1 eV. If transitions between the unoccupied hole states and occupied valence bands within 3.1 eV of the VBM were allowed, the material would not be transparent. Therefore we conclude that SCSOS has all the attributes of transparency, namely a wide fundamental band gap and no visible light absorption between the bands below the VBM and the VBM.

The hole effective mass at the VBM of SCSOS has been calculated (as described in Section 3.3.3 to gain insights into the materials p-type ability. The calculated effective masses in the different lattice directions and high symmetry line from Γ to M are presented in 9.2. It is clear from the calculated masses, that *all* conductivity takes place in the the AB plane, most likely in the $[Cu_2S_2]^{2-}$ layers, and the material does not conduct in the c direction. The effective hole masses at the VBM are isotropic in both the a and b directions with effective masses of $2.8\,m_e$. The lowest hole masses occurs on the line from Γ to M and is $0.9\,m_e$

	[001]	[010]	[100]	Γ–M
Effective hole mass	∞	2.86	2.86	0.96

Table 9.2: Effective hole masses of $[Cu_2S_2][Sr_3Sc_2O_5]$ calculated using GGA+U. All hole effective masses given in m_e.

It is instructive to note that a similar analysis of the industry standard n-type TCO, In_2O_3, was carried out, and it resulted in an effective hole mass at the VBM of $16\,m_e$ and an effective electron mass at the CBM of $0.24\,m_e$.[21] If this is taken to be indicative of excellent n-type ability and very poor p-type ability, then the effective masses calculated for SCSOS suggest reasonable p-type ability. This highlights that strong mixing of low binding energy cation states (here Cu 3d) with S 3p is required to provide valence band dispersion.

9.4 Discussion

Optimizing conductivity and transparency in layered oxychalcogenides is a very dificult task.[345] Replacement of S with Se or Te in the $[Cu_2Ch_2]^-$ layers can increase the p-type ability of these materials, but such an improvement normally comes at the expense of transparency.[345] A correlation between the basal lattice parameter (a) and band gap has been investigated for various layered oxychalcogenides and fluoride chalcogenides [345], and the correlation is by no means linear. It is instructive to note that the bandgaps for Te based layered chalcogenides range between $2.2 - 2.4$ eV regardless of lattice parameter while the Se based materials have bandgaps ranging from just under 3 eV (BaFCuSe, $a = \sim 4.25$ Å) to ~ 2.5 eV (YCuOSe, $a = \sim 3.9$ Å). The oxychalcogenides and fluoride chalcogenides that contain sulfur have band gaps between 3.2 eV and $\sim$ 3 eV, with the largest band gaps corresponding to basal lattice parameters bigger than 4.0 Å, with SCSOS fitting nicely into that trend, having a basal lattice parameter of 4.08 Å.[139]

The reduction of the band gap when the basal lattice parameter is smaller, is ascribed to the shortening of the Cu-Cu distances in the $[Cu_2Ch_2]^-$ layers, which is thought to result in the broadening of the valence band and conduction band.[345] This has been discussed in detail in the case of LaCuOSe (band gap of 2.8 eV) and YCuOSe (band gap of 2.3 eV).[352] In contrast to this, for Cu(I)-based Delafossite TCOs, the *a* lattice parameter does not control the band-gap, but rather has an impact on the conductivity of these materials, as conductivity is know to occur via a polaronic, hopping mechanisms[60,61,166], with the Cu–Cu distances placing a limit on conductivity.

Interestingly, as SCSOS contains Sc as its trivalent cation in the perovskite like layer, doping with bigger trivalent cations like Y or La *should* increase the basal lattice parameter, increase the Cu-Cu distance, and possibly increase the transparency. Replacing Sr with Ba could also be another method of increasing the *a* lattice parameter. Undoubtedly, the ability to tune the transparency of SCSOS would be of much interest, but the ability to increase the *p*-type ability would be equally attractive. If the transparency could be increased by isovalent doping, to such an extent that doping with Se in the S site could be accommodated without decreasing the band gap below the 3.1 eV limit of transparency to visible light, then it is quite possible that an improved transparent conducting material could be designed.

Typically hole carriers in layered oxychalcogenides are the product of Cu deficiency, and this could be the case for $[Cu_2S_2][Sr_3Sc_2O_5]$.[139] One of the advantages of the thick perovskite-like layer in SCSOS is that it provides a robust structural block, with two cation sites for *p*-type doping, *and* could also be an extra source of cation deficiency, in both the Sr and Sc cation positions.[139] Defects and conductivity in layered oxychalcogenides have recieved limited experimental characterization, and surprisingly no theoretical attention. Undoped LaCuOSe has been reported to have a shallow acceptor level $\sim$ 20 meV above the VBM with temperature dependent *p*-type conduction.[353] Mg-doped LaCuOSe, however, exhibits no temperature dependence of hole concentration or mobility, indicating that it is a degenerate semiconductor,[348] with a conductivity as high as 910 S cm^{-1}. Thus it is quite plausible that doping of the Sc site with Ca or Mg would lead to a marked improvement in conductivity and possibly lead to degenerate semiconductor behaviour, as has been demonstrated in the case of LaCuOSe:Mg.[353] Alternatively doping of the Sr site with K, Na or Li would also increase the number of hole carriers in the material. Allied to the extremely high undoped conductivity reported for SCSOS, the *exceptionally* large mobility of holes in SCSOS indicate the possibility of much improved conductivity when doped *p*-type.[139] Thus SCSOS, which was originally synthesized as a candidate superconductor[350], could possibly represent the ideal structural motif for designing high figure of merit *p*-type transparent conducting materials that are so sought after by materials scientists. Further investigation of aliovalent and isovalent doping of SCSOS is thus warranted.

9.5 Conclusion

In this chapter, we have performed a detailed DFT examination of the new layered transparent conducting oxychalcogenide $[Cu_2S_2][Sr_3Sc_2O_5]$, using GGA corrected for on-site Coulombic interactions (GGA+U) and a hybrid density functional (HSE06). $[Cu_2S_2][Sr_3Sc_2O_5]$ is found using HSE06 to possess a direct optical band gap of $\sim$ 3.5 eV, which is a slight overestimation of the experimentally predicted optical band gap. Analysis of the band edges and effective masses indicate the potential for excellent *p*-type ability, consistent with the experimentally reported high hole mobility. This increased hole mobility is caused by the favourable mixing of the S 3*p* states and the Cu 3*d* states at the valence band maximum.

Chapter 10

Conclusions

10.1 Conclusions

The main aim of this thesis was to gain an understanding of the complex chemistry of Cu^{I}-based oxide materials, and to evaluate their ability as both semiconductor and TCO materials. Through detailed analysis of the electronic structure of the stoichiometric copper delafossites, we have shown that the electronic structure of the M^{III} cation in $CuM^{III}O_2$ delafossites play a very important role in the conductivity of these materials. The influence of the *d* states of Y, Sc and Cr on the density of states was investigated, with the Cr *d* states of $CuCrO_2$ found to have the greatest influence on the valence band makeup of the delafossites. Bader analysis indicated that the covalent interactions between the trivalent metal and oxygen follows the trend Cr>Sc>Y>Al with Cr having the greatest covalent interaction with oxygen. This trend follows the experimental trend of conductivity in doped delafossites. Thus we conclude that favourable cation size *and* favourable mixing between the *d* states of the M^{III} ion and the O $2p$ states, are likely to determine mobility and conduction in these delafossite type materials.

We have also investigated the most recent Cu-based delafossite to be discovered, $CuBO_2$. Using GGA $+U$ and HSE06 we have shown that the lattice parameters reported from the sole experiment are highly questionable, with our GGA + U and

HSE06 calculated lattice parameters comparing excellently with known experimental trends. We found that $CuBO_2$ possesses a fundamental indirect band gap of $\sim 3.1\,\mathrm{eV}$, with a predicted optical band gap of $\sim 3.6\,\mathrm{eV}$, which are an underestimation and overestimation respectively, of previous experimental absorption data. Analysis of the band extrema shows that B plays virtually no role in the states that govern conduction. Calculated effective masses of the band edges predict good *p*-type conductivity, consistent with experiment. This increased intrinsic conductivity relative to other delafossite TCOs is attributed to the Cu–Cu distances in $CuBO_2$ being smaller than in any other delafossite, as the B states play no part in mediating conductivity

In Chapter 6 we investigated the defect chemistry of Cu_2O, the parent compound of all the Cu-based delafossites, using PBE, PBE+U and the HSE functional. The defect chemistry of Cu_2O is considered to be very similar to that of the delafossites, and thus understanding defects in Cu_2O is a vital starting point to understanding the defect chemistry of the copper delafossites. Our results clearly show that PBE and PBE+U cannot recreate the experimentally known activated polaronic conductivity of Cu_2O. HSE, however, provides a much better description of conductivity in Cu_2O, predicting deep single particle levels, with localized defect state, consistent with a polaronic material. In addition the calculated ionization levels are in excellent agreement with the most recent DLTS studies of this system. We have also examined the *n*-type defect chemistry of this system, and found that native donor defects in Cu_2O cannot be the cause of the *n*-type Cu_2O samples frequently reported in the literature. We have also investigated the effect of H impurities on the *n*-type conductivity of Cu_2O, finding that H does not act as a donor in Cu_2O, and in fact acts as a hole killer, passivating any *p*-type conductivity in the system.

Using the knowledge that a hybrid DFT method is necessary to accurately describe conductivity in Cu^{I}-based oxides, we used the HSE functional to investigate the defect chemistry of $CuAlO_2$. We found that *p*-type defects will dominate under all growth conditions in this material, however the ionization levels of the defects were found to be quite deep in the band gap, indicating that high-performance *p*-type TCO performance will never be realised in $CuAlO_2$. Interestingly, we found that the defect with the lowest formation energy was Cu_{Al} and not V_{Cu}, as had previously been predicted. Our calculations match very well with the most recent experimental studies, and explain for the first time the defect signals seen in recent optical absorption experiments. We have also identified that the optical transition level of Cu_{Al} is most likely to be the source of defect signals which were believed to be indirect band gap signals.

We also examined the defect chemistry of $CuCrO_2$, the delafossite with the highest reported conductivity, finding that the ionization levels of *p*-type defects in $CuCrO_2$ are considerably shallower than for $CuAlO_2$. In addition, the hole state is less-localized on the Cu atoms near a V_{Cu} in $CuCrO_2$ than in $CuAlO_2$, which can explain the higher conductivity of $CuCrO_2$ relative to $CuCrO_2$. As indicated in Chapter 7, the increased covalency of the $CuCrO_2$ valence band is thought to mediate the shallower defect levels in $CuCrO_2$ relative to $CuAlO_2$.

Although we have now gained an understanding of conductivity in Cu^I-based oxides oxides, its is apparent that conductivity in these materials will always be activated, and thus the delafossite structure is not going to produce a degenerate *p*-type semiconductor. Therefore, we investigated two other possible structural motifs which have been reported to display *p*-type TCO ability. Firstly we examined the electronic structure of $ZnM_2^{III}O_4$ (M^{III} = Co, Rh, Ir). Unfortunately, the lack of dispersion at the VBMs of all three spinels indicates that these materials will be dominated by polaronic conductivity, and will *never* be a suitable *p*-type alternative to the industry standard *n*-type TCOs. Our results also call into question the transparency of $ZnIr_2O_4$, and we therefore suggest a re-investigation of the band gaps of these materials is warranted.

Finally we have examined the electronic structure of $[Cu_2S_2][Sr_3Sc_2O_5]$, a transparent layered oxysulphide which has been reported to possess a high hole mobility. Analysis of the band edges and effective masses indicate the potential for good *p*-type ability, consistent with the experimentally reported high hole mobility. This increased hole mobility is caused by the favourable mixing of the S 3*p* states and the Cu 3*d* states at the valence band maximum.

Transport in delafossite materials such as $CuAlO_2$ will likely be dominated by *deep* defect levels, and therefore will never realize the high figure of merit performances needed to rival their n-type counterparts. The conductivities of these p-type TCOs are on average *three* orders of magnitude lower than their high performance n-type counterparts,[51] and the majority of the delafossites possess indirect band gaps, which limit their efficiency in optoelectronic devices.[354] It is becoming increasingly clear that materials based on Cu–O mixing at the VBM will not produce degenerate semiconductors, unless strategies to mix other cations with states that will resonate near the VBM and enhance conductivity can be found.[257] $CuCrO_2$:Mg displays the highest conductivity of all the delafossites, possibly due to favourable mixing of Cr d states with the Cu and O states in the VBM,[257] however, the conductivity is still ~ 2 orders of magnitude below that of the standard n-type TCOs. The most promising approach to develop high performance p-type TCOs would appear to be to explore the rich chemistry of layered oxychalcogenides.[345] These materials are composed of layers of $[Cu_2S_2]^{2-}$, sandwiched between layers of ionic metal oxides.[345] To date oxychalcogenides have shown great promise, displaying large mobilities (e.g. $(Cu_2S_2)(Sr_3Sc_2O_5)$, $150\,cm^2V^{-1}s^{-1}$), [139] and to have the ability to become degenerate semiconductors when doped (e.g. LaCuOSe:Mg).[353] The challenge remains to engineer a layered oxychalcogenide with sufficient p-type conductivity and transparency, to equal the performance of the n-type TCOs.

10.2 Future research directions

10.2.1 p-type TCOs

As the limitations of Cu-based delafosssite oxides as TCO materials is now apparent, research must now focus on new structural motifs to provide degenerate p-type semiconducting ability. As mentioned above, layered oxychalcogenides represent a very promising structural platform for enhanced p-type ability. Stoichiometric cation substitutions should be examined in the $(Cu_2S_2)(Sr_3Sc_2O_5)$ motif and its sister compound,

$(Cu_2S_2)(Sr_4Cr_2O_6)$. Optimization of transpareny and conductivity should be examined with complementary cation and anion substitutions used to tune the band gaps of these materials to the specific device requirement. Also, the large, robust perovskite-like layers in these systems provide an ideal platform for acceptor doping.

10.2.2 *p*-type PEC electrodes

Reduction of the global dependence on fossil fuels, and the realization of effective renewable energy technologies are much sought after goals in this environmentally conscious age. Construction of clean energy systems is therefore a key objective, with hydrogen representing the ultimate clean fuel. To date, the majority of hydrogen produced emanates from fossil fuels, which unfortunately yield CO_2 as a major product. The production of hydrogen directly through the conversion of visible light to electrical energy thus represents an ideal alternative. Photoelectrochemical (PEC) decomposition of water by visible light to form hydrogen and oxygen is currently considered as the most desirable method of hydrogen production.[355] The products can subsequently be stored and utilised in fuel cell technologies to generate emission-free electricity.

Metal oxides have generally been the ideal candidate photoelectrodes for PEC water splitting due to: (a) their low cost, and (b) their relatively high stability in aqueous media.[355] However, most metal oxides possess optical band gaps that are larger than the visible range ($> 3\,\mathrm{eV}$), which means they are excellent for transparent electronics, but yield poor solar to hydrogen conversion efficiencies. It is now well established that the criteria for a suitable PEC photoelectrode are: (i) low band gap ($1.7 - 2.2\,\mathrm{eV}$), (ii) low resistivity, (iii) corrosion resistant, (iv) low cost and (v) correct alignment of the band edges relative to the water redox potentials.[355] TiO_2, with its good catalytic activity has been extensively studied for PEC applications, however efforts to reduce its large band gap (Anatase 3.2 eV, Rutile 3.0 eV) by doping or co-doping have failed to produce a truly promising material. Thus the grand challenge is to discover a low band gap semiconductor that is catalytically active, stable in solution and possesses a high overall solar-to-hydrogen conversion efficiency.

An important factor that is often overlooked in PEC research is that *p*-type materials are extremely desirable for self-biased pn junctions, termed PEC diodes.[178] The delafossite structure has recently gathered attention as a possible PEC photoelectrode, [178] however the overly large band gaps have proved prohibitive to performance. Taking inspiration from decades of solar cell absorber research,[199] it should be possible to cation mutate the $\mathrm{M^{III}}$ position in the delafossite structure. Cation mutation of the $\mathrm{Cu^{I}M^{III}O2}$ ($\mathrm{M^{III}}$= Al, Cr, In etc.) delafossites, by replacing $\mathrm{M^{III}}$ with $\mathrm{A^{II}/B^{IV}}$ or $\mathrm{A^{II}/B^{V}}$ cation mixes, whilst retaining the overall structure of the delafossite, should be plausible, and in fact the synthesis of $\mathrm{Cu_2NiTiO_4}$ and $\mathrm{Cu_3Zn_2SbO_6}$ delafossites has been reported.[51]

The mixing of the Cu $3d$ states with the O $2p$ states at the valence band maximum (VBM) will raise the valence band nearer to the $\mathrm{O_2/H_2O}$ redox potential than for standard oxide VBMs (e.g. $\mathrm{TiO_2}$). Specifically cations should be targeted that are expected to lead to good photocatalytic properties (e.g. Ti, Ta, Nb) or good *n*-type conductivity (e.g. Ge, Sn, Zn, Cd), using established chemical design strategies to predict materials that hit the target criteria for PEC applications and are also abundant within the earth's crust. In this respect, computational modeling can lead the field in the prediction of next generation materials for PEC applications

Bibliography

[1] H. Hosono. *Thin Solid Films*, **515**(15), 6000 (2007).

[2] T. Minami. *Thin Solid Films*, **516**, 5822 (2008).

[3] B. J. Ingram, G. B. Gonzalez, D. R. Kammler, M. I. Bertoni and T. O. Mason. *J. Electroceram.*, **13**, 167 (2004).

[4] K. Bädeker. *Ann. Phys. Berlin*, **327**(4), 749 (1907).

[5] J. T. Littleton. Insulator, (1938).

[6] R. G. Gordon. *MRS Bull.*, **25**, 52–57 (2000).

[7] M. J. Zunick. Conductive coating on glass, (1950).

[8] K. Wasa, S. Hayakawa and T. Hada. *Jap. J. Appl. Phys.*, **10**, 1732 (1971).

[9] T. Minami. *Semicond. Sci. Tech.*, **20**, S35–S44 (2005).

[10] A. Suzuki, T. Matsushita, T. Aoki, Y. Yoneyama and M. Okuda. *Jap. J. Appl. Phys.*, **40**, L401 (2001).

[11] G. Thomas. *Nature*, **389**, 907 (1997).

[12] H. Kawazoe, H. Yasakuwa, H. Hyodo, M. Kurita, H. Yanagi and H. Hosono. *Nature*, **389**, 939 (1997).

[13] A. N. Banerjee and K. K. Chattopadhyay. *Prog. Cryst. Growth Char. Mater.*, **50**, 52 (2005).

[14] Y. Ishii. *J. Display Technol.*, **3**, 351 (2007).

[15] http://www.fokus-technologies.de/technology_en.phtml.

[16] G. A. Niklasson and C. G. Granqvist. *J. Mater. Chem.*, **17**, 127 (2007).

[17] C. G. Granqvist. *Solar Energy Mater. Solar Cells*, **91**, 1529 (2007).

[18] A. Walsh, J. L. F. Da Silva, S. H. Wei, C. Korber, A. Klein, L. F. J. Piper, A. DeMasi, K. E. Smith, G. Panaccione, P. Torelli, D. J. Payne, A. Bourlange and R. G. Egdell. *Phys. Rev. Lett.*, **100**, 167402 (2008).

[19] Ç. Kılıç and A. Zunger. *Phys. Rev. Lett.*, **88**, 095501 (2002).

[20] X. L. Nie, S. H. Wei and S. B. Zhang. *Phys. Rev. B*, **65**, 075111 (2002).

[21] A. Walsh, J. L. F. Da Silva and S. H. Wei. *Phys. Rev. B.*, **78**, 075211 (2008).

[22] O. N. Mryasov and A. J. Freeman. *Phys. Rev. B*, **64**, 233111 (2001).

[23] H. Kawazoe and K. Ueda. *J. Am. Ceram. Soc.*, **82**, 3330 (1999).

[24] Y. Yang, S. Jin, J. E. Medvedeva, J. R. Ireland, A. W. Metz, J. Ni, M. C. Hersam, A. J. Freeman and T. J. Marks. *J. Am. Chem. Soc.*, **127**, 8796 (2005).

[25] A. F. Kohan, G. Ceder, D. Morgan and C. G. Van de Walle. *Phys. Rev. B*, **61**, 15019–15027 (2000).

[26] A. Janotti and C. G. Van de Walle. *Phys. Rev. B*, **76**, 165202 (2007).

[27] S. J. Clark, J. Robertson, S. Lany and A. Zunger. *Phys. Rev. B*, **81**, 115311 (2010).

[28] A. K. Singh, A. Janotti, M. Scheffler and C. G. Van de Walle. *Phys. Rev. Lett.*, **101**, 055502 (2008).

[29] C. G. Van de Walle. *Phys. Rev. Lett.*, **85**, 1012–1015 (2000).

[30] A. Janotti and C. G. Van de Walle. *Nat. Mater.*, **6**, 44–47 (2007).

[31] S. F. J. Cox, E. A. Davis, S. P. Cottrell, P. J. C. King, J. S. Lord, J. M. Gil, H. V. Alberto, R. C. Vilao, J. Piroto Duarte, N. Ayres de Campos, A. Wiedinger, R. L. Lichti and S. J. C. Irvine. *Phys. Rev. B*, **86**, 2601–2604 (2001).

[32] S. F. J. Cox, J. S. Lord, S. P. Cottrell, J. M. Gil, H. V. Alberto, A. Keren, D. Prabhakaran, R. Scheuermann and A. Stoykov. *J. Physics-condensed Mat.*, **18**(3), 1061–1078 (2006).

[33] P. D. C. King, R. L. Lichti, Y. G. Celebi, M. Gil, R. C. Vilao, H. V. Alberto, Piroto Duarte, D. J. Payne, R. G. Egdell, I. McKenzie, C. F. McConville, S. F. J. Cox and T. D. Veal. *Phys. Rev. B*, **80**, 081201(R) (2009).

[34] O. F. Schirmer. *J. Phys. Condens. Matter*, **18**, R667–R704 (2006).

[35] A. M. Stoneham, J. Gavartin, A. L. Shlugher, A. V. Kimmel, D. Mũnoz Ramo, H. M. Rønnow, G. Aeppli and C. Renner. *J. Phys.: Condens. Matter*, **19**, 255208 (2007).

[36] J. Li, S. H. Wei, S. S. Li and J. B. Xia. *Phys. Rev. B*, **74**, 081201 (2006).

[37] J. B. Yan, Y. F. amd Li, S. H. Wei and M. M. Al-Jassim. *Phys. Rev. Lett.*, **98**, 135506 (2007).

[38] S. Lany and A. Zunger. *Physical Review B*, **80**(8), 085202 (2009). 492FC Times Cited:0 Cited References Count:33.

[39] J. P. Hu, D. J. Payne, R. G. Egdell, P. A. Glans, T. Learmonth, K. E. Smith, J. Guo and N. M. Harrison. *Phys. Rev. B*, **77**, 155115 (2008).

[40] H. Kawazoe, H. Yanagi, K. Ueda and H. Hosono. *MRS Bull.*, **25**, 28–36 (2000).

[41] A. Buljan, P. Alemany and E. Ruiz. *J. Phys. Chem. B*, **103**, 8060–8066 (1999).

[42] H. C. Kandpal and R. Seshadri. *Solid State Sci.*, **4**, 1045–1052 (2002).

[43] D. J. Aston, D. J. Payne, A. J. H. Green, R. G. Egdell, D. S. L. Law, J. Guo, P. A. Glans, T. Learmonth and K. E. Smith. *Phys. Rev. B*, **72**, 195115 (2005).

[44] H. Yanagi, S. Inoue, K. Ueda, H. Kawazoe, H. Hosono and N. Hamada. *J. Appl. Phys.*, **88**, 4059–4163 (2000).

[45] A. Önsten, M. Månsson, T. Claesson, T. Muro, T. Matsushita, T. Nakamura, T. Kinoshita, U. O. Karlsson and O. Tjernberg. *Phys. Rev. B*, **76**, 115127 (2007).

[46] R. Laskowski, P. Blaha and K. Schwarz. *Phys. Rev. B*, **67**, 075102 (2003).

[47] B. U. Köhler and M. Jansen. *Z. Anorg. Allg. Chem.*, **543**, 73 (1986).

[48] A. Filippetti and V. Fiorentini. *Phys. Rev. B*, **72**, 035128 (2005).

[49] E. Ruiz, S. Alvarez, A. Alemany and R. Evarestov. *Phys. Rev. B*, **56**, 7189 (1997).

[50] A. Buljan, M. Llunell, E. Ruiz and P. Alemany. *Chem. Mater.*, **13**, 338–344 (2001).

[51] M. A. Marquardt, N. A. Ashmore and D. P. Cann. *Thin Solid Films*, **496**, 146–156 (2006).

[52] A. Kudo, H. Yanagi, H. Hosono and H. Kawazoe. *Appl. Phys. Lett.*, **73**, 220–222 (1998).

[53] K. G. Godinho, G. W. Watson, A. Walsh, A. J. H. Green, D. J. Payne, J. Harmer and R. G. Egdell. *J. Mater. Chem.*, **18**, 2798–2806 (2008).

[54] K. Ueda, S. Inoue, S. Hirose, H. Kawazoe and H. Hosono. *Appl. Phys. Lett.*, **77**, 2701–2703 (2000).

[55] R. Nagarajan, A. D. Draeseke, A. W. Sleight and J. Tate. *J. Appl. Phys.*, **89**, 8022 (2001).

[56] H. Katayama-Yoshida, K. Sato, H. Kizaki, H. Funashima, I. Hamada, T. Fukushima, V. A. Dinh and M. Toyoda. *Appl. Phys. A*, **89**, 19–27 (2007).

[57] I. Hamada and H. Katayama-Yoshida. *Physica. B*, **376–377**, 808–811 (2006).

[58] B. J. Ingram, T. O. Mason, R. Asahi, K. T. Park and A. J. Freeman. *Phys. Rev. B*, **64**, 155114 (2001).

[59] B. J. Ingram, M. I. Bertoni, K. R. Peoppelmeier and T. O. Mason. *Thin Solid Films*, **486**, 86–93 (2005).

[60] B. J. Ingram, G. B. Gonzalez, T. O. Mason, D. Y. Shahriari, A. Barnabe, D. Ko and K. R. Poeppelmeier. *Chem Mater.*, **16**, 5616–5622 (2004).

[61] B. J. Ingram, B. J. Harder, N. W. Hrabe, T. A. Mason and K. R. Poeppelmeier. *Chem. Mater.*, **16**, 5623–5629 (2004).

[62] V. Fock. *Z. Phys. A: Hadrons Nucl.*, **62**, 795 (1930).

[63] A. R. Leach. *Molecular Modelling. Prinicples and Applications.* Prentice Hall, (2001).

[64] P. Lowdin. *Phys. Rev.*, **97**, 1509–1520 (1955).

[65] P. Hohenburg and W. Kohn. *Phys. Rev.*, **136**, B864 (1964).

[66] W. Kohn and L. J. Sham. *Phys. Rev.*, **140**, A1133–A1138 (1965).

[67] W. Koch and M. C. Holthausen. *A Chemist's Guide to Denisty Functional Theory.* Wiley-VCH, (2002).

[68] F. Bloch. *Z. Phys. A: Hadrons Nucl.*, **57**, 545 (1919).

[69] P. A. M. Dirac. *Math. Proc. Camb. Phil. Soc.*, **26**, 376 (1930).

[70] D. Ceperley and B. Alder. *Phys. Rev. Lett.*, **45**, 566 (1980).

[71] S. H. Vosko, L. Wilk and M. Nusair. *Can. J. Phys.*, **58**, 1200 (1980).

[72] A. D. Becke. *Phys. Rev. A*, **38**, 3098 (1988).

[73] C. T. Lee, W. T. Yang and R. G. Parr. *Phys. Rev. B*, **37**, 785 (1988).

[74] J. P. Perdew and W. Y. *Phys. Rev. B*, **33**, 8800 (1986).

[75] J. P. Perdew, K. Burke and M. Ernzerhof. *Phys. Rev. Lett.*, **77**, 3865 (1996).

[76] M. A. Henderson, C. Perkins, M. H. Engelhard, S. Thevuthasan and C. H. F. Peden. *Surf. Sci.*, **526**, 1–18 (2003).

[77] M. Nolan, S. Grigoleit, D. C. Sayle, S. C. Parker and G. W. Watson. *Surf. Sci.*, **576**, 217–229 (2005).

[78] J. P. Allen, D. O. Scanlon and G. W. Watson. *Phys. Rev. B*, **81**, 161103(R) (2010).

[79] R. W. Godby, M. Schluter and L. J. Sham. *Phys. Rev. Lett.*, **56**(22), 2415–2418 (1986).

[80] J. P. Perdew and A. Zunger. *Phys. Rev. B*, **23**, 5048 (1981).

[81] G. I. Csonka, O. A. Vydrov, G. E. Scuseria, A. Ruzsissky and J. P. Perdew. *J. Chem. Phys.*, **126**, 244107 (2007).

[82] L. Ackermann, J. D. Gale and C. R. A. Catlow. *J. Phys. Chem. B*, **101**(48), 10028 (1997).

[83] S. L. Dudarev, G. A. Botton, S. Y. Savrasov, C. J. Humphreys and A. P. Sutton. *Phys. Rev. B*, **57**, 1505 (1998).

[84] A. B. Shick, W. E. Picket and A. I. Liechtenstein. *J. Electron Spec. Rel. Phen.*, **114–116**, 753–758 (2001).

[85] M. Cococcioni and S. de Gironcoli. *Phys. Rev. B*, **71**, 035105 (2005).

[86] N. J. Mosey and E. A. Carter. *Phys. Rev. B*, **76**, 155123 (2007).

[87] S. F. Li, H. Lu, P. Li, Z. Yang and Z. X. Guo. *J. Chem. Phys.*, **128**, 164718 (2008).

[88] D. O. Scanlon, A. Walsh, B. J. Morgan and G. W. Watson. *J. Phys. Chem. C*, **112**, 9903–9911 (2008).

[89] S. Laubach, P. C. Schmidt, A. Thissen, F. J. Fernandez-Madrigal, Q. H. Wu, W. Jaegermann, M. Klemm and S. Horn. *Phys. Chem. Chem. Phys.*, **9**(20), 2564–2576 (2007).

[90] R. Coquet and D. J. Willock. *Phys. Chem. Chem. Phys.*, **7**, 3819–3828 (2005).

[91] B. J. Morgan, D. O. Scanlon and G. W. Watson. *J. Mater. Chem.*, **19**, 5175–5178 (2009).

[92] D. O. Scanlon, N. M. Galea, B. J. Morgan and G. W. Watson. *J. Phys. Chem. C*, **113**, 11095–11103 (2009).

[93] A. D. Becke. *J. Chem. Phys.*, **98**, 1372 (1993).

[94] A. D. Becke. *J. Chem. Phys.*, **98**, 5648 (1993).

[95] P. J. Stephens, F. J. Devlin, C. F. Chabalowski and M. J. Frisch. *J. Phys. Chem.*, **98**, 11623 (1994).

[96] J. Paier, M. Marsmann and G. Kress. *J. Chem. Phys.*, **127**, 024103 (2007).

[97] C. Adamo and V. Barone. *J. Chem. Phys.*, **110**, 6158 (1999).

[98] J. P. Perdew, M. Ernzerhof and K. Burke. *J. Chem. Phys.*, **105**, 9982 (1996).

[99] S. Heyd, G. E. Scuseria and M. Ernzerhof. *J. Chem. Phys.*, **118**, 8207–8215 (2003).

[100] A. Walsh, J. L. F. Da Silva and S. H. Wei. *Phys. Rev. Lett.*, **100**, 256401 (2008).

[101] E. Wimmer, A. Freeman, M. Weinert, H. Krakauer, J. Hiskes and A. Karo. *Phys. Rev. Lett.*, **48**, 1128 (1982).

[102] R. King-Smith and D. Vanderbildt. *Phys. Rev. B*, **149**, 5828 (1990).

[103] P. E. Blöchl. *Phys. Rev. B*, **50**, 17953 (1994).

[104] S. R. Elliott. *The Physics and Chemistry of Solids.* Wiley, Chichester, (1998).

[105] A. Baldereschi. *Phys. Rev. B*, **41**, 5212 (1973).

[106] H. J. Monkhorst and J. D. Pack. *Phys. Rev. B*, **13**, 5188–5192 (1976).

[107] E. Davidson. *Methods in Computational Molecular physics*, volume 113 of *NATO Advanced Study Institute Series*. Plenum, New York, (1983).

[108] R. P. Feynman. *Phys. Rev.*, **56**, 340 (1939).

[109] P. Pulay. *Mol. Phys.*, **17**, 197 (1969).

[110] G. Kresse and J. Furthmuller. *Comp. Mater. Sci.*, **6**, 15–50 (1996).

[111] G. Kresse and D. Joubert. *Phys. Rev. B*, **59**, 1758–1775 (1999).

[112] G. Kresse and J. Hafner. *Phys. Rev. B*, **49**, 14251–14271 (1994).

[113] F. D. Murnaghan. *Proc. Nat. Acad. Sci. USA*, **30**(9), 244–247 (1944).

[114] C. J. Bradley and A. P. Cracknell. *Mathematical Theory of Symmetry in Solids*. Oxford Univeristy Press, (1972).

[115] D. Segev and S. H. Wei. *Phys. Rev. B*, **71**, 125129 (2005).

[116] M. Gajdos, K. Hummer, G. Kresse, J. Furthmuller and F. Bechstedt. *Phys. Rev. B.*, **73**, 045112 (2006).

[117] B. Adolph, J. Furthmuller and F. Beckstedt. *Phys. Rev. B*, **63**, 125108 (2001).

[118] P. E. Blöchl, O. Jepsen and O. K. Andersen. *Phys. Rev. B*, **49**, 16223–16233 (1994).

[119] P. Y. Yu and M. Cardona. *Fundamentals of Semiconductors*. Springer, 2 edition, (1999).

[120] L. E. Ramos, J. Paier, G. Kresse and F. Bechstedt. *Phys. Rev. B*, **78**, 195423 (2008).

[121] J. Paier, M. Marsman and G. Kresse. *Phys. Rev. B*, **78**, 121201 (2008).

[122] X. Nie, S. H. Wei and S. B. Zhang. *Phys. Rev. Lett.*, **88**, 066405 (2002).

[123] A. Walsh, J. L. F. Da Silva, Y. Yan, M. M. Al-Jassim and S. H. Wei. *Phys. Rev. B*, **79**, 073105 (2009).

[124] A. Walsh, Y. Yan, M. N. Huda, M. M. Al-Jassim and S. H. Wei. *Chem. Mater.*, **21**, 547–551 (2009).

[125] S. B. Zhang, S. H. Wei and A. Zunger. *J. Appl. Phys.*, **83**, 3192 (1998).

[126] S. B. Zhang, S. H. Wei and A. Zunger. *Phys. Rev. Lett.*, **84**, 1232 (2000).

[127] S. H. Wei and A. Zunger. *Appl. Phys. Lett.*, **72**, 2011 (1998).

[128] S.-H. Wei and A. Zunger. *Phys. Rev. Lett.*, **59**, 144–147 (1987).

[129] Y. Z. Zhu, G. D. Chen, H. Ye, A. Walsh, C. Y. Moon and S. H. Wei. *Phys. Rev. B*, **77**, 245209 (2008).

[130] A. Janotti and C. G. Van de Walle. *Phys. Rev. B*, **75**, 121201 (2007).

[131] R. F. W. Bader. *Atoms in Molecules - A Quantum Theory*. Oxford University Press, (1990).

[132] E. Sanville, S. D. Kenny, R. Smith and G. Henkelman. *J. Comp. Chem.*, **28**(5), 899 (2007).

[133] C. G. Van de Walle and J. Neugebauer. *J. Appl. Phys.*, **95**, 3851 (2004).

[134] C. Freysoldt, J. Neugebauer and C. G. Van de Walle. *Phys. Rev. Lett.*, **102**, 016402 (2009).

[135] R. M. Nieminen. *Theory of Defects in Semiconductors*. Topics in Applied Physics. Springer, (2007).

[136] S. Lany and A. Zunger. *Phys. Rev. Lett.*, **98**, 045501 (2007).

[137] K. G. Godinho, A. Walsh and G. W. Watson. *J. Phys. Chem. C*, **113**, 439–448 (2008).

[138] K. Ueda and H. Hosono. *Thin Solid Films*, **411**, 115–118 (2002).

[139] M. L. Liu, L. B. Wu, F. Q. Huang, L. D. Chen and I. W. Chen. *J. Appl. Phys.*, **102**, 116108 (2007).

[140] D. O. Scanlon and G. W. Watson. *Chem. Mater.*, **21**, 5435–5442 (2009).

[141] R. Nagarajan, N. Duan, M. K. Jayaraj, J. Li, K. A. Vanaja, A. Yokochi, A. Draeseke, J. Tate and A. W. Sleight. *Intl. J. Inorg. Mater.*, **3**, 265–270 (2001).

[142] J. Robertson, P. Peacock, M. Towler and R. Needs. *Thin Solid Films*, **411**, 96–100 (2002).

[143] I. Hamada and H. Katayama-Yoshida. *Physica B*, **376-377**, 808–811 (2006).

[144] H. Katayama-Yoshida, T. Koyanagi, H. Funashima, H. Harima and A. Yanase. *Solid State Commun.*, **126**, 135–139 (2003).

[145] H. Kizaki, K. . Sato and H. Katayama-Yoshida. *Jpn. J. Appl. Phys.*, **47**, 6488 (2008).

[146] S. Gilliland, J. F. Sanchez-Roya, J. Pellicer-Porres, A. Segura, A. Munoz, P. Rodriguez-Hernandez and J. Lopez-Solano. *Thin Solid Films*, **516**, 1431–1433 (2008).

[147] F. Zhi-Jie, S. Li-Jie and L. Yong-Hui. *Chin. Phys. B*, **17**, 4279–4284 (2008).

[148] S. L. J. Fang, Z. L. *Phys. Lett. A*, **372**, 3759–3762 (2008).

[149] L. J. Shi, Z. J. Fang and J. Li. *J. Appl. Phys.*, **104**, 073527 (2008).

[150] A. Maignan, C. Martin, R. Frésard, V. Eyert, E. Giuilmeau, S. Hébert, M. Poienar and D. Pelloquin. *Solid. State. Commun.*, **149**, 962–967 (2009).

[151] M. Poienar, F. Damay, C. Martin, V. Hardy, A. Maignan and G. Andre. *Phys. Rev. B*, **79**, 014412 (2009).

[152] T. Arnold, D. J. Payne, A. Bourlange, J. P. Hu, R. G. Egdell, L. F. J. Piper, L. Colakerol, A. De Masi, P. A. Glans, T. Learmonth, K. E. Smith, J. Guo, D. O. Scanlon, A. Walsh, B. J. Morgan and G. W. Watson. *Phys. Rev. B*, **79**, 075102 (2009).

[153] G. Kresse and J. Furthmüller. *Phys. Rev. B*, **54**, 11169–11186 (1996).

[154] B. J. Morgan, D. O. Scanlon and G. W. Watson. *e J. Surf. Sci. Nano Tech.*, **7**, 395–404 (2009).

[155] D. O. Scanlon, A. Walsh, B. J. Morgan, G. W. Watson, D. J. Payne and R. G. Egdell. *Phys. Rev. B*, **79**, 035101 (2009).

[156] H. Raebiger, S. Lany and A. Zunger. *Phys. Rev. B*, **76**, 045209 (2007).

[157] M. N. Huda, Y. Yan, A. Walsh, S. H. Wei and M. M. Al-Jassim. *Phys. Rev. B*, **80**, 135205 (2009).

[158] A. Rohrbach, J. Hafner and G. Kresse. *Phys. Rev. B*, **70**, 125426 (2004).

[159] K. Momma and F. Izumi. *J. Appl. Cryst.*, **41**, 653–658 (2008).

[160] B. U. Koehler and M. Jansen. *Zeits. Fuer. Kristall.*, **543**, 73–80 (1986).

[161] T. Ishiguro, N. Ishizawa, N. Mizutani and M. Kato. *J. Solid State. Chem.*, **49**, 232–236 (1983).

[162] T. Okuda, N. Jufuku, S. Hidaka and T. N. *Phys. Rev. B*, **72**, 144403 (2005).

[163] N. Duan, A. W. Sleight, M. K. Jayaraj and J. Tate. *Appl Phys. Lett.*, **77**, 1325 (2000).

[164] M. Trari, A. Bouguelia and Y. Bessekhouad. *Solar Energy Mater Solar Cells*, **90**, 190–202 (2005).

[165] X. L. Nie, S. H. Wei and S. B. Zhang. *Phys. Rev. B*, **65**, 075111 (2002).

[166] F. A. Benko and F. P. Koffyberg. *J. Phys. Chem. Solids*, **48**, 431–43 (1987).

[167] Y. H. Li, X. G. Gong and S. H. Wei. *Appl. Phys. Lett.*, **88**, 042104 (2006).

[168] M. Snure and A. Tiwari. *Appl. Phys. Lett.*, **91**, 092123 (2007).

[169] D. O. Scanlon, A. Walsh and G. W. Watson. *Chem. Mater.*, **21**, 4568–4576 (2009).

[170] Y. Bessekhouad, M. . Trari and J. P. Doumerc. *Int. J. Hyd. Prod.*, **28**, 43–48 (2003).

[171] M. Younsi, A. Aider, A. Bouguelia and M. Trari. *Solar Energy*, **78**, 574–580 (2005).

[172] M. Trari, A. Bouguelia and Y. Bessekhouad. *Sol. Energy Mater. Sol. Cells*, **90**, 190–202 (2006).

[173] R. Brahimi, Y. Bessekhouad, A. Bouguelia and M. Trari. *J. Photochem. Photobio. A: Chem.*, **186**, 242–247 (2007).

[174] S. Saadi, A. Bouguelia, A. Derbal and M. Trari. *J. Photochem. Photobiol. A*, **187**, 97 (2007).

[175] S. Younsi, M. Saadi, A. Bouguelia, A. Aider and M. Trari. *Solar. Energy. Mater. Solar Cells*, **91**, 1102–1109 (2007).

[176] A. Derbal, S. Omeiri, A. Bouguelia and M. Trari. *Int. J. Hyd. Prod.*, **33**, 4274–4282 (2008).

[177] S. Omeiri, B. Bellal, A. Bouguelia, Y. Bessekhouad and M. Trari. *J. Solid. State Electrochem.*, **13**, 1395–1401 (2009).

[178] M. N. Huda, Y. Yan, A. Walsh, S. H. Wei and M. M. Al-Jassim. *Appl. Phys. Lett.*, **94**, 251907 (2009).

[179] J. W. Hodby, T. E. Jenkins, C. Schwab, H. Tamura and D. Trivich. *J. Phys. C: Solid State Phys.*, **9**, 1429–1439 (1976).

[180] J. H. Park and K. Natesan. *Oxidation of Metals*, **39**, 411–435 (1993).

[181] A. Bose, S. Basu, S. Banerjee and D. Chakravorty. *J. Appl. Phys.*, **98**, 074307 (2005).

[182] R. S. Toth, R. Kilkson and D. Trivich. *Phys. Rev.*, **122**, 482–488 (1961).

[183] J. Maluenda, R. Farhi and G. Petot-Ervas. *J. Phys. Chem. Solids*, **42**, 911–921 (1981).

[184] L. C. Bourne, P. Y. Yu, A. Zettl and M. L. Cohen. *Phys. Rev. B*, **40**, 10973 (1989).

[185] T. Mahalingham, J. Chitra, S. Rajendran and P. Sebastian. *Semicond. Sci and Technol.*, **17**, 565–569 (2002).

[186] D. O. Scanlon, B. J. Morgan, G. W. Watson and A. Walsh. *Phys. Rev. Lett.*, **103**, 096405 (2009).

[187] D. O. Scanlon, B. J. Morgan and G. W. Watson. *J. Chem. Phys.*, **131**, 124703 (2009).

[188] J. Tate, M. K. Jayaraj, A. D. Draeseke, T. Ulbrich, A. W. Sleight, K. A. Vanaja, R. Nagarajan, J. F. Wager and R. L. Hoffman. *Thin Solid Films*, **411**, 119 (2002).

[189] Y. Kakehi, S. Nakao, K. Satoh and T. Yotsuya. *Thin Solid Films*, **445**, 294 (2003).

[190] K. Ueda, t. Hase, H. Yanagi, H. Kawazoe, H. Hosono, H. Ohta, M. Orita and M. Hirano. *J. Appl. Phys.*, **89**, 1790 (2001).

[191] H. Yanagi, T. Hase, S. Ibuki, k. Ueda and H. Hosono. *Appl. Phys. Lett..*, **78**, 1583 (2001).

[192] O. Madelung and M. Schulz, editors. *Landolt-Bornstein: Numerical Data and Functional Relationships in Science and technology*, volume 22a of *Group III*. Springer-Verlag, Berlin, (1987).

[193] J. P. Perdew, K. Burke and M. Ernzerhof. *Phys. Rev. Lett.*, **77**(18), 3865 (1996).

[194] M. Shimode, M. Sasaki and K. Mukaida. *J. Solid State Chem.*, **151**, 16–20 (2000).

[195] J. L. F. Da Silva, M. V. Ganduglia-Pirovano, J. Sauer, V. Bayer and G. Kresse. *Phys. Rev. B*, **75**, 045121 (2007).

[196] K. G. Godinho, D. O. Scanlon and G. W. Watson. Unpublished.

[197] J. Heyd and G. E. Scuseria. *J. Chem. Phys.*, **121**, 1187–1192 (2004).

[198] J. Heyd, J. E. Peralta, G. E. Scuseria and R. L. Martin. *J. Chem. Phys.*, **123**, 174101 (2005).

[199] S. Chen, Z. G. Gong, A. Walsh and S. H. Wei. *Appl Phys. Lett.*, **94**, 041903 (2009).

[200] J. Paier, R. Asahi, A. Nagoya and G. Kresse. *Phys. Rev. B*, **79**, 115126 (2009).

[201] J. L. F. Da Silva, A. Walsh and H. Lee. *Phys. Rev. B*, **78**, 224111 (2008).

[202] U. Eibenstein and W. Jung. *J. Solid State Chem.*, **133**, 21–24 (1997).

[203] S. Kale, S. Ogale, S. Shinde, M. Sahasrabuddhe, V. Kulkarni, R. Greene and T. Venkatesan. *Appl. Phys. Lett.*, **82**, 2100 (2003).

[204] J. N. Nian, C. C. Hu and H. Teng. *Int. J. Hydrogen Energy*, **33**, 2897 (2008).

[205] T. Mahalingham, J. S. P. Chitra, J. P. Chu, S. Velumani and P. J. Sebastian. *Sol. Energy Mater. Sol. Cells*, **88**, 209–216 (2005).

[206] B. P. Rai. *Solar Cells*, **25**, 265–272 (1988).

[207] S. L. Hulbert, B. A. Bunker, F. C. Brown and P. Pianetta. *Phys. Rev. B*, **30**, 2120 (1984).

[208] N. L. Peterson and C. L. Wiley. *J. Phys. Chem. Solids*, **45**, 281–294 (1984).

[209] A. E. Rakshani. *J. Appl. Phys.*, **69**, 2290–2295 (1991).

[210] G. P. Pollack and D. Trivich. *J. Appl. Phys.*, **46**, 163 (1975).

[211] A. E. Rakhshani. *J. Appl. Phys.*, **69**, 2365–2369 (1991).

[212] A. E. Rakhshani, Y. Makdisi and X. Mathew. *J. Mater. Sci: Mater in Elec*, **8**, 207–211 (1997).

[213] R. Garuthara and W. Siripala. *J. Lumin.*, **121**, 173–178 (2006).

[214] N. Kikuchi, K. Tonooka and E. Kusano. *Vacuum*, **80**, 756–760 (2006).

[215] A. E. Rakhshani, Y. Makdisi and X. Mathew. *Thin Solid Films*, **288**, 69–75 (1996).

[216] L. Papadimitiriou. *Solid State Electron.*, **36**, 431 (1993).

[217] G. K. Paul, Y. Nawa, H. Sato, T. Sakuri and K. Akimoto. *Appl. Phys. Lett.*, **88**, 141901 (2006).

[218] L. Papadimitiriou, C. A. Dimitriadis and L. Dozsa. *Solid State Electron.*, **31**, 1477–1482 (1988).

[219] L. Papadimitiriou. *Solid State Commun.*, **71**, 181–185 (1989).

[220] O. Porat and I. Riess. *Solid State Ionics*, **81**, 29–41 (1995).

[221] M. O'Keefe and W. J. Moore. *J. Chem. Phys.*, **36**, 3009 (1962).

[222] A. F. Wright and J. S. Nelson. *J. Appl. Phys.*, **92**, 5849–5851 (2002).

[223] M. Nolan and S. D. Elliot. *Phys. Chem. Chem. Phys.*, **8**, 5350–5358 (2006).

[224] H. Raebinger, S. Lany and A. Zunger. *Phys. Rev. B*, **76**, 045209 (2007).

[225] A. Soon, X. Y. Cui, B. Delley, S.-H. Wei and C. Stampfl. *Phys. Rev. B*, **79**, 035205 (2009).

[226] D. Redfield and R. H. Bube. *Photoinduced Defects in Semiconductors.* Cambridge Univeristy Press, (1996).

[227] J. Ghijsen, L. H. Tjeng, J. van Elp, H. Eskes, J. Westerink, G. A. Sawatzky and M. T. Czyzyk. *Phys. Rev. B*, **38**, 11322–11330 (1988).

[228] C. W. M. Castleton, A. Hoglund and S. Mirbt. *Phy. Rev. B*, **73**(3), 035215 (2006).

[229] A. Werner and H. D. Hochheimer. *Phys. Rev. B*, **25**, 5929 (1982).

[230] O. M. Madelung. *Semiconductors: Data Handbook*. Springer, Berlin, (2004).

[231] G. K. Paul, Y. Nawa, H. Sato, T. Sakurai and K. Akimoto. *Appl. Phys. Lett.*, **88**, 141901 (2006).

[232] G. K. Paul, R. Ghosh, . K. Bera, S, S. Bandyopadhyay, T. Sakurai and K. Akimoto. *Chem. Phys. Lett.*, **463**, 117–120 (2008).

[233] A. Mittiga, E. Salza, F. Sarto, M. Tucci and R. Vasanthi. *Appl. Phys. Lett.*, **88**, 163502 (2006).

[234] L. C. Olsen, F. W. Addis and W. Miller. *Solar Cells*, **7**, 247–279 (1982-1983).

[235] W. Siripala and J. R. P. Jayakody. *Sol.Energy. Mater.*, **14**, 23–27 (1986).

[236] C. Jayewardena, K. P. Hewaparakrama, D. L. A. Wijewardena and H. Guruge. *Sol. Energy Mater. Sol. Cells*, **56**, 29–33 (1998).

[237] C. A. N. Fernando and S. K. Wetthasinghe. *Sol. Energy Mater. Sol. Cells*, **63**, 299–308 (2000).

[238] R. Garuthara and W. Siripala. *J. Lumin.*, **121**, 173–178 (2006).

[239] L. Wang and M. Tao. *Electrochem. Solid State Lett.*, **10**, H248–H250 (2007).

[240] W. Wang, D. Wu, Q. Zhang, L. Wang and M. Tao. *J. Appl. Phys.*, **107**, 123717 (2010).

[241] C. G. Van de Walle. *Phys. Stat. Sol. B*, **235**, 89–95 (2003).

[242] J. I. Pankove and N. M. Johnson. *Hydrogen in Semiconductors, Semiconductors and Semimetals*, volume 34. Academic Press, Boston, (1991).

[243] P. D. C. King, I. McKenzie and T. D. Veal. *Appl. Phys. Lett.*, **96**, 062110 (2010).

[244] A. Mittiga, F. Biccari and M. C. *Thin Solid Films*, **517**, 2469–2472 (2009).

[245] H. Raebiger, S. Lany and A. Zunger. *Phys. Rev. B*, **76**, 045209 (2007).

[246] S. Limpijumnong, J. E. Northrup and C. G. Van de Walle. *Phys. Rev. B*, **68**, 075206 (2003).

[247] S. Limpijumnong, P. Reunchan, A. Janotti and C. G. Van de Walle. *Phys. Rev. B*, **80**, 193202 (2009).

[248] C. R. A. Catlow, Z. X. Guo, M. Miskufova, S. A. Shevlin, A. G. H. Smith, A. A. Sokol, A. Walsh, D. J. Wilson and S. M. Woodley. *Phil. Trans. R. Soc. A*, **368**, 3379–3456 (2010).

[249] J. B. Varley, A. Janotti, A. K. Singh and C. G. Van de Walle. *Phys. Rev. B*, **79**, 245206 (2009).

[250] J. Neugebauer and C. G. Van de Walle. *Phys. Rev. Lett.*, **75**, 4452–4455 (1995).

[251] W. Götz, N. M. Johnson, J. Walker, D. P. Bour and R. A. Street. *App. Phys. Lett.*, **68**, 667 (1996).

[252] A. Janotti, E. Snow and C. G. Van de Walle. *Appl. Phys. Lett.*, **95**, 172109 (2009).

[253] G. H. Vineyard. *J. Phys. Chem. Solids*, **3**, 121–127 (1957).

[254] J. Bloem. *Phillips Res. Reports*, **13**, 167 (1958).

[255] J. D. Schick and D. Trivich. *J. Electrochem. Soc.*, **119**, 376 (1972).

[256] M. Y. Onmisi. *Intl. J. Phys. Sci.*, **3**, 194–196 (2008).

[257] D. O. Scanlon, K. G. Godinho, B. J. Morgan and G. W. Watson. *J. Chem. Phys.*, **132**, 024707 (2010).

[258] W. Lan, W. L. Cao, M. Zhang, Z. Q. Liu, Y. Y. Wang, E. Q. Xie and H. Yan. *J. Mater. Sci.*, **44**, 1594–1599 (2009).

[259] J. Liu, S. Lee and C. Yang. *Mater. Trans.*, **49**, 1694–1697 (2008).

[260] Ç. Kiliç and A. Zunger. *Phys. Rev. B*, **68**, 075201 (2003).

[261] K. Otte, G. Lippold, D. Hirsch, R. K. Gebhardt and T. Chassé. *Appl. Surf. Sci.*, **179**, 203–208 (2001).

[262] J. Nian, C. Tsai, P. Lin and H. Teng. *J. Electrochem. Soc.*, **156**, H567–H573 (2009).

[263] W. M. Sears and E. Fortin. *Solar Energy Mater.*, **10**, 93–103 (1984).

[264] J. A. Assimos and D. Trivich. *J. Appl. Phys. B*, **44**, 1687–1693 (1973).

[265] X. Han, K. Han and M. Tao. *Electrochem. Solid State Lett.*, **12**, H89–H91 (2009).

[266] D. S. Kim, S. J. Park, E. K. Jeong, H. K. Lee and S. Y. Choi. *Thin Solid Films*, **515**, 5103–5108 (2007).

[267] J. Pellicer-Porres, A. Segura, A. S. Gilliland, A. Munoz, Rodriguez-Hernandez, D. Kim, M. S. Lee and T. Y. Kim. *Appl. Phys. Lett.*, **88**, 181904 (2006).

[268] J. Tate, H. L. Ju, J. C. Moon, A. Zakutayev, A. P. Richard, J. Russell and D. H. McIntyre. *Phys. Rev. B*, **80**, 165206 (2009).

[269] J. Vidal, F. Trani, F. Bruneval, M. A. L. Marques and S. Botti. *Phys. Rev. Lett.*, **104**, 136401 (2010).

[270] H. Katayama-Yoshida, T. Koyanagi, H. Funashima, H. Harima and A. Yanase. *Sol. Stat. Comm.*, **126**, 135–139 (2003).

[271] J. Paier, M. Marsman, K. Hummer, G. Kresse, I. C. Gerber and J. G. Ángyán. *J. Chem. Phys.*, **124**, 154709–154713 (2006).

[272] T. Koyanagi, H. Harima, A. Yanase and H. Katayama-Yoshida. *J. Phys. Chem. Solids*, **64**, 1443–1446 (2003).

[273] A. Walsh, Y. Yan, M. M. Al-Jassim and S. H. Wei. *J. Phys. Chem. C*, **125**, 12044–12050 (2008).

[274] C. Persson, Y.-J. Zhao, S. Lany and A. Zunger. *Phys. Rev. B*, **72**, 035211 (2005).

[275] T. Okuda, T. Onoe, Y. Beppu, N. Terada, T. Doi, S. Miyasaka and Y. Tokura. *J. Magn. Magn. Mater.*, **310**, 890–892 (2007).

[276] S. Luo, K. F. Wang, S. Z. Li, X. W. Dong, Z. B. Yan, H. L. Cai and J. Liu. *App. Phys. Lett.*, **94**, 172504 (2009).

[277] K. Kimura, H. Nakamura, S. Kimura, M. Hagiwara and T. Kumura. *Phys. Rev. Lett.*, **103**, 107201 (2009).

[278] M. Soda, K. Kimura, T. Kimura, M. Matsuura and H. K. *J. Phys. Soc. Jpn.*, **78**, 124703 (2009).

[279] K. Kimura, T. Otani, H. Nakamura, Y. Wakabayashi and T. Kimura. *J. Phys. Soc. Jpn.*, **78**, 113710 (2009).

[280] O. S. Yamaguchi, H, S. Kimura, M. Hagiwara, K. Kimura, T. Kimura, T. Okuda and K. Kindo. *Phys. Rev. B*, **81**, 033104 (2010).

[281] H. Yamaguchi, S. Otomo, S. Kimura, M. Hagiwara, K. Kimura, T. Kimura and K. Kindo. *J. Low Temp. Phys.*, **159**, 130–133 (2010).

[282] T. Okuda, Y. Beppu, Y. Fujii, T. Kishimoto, K. Uto, T. Onoe, N. Jufuku, S. Hidaka, N. Terada and S. Miyasaka. *J. Phys.: Conf. Series*, **150**, 042157 (2009).

[283] M. Poienar, F. Damay, C. Martin, J. Robert and S. Petit. *Phys. Rev. B*, **81**, 104411 (2010).

[284] S. Luo, L. Li, K. F. Wang, S. Z. Li, X. W. Dong, Z. B. Yan and J. Liu. *Thin Solid Films*, (2010).

[285] R. Rao, A. Dandekar, R. T. K. Baker and M. A. Vannice. *J. Catal.*, **171**, 406–429 (1997).

[286] S. Zhou, X. Fang, Z. Deng, D. Li, W. Dong, R. Tao, G. Meng and T. Wang. *Sens. Actuators, B*, **143**, 119–123 (2009).

[287] Z. Deng, X. Fang, D. Li, S. Zhou, R. Tao, W. Dong, T. Wang, G. Meng and X. Zhu. *J. Alloys. Compd.*, **484**, 619–621 (2009).

[288] Y. Ono, K. Satoh, T. Nozaki and T. Kajitani. *Jpn. J. Appl. Phys.*, **46**, 1071–1075 (2007).

[289] K. Hayashi, K. Sato, T. Nozaki and T. Kajitani. *Jpn. J. Appl. Phys.*, **47**, 59–63 (2008).

[290] S. Saadi, A. Bouguelia and M. Trari. *Solar Energy*, **80**, 272–280 (2006).

[291] W. Ketir, A. Boug and M. Trari. *Water Air Soil Pollut.*, **199**, 115–122 (2009).

[292] W. Ketir, A. Bougu and M. Trari. *Desalination*, **244**, 144–152 (2009).

[293] W. Ketir, A. Bouguelia and M. Trari. *J. Hazard. Mater.*, **158**, 257–263 (2008).

[294] F. A. Benko and F. P. Koffyberg. *Mat. Res. Bull.*, **21**, 753–757 (1986).

[295] A. C. Rastogi, S. H. Lim and S. B. Desu. *J. Appl. Phys.*, **104**, 032712 (2008).

[296] S. Mahapatra and S. A. Shivashankar. *Chem. Vap. Deposition*, **9**, 238–240 (2003).

[297] D. Li, X. D. Fang, Z. H. Deng, S. Zhou, R. H. Tao, W. W. Dong, T. Wang, Y. P. Zhao, G. Meng and X. B. Zhu. *J. Phys. D. - Appl. Phys.*, **40**, 4910–4915 (2007).

[298] D. Li, X. Fang, A. Zhao, Z. Deng, W. Dong and R. Tao. *Vacuum*, **84**, 851–856 (2010).

[299] R. Bywalez, S. Gotzendorfer and P. Lobmann. *J. Mater. Chem.*, **20**, 6562–6570 (2010).

[300] P. W. Sadik, M. Ivill, V. Craciun and D. P. Norton. *Thin Solid Films*, **517**, 3211–3215 (2009).

[301] W. T. Lim, L. Stafford, P. W. Sadik, D. P. Norton, S. J. Pearton, Y. L. Wang and F. Ren. *Appl. Phys. Lett.*, **90**, 142101 (2007).

[302] S. Zhou, X. Fang, Z. Deng, D. Li, W. Dong, R. Tao, T. Meng and X. Zhu. *J. Cryst. Growth*, **310**, 5375–5379 (2008).

[303] M. O'Sullivan, P. Stamenov, J. Alaria, M. Venkatesan and J. M. D. Coey. *J. Phys.: Conf. Series*, **200**, 052021 (2010).

[304] S. Zheng, G. S. Jiang, J. R. Su and C. F. Zhu. *Mater. Lett.*, **60**, 3871–3873 (2006).

[305] T. Okuda, Y. Beppu, T. Onoe, N. Terada and S. Miyasaka. *Phys Rev. B*, **77**, 134423 (2005).

[306] F. A. Benko and F. P. Koffyberg. *J. Phys. Chem. Solids*, **45**, 57–59 (1984).

[307] D. O. Scanlon, G. W. Watson, D. J. Payne, G. R. Atkinson, R. G. Egdell and D. S. L. Law. *J. Phys. Chem. C*, **114**, 4636–4645 (2010).

[308] O. Crottaz and F. Kubel. *Zeits. Fuer. Kristall.*, **211**, 481 (1996).

[309] D. O. Scanlon and G. W. Watson. *J. Phys. Chem. Lett.*, **1**, 3195–3199 (2010).

[310] D. R. Lide, editor. *CRC Handbook of Chemistry and Physics*. CRC Press, 79th edition, (1998).

[311] D. O. Scanlon, A. Walsh, B. J. Morgan, M. Nolan, J. Fearon and G. W. Watson. *J. Phys. Chem. C*, **111**, 7971–7979 (2007).

[312] D. O. Scanlon and G. W. Watson. *J. Phys. Chem. Lett.*, **1**, 2582–2585 (2010).

[313] H. Mizoguchi, M. Hirano, S. Fujitsu, T. Tomonari, K. Ueda and H. Hosono. *Appl. Phys. Lett.*, **80**, 1207 (2002).

[314] G. B. Wilson-Short, D. J. Singh, M. Fornari and M. Suewattana. *Phys. Rev. B*, **75**, 035121 (2007).

[315] D. J. Singh, R. C. Rai, J. L. Musfeldt, S. Auluck, N. Singh, P. Khalifah, S. McClure and D. G. Mandrus. *Chem. Mater.*, **18**, 2696–2700 (2006).

[316] S. Narishuma, H. Mizoguchi, K. Shimizu, K. Ueda, H. Ohta, M. Hirano and H. Kamiya, T. Hosono. *Adv. Mater.*, **15**, 1409–1413 (2003).

[317] T. Kamiya, S. Narushima, H. Mizoguchi, K. Shimizu, K. Ueda, H. Ohta, H. M. and H. Hosono. *Adv. Funct. Mater.*, **15**, 968–964 (2005).

[318] H. Ohta, H. Mizoguchi, H. Hirano, S. Narushima, T. Kamiya and H. Hosono. *Appl. Phys. Lett.*, **82**, 832 (2003).

[319] N. Mansourian-Hadavi, S. Wansom, N. H. Perry, A. R. Nagaraja, T. O. Mason, L. Ye and A. J. Freeman. *Phys. Rev. B*, **81**, 075112 (2010).

[320] M. Dekkers, G. Rijnders and D. H. A. Blank. *Appl. Phys. Lett.*, **90**, 021903 (2007).

[321] C. K. Jørgensen. *Modern Aspects of Ligand Field Theory.* North-Holland Pub. Co., Amsterdam, The Netherlands, (1971).

[322] X. Niu, W. Du and W. Du. *Sens. Actu. B*, **99**, 405–409 (2004).

[323] G. Y. Zhang, B. Guo and J. Chen. *Sens. Actu. B*, **114**, 402–409 (2006).

[324] B. Chi, J. Li, X. Yang, H. Lin and N. Wang. *Electrochimica Acta*, **50**, 2059–2064 (2005).

[325] K. Karthikeyan, D. Kelpana and N. G. Renganathan. *Ionics*, **15**, 107–110 (2009).

[326] C. Ai, M. Yin, C. Wang and J. Sun. *J. Mater. Sci.*, **39**, 1077–1079 (2004).

[327] Y. Sharma, N. Sharma, G. V. Subba Rao and B. V. R. Chowdari. *Adv. Funct. Mater.*, **17**, 2855–2861 (2007).

[328] Y. Qui, S. Yang, H. Deng, L. Jin and W. Li. *J. Mater. Chem.*, **20**, 4439–4444 (2010).

[329] H. J. Kim, I. C. Song, J. H. Sin, H. Kim, D. Kim, Y. E. Ihm and W. K. Choo. *Phys. Stat. Sol. B*, **241**, 1553–1556 (2004).

[330] H. J. Kim, I. C. Song, J. H. Sim, H. Kim, D. Kim, Y. E. Ihm and W. K. Choo. *J. Appl. Phys.*, **95**, 7387–7389 (2004).

[331] K. Samanta, P. Bhattacharya, R. S. Katiyar, W. Iwamoto, R. R. Urbano, P. G. Pagliuso and C. Rettori. *Mater. Res. Soc. Symp. Proc.*, **891**, 0891 (2006).

[332] F. Bertaut, F. Forrat and J. Dulac. *C. R. Acad. Sci. Fr.*, **249**, 726–727 (1959).

[333] K. Krezhov and P. Konstantinov. *J. Phys. Condens. Matt.*, **5**, 9287–9284 (1993).

[334] R. D. Shannon. *Acta Cryst. A*, **32**, 155–169 (1976).

[335] D. J. Payne, R. G. Egdell, D. S. L. Law, P. A. Glans, T. Learmonth, K. E. Smith, J. H. Guo, A. Walsh and G. W. Watson. *J. Mater. Chem.*, **178**, 1422–1428 (2007).

[336] D. J. Payne, R. G. Egdell, A. Walsh, G. W. Watson, J. H. Guo, P. A. Glans, T. Learmonth and K. E. Smith. *Phys. Rev. Lett.*, **96**, 157403 (2006).

[337] D. Shin, J. S. Foord, D. J. Payne, T. Arnold, D. J. Aston, R. G. Egdell, K. G. Godinho, D. O. Scanlon, B. J. Morgan, G. W. Watson, E. Mugnier, C. Yaicle,

A. Rougier, P. A. Glans, L. F. J. Piper and K. E. Smith. *Phys. Rev. B*, **80**, 233105 (2009).

[338] R. Janes and E. Moore. *Metal Ligand Bonding.* Royal Soc. Chem., (2004).

[339] C. J. Exarhos, C. F. Windisch, K. F. Ferris and R. R. Owings. *Appl. Phys. A*, **89**, 9–18 (2007).

[340] C. S. Cheng, M. Serizawa, H. Sakata and T. Hirayama. *Mater. Chem. Phys.*, **53**, 225–230 (1998).

[341] H. Yanagi, T. Hase, S. Ibuki, K. Ueda and H. Hosono. *Appl. Phys. Lett.*, **78**, 1583–1585 (2001).

[342] K. Ueda, T. Hase, H. Yanagi, H. Kawazoe, H. Hosono, H. Ohta, M. Orita and M. Hirano. *J. Appl. Phys.*, **89**, 1790–1793 (2001).

[343] K. Ueda, H. Hiramatsu, M. Hirano, T. Kamiya and H. Hosono. *Thin Solid Films*, **496**, 8–15 (2006).

[344] M. L. Liu, L. B. Wu, F. Q. Huang, L. D. Chen and J. A. Ibers. *J. Solid. State. Chem.*, **180**, 62–69 (2007).

[345] S. J. Clarke, P. Adamson, S. J. C. Herkelrath, O. J. Rutt, D. R. Parker, M. J. Pitcher and C. F. Smura. *Inorg. Chem.*, **47**, 8473–8486 (2008).

[346] H. Jiramatsu, K. Ueda, H. Ohta, M. Orita, M. Hirano and H. Hosono. *Thin Solid Films*, **411**, 125–128 (2002).

[347] K. Ueda, H. Hosono and N. Hamada. *J. Phys. Conds. Matter*, **16**, 5179–5186 (2004).

[348] H. Hiramatsu, K. Ueda, H. Ohta, H. Hirano, M. Kikuchi, H. Yanagi, T. Kamiya and H. Hosono. *Appl. Phys. Lett.*, **91**, 012104 (2007).

[349] A. Walsh and G. W. Watson. *J. Solid State Chem.*, **178**, 1422–1428 (2005).

[350] K. Otzschi, H. Ogino, J. Shimoyama and K. Kishio. *J. Low Temp. Phys.*, **117**, 729–733 (1999).

[351] H. Hiramatsu, H. Yanagi, T. Kamiya, K. Ueda, M. Hirano and H. Hosono. *Chem. Mater.*, **20**, 326–334 (2008).

[352] K. Ueda, K. Takafuji, H. Yanagi, T. Kamiya, H. Hosono, H. Hiramatsu, M. Hirano and N. Hamada. *J. Appl. Phys.*, **102**, 113714 (2007).

[353] H. Hiramatsu, K. Ueda, H. Ohta, M. Hirano, T. Kamiya and H. Hosono. *Thin. Solid Films*, **445**, 304–308 (2003).

[354] R. W. Brander. *Rev. Phys. Technol.*, **21**, 145–194 (1972).

[355] A. Kudo and Y. Miseki. *Chem. Soc. Rev.*, **38**, 253–278 (2009).